Title

Characteristics of Energetic Charged Particle Isotropy Boundaries in Earth's Magnetosphere

ISBN

9798263312114

Author

Wilkins, Colin William

Publication Date

2025-11-13

Peer reviewed|Thesis/dissertation

UNIVERSITY OF CALIFORNIA
Los Angeles

Characteristics of Energetic Charged Particle Isotropy Boundaries in Earth's Magnetosphere

A dissertation submitted in partial satisfaction
of the requirements for the degree
Doctor of Philosophy in Geophysics and Space Physics

by

Colin Wilkins

2025

ABSTRACT OF THE DISSERTATION

Characteristics of Energetic Charged Particle Isotropy Boundaries in Earth's Magnetosphere

by

Colin Wilkins
Doctor of Philosophy in Geophysics and Space Physics
University of California, Los Angeles, 2025
Professor Vassilis Angelopoulos, Chair

In this dissertation, I investigate the observational characteristics of 50 keV to ∼5 MeV electron and 50 keV to ∼2 MeV proton isotropy boundaries in Earth's magnetosphere. Viewed from Low Earth Orbit, the isotropy boundary (IB) is the magnetic latitude poleward of which persistently isotropic pitch-angle distributions ($J_{prec}/J_{perp} \sim 1$) are first detected, representing a fundamental transition from an adiabatic "inner magnetosphere" to a non-adiabatic "outer magnetosphere." The IB is a near-instantaneous tracer of the equatorial magnetospheric field configuration, and provides a means to remote-sense its evolution under any geomagnetic conditions.

Here, I use particle data from the ELFIN mission to characterize the IB distribution in local time, energy, geomagnetic activity, and ≥50 keV precipitation from isotropic particles. I find these IBs primarily exhibit negative energy-latitude dispersion patterns consistent with equatorial magnetic field-line curvature (FLC) scattering, with a 10%-30% chance of any particular energy channel exhibiting mesoscale-embedded positive dispersion structures, associated with wave-particle interactions and localized B_z gradients. The lowest latitude and most energetic IBs were in the pre-midnight sector, consistent with the location of maximal cross-tail current-sheet thinning. I identify that electron and proton IBs form the lower-latitude boundary of an FLC-dominated transition region, separating the outer radiation belt/ring current from the inner edge of the plasma sheet ("PS2ORB" and "PS2RC"), resulting in perpetual loss of electrons and protons exceeding typical

plasma sheet energies. I show this $\geq$50 keV precipitation is often sufficiently intense and distributed to produce ionization enhancements over a range of altitudes at auroral/sub-auroral latitudes.

Lastly, I use the information-theoretic technique of Mutual Information (MI) to characterize the drivers of IB characteristics in the solar wind and magnetosphere. From these observables, I construct an empirical predictive model of IB properties, which had previously never been reported for electrons, and extends the previously reported <200 keV proton IB models up to MeV energies. These results demonstrate a deep connection between the IB latitude, particle precipitation, and the evolution of the magnetosphere.

The dissertation of Colin Wilkins is approved.

Jacob Bortnik

Marco CM Velli

Hao Cao

Vassilis Angelopoulos, Committee Chair

University of California, Los Angeles

2025

Table of Contents

List of Figures

List of Tables

List of Acronyms

- AE - Auroral Electrojet (index)
- Dst - Storm-time horizontal magnetic field disturbance (index)
- ELFIN - Electron Losses and Fields Investigation
- EPD - Energetic Particle Detector
- EPD-E - Energetic Particle Detector for electrons
- EPD-I - Energetic Particle Detector for ions
- FGM - Fluxgate Magnetometer
- FLC - Field-line curvature
- FLCS - Field-line curvature scattering
- GSM - Geocentric Solar Magnetospheric
- IEFlux - Energy-integral, latitude-averaged energy flux
- IB - Isotropy boundary
- IBe - Electron isotropy boundary
- IBp - Proton isotropy boundary
- IGRF - International Geomagnetic Reference Field
- IMF - Interplanetary magnetic field
- IRB - Inner radiation belt
- Kp - Planetary K (index)
- LEO - Low Earth Orbit

– MLAT - Magnetic latitude

– MLT - Magnetic local time

– NASA - National Aeronautics and Space Administration

– NOAA - National Oceanic and Atmospheric Administration

– NSF - National Science Foundation

– OMNI[1] - "no special abbreviation, just *variety*"

– PA - Pitch-angle

– PS2ORB - Plasma Sheet to Outer Radiation Belt interface

– PS2RC - Plasma Sheet to Ring Current interface

– POES - Polar-orbiting Operational Environmental Satellite

– SPEDAS - Space Physics Environmental Data Analysis System

– SW - Solar wind

– T89 - Tsyganenko 1989 magnetic field model

– THEMIS - Time History of Events and Macroscale Interactions during Substorms

– UCLA - University of California, Los Angeles

– ULF - Ultra low frequency

– UV - Ultraviolet

– VLF - Very low frequency

[1]Quoted from https://omniweb.gsfc.nasa.gov/html/about_data.html

Acknowledgments

A number of people have had a profound impact in the shaping and success of my early career. First, and foremost, I am eternally grateful for the support of my advisor, Prof. Vassilis Angelopoulos. His guidance, resourcefulness, and open-mindedness have made this dissertation possible. He has been a wonderful mentor and colleague, always informing and inspiring my efforts in both a geophysical research and technical development capacity. In this spirit, I would also thank the researchers in the UCLA EPSS Experimental Space Physics (ESP) group, and especially Anton Artemyev and Andrei Runov, for providing invaluable insight into space physics, including my introduction to this thesis topic. I would also share my emphatic appreciation toward the members of the both the technical staff and students in the ESP group and on the ELFIN team, including Ethan Tsai, Ryan Caron, Emmanuel Masongsong, Fik Beyene, Pat Cruce, and Cindy Russell, who brought to life a prolific mission, and who collectively provided one of the most productive learning environments imaginable. I must also express my gratitude toward the members of this committee, from whom I have absorbed a great deal of advanced knowledge, including Prof. Bortnik and his courses in Solar System particle processes (AOS 250B) and space weather/data science (AOS 259), and from Prof. Velli and his course in space/solar plasmas (EPSS 240), and in the plenty of interesting discussions with Prof. Cao in space physics journal club (EPSS 293). In this vein, my education would not be complete without fundamental instruction in electromagnetism and plasma physics by Profs. Russell (EPSS 200C), Carter (PHYS 210A/B), Morales (PHYS 222A/B), Gekelman (PHYS 180E), and Mori (PHYS M122), whose varied perspectives provided valuable and well-rounded viewpoints from all angles of space/plasma science. Tracing my origins, I am humbled by the opportunity to laud my pre-graduate physics and engineering mentors at the UC Berkeley Space Sciences Laboratory (SSL), including Thomas Immel, Scott England, Stephen Mende, Harald Frey, Dave McMahon, Will Rachelson, Stu Harris, Dorothy Gordon, and Matt Dexter, without whose tutelage and interaction I may never have pursued a career in this field. Lastly, I must extend heartfelt gratitude to my family and friends—and especially my mother and brothers, who have been unconditionally supportive in the spectrum of life experience leading to the completion of this work.

This thesis draws from a number of published works I have been involved in. Chapter 2 is based in part on: Angelopoulos, V., Tsai, E., Bingley, L. et al. The ELFIN Mission. Space Sci Rev 216, 103 (2020). https://doi.org/10.1007/s11214-020-00721-7

Chapters 3 and 4 are both based in part on:

1. Wilkins, C., Angelopoulos, V., Runov, A., Artemyev, A., Zhang, X.-J., Liu, J., & Tsai, E. (2023). Statistical characteristics of the electron isotropy boundary. Journal of Geophysical Research: Space Physics, 128, e2023JA031774. https://doi.org/10.1029/2023JA031774

2. Wilkins, C., Angelopoulos, V., Runov, A., Artemyev, A., Zhang, X.-J., Liu, J., & Tsai, E. (2025). Statistical characteristics of the proton isotropy boundary. Journal of Geophysical Research: Space Physics, TBD. https://doi.org/10.1029/2024JA033412 [Accepted pending minor revision]

Chapter 5 is based on the manuscript: Wilkins, C., et al. (2025), Empirical model of >50 keV electron and proton isotropy boundaries. [JGR submission imminent]

- Colin Wilkins

Final Defense on October 1, 2025

I acknowledge funding support from NASA SMD grants NNX14AN68G, 80NSSC19K1439, NASA contract NAS5-02099, NSF Division of Atmospheric and Geospace Sciences and grant grants AGS-1242918, AGS-2019914, and Air Force Office of Scientific Research grant FA9453-12-D-0285

Curriculum Vitae

2025	M.S. & Ph.D. (expected), Geophysics and Space Physics, UCLA
2014	B.A., Physics & B.S., Electrical Engineering and Computer Sciences (EECS), University of California, Berkeley
2014-2016	UC Berkeley Space Sciences Laboratory, R&D Engineer II
2009	Optical Navigation Group, Jet Propulsion Laboratory, Summer intern
2022	Top IMAG Poster, Geospace Environment Modeling (GEM) workshop
2020	Vela Fellowship awardee, Los Alamos National Laboratory (LANL) Space Weather Summer School [declined offer due to conflict]
2019-2022	NASA SMD Heliophysics Future Investigators in NASA Earth and Space Science and Technology (FINESST) research grant awardee
2019	Top Poster, UCLA Institute of Digital Research and Education (IDRE) Early-Career Researcher Day
2009	Caltech Summer Undergraduate Research (SURF) Fellowship

Publications

1. Wilkins, C., Angelopoulos, V., Runov, A., Artemyev, A., Zhang, X.-J., Liu, J., & Tsai, E. (2025). Statistical Characteristics of the Proton Isotropy Boundary. Journal of Geophysical Research: Space Physics [Manuscript 2024JA033412, accepted pending minor revision]
2. Wilkins, C., Angelopoulos, V., Runov, A., Artemyev, A., Zhang, X.-J., Liu, J., & Tsai, E. (2023). Statistical Characteristics of the Electron Isotropy Boundary. Journal of Geophysical Research: Space Physics, 128(10). https://doi.org/10.1029/2023ja031774
3. Angelopoulos, V., et al. (2020). The ELFIN Mission. Space Science Reviews, 216(5). https://doi.org/10.1007/s11214-020-00721-7
4. Wilkins, C. W., Mende, S. B., Frey, H. U., & England, S. L. (2017). Time-Delay Integration Imaging with ICON's Far-Ultraviolet Imager. Space Science Reviews, 212(1-2), 715-730. https://doi.org/10.1007/s11214-017-0410-4
5. Shumko, M., et al. (2025). On the Spatial Relationship Between the Aurora and Relativistic Electron Precipitation During a Storm-Time Substorm. Geophysical Research Letters, 52(17). https://doi.org/10.1029/2025gl116477
6. Artemyev, A. V., et al. (2025). Coupling Between Earth's Magnetotail and the Outer Radiation Belt via Field-Line Curvature Scattering. Journal of Geophysical Research: Space Physics, https://doi.org/10.1029/2025ja034184
7. Tsai, E., et al. (2025). Remote sensing of electron precipitation mechanisms enabled by ELFIN mission operations and ADCS. Advances in Space Research, 75(9), 6706-6 https://doi.org/10.1016/j.asr.2024.07.008

8. Shen, X., et al. (2025). Whistler Mode Wave-Driven Electron Scattering Properties From ELFIN Measurements of the Precipitation Ratio. Journal of Geophysical Research: Space Physics, 130(4). https://doi.org/10.1029/2024ja033363

9. Artemyev, A. V., et al. (2024). Categorization of Electron Isotropy Boundary Patterns: ELFIN and POES Observations. Journal of Geophysical Research: Space Physics, 129(12). https://doi.org/10.1029/2024ja033231

10. Bashir, M. F., et al. (2024). Observations of Relativistic Electron Precipitation Due To Combined Scattering of Whistler-Mode and EMIC Waves. Journal of Geophysical Research: Space Physics, 129(5). https://doi.org/10.1029/2024ja032432

11. Shen, Y., et al. (2023). Energetic Electron Flux Dropouts Measured by ELFIN in the Ionospheric Projection of the Plasma Sheet. Journal of Geophysical Research: Space Physics, 128(9). https://doi.org/10.1029/2023ja031631

12. Angelopoulos, V., et al. (2023). Energetic Electron Precipitation Driven by Electromagnetic Ion Cyclotron Waves from ELFIN's Low Altitude Perspective. Space Science Reviews, 219(5). https://doi.org/10.1007/s11214-023-00984-w

13. Shen, Y., et al. (2023). Contribution of Kinetic Alfvén Waves to Energetic Electron Precipitation From the Plasma Sheet During a Substorm. Journal of Geophysical Research: Space Physics, 128(4). https://doi.org/10.1029/2023ja031350

14. Artemyev, A. V., et al. (2022). Thinning of the Magnetotail Current Sheet Inferred From Low-Altitude Observations of Energetic Electrons. Journal of Geophysical Research: Space Physics, 127(10). https://doi.org/10.1029/2022ja030705

15. Shen, Y., et al. (2022). Tens to Hundreds of keV Electron Precipitation Driven by Kinetic Alfvén Waves During an Electron Injection. Journal of Geophysical Research: Space Physics, 127(8). https://doi.org/10.1029/2022ja030360

16. Artemyev, A. V., et al. (2022). On the Nature of Intense Sub-Relativistic Electron Precipitation. Journal of Geophysical Research: Space Physics, 127(6). https://doi.org/10.1029/2022ja030571

17. Zhang, X., et al. (2022). Characteristics of Electron Microburst Precipitation Based on High-Resolution ELFIN Measurements. Journal of Geophysical Research: Space Physics, 127(5). https://doi.org/10.1029/2022ja030509

18. Zhang, X.-J., et al. (2022). Superfast precipitation of energetic electrons in the radiation belts of the Earth. Nature Communications, 13(1). https://doi.org/10.1038/s41467-022-29291-8

19. Mourenas, D., et al. (2021). Electron Lifetimes and Diffusion Rates Inferred From ELFIN Measurements at Low Altitude: First Results. Journal of Geophysical Research: Space Physics, 126(11). https://doi.org/10.1029/2021ja029757

20. Mende, S. B., et al. (2017). The Far Ultra-Violet Imager on the Icon Mission. Space Science Reviews, 212(1-2), 655–696. https://doi.org/10.1007/s11214-017-0386-0

21. "UCLA researchers discover source of super-fast 'electron rain' ", 2022 UCLA Newsroom[2]

22. "IDRE Early Career Research Day Winner uses statistical machine learning to improve space weather forecasting", 2020 UCLA Institute for Digital Research and Education (featured)[3]

[2] https://newsroom.ucla.edu/releases/researchers-discover-source-of-superfast-electron-rain

[3] https://idre.ucla.edu/news/idre-early-career-research-day-winner...-space-weather-forecasting

CHAPTER 1

Introduction

This dissertation expounds on a phenomenon in Earth's magnetosphere known as the *isotropy boundary* (IB) of charged particles, whereby loss-cone filling in the strong diffusion limit results in characteristic energy- and latitude-dependent pitch-angle isotropization and ionospheric precipitation. The IB represents the location in space (or, equivalently, its ionospheric foot-point) where particles transition abruptly from adiabatic to non-adiabatic crossings of the magnetosphere's equatorial region. As I demonstrate in this work, isotropy boundaries provide a near-instantaneous measure of the large-scale evolution and structure of Earth's magnetosphere over a range of conditions, and act to directly enhance its coupling with the ionosphere. To establish the contextual background and geophysical significance underlying these processes, this chapter presents an abridged overview of the Earth's magnetosphere,[1] including concepts of charged particle dynamics and pitch-angle scattering. Building on this foundation, I introduce the isotropy boundary, accompanied by a review of pertinent historical research and open questions. The chapter concludes with an outline of thesis objectives addressed in this work.

1.1 Earth's magnetosphere: Particle and field concepts

The concept of the isotropy boundary is one rooted in the interaction of charged particles, such as electrons and protons, with electromagnetic fields in space. In this work, the primary reservoir of these particles, and the source of their pitch-angle isotropization (described below), is Earth's magnetosphere ((Borovsky and Valdivia, 2018), herein "the magneto-

[1]Supporting material and general references may be found in (Russell, 2017) and (Chen, 2016).

sphere").[2] The magnetosphere is the region of space surrounding the planet in which plasmas and energetic charged particles are largely governed by the planet's internally-generated magnetic field (colloquially, the "geomagnetic field"). In this context, "plasma" refers to a highly ionized fluid of electrons and heavier ions (e.g. protons), which is overall quasi-neutral (approximately zero net charge), and which exhibits "collective behavior," such as the ability to dynamically shield against externally-applied electric fields (implying very high electrical conductivity) (Chen, 2016).

The magnetosphere is host to a diverse population of charged particles and electromagnetic fields, giving rise to a plethora of potential dynamical interactions (Alberti, 2022). These magnetospheric particles often span a wide range of kinetic energies, as low as tenths of eVs[3] and up to 100s of MeV (>9 orders of magnitude), with number densities between 10^0-10^4 per cm^3. Depending on the region, magnetic field configurations can vary significantly in their curvature and connectivity, with strengths on the order of 10^0-10^4 nT, accompanied by electric fields of 0 to 10s of mV/m. This work concerns a subset of these particles and fields, onward using the term "energetic particles" to refer to a range of the more energetic tail (exceeding typical energies), from 10s of keV up to MeVs.

1.1.1 Solar-terrestrial interactions

As a starting point in the description of IBs, it is natural to begin with the underlying source which drives the magnetosphere: the solar wind. This stream consists of the perpetual supersonic[4] outflow of charged particles emanating from the solar corona, transporting ejected solar plasma along with the interplanetary magnetic field (IMF) in all directions (Rouillard et al., 2021). The magnetosphere separates the space surrounding the planet from solar

[2]Despite its name, the magnetosphere is *not* spherical in shape. Rather, it is more of a solar "wind sock."

[3]Particle energies are usually specified in units of electron volts (eV), defined as the energy required to accelerate an electron through a 1 volt potential. The energy required to ionize a neutral atom is often on the order of 10s of eV, down to single eVs; it is thus a useful unit in describing plasmas.

[4]Technically *super-Alfvenic*, although shock formation and Alfven wave propagation are beyond the scope of this work.

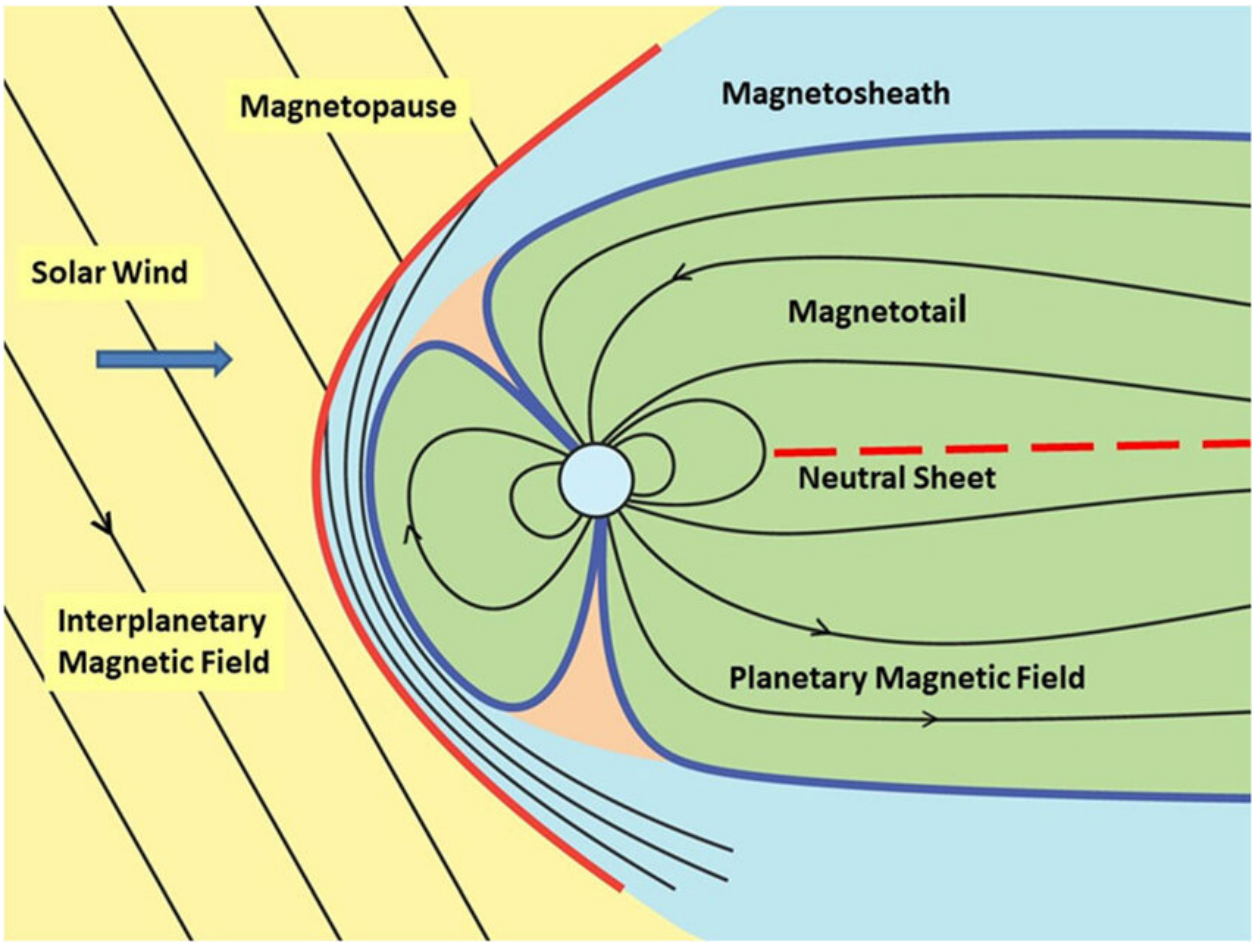

Figure 1.1: Cartoon of the solar wind-magnetosphere interaction, viewed from the noon-midnight meridian. Taken from Fig. 17 of (Tsurutani et al., 2023).

plasma, forming a current sheet interface known as the "magnetopause" (Haaland et al., 2021). Fig. 1.1 (adapted from Fig. 17 of (Tsurutani et al., 2023)) shows an example cartoon of the configuration of solar wind flow, IMF, and the magnetopause, viewed from the noon-midnight meridian. Interactions between the two systems at and near the magnetopause are ultimately responsible[5] for supplying the energy required to generate and sustain isotropy boundaries.

The solar wind and magnetosphere interact through several mechanisms, including "magnetic reconnection" on the equatorial dayside and high-latitude polar regions of the mag-

[5]Although the sun's thermal blackbody emission of electromagnetic radiation (e.g. visible, UV, and infrared wavelengths) is the predominant source of energy input to Earth's atmosphere/ionosphere.

netopause (Hesse and Cassak, 2020). This allows particle populations and plasma waves from both sides to locally cross the boundary. The magnetosphere also acts as a barrier to the bulk solar wind flow, forming a "bow shock" (Formisano, 1974). This shockwave exists indefinitely upstream of the magnetopause, acting to rapidly decelerate and compress the incident flow around the planet.[6] This increases the particle and magnetic pressure in the region immediately surrounding the magnetopause, known as the "magnetosheath" (Lucek et al., 2005), which may then further act on the magnetosphere, forcing its boundary inward or outward. Similarly, if the dynamic pressure (head-on momentum) of the upstream solar wind is enhanced, the exposed flank cross-section of the magnetosphere may be directly impacted, giving rise to shear flow instabilities such as Kelvin-Helmholtz (Faganello and Califano, 2017). Like reconnection, these instabilities allow particles to penetrate beyond the magnetopause. The effect of these processes is to drive the continual evolution of the magnetosphere's internal state. As described later, a primary objective of my thesis is to determine how the combination of magnetospheric state and upstream conditions in the solar wind affect the occurrence and properties of isotropy boundaries.

In order for isotropy boundaries to form, particles must first find their way into the equatorial magnetosphere, as well as experience energization. A primary means of achieving both conditions is through the evolution of global-scale magnetic fields in the system. Because the solar wind and magnetosphere are typically highly-conducting plasma environments, charged particles tend to be "frozen-in" to the magnetic field-lines (bundles of magnetic flux) in their vicinity—co-propagating through space like pearls on a string (Lundin et al., 2005). Consequently, the two magnetic domains do not tend to mix, forming an interface (the magnetopause) to maintain domain separation. However, under certain conditions, such as when the interplanetary magnetic field is oriented southward (opposite to Earth's northward field), the two domains can snap together like a rubber band, allowing a subset of previously disjoined field lines to "reconnect," as earlier alluded. This reconfiguration of field-lines results in a conversion of excess magnetic field energy (destroyed magnetic flux) to

[6]Imagine a jet exceeding the sound barrier.

both adiabatic and non-adiabatic particle acceleration, induction electric fields, and Poynting flux of electromagnetic/plasma waves (Oka et al., 2023). In turn, directly or indirectly, these processes establish the conditions required for isotropy boundary formation.[7]

To see how the particle transport occurs, we may follow their path-evolution upon reconnection at the dayside magnetopause. The newly-connected field line once again "freezes in" the mix of plasma, but now critically, only one end is anchored to the Earth, while the other remains (distantly) connected to the solar wind, which continually propagates downstream. To maintain continuity of the field-line, the Earth-anchored segment is forced to follow the solar wind motion over the northern and southern polar caps of the planet (Milan et al., 2017; Newell et al., 2009b), and in the process, generates a global-scale dawn-dusk electric field (and associated "polar cap potential," (Adhikari et al., 2018)). As the field-line travels down-tail, the segment within the magnetosphere curves equatorward to follow the contour of the magnetopause, beginning to "sink," forming a region of sunward (northern) and anti-sunward (southern) field lines, known as the "tail lobes" (Nishida, 2000). This process establishes a cross-tail electric field within the lobes consistent with the polar cap potential drop, accumulating energy in the form of loaded magnetic flux in the lobes. Due to the orientation of the lobe magnetic field and cross-tail electric field, particles transiting this region may drift radially inward (away from the magnetopause) toward the equatorial region, over a wide range of distances from the planet. From there, they enter the equatorial magnetosphere.

Upon reaching the equatorial magnetosphere, particles encounter yet another current sheet, known as the "cross-tail current" (Ganushkina et al., 2018), which acts to separate the northern and southern tail lobes. Like the magnetopause, the cross-tail current sheet is capable of magnetic reconnection, acting to balance the change in magnetic flux on the dayside, mediated by the amount of pre-loaded magnetic flux in the tail lobes. Co-located with the cross-tail current is a region of concentrated hot plasma known as the "plasma sheet" (Vasyliunas, 1972). Due to the reconnection process, particles in this region may

[7]While a rich topic, the particulars of magnetic reconnection are not the focus of this work.

experience further acceleration and transport, such as back toward the Earth through the process of "magnetospheric convection" ((Axford, 1969), described later), or drift east/west toward the flanks of the magnetopause due to plasma pressure and field gradients, where they are either recirculated, or reenter the solar wind. This cycle of transporting particles and magnetic flux from the dayside to the nightside, and back, is a fundamental solar-terrestrial process first described by (Dungey, 1961)[8], which continually replenishes particles and field energy required for IB evolution.

Closer to the planet, Earth's ionosphere provides an additional source of charged particles and fields accessible to the equatorial magnetosphere (Bilitza et al., 2022). In this region, high-altitude atmospheric gasses including hydrogen, oxygen, and nitrogen are ionized by solar ultraviolet (UV) radiation, as well as by energetic particle precipitation and plasma waves, to form an electrically conducting interface. Fig. 1.2 shows the typical electron density profile in the ionosphere versus altitude above the surface of Earth on the dayside and nightside, taken from (SuperDARN, 2025). The electrical conductivity imparted by these electrons is dependent on quantities such as the ionization rate and collision/recombination frequency between neutral molecules and charged particles (Rycroft et al., 2008). This conductivity, which is typically highest along the magnetic field, allows electrical currents and particles in the more distant magnetosphere and solar wind to flow directly into (and out) of the planet's high-altitude, high-latitude atmosphere (Ganushkina et al., 2018). Because the horizontal conductivity is typically smaller, these currents will tend to heat the ionosphere through collisional (ohmic) dissipation, imparting kinetic energy to the particles. The conductivity also allows the ionosphere to mediate its response to plasma waves, including their absorption, scattering, and mode-conversion.

Through particle heating from plasma waves and ohmic current dissipation, the ionosphere provides a second seed[9] population of magnetotail particles, by a process known as

[8]It is now known that the Dungey Cycle is an approximation to typical magnetospheric evolution, which does not always require equal rates of reconnection on the dayside and nightside magnetosphere.

[9]Called "seeds" because these particles are precursors which have not yet undergone the energization required to be isotropized.

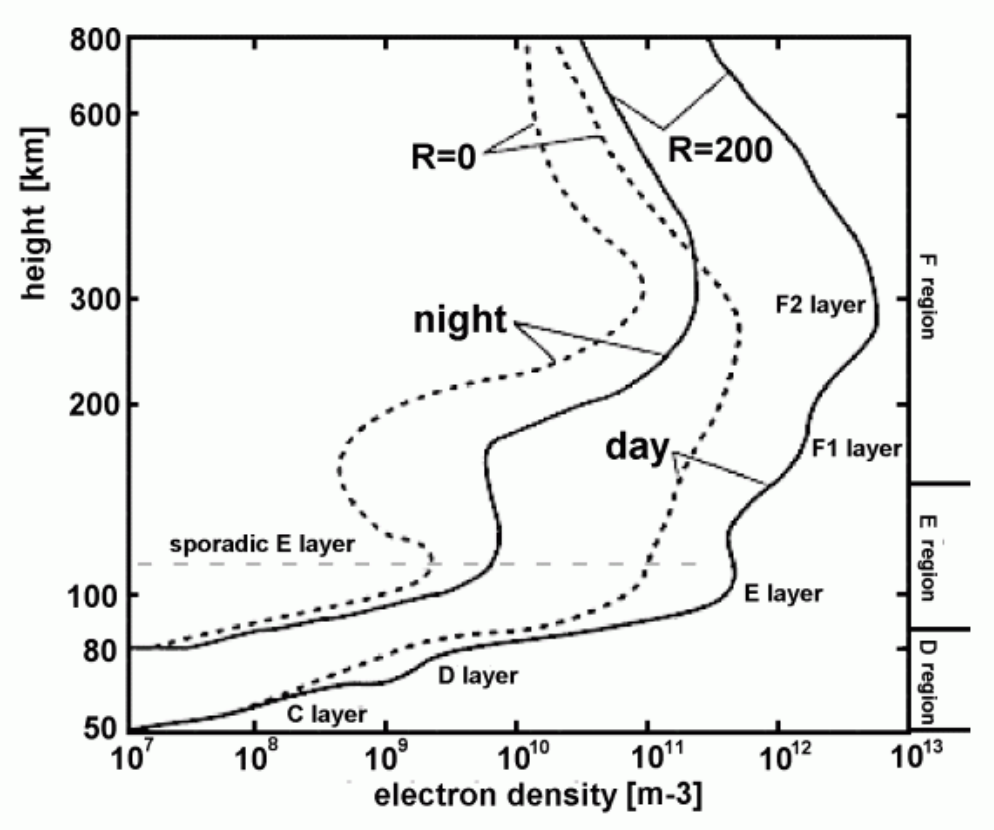

Figure 1.2: Typical electron density profiles versus altitude in the ionosphere on the dayside and nightside of Earth. Taken from (SuperDARN, 2025).

ionospheric outflow (Strangeway et al., 2005). In these events, charged particles leave the atmosphere along magnetic field-lines by virtue of being accelerated beyond gravitational escape velocity. Many end up in the magnetosphere, and are responsible for a fraction of the initial electrons and protons considered in this work. Ionospheric outflow is also responsible for the appearance of heavier ions in the magnetosphere, such as O^+ during geomagnetic storms.[10]

The net effect of the above magnetospheric and ionospheric processes is to form a coupled system, in which energy and momentum can be exchanged dynamically, as well as with the solar wind (Borovsky and Valdivia, 2018).[11] Isotropy boundaries not only serve as a near-instantaneous tracer of these system interactions, but as demonstrated later, also provide a direct contribution to their coupling through particle precipitation.

1.1.2 The Lorentz force and charged particle motion

Knowing where the charged particles and free energy originate, we may begin to address the connections between electromagnetic fields and charged particles that lead to the formation of isotropy boundaries. From the particle perspective, this interaction occurs primarily through the Lorentz force:

$$\mathbf{F} = q\left(\mathbf{E} + \mathbf{v} \times \mathbf{B}\right) \tag{1.1}$$

where q is the particle's charge (negative for electrons, and positive for heavier ions such as protons), $\mathbf{E}$ is the local electric field, $\mathbf{v}$ is the particle's velocity, $\times$ is the vector cross-product, and $\mathbf{B}$ is the local magnetic field. The Lorentz force acting over space gives rise to several fundamental types of relevant particle motion phenomena (see (Chen, 2016)):

1. **Magnetic forces and cyclotron motion**

   A fundamental scenario in understanding IB formation is that of a particle with velocity

[10] Such ions likely have their own isotropy boundaries, which present a ripe avenue for future investigation.

[11] This connection is perhaps most famously known for producing the auroral oval—the latitudinal range in which the aurora are generated.

$\mathbf{v}$ and mass m immersed in a magnetic field $\mathbf{B}$, in the absence of an external electric field (i.e., $\mathbf{E} = \mathbf{0}$). In the non-relativistic limit ($v \ll c$, where c is the speed of light), the equation of motion for such a particle reduces to:

$$\frac{d\mathbf{v}}{dt} = \frac{q}{m}\mathbf{v} \times \mathbf{B} \tag{1.2}$$

This relationship encodes two important dynamical properties. First, since the time variation in velocity $\mathbf{v}$ is perpendicular to $\mathbf{v}$ (via the cross-product), this force may change the direction of velocity, but cannot change the particle's speed $v = |\mathbf{v}|$. The particle's total kinetic energy is therefore constant. This condition is often expressed as "magnetic fields do no work,"[12] and requires that any change in speed perpendicular to the magnetic field ($v_\perp$) must be accompanied by a corresponding opposite change in parallel speed ($v_\parallel$). This property will later prove essential in describing the "magnetic mirror force," responsible for how isotropy boundary signatures may be sensed by spacecraft far away from the original location of isotropization.

Second, the strength of the acceleration in Eqn. 1.2 depends on the particle's charge-to-mass-ratio (q/m), and therefore electrons will experience a much stronger effect than heavier ions like protons ($m_p/m_e \sim 1840$) for the same particle speed. This property is critical in explaining the differing characteristics of electron versus proton isotropy boundaries. Additionally, due to the charge dependence, electrons and protons will experience the force in opposite directions, consistent with the asymmetric IB distribution in local time, later shown in Ch. 3.

The most fundamental example of Eqn. 1.2 is that of a particle immersed in a uniform magnetic field $\mathbf{B}$ (constant magnitude and direction). In a coordinate system with one axis aligned along the magnetic field, Eqn. 1.2 can be decomposed into two second-order ordinary differential equations of position and time, corresponding to uniform circular motion in the plane orthogonal to the magnetic field. The circular trajectory

[12]However, time-varying magnetic fields certainly *can* do work through their induction electric field, via Eqn. 1.17

of the particle is known as cyclotron motion, and has a characteristic (non-relativistic) angular rotation rate known as the cyclotron frequency (or gyro-frequency), given by:

$$\omega_c = qB/m \tag{1.3}$$

where $B = |\mathbf{B}|$ is the magnitude of the magnetic field. This frequency sets a natural timescale for comparison against processes involving variations in electromagnetic fields, as well as resonances with plasma waves, resulting in the possibility of non-adiabatic particle acceleration (described below). The direction of rotation also depends on the sign of the particle's charge, leading to opposite directions of motion for electrons and protons. Fig. 1.3 shows the values that ω_c may take on as a function of electron and proton energy over the range of magnetic field strengths encountered in the magnetosphere. It can be seen that for magnetospheric electrons, the frequency may span the range of 10^0 to 10^7 Hz, and 10^{-2} to 10^4 Hz for magnetospheric protons. Additionally, the introduction of the relativistic correction to the gyro-frequency (Ch. 3) results in a frequency reduction for energetic electrons in the magnetosphere, but not for protons, due to their much higher mass.

Perhaps most crucially in the context of isotropy boundary characteristics, cyclotron motion has an associated orbit radius known as the gyro-radius (or Larmor radius), which is given (non-relativistically) by:

$$r_L = v_\perp/\omega_c = mv_\perp/qB \tag{1.4}$$

where $v_\perp$ is the particle speed perpendicular to the magnetic field. As will be demonstrated later, the relative scale between the gyro-radius and the spatial variations in the magnetic field (either in strength or direction) is a critical parameter in the scattering of particles in Earth's equatorial magnetosphere. Fig. 1.4 shows the values that r_L may take on as a function of electron and proton energy over the range of magnetic field strengths encountered in the magnetosphere. Critically, in the context of

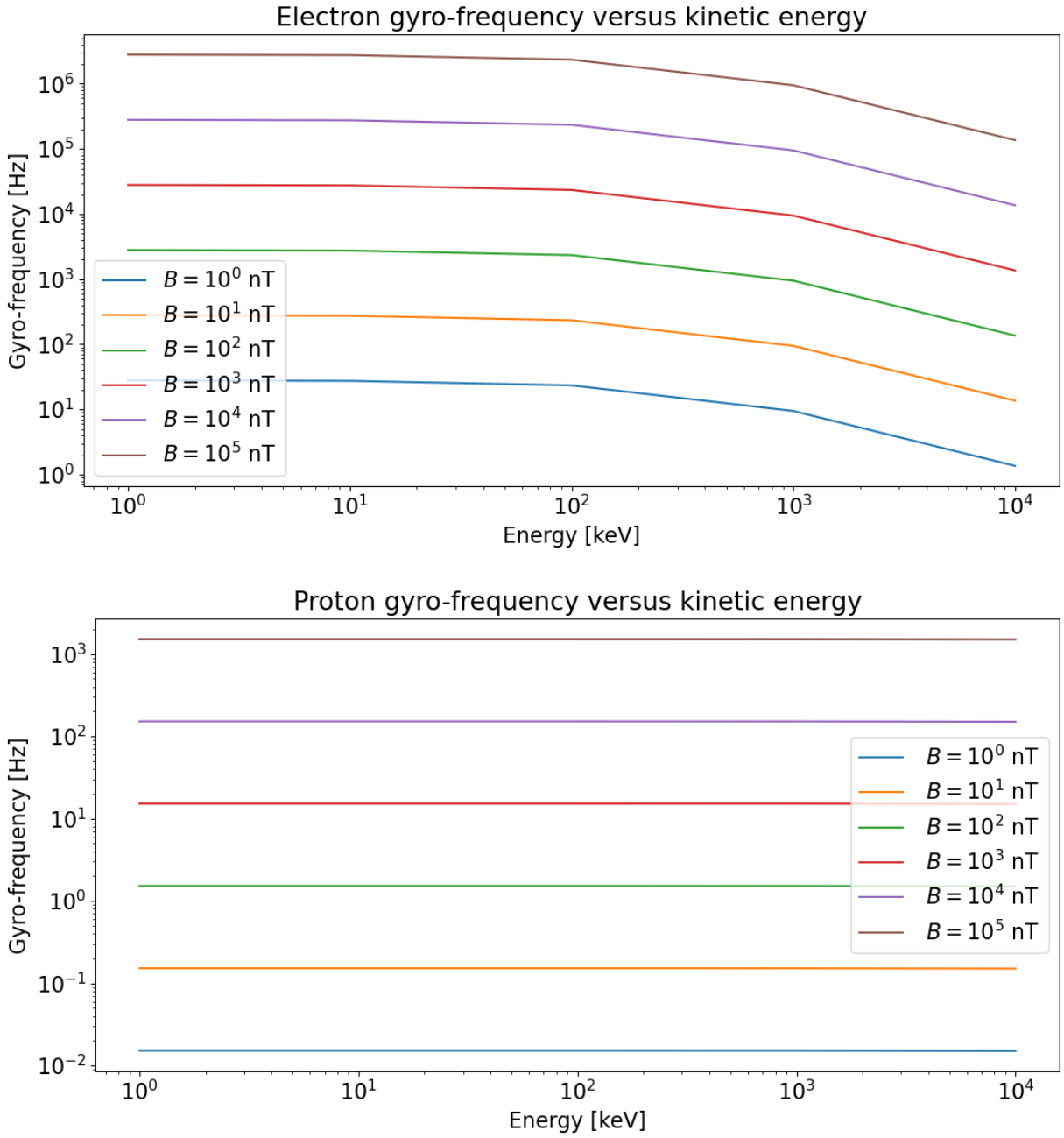

Figure 1.3: Cyclotron frequency of electrons (top) and protons (bottom) versus particle energy the range of magnetic field strengths encountered within the magnetosphere. Note that these curves include the relativistic velocity correction described in Ch. 3, acting to reduce the frequency at the highest electron energies.

IB formation, as the particle's perpendicular kinetic energy increases, its gyro-radius may begin to approach the scale of the background magnetic field curvature, which can result in particle scattering (described later).

In the preceding example, the component of velocity parallel to the magnetic field ($v_\parallel$) did not directly take part in the circular motion. If it is non-zero, the overall motion becomes helical in shape, tracing out a cylindrical spiral of radius r_L and length $v_\parallel \Delta t$ in a time Δt. If however the background magnetic field is allowed to vary across space, the parallel component can affect the perpendicular component over time (and vice versa), by virtue of transporting the particle into a location of altered field direction or strength. In the case of plasma waves, this motion can also cause a Doppler shift in the apparent wave frequency experienced in the particle frame. These effects are explored in detail below, and are fundamental to the formation of IBs. In the relativistic limit (introduced in Ch. 3), $v_\parallel$ also imparts an additional effect on the gyro-motion, due to the appearance of the relativistically constrained total speed $v^2 = v_\perp^2 + v_\parallel^2$ in the Lorentz factor of the corrected gyro-frequency.

Rather than think only in terms of $v_\parallel$ and $v_\perp$, it is useful to recast the components in terms of the total speed v (or alternatively its kinetic energy) and a geometric quantity known as the pitch-angle (α), representing the angle between the velocity and magnetic field vectors; i.e.:

$$(v_\perp, v_\parallel) = (v \sin\alpha, v \cos\alpha), \text{ with } \cos\alpha = \mathbf{v} \cdot \mathbf{B}/vB \tag{1.5}$$

Fig. 1.5 (top) shows an example of cyclotron motion along a magnetic field line with approximately 45° pitch-angle, adapted from (Case, 2014), along with the total speed of the particle (bottom) as a function of its kinetic energy. The units are specified in terms of Earth radii per second (∼6400 km/s), to provide a sense of scale and crossing time within the magnetosphere.

A particle's pitch-angle is a critical parameter in determining its acceleration and

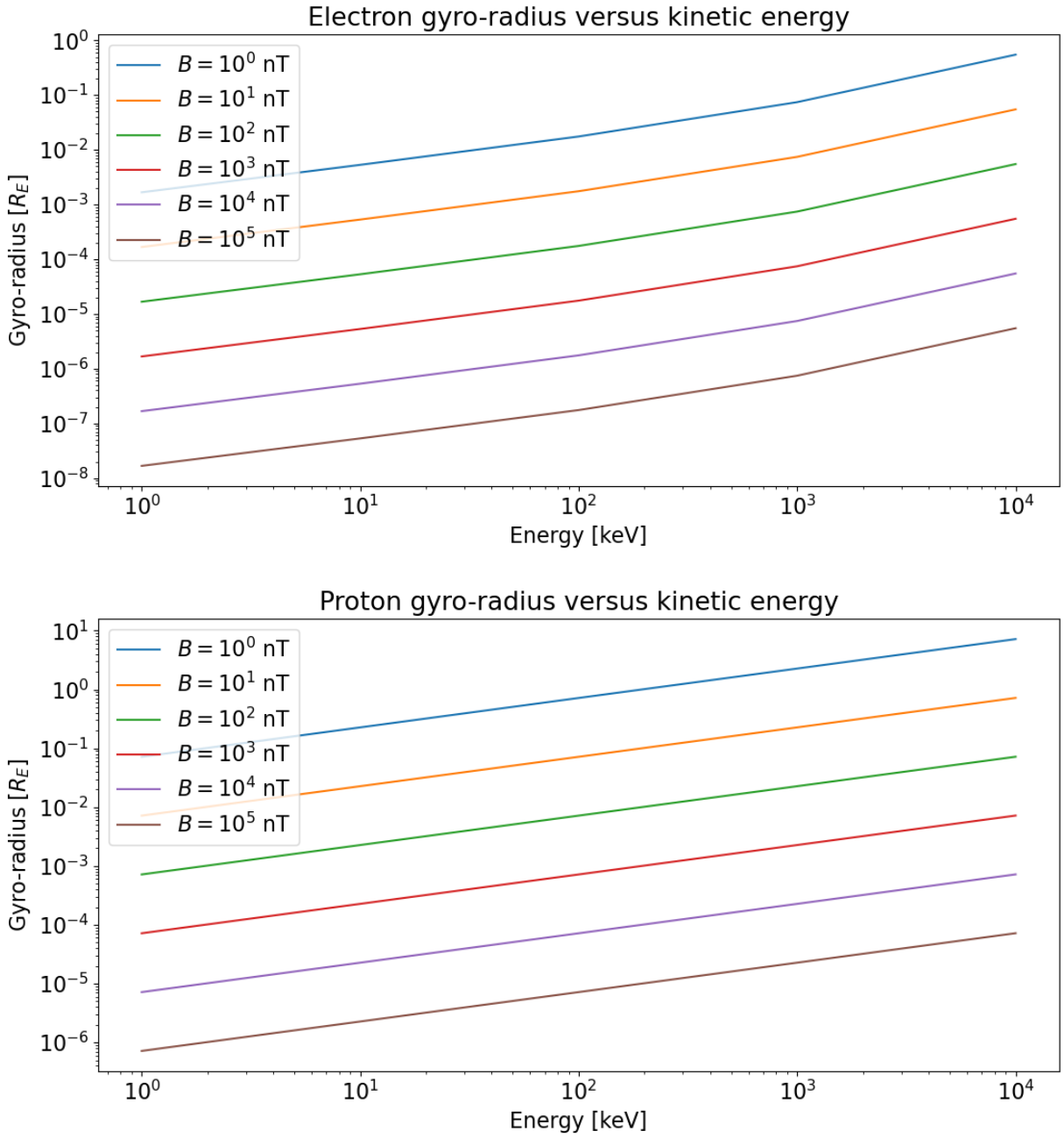

Figure 1.4: Gyro-radius of electrons (top) and protons (bottom) versus particle energy the range of magnetic field strengths encountered within the magnetosphere. Note that these curves include the relativistic velocity correction described in Ch. 3, acting to reduce the frequency at the highest electron energies.

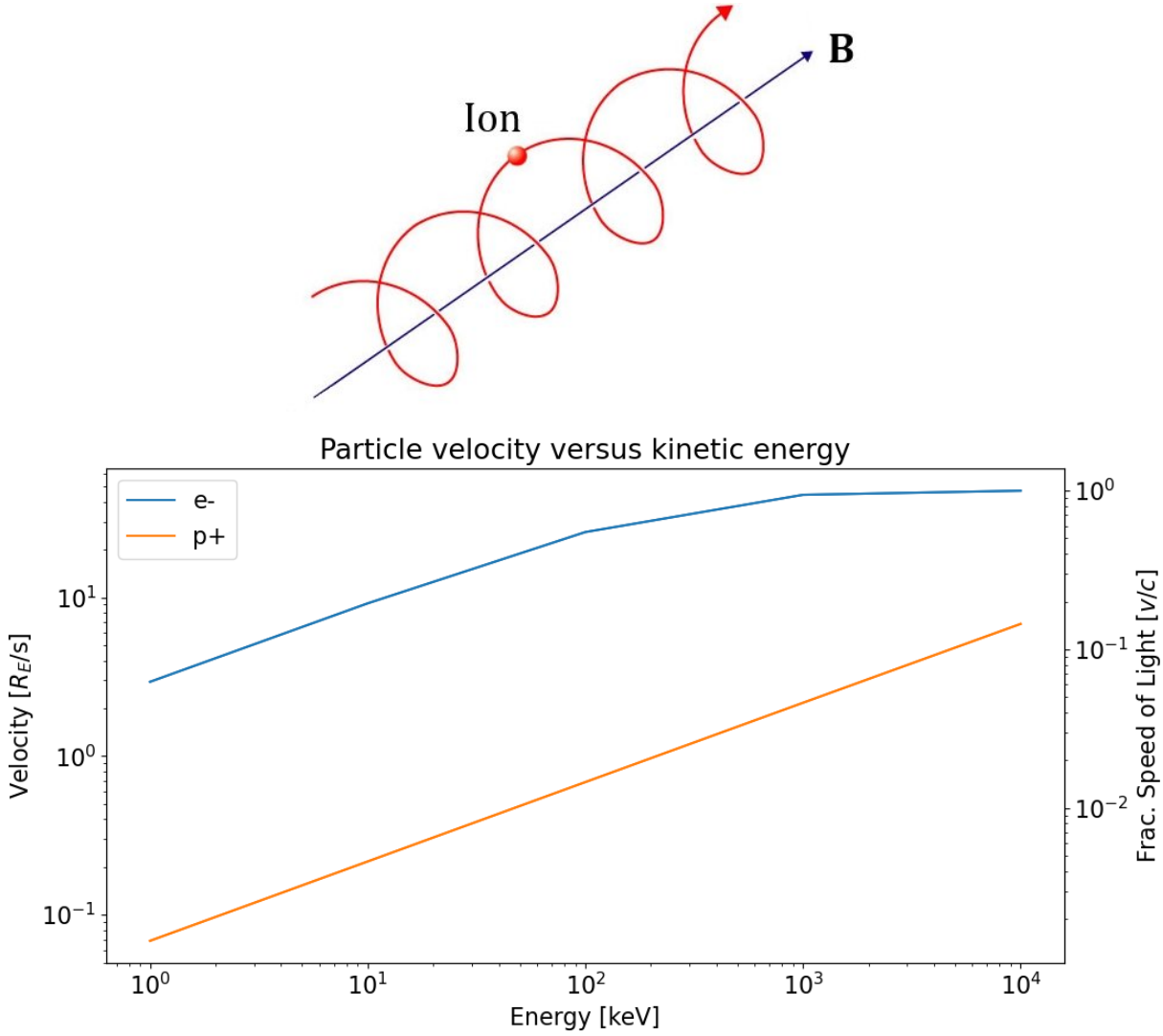

Figure 1.5: Example cyclotron motion of a proton along a constant magnetic field line with non-zero pitch-angle (top, taken from (Case, 2014)), and particle speed versus relativistic kinetic energy (bottom) in units of earth radii per second and as a fraction of the speed of light.

trajectory over time. When considering a population of particles, the distribution of their pitch-angles versus their kinetic energy (i.e., "pitch-angle spectrum") is thus an important quantifiable characteristic. Such observations using satellite particle data are ubiquitous throughout the remainder of this manuscript.

For completeness, when necessary, the particle's gyro-phase angle (ϕ) can be specified, corresponding to the instantaneous direction of $\mathbf{v}_\perp$ within a gyro-period. However, in this work, the gyro-phase of detected particles is undetermined, and does not appear in the pitch-angle spectra. This is a limitation of both the instrumentation used in my research, as well as a physical consequence of measuring particles far away from their source of isotropization (i.e., where gyro-phase may actually matter). Gyro-phase knowledge does not affect the results of the study, but is mentioned for its conceptual role in non-adiabatic pitch-angle scattering below.

2. **Adiabatic invariance: Non-uniform field forces and particle drifts**

Isotropy boundaries represent a location in space where particles transition between two mutually exclusive types of motion: adiabatic and non-adiabatic. To define these terms, we may return to the scenario described by Eqn. 1.2, where now the magnetic field $\mathbf{B}$ is no longer required to be uniform in space or time. In either case, a moving particle experiences "time" variations in the background field, caused by either the particle motion itself to impart a convective $\mathbf{v} \cdot \nabla$ term, as well as due to any explicit time variation via $\partial/\partial t$.

In the adiabatic case, a particle executes its periodic, approximately cyclical motion perpendicular to the magnetic field much faster than any temporal or spatial gradients in the background field it passes through. In this regime, even though the motion may deviate from perfectly circular, the particle will still experience some form of near-circular, near-periodic motion close to the instantaneous cyclotron frequency. Consequently, the particle gyro-radius within each period of the motion will no longer be constant, nor will it necessarily have the same field-line as its instantaneous orbit center (as in purely cyclotron motion). This occurs, for instance, as in the earlier ex-

ample of a particle moving from a region of weaker to stronger magnetic field (or vice versa). Despite the deviation from idealized cyclotron motion, if the effective gradient in field strength at the particle location scaled by its local average gyro-radius is much smaller than the field-strength (i.e., $r_{L,avg}|\nabla B| \ll B$), the particle will conserve a trajectory-averaged quantity known as the first adiabatic invariant (μ), or "magnetic moment," given (non-relativistically) by:

$$\mu = mv_{\perp}^2/2B \tag{1.6}$$

The conservation of μ implies that as a particle moves into a region of higher or lower field strength, the perpendicular kinetic energy will also change, in proportion to the field. Crucially, since there is not an externally-applied electric field to energize the particle, this change in perpendicular energy must come from the parallel component, via Eqn. 1.2. This coupling between the two components can be understood to result from a motional electric field in the frame following the parallel velocity, caused by an apparent change in enclosed magnetic flux within the cross-sectional area subtended by the average gyro-radius. The effect imparted by this electric field is known as the "magnetic mirror force," given by:

$$\mathbf{F}_{\nabla B} = -\mu \nabla B \tag{1.7}$$

As the name suggests, this results in a fundamental phenomenon known magnetic mirroring,[13] which can confine particles moving along particular field-lines into a new type of periodic "bounce" motion, depending on their pitch-angle and the range of magnetic field strengths encountered along their trajectory. This occurs due to the requirement of μ-conservation combined with Eqn. 1.7: If a particle's entire kinetic energy becomes perpendicular to the field, the parallel speed ($v_{\parallel}$) must be reduced to zero. Since the mirror force provides a negative contribution to $dv_{\parallel}/dt$ relative to the

[13] As well as all fields of research involving plasmas and charged particle confinement.

field gradient, the particle is reflected, and begins to move in the opposite direction along the field line. This implies that, under certain conditions, particles will be "trapped" between two mirror points along a field line. In the magnetosphere, particles experiencing such bounce-trapping are the population involved in IB formation.

If the trajectory-integrated magnetic gradient ∇B is insufficient to reduce $v_{\|}$ to zero, the particle cannot be trapped by the field, and will eventually be lost from the system. The criterion for this condition can be specified by a quantity called the "mirror ratio," which by Eqn. 1.5 describes the particular pitch-angle under which particles transition from trapping to loss, known as the bounce loss-cone (α_{LC}):

$$\sin \alpha_{LC} = \sqrt{B/B_{max}} \tag{1.8}$$

where B is the instantaneous field strength, and B_{max} is the local maximum field strength encountered along the path of the particle.

As particles move along the field line in the presence of the mirror force, they experience a continuous change in pitch-angle, reaching a possible maximum of 90°, and a minimum of ∼0° ("field-aligned" parallel) or ∼180° (field-aligned anti-parallel) in accordance with the first adiabatic invariant. Particles within the loss cone ($\alpha < \alpha_{LC}$) will also experience continuous variation in pitch-angle along the field-line, but will not be mirrored at the field maximum. When this occurs in the magnetosphere, the particles "precipitate" into (i.e., collide with) the atmosphere, giving up their energy. In my research, the ratio of particles inside and outside the bounce loss cone is one of the essential features in isotropy boundary identification.

In tandem with the mirror force, the divergence-free requirement of magnetic fields ($\nabla \cdot \mathbf{B} = 0$; see section below on Maxwell's equations) requires that if a gradient in magnetic field strength exists, it must also occur along with a change in the local field-line curvature. This differential geometry condition is specified by a vector quantity

known as the radius of curvature ($\mathbf{R}_C$) of the field, given by:

$$\mathbf{R}_C = (\hat{\mathbf{b}} \cdot \nabla)\hat{\mathbf{b}} / |(\hat{\mathbf{b}} \cdot \nabla)\hat{\mathbf{b}}|^2 \tag{1.9}$$

where $\hat{\mathbf{b}} = \mathbf{B}/B$ is the unit tangent vector to the magnetic field. By Ampere's Law (Eqn. 1.18 below), this curvature expression also implicitly includes effects from electric currents in the system, such as Earth's magnetopause, cross-tail current, ring current, and other sources discussed below. The curvature may also be affected during instances of electromagnetic induction, such as during magnetic reconnection, or in the presence of certain plasma waves, although they must occur over timescales longer than gyro-motion if adiabatic invariance is preserved.

Complementary to the mirror force, an adiabatic particle in the presence of field-line curvature experiences an effective centrifugal "curvature force," given by:

$$\mathbf{F}_C = (m v_\parallel^2 / R_C)\hat{\mathbf{R}}_C \tag{1.10}$$

This force is responsible for confining the particle undergoing bounce motion to its particular field-line where it changes direction in space. The effect can similarly be understood as resulting from an apparent motional electric field in the frame following the particle's guiding center motion (described below), acting to push the particle back toward the original field-line center of cyclotron motion. Fig. 1.6c shows the example motion of a magnetic mirroring particle in Earth's inner (dipole-like) magnetosphere.

As I will describe in the next section, field-line curvature results in very different effect on particles if the radius of curvature (R_C) is of comparable spatial scale to the particle's gyro-radius (crucially, becoming non-adiabatic motion). The role of this mechanism in generating energetic particle isotropy boundaries is later demonstrated as a key conclusion of my thesis.

In general, forces acting on gyrating (adiabatic) particles give rise to another important phenomenon: "guiding-center" drift motion, in which the cyclotron orbit center is

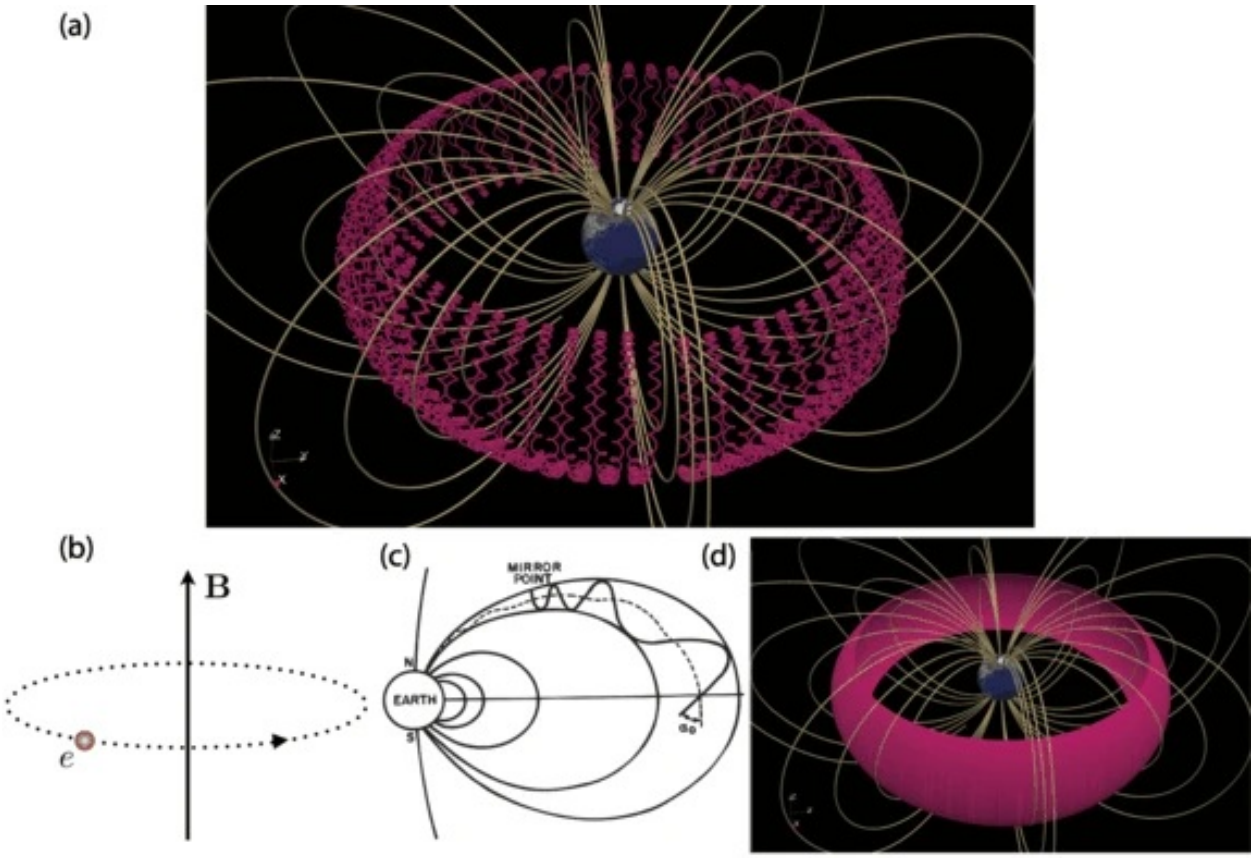

Figure 1.6: Example electron particle motion in dipole-like magnetic field, akin to the inner magnetosphere (taken from (Ukhorskiy and Sitnov, 2012)). Panel (b) shows the motion of an equatorial 90° pitch-angle electron. Panel (c) shows electron bounce motion between the two hemispheres along a magnetic field line under the presence of magnetic mirror and curvature forces. Panel (a) shows the motion of panel (c) over a longer timescale, including the effects of magnetic gradient and curvature drift. Panel (d) shows the "drift L-shell" traced by the overall adiabatic motion in panel (a).

displaced by an amount $\Delta \mathbf{r}_d = \mathbf{v}_d \tau_c$ perpendicular to the magnetic field upon each gyro-period, where $\tau_c = 2\pi/\omega_c$ is the gyro-period, and $\mathbf{v}_d$ is the guiding-center drift velocity, given by:

$$\mathbf{v}_d = \mathbf{F} \times \mathbf{B}/qB^2 \tag{1.11}$$

Here, $\mathbf{F}$ is the average force acting on the particle over its gyro-period. Drift motion is responsible for much of the charged particle transport within the magnetosphere, including the important cases of gradient and curvature drifts (force from Eqns. 1.7 and 1.10), resulting in the characteristic drift shells of the radiation belts and ring current.[14] Fig. 1.6a (based on Fig. 1 of (Ukhorskiy and Sitnov, 2012)) shows an example of an electron undergoing azimuthal guiding-center drift and polar bounce motion together to form a "drift shell" of the electron, trapping it around the planet, and forming, for example, a characteristic cross-section of Earth's radition belts.

An especially important case of Eqn. 1.11, is that of "E cross B" drift, in which an electric field in the rest frame acts perpendicular to the magnetic field by the first term in Eqn. 1.1. While plasmas tend to shield out external electric fields, the high conductivity "frozen-in" condition requires that if the plasma is moving relative to an observer (such as the frame of the magnetosphere), a self-consistent motional electric field must develop perpendicular to both the field $\mathbf{B}$ and field-line velocity $\mathbf{v}$ (see Eqns. 1.19 and 1.20 below). This field is what keeps particles "frozen" to the field-lines; as such, it is zero in the frame moving at the flow velocity of the bulk plasma (or equivalently, the field-line). Bundles of field-lines therefore can be thought of as "flux tubes" carrying plasma at the $\mathbf{E} \times \mathbf{B}$ drift speed, with magnitude proportional to E/B. The drift path of particles under the large-scale cross-tail electric field is known as magnetospheric convection, and serves as the primary transport mechanism in the earlier described Dungey-type magnetic flux transport.

In reality, particles will experience the sum of all applicable drifts (i.e., $\mathbf{v}_d = \sum_i \mathbf{v}_{d,i}$), and can adiabatically gain or lose energy from the imposed electric field, if $\mathbf{E} \cdot \mathbf{v}_d \neq 0$.

[14] Although ring current particles off of the equator are rapidly lost for other reasons, described below.

This implies that from the perspective of particle detection, a significant consequence of large-scale fields satisfying $\mathbf{E} \perp \mathbf{B}$ is that bundles of convecting (as well as stationary) field-lines can be regarded as electric equipotentials, since the electric field vanishes in the co-moving frame. *Crucially, this implies that a particle which originates on a distant Earth-connected field-line can be sensed from LEO at its ionospheric footpoint, without appreciable distortion of its energy.* This means that, even though a satellite may be far away from the regions of space where magnetospheric processes occur, the particles can still be sensed from any position along their field-line projections. This holds true for IB observations from ionospheric altitudes, which map into the equatorial magnetosphere at distances beyond several Earth radii. In this case, the particles ($\geq$50 keV) are sufficiently energetic to warrant consideration of off-equator azimuthal motion from curvature and gradient drifts. However, as shown in the following section, the process which generates isotropy boundaries occurs on timescales of a single bounce-period (the "strong-diffusion" limit), and the net drift therefore does not result in significant spatial aliasing of the field-line being observed.[15]

It is also possible for the magnetic field to vary explicitly with time in the rest frame. If the rate of change is much slower than the gyro-frequency, the first adiabatic invariant will still be conserved. Notably different however, is that the explicit time variation in the field ($\partial B/\partial t$) gives rise to a perpendicular electric field which can directly energize the particle. This process is known as betatron acceleration, and is responsible for some of the initial particle energization required for isotropy boundary formation. Such a process may for example occur as a result of magnetic flux loading in the tail, which may evolve over long timescales (minutes to hours).

Beyond μ-invariance, there are two additional adiabatic invariants associated with the aforementioned types of periodic particle motion in a magnetic mirror. The second adiabatic invariant J[16] relates to the periodic bounce motion between local field-strength

[15] Although it is limited by knowledge of the magnetic field configuration, which generally becomes less accurate as distance from Earth increases.

[16] *Not* to be confused with particle flux, which unfortunately is also often historically denoted by J.

maxima along field-lines, such as those connecting to Earth's northern and southern hemispheres at a given magnetic local time. The invariant is given by the line integral:

$$J = \oint_{s_1}^{s_2} p_{\parallel} ds \tag{1.12}$$

where $p_{\parallel}$ is the particle's momentum along the instantaneous field vector, and the path is tracing the field-line between mirror points s_1 and s_2. This implies that if the length of the field line is varied over timescales longer than bounce motion, the particle's parallel momentum will change in the opposite way—a process known as Fermi acceleration, which can occur near reconnection sites. In the context of IB observations, such enhancements could be detectable as changes in the IB latitude and energy-latitude dispersion pattern, described later.

The third invariant is associated with the periodic azimuthal (i.e., eastward or westward) particle drift motion around the planet, which conserves the magnetic flux (Φ_B) enclosed by a completed planetary drift orbit:

$$\Phi_B = \oint_S \mathbf{B} \cdot d\mathbf{S} \tag{1.13}$$

where S is the surface enclosed by the azimuthal drift path of the particle. In this scenario, if the background magnetic field is varied over timescales slower than than the drift orbit around the planet, the particle may experience a variation in its radial distance from the planet, in order to preserve the magnetic flux passing through the drift surface. This can occur during certain space weather events, such the recovery phase of geomagnetic storms. These can in turn affect the location of isotropy boundaries, as suggested by the finings of Chs. 3 and 5.

3. **Non-adiabatic pitch-angle scattering and diffusion**

With a basic understanding of adiabatic invariance, we may now consider the non-adiabatic regime, in which isotropy boundaries form. To understand how this arises, it is instructive to consider the minimum time-scales τ_n which the n^{th} invariants presumed

in their derivation. The first invariant μ required that any variation in the background field experienced by the particle occurred over timescales much longer than a single gyro-period; i.e., $\tau_1 \gg 2\pi/\omega_c$. The second invariant J required that variations in the background occur over longer times than field-line bounce periods, which themselves involve many gyro-periods; therefore, $\tau_2 \gg \tau_1$. The third invariant Φ required that variations in the background occur over azimuthal drift periods around the planet, which themselves involve many bounce periods; therefore $\tau_3 \ggg \tau_1$. This minimum timescale relationship may be summarized as:

$$2\pi/\omega_c \ll \tau_1 \ll \tau_2 \ll \tau_3 \tag{1.14}$$

Eqn. 1.14 implies that, when tracing a particle which initially conserves all three invariants, if the material field gradient $(\mathbf{v} \cdot \nabla + \partial/\partial t)$ is increased incrementally at the start of each bounce period, the invariance of Φ will be violated first, followed by J, and lastly by μ. This means, conversely, if the first invariant is violated, *all three* invariants must be violated. This is a circumstance in which rapid particle flux isotropization in velocity space can occur.

To understand the cause and effects of μ-variance, we may consider a particle initially mirroring on a curved magnetic field-line, as in the dipole field of Earth's inner magnetosphere. If the field strength and curvature remain constant over time, the particle will remain trapped indefinitely, conserving all invariants. However, if a spatially localized magnetic field disturbance is introduced along the bounce path, such as a current sheet or certain plasma waves, there now exists the possibility of a non-adiabatic particle interaction. This can be manifested in two ways: variations in field curvature, and/or strength, over a scale comparable to the particle's incident gyro-radius (equivalently, timescales on the order of a gyro-period).

If the disturbance acts to increase the curvature radius ("straightening" the field-line), the particle motion will still preserve μ, and possibly J, Φ. However, if the curvature radius is reduced ("bending" the field-line), it is then possible that the particle may

experience a field gradient on timescales comparable to the gyro-period. In the most extreme example, we may imagine an abrupt 90° bend in the field, and a particle which begins nearly field-aligned ($v \sim v_{\parallel}$), initially having a very small magnetic moment $\mu \sim 0$ (since $v_{\perp} \sim 0$). Upon encountering the abrupt 90° change in field direction (sharp curvature), its parallel velocity will suddenly become perpendicular. This implies an extreme violation of the first adiabatic invariant, since $\Delta\mu \propto v_{\parallel}^2 \neq 0$. In this case, the pitch-angle α (initially zero) at which it exits this region depends on the scale length of the magnetic distortion, and whether a full cycle of cyclotron motion can be completed. The effect is to "pitch-angle scatter" the particle by an amount $\Delta\alpha$.

A similar scenario occurs when the magnetic field strength is instead locally reduced along the field-line. In the most extreme case, we can imagine an abrupt drop to $B \sim 0$ localized over some distance. When a particle with non-zero pitch-angle suddenly encounters the null field, it will no longer have a magnetic moment (μ is undefined since $B \to 0$). The particle will thus travel under its inertia away from the field line until it reaches another nearby location of non-zero field strength. Because the field-lines are necessarily curved near the disturbance via $\nabla \cdot \mathbf{B} = 0$, when the particle re-emerges in a region of non-zero field, it will no longer have the same magnetic orientation as it entered. The particle therefore experiences non-adiabatic pitch-angle scattering, since $\Delta\mu \neq 0$.

In these scenarios, the deflection in pitch-angle ($\Delta\alpha$) resulting from the field encounter depended itself on the incident pitch-angle, as well as the incident gyro-phase. This in turn results in further pitch-angle variations on the next bounce period, and so on. When averaged over the particle bounce motion and "randomness" associated with gyro-phase, etc., such a variational process is known as pitch-angle diffusion, with coefficients (e.g., $D_{\alpha\alpha}$) dependent on the background field and its gradients (Schulz, 1991).

If instead of a single particle, an entire population of differing pitch-angle particles are subject to this process under strong field gradients, the pitch-angle distribution will

be very rapidly (i.e. non-adiabatically) altered, on the scale of single bounce periods, until a stochastic equilibrium is reached, with nearly equal production and loss rates at any particular pitch-angle. This is known as the strong-diffusion limit (Zhou et al., 2013), which acts to rapidly isotropize the pitch-angle distribution, and thus fills the bounce loss-cone. Hereon, the term "isotropy" refers to approximately equal numbers of particles occupying any particular pitch-angle (i.e., no preferred direction). From the vantage point of LEO, this definition is relaxed to consider only precipitating and mirroring pitch-angle ranges, since the atmosphere tends to absorb particles, and therefore erodes the up-going portion of the originally (full) isotropic distribution.

4. **Wave-particle interactions and gyro-resonance**

In addition to sharp gradients in the background magnetic field, another type of process is known to cause the non-adiabatic pitch-angle scattering required for isotropy boundary formation: wave-particle interactions. In the context of this work, a "wave" is a propagating electromagnetic disturbance which couples to the local plasma, as well as also potentially the background magnetic field. In general, such waves can be described as a sum over an infinite number of complex Fourier plane-wave modes $Ae^{i(\mathbf{k}\cdot\mathbf{x}-\omega t)}$ of frequency ω and wave-vector $\mathbf{k} = \mathbf{k}_{\parallel} + \mathbf{k}_{\perp}$, where the parallel and perpendicular components are taken relative to the instantaneous background magnetic field direction. The $\mathbf{k}$ vector establishes the direction of the wave phase fronts, and its magnitude represents spatial periodicity (known as the wavenumber). The Fourier method is utilized due to the fact it greatly simplifies the solution of differential equations, exchanging differential operators for algebraic ones, via $\partial/\partial t \rightarrow -i\omega$ and $\nabla \rightarrow i\mathbf{k}$.

The relationship between ω and $\mathbf{k}$ is known as the "dispersion relation" of the wave, which establishes its phase velocity $v_\phi = \omega/k$ and group velocity $v_g = \partial\omega/\partial k$. The phase velocity represents the speed at which the wavefront propagates within the envelope of the larger wave-packet structure moving at the group velocity.[17] Fig. 1.7

[17]The phase velocity can take on any value, including exceeding the speed of light. However, information always propagates at the group velocity, which is less than or equal to light speed.

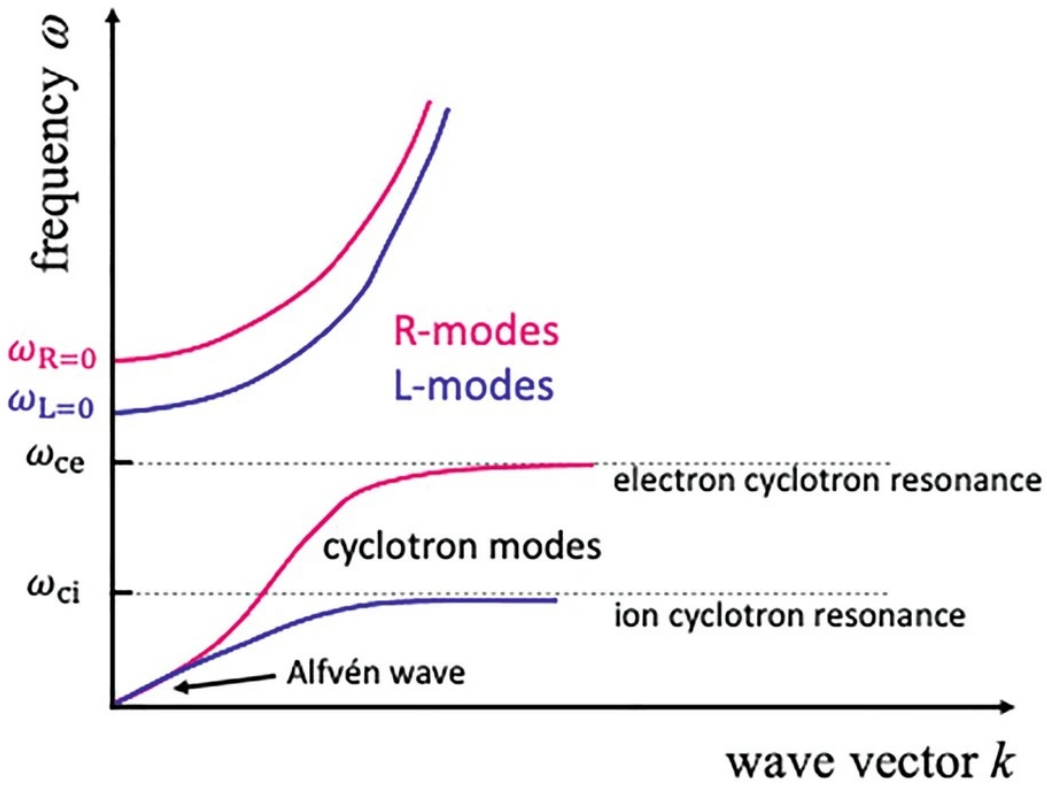

Figure 1.7: Example dispersion relation relating wave frequency (ω) to wavenumber (k) for several types of parallel-propagating electromagnetic plasma waves, taken from Fig. 4.4 of (Koskinen and Kilpua, 2021). Dashed lines represent the cutoff frequency of the wave beyond which is can no longer propagate, while R and L refer to the polarization of the wave.

(based on Fig. 4.4 of (Koskinen and Kilpua, 2021))

Because background plasma is involved, an additional timescale associated with the system must also be considered, known as the plasma frequency ω_p, given (for singly-ionized particles) by:

$$\omega_p = \sqrt{ne^2/\varepsilon_0 m} \tag{1.15}$$

where n is the local plasma number density, e is the electronic charge, ε_0 is the permittivity of free space, and m is the particle mass. The plasma frequency establishes a low-frequency limit in which the plasma will begin to permit externally applied electromagnetic waves to propagate within it, as well as limits the growth or damping of certain types of plasma waves (depending on the dispersion). Fig. 1.8 shows the range

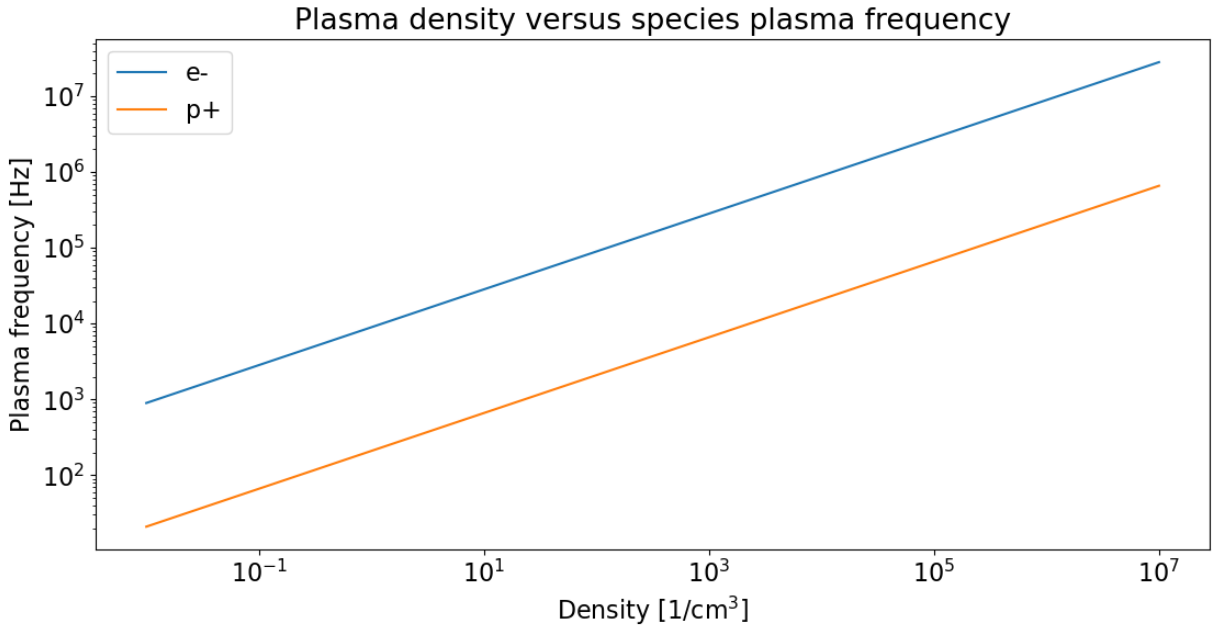

Figure 1.8: Plasma frequency as a function of plasma density over the parameter space of commonly encountered values in the magnetosphere.

of plasma frequencies that may be encountered in the magnetosphere as a function of plasma density.

A charged particle traveling through space which encounters a wave has the potential of interacting with its electromagnetic fields and plasma perturbations. In particular, if a particle moves at the phase velocity of the wave, there now exists the possibility of a resonant wave-particle interaction, where it coherently experiences the wave's electromagnetic forces for a sustained time interval. In this circumstance, the particle may be non-adiabatically energized and/or pitch-angle scattered. The resulting interaction depends on the properties of the wave, such as a quantity known as "polarization," which describes the angular distribution the wave's electric and magnetic fields over a complete oscillation period.

A special type of wave polarization in this study is that of circular polarization, wherein the wave electric and magnetic fields trace out a circular revolution perpendicular to $\mathbf{k}$ in every period of motion. This motion may be clockwise ("left-landed") or counter-

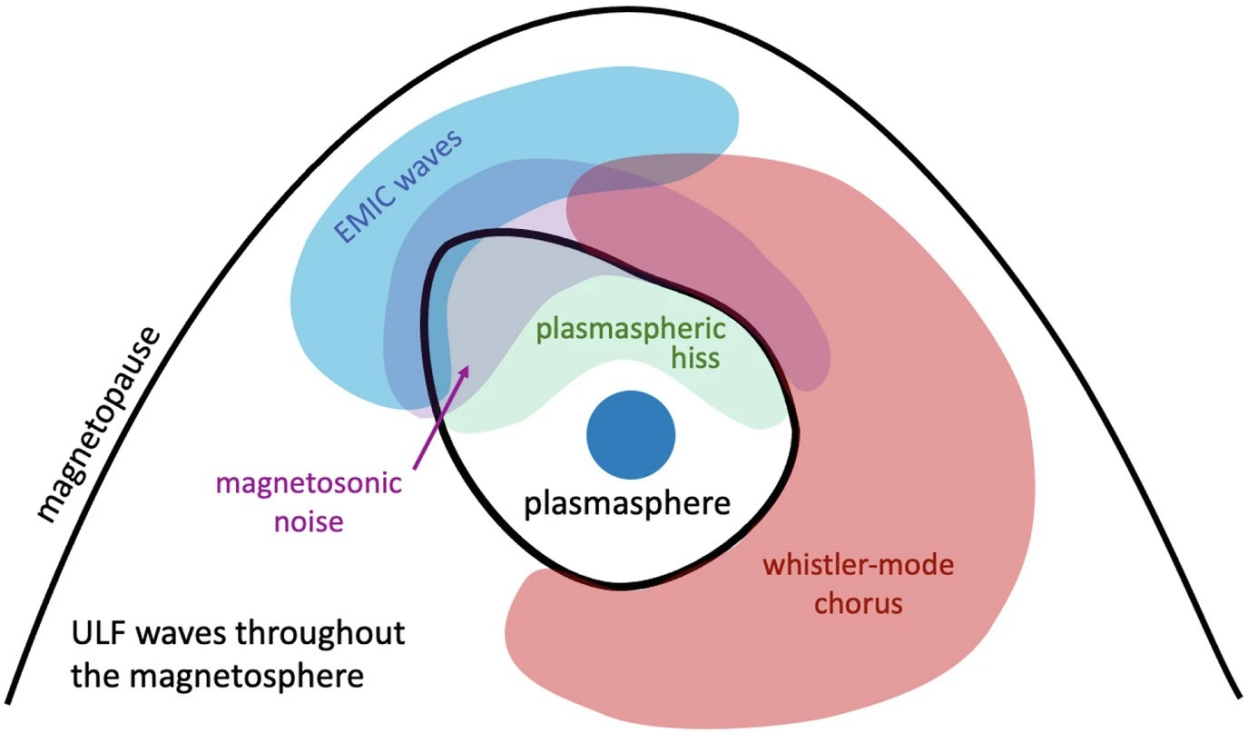

Figure 1.9: Locations in the equatorial magnetosphere (xy-plane) where particular types of plasma waves are commonly encountered, including EMIC and whistlers. Adapted from Fig. 4.1 of (Koskinen and Kilpua, 2021).

clockwise ("right-handed"). This implies that a particle undergoing cyclotron motion may experience very strong acceleration if the wave frequency (or a harmonic) matches the particle's gyro-frequency, owing to the fixed gyro-phase between the wave electric field and the particle's perpendicular velocity. The result is a cumulative energy or pitch-angle change within every gyro-period until the magnetic moment varies significantly from its initial value. This phenomenon is called gyro-resonance, and occurs in the equatorial magnetosphere for several types of propagating waves, including the left-handed Electromagnetic Ion-Cyclotron (EMIC) mode and right-handed "whistler" mode. Ch. 3 explores the effect of these waves in IB formation, along with criteria for which their energy-latitude signature can be distinguished from curvature scattering. Fig. 1.9 (based on Fig. 4.1 of (Koskinen and Kilpua, 2021)) shows the typical equatorial regions where certain types of equatorial plasma waves may be found.

1.1.3 Electrodynamics, distribution functions, and particle flux

The preceding section considered examples of a single particle immersed in electric and magnetic background fields. However, in reality, the magnetosphere and solar wind are filled with many particles, which the electric and magnetic fields themselves arise from. This connection is captured by Maxwell's equations (in SI units):[18]

$$\nabla \cdot \mathbf{E} = \rho/\varepsilon_0, \tag{1.16}$$

$$\nabla \cdot \mathbf{B} = 0, \tag{1.17}$$

$$\nabla \times \mathbf{E} = -\partial \mathbf{B}/\partial t, \tag{1.18}$$

$$\nabla \times \mathbf{B} = \mu_0 \mathbf{j} + \mu_0 \varepsilon_0 \partial \mathbf{E}/\partial t \tag{1.19}$$

where ρ is the local charge density, $\mathbf{j}$ is the local electric current density, and ε_0 and μ_0 are the permittivity and permeability of free space, respectively. In addition, the field experienced by a particle in its own frame of motion may not be equal to that observed from a fixed reference frame. It can be shown that between any two inertial frames (un-primed and primed) moving at different velocities, the Lorentz transformation applied to Maxwell's equations requires that two conditions hold:

$$\mathbf{E} \cdot \mathbf{B} = \mathbf{E}' \cdot \mathbf{B}' \tag{1.20}$$

$$(cB)^2 - E^2 = (cB')^2 - (E')^2 \tag{1.21}$$

where c is the speed of light.

These frame transform relations imply two important rules, which were used to justify earlier conclusions in the introduction: (1) If a reference frame exists where $E = 0$ at a given location, then by Eqn. 1.19, the electric field must be perpendicular to the magnetic field in any other reference frame, consistent with the frozen-in condition. (2) By Eqn. 1.20, if the

[18] In listed order, these relationships are famously known as Gauss's Law, the "no magnetic monopoles" condition, Faraday's Law, and Ampere's Law.

scaled magnetic field strength (cB) exceeds the electric field strength in one frame, then it must do so in all frames. This is important in ensuring that all frames still possess a magnetic field capable of performing the motion described in the sections described on magnetic forces (and therefore that methods such as particle tracing along field-line projections are valid).

The section on single particle motion can be extended to systems with many charged particles, such as the plasma environment of the magnetosphere and solar wind. It is customary to describe the particle population using a distribution function $f(\mathbf{x}, \mathbf{v}; t)$, which tracks the number of particles per unit spatial volume, per unit velocity space volume. The position $\mathbf{x}$ and velocity $\mathbf{v}$ are treated as independent parameters in configuration or phase space, along with a shared time coordinate (t). Each particle species has its own distribution function f_s, normalized such that integrating over all velocity space yields the local number density of the specific particle species (e.g., electrons per cm^3). Under this convention, the net charge density and current density (summed over all particle species s) are given by:

$$\rho(\mathbf{x}; t) = \sum_s \int_{\mathbb{R}^3_v} q_s f_s(\mathbf{x}, \mathbf{v}'; t) d^3\mathbf{v}' \tag{1.22}$$

$$\mathbf{j}(\mathbf{x}; t) = \sum_s \int_{\mathbb{R}^3_v} q_s \mathbf{v}' f_s(\mathbf{x}, \mathbf{v}'; t) d^3\mathbf{v}' \tag{1.23}$$

where q_s is the species charge, $\mathbf{v}'$ is the integration variable over the three-dimensional velocity space $\mathbb{R}^3_v$ with volume element $d^3\mathbf{v}'$. Knowledge of the distribution function is sufficient to describe the evolution of the entire system over time, such as through the Vlasov Equation (Palmroth et al., 2018) for the case of collisionless plasmas, or Fokker-Planck Equation (Risken, 1996), which can accommodate collisional effects and particle sources/sinks.[19] The findings presented in my thesis do not aim to solve these equations, but rather inform other studies in the potential model inputs of the large-scale magnetic structure in the magnetic field ($\mathbf{B}$), as well as energy flux evolution due to isotropic particle

[19]Such equations may also be simplified into fluid models, allowing for the self-consistent description of the magnetosphere and its boundaries, as well as electromagnetic and plasma waves, such as in magnetohydrodynamics ("MHD"). "Moments" of the distribution function may also be taken to determine bulk plasma parameters, such as flow velocity, pressure, and heat flux.

precipitation.

In actual in-situ particle measurements taken by satellites, the distribution functions are not measured directly. Rather, the differential-directional flux $\mathbf{J}$[20] of particles through a particle detector are recorded over a certain range of energies dE, time dt, cross-sectional area dA, and solid-angle $d\Omega$. The field of view and particular pointing direction of the detector allow for the reconstruction of 2D/3D distribution functions over certain velocity ranges (corresponding to the particle energies). From these distributions, particle pitch-angle energy-time spectrograms may be computed, which I use to identify and characterize isotropy boundaries.

1.1.4 Regions of the magnetosphere: Particles and fields

With an in-hand understanding of particles and field connections, I now identify the regions of the magnetosphere pertinent in this investigation. To specify their locations, I utilize two complementary methods: Earth-centered cartesian coordinates relative to the Earth-sun line, and polar coordinates relative to its magnetic dipole axis.

The cartesian representation is useful in describing an absolute position within the magnetosphere or solar wind, such as the equatorial foot-point projection along a closed field-line. These coordinates are also useful if a field-line at some location is disconnected from the Earth, or its true mapping is uncertain. In particular, I have used cartesian Geocentric Solar Magnetospheric (GSM) coordinates in this work, where the $\hat{\mathbf{x}}$ axis points from Earth's center to the sun, $\hat{\mathbf{y}}$ points approximately duskward in the direction of the cross-product between $\hat{\mathbf{x}}$ and Earth's magnetic dipole axis, and $\hat{\mathbf{z}} = \hat{\mathbf{x}} \times \hat{\mathbf{y}}$ completes the triad, forming a plane containing the Earth's magnetic dipole axis. The advantage of GSM is its approximate alignment with the equatorial magnetotail, where isotropy boundaries are formed. It should be noted that due to the dipole tilt of the planet relative to the Earth-sun line, the magnetotail exhibits both daily and seasonal "hinging" motion, as well as flapping due to

[20] *Not* to be confused with the second adiabatic invariant "J," or the current density $\mathbf{j}$.

solar wind dynamic pressure in the $\hat{\mathbf{z}}$ direction (Gao et al., 2018). Therefore the magnetotail is not necessarily centered at $z = 0$.

For the remainder of position information, I have relied on Earth-centered spherical Solar Magnetic (SM) coordinates, in which the equivalent cartesian components are defined as follows: $\hat{\mathbf{z}}$ direction is aligned with the Earth's magnetic dipole axis, $\hat{\mathbf{y}}$ points approximately toward dusk, defined as the cross product between the dipole axis and sunward direction, and $\hat{\mathbf{x}} = \hat{\mathbf{y}} \times \hat{\mathbf{z}}$ completes the triad, such that the XZ-plane contains the Earth-Sun line. This choice of coordinates is invaluable in describing the different regions of Earth's magnetosphere from the perspective of their field-line connectivity relative to Earth's magnetic poles. This is because, as shown in preceding sections, particles within the magnetosphere are typically confined to their particular field line, or its adiabatic drift equivalent. Field-lines with both ends connected to the Earth are referred to as "closed," while those with only one end connected are called "open." Both cases are of interest in this study.

Expanding on this definition, I use a common variant of SM polar coordinates to uniquely describe a particular *field-line*, under the assumption of a closed dipole field:[21]

1. The polar coordinate is magnetic latitude (MLAT): the complement of the standard polar coordinate θ (i.e., $MLAT = 90° - \theta$), corresponding to the location where the field-line intersects Earth's surface (or its ionosphere). In a purely dipolar field, field-lines foot-points are exactly conjugate between hemisphere (the same $\pm$ value), although if a more realistic field model is used (such as IGRF in this work), they will not necessarily be the same, due to inherent asymmetries in Earth's internal dynamo.

2. The azimuthal coordinate of the field-line foot-point is represented by Magnetic Local Time (MLT) mod 24, where 0 hr, 6 hr, 12 hr, and 18 hr correspond to magnetic midnight, dawn, noon, and dusk, respectively. The range of MLTs between 6 and 18 hours may be regarded as the "dayside," with the remaining hours considered the

[21]It should be noted that in these coordinates, the field-line is *presumed* closed regardless of whether it actually is in reality.

"nightside." Sub-sectors of these ranges are also used, such as "pre-midnight" (20-24 hr), and "post-midnight" (0-4 hr).

3. The radial coordinate r can either be a position *along* a field-line, or it can represent the *apex* of the field-line. Under the dipole assumption, r (the radial distance of a point along the field-line) and $MLAT$ are no longer independent; instead, they obey the well-known relationship $r = R_{apex}\cos^2(MLAT)$, where R_{apex} is the furthest distance from the dipole origin to a point on the field-line. In practice, it is common to normalize R_{apex} by Earth's radius ($R_E \sim 6438$ km). This normalized distance is known as the "L-shell" of the field-line, and is related to the magnetic latitude of its foot-point by:

$$L = 1/\cos^2(MLAT) \tag{1.24}$$

The L-shell is positive regardless of hemisphere, although in reality, its actual conjugate value will vary, due to the geomagnetic field's higher order multi-pole terms, as in IGRF (Alken et al., 2021). It should be noted that the dipolar field approximation breaks down the further a field-line maps from the Earth—especially beyond $L \sim 6$, where the inclusion of external field models are required. It is nonetheless a convenient means of organizing the regions of the magnetosphere by latitude or L-shell with respect to the "invariant latitude" measured at Earth's surface or ionosphere.

Using dipole L-shell and MLT to define field-lines (as above), I now summarize the magnetospheric regions of interest, based on their particle populations, field configuration, and potential for isotropization. Fig. 1.10 displays a cartoon cross-section of the main magnetospheric regions, taken from (Lang, 2005). To provide a sense of spatial orientation, Fig. 1.11 shows a noon-midnight meridional cross-sectional cut of the magnetic field strength and radius of curvature in the inner magnetosphere, while Fig. 1.12 shows the same plots for the night-side magnetotail. Such features will later prove important in modeling the location and energy-latitude dispersion of isotropy boundaries in Ch. 3.

Beginning at the magnetic equator and moving poleward, the primary regions of signifi-

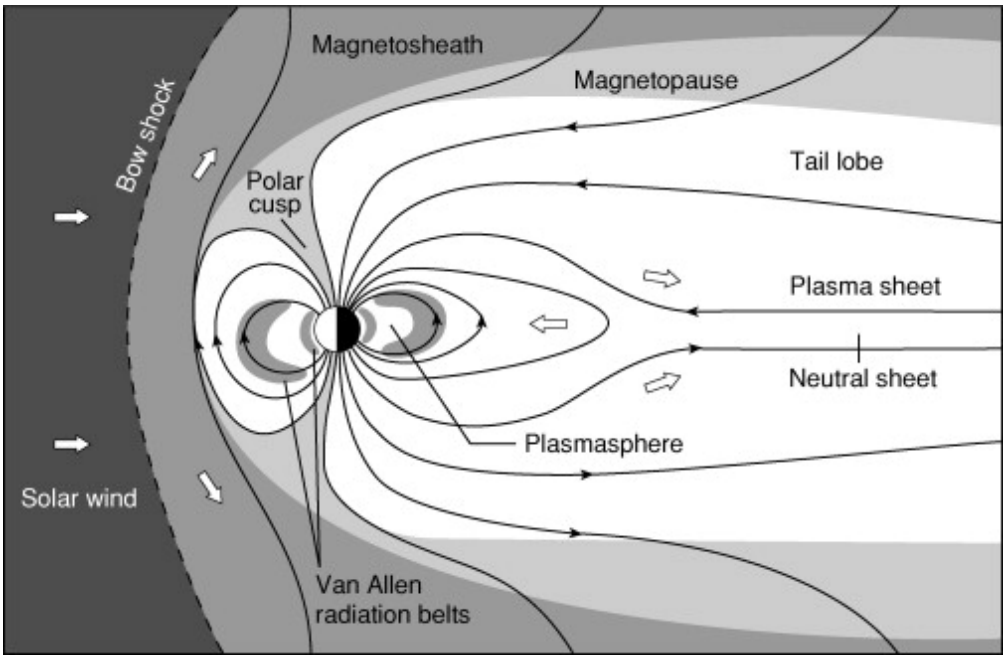

Figure 1.10: Cartoon of the magnetosphere and solar wind, taken from (Lang, 2005).

cance to IB formation are:

1. **The inner radiation belt (IRB)**

   The lowest-latitude portion of the magnetosphere containing energetic particles is Earth's inner radiation belt (IRB) (Li et al., 2023). It typically spans L of 1.1-3, and consists of extremely energetic protons between 100s of keV to 100s of MeV,[22] co-located with predominantly 10s to 100s of keV electrons. Here, energetic particles undergo adiabatic motion, with very long trapped population lifetimes, owing to the strong magnetic field close to the planet (10^3-10^4 nT). The field-lines are also highly stable and dipolar, giving rise to both gradient and curvature drifts, which maintain long duration particle confinement. Consequently, it would not be expected for these particles to become isotropized by magnetic forces, except for possibly the most extreme proton energies at its outward edge, as demonstrated by (Selesnick and Looper, 2023). This energy range is outside the scope of my research, and likely represents

[22] Consequently why the "South Atlantic Anomaly" in this region is hazardous to satellites and astronauts.

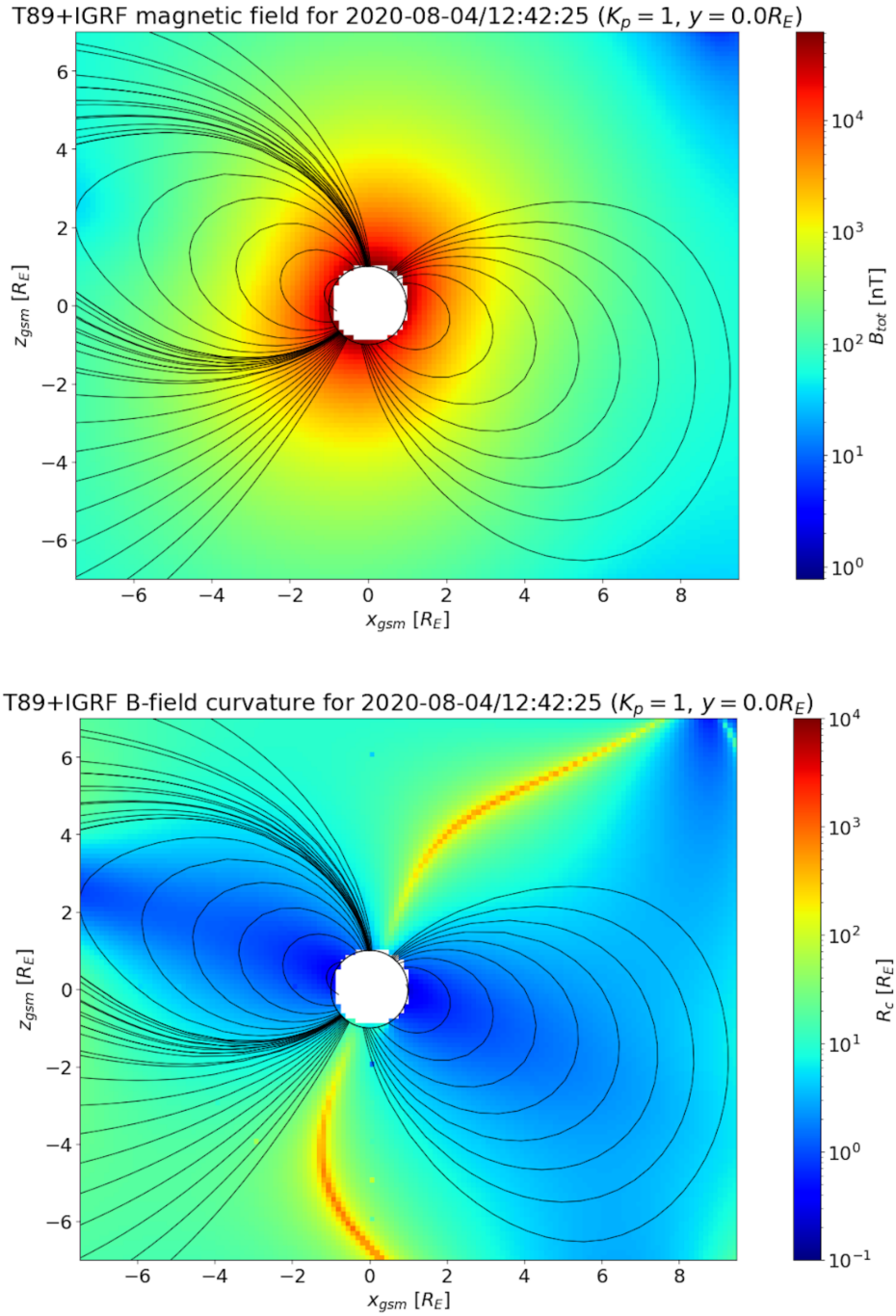

Figure 1.11: Example noon-midnight meridional cut of magnetic field strength (B; top) and radius of curvature (R_C; bottom) in the inner magnetosphere, based on the T89 field model. The field strength and curvature scale largely as a dipole, where the field strength drops off as the reciprocal of cubic distance, and curvature is approximately directly proportional to distance.

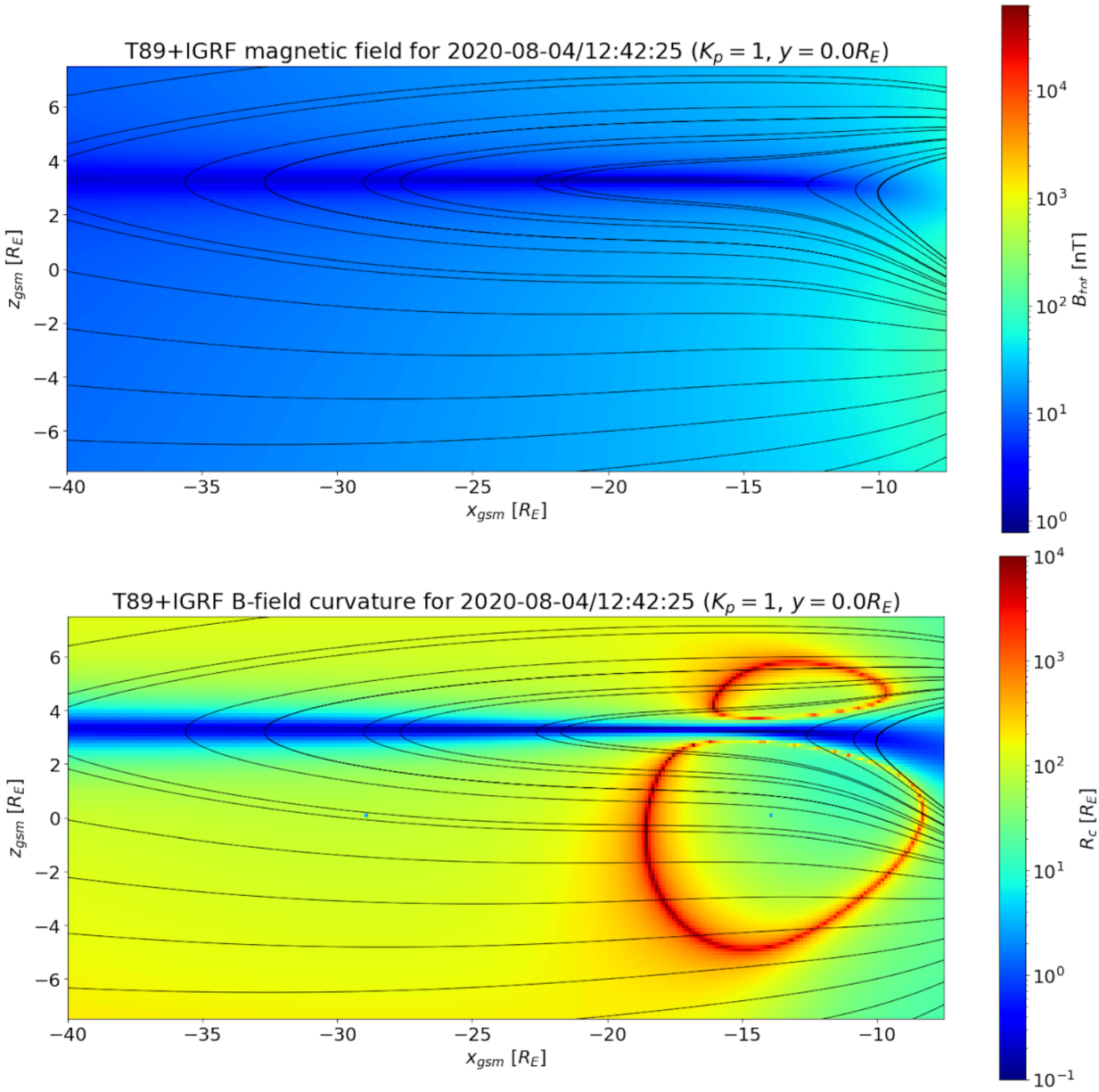

Figure 1.12: Example noon-midnight meridional cut of magnetic field strength (B; top) and radius of curvature (R_C; bottom) in the magnetotail, based on the T89 field model. The contours of high curvature (deep red) correspond to inflection points in the magnetotail configuration due to the lobe fields.

a fundamentally different source of particles of non-magnetospheric origin, such as cosmic rays and their decay, which are not associated with solar wind driving.

The inner belt also overlaps with the bulk of the cold (non-energetic), dense, co-rotating ionospheric outflow population known as the plasmasphere (Singh et al., 2011). This background provides appropriate conditions to support the generation of plasma waves, such as hiss and whistler-mode waves at VLF frequencies, which can preferentially interact with energetic particles, depending on the wave's dispersion. This gives rise to the infamous "slot region," separating the inner and outer belt, by pitch-angle scattering particles into the loss-cone, precipitating at a faster rate than they can be replenished by radial transport. Therefore this mechanism does not maintain a reservoir of isotropic particles, nor does it continue to occur outside of the plasmasphere, and so does not form an isotropy boundary (as defined in the next section).

2. **The outer radiation belt (ORB)**

Moving poleward from the IRB, we next encounter the outer radiation belt (ORB) (Ukhorskiy and Sitnov, 2012). It typically spans L of 3 through 6, composed mainly of energetic electrons with energies between 10s of keV and 10 MeV. These electrons tend to primarily conserve adiabatic invariants in the presence of gradient and curvature drifts, but are more prone to more variability than the inner belt. This is due to the relatively weaker field of the region, and its proximity to the magnetic energy conversion processes of the tail, where fluxes may change rapidly on the timescale of minutes to hours, such as through radial diffusion and injections, as well as "shadowing" due to compressions of the magnetopause. The inner edge of the ORB is primarily dipolar in field configuration, but at higher L-shells on the nightside, begins to experience the effects of field-line stretching, consistent with the tail-dipole transition. Similarly, the magnetic field strength drops from 10^3 to 10^2 nT. It is in such scenarios that the effects of non-adiabatic curvature scattering may begin to manifest.

The outer belt also overlaps with the typical location of the plasmapause—the sharp drop-off in plasma density at the edge of the plasmasphere, typically between L of

4 and 5. Such density gradients can give rise to the production of Electromagnetic Ion-Cyclotron (EMIC) waves, which can also pitch-angle isotropize particles in the non-adiabatic regime. Whistler-mode waves are also present in this region, and can similarly interact with energetic electrons. As discussed in the next section, a long standing question in the study of isotropy boundaries is whether such waves are the dominant source of IBs compared to curvature scattering.

3. **The ring current (RC)**

   Overlapping with much of the same equatorial space as the outer belt, the ring current (RC) typically spans L of 4 to 7 (Daglis et al., 1999). It is composed mainly of an azimuthally-drifting energetic proton population with energies ranging from single keVs to 100s of keV, although as shown in this work, sometimes reach MeV energies at higher L-shells, which are rapidly lost by pitch-angle scattering, among other processes. Like the outer belt, ring current particles often drift adiabatically, but the larger collision cross-section of H^+ and heavier ions results in additional losses, including Coulomb scattering with background plasma (e.g. in the plasmasphere), as well as charge-exchange collisions with exospheric neutrals. This leads to a pitch-angle distribution of particles which mirror near the equatorial plane, whose lower-latitude fluxes are largely undetectable to polar satellites in LEO.

   On the nightside, the outer portions of the ring current extend into a region of weak and curved magnetic field, approaching the plasma sheet. During geomagnetic storms, this proximity leads to significant enhancement in ion energy and density (i.e., pressure). This disturbance is often quantified at Earth's surface by measuring the low-latitude change in the horizontal component of the field due to the ring current, known as the Dst index (alternatively, sym-H). In such intervals, the composition of the ring current also incorporates heavier outflow ions, such as O^+ and N^+. These ions may also theoretically form distinct isotropy boundaries, although they are not the focus in this study.

4. **The plasma sheet (PS)**

The plasma sheet is the primary reservoir of particles associated with Earth's auroral zones (Vasyliunas, 1972). Its extent in L-shell is variable, but often spans the range of 7-12. It consists of an isotropic hot ion plasma population from single keVs up to 100s of keV, and typically an order of magnitude higher in temperature than the local electron population. It also embeds the cross-tail current described earlier.

The "inner edge" of the plasma sheet has historically been determined in at least two ways: (1) for <10s of keV particles as the energy- and species-dependent "Alfven layer" of particles of a given magnetic moment (Zhang et al., 2015); and (2), for more energetic particles, as the location of sudden drop-out in equatorial isotropic omnidirectional particle flux above a characteristic particle energy, from the perspective of radially approaching the earth (Vasyliunas, 1968). In case (1), the Alfven layer defines a topological separator between particles whose equatorial adiabatic drift motion terminates at the magnetopause versus orbits the Earth in a closed drift-shell. A modeled example of such equatorially-mirroring electron drift paths is shown in Fig. 1.13, taken from Fig. 3 of (Zhang et al., 2015). The drift paths correspond to the listed cross-tail electric potential (U) in kV, where the particle's total energy is related by $W = qU + \mu B$.

It can be seen that many drift paths of 10s of keV particles directly impact the magnetopause, while a subset within $L \sim 6$ would result in closed orbits around the planet. This separator can be interpreted as the plasma sheet inner boundary; however, it is impractical to deduce from localized in-situ particle measurements, and does not necessarily apply in the context of particles which are scattered in the strong diffusion limit at the equator, whose magnetic moments are not conserved. Hence, in this work, case (2) is the applicable technique, with the particular "flux drop-out" approach being described in detail in Ch. 3.

In the context of isotropy boundaries, the nightside magnetic field in the vicinity of the plasma sheet is especially interesting, transitioning from a stretched dipole-like field at

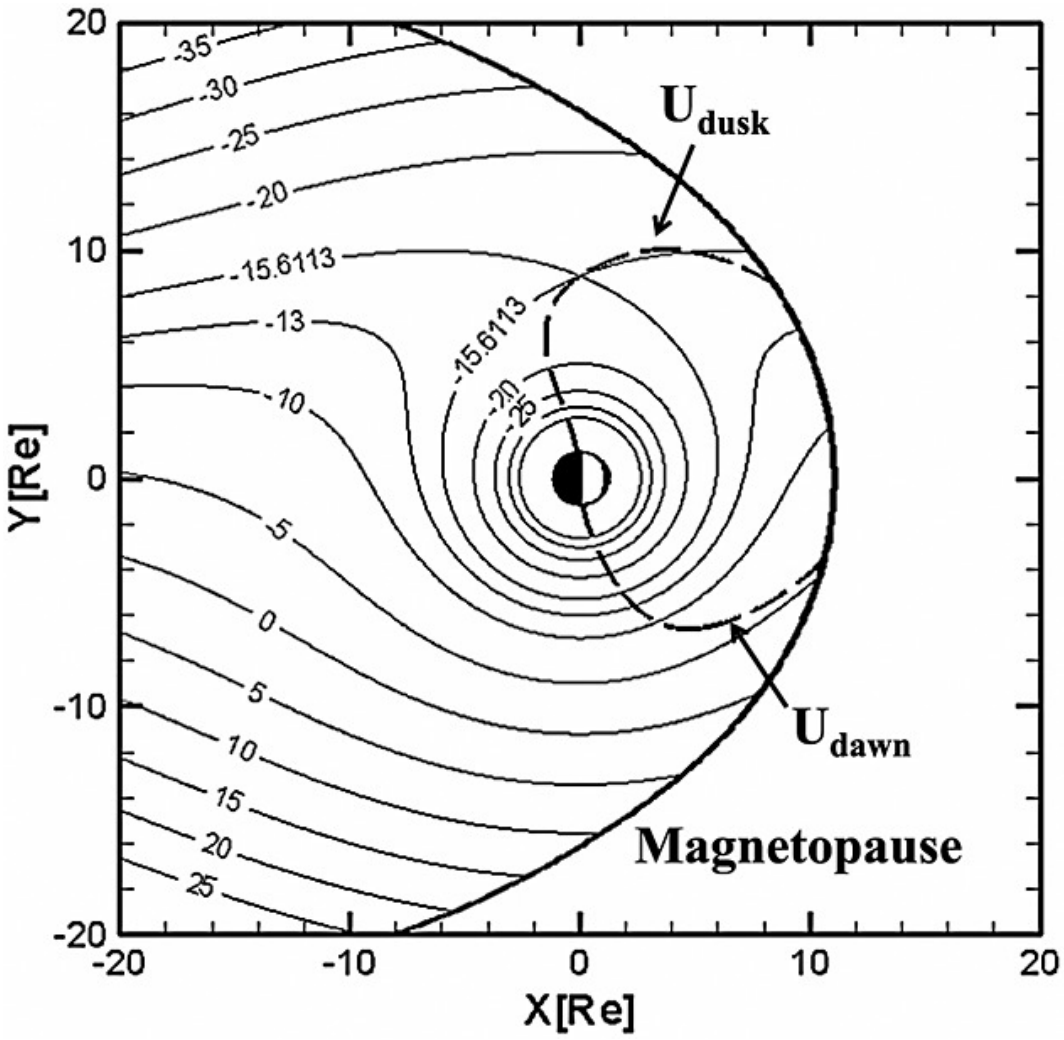

Figure 1.13: Example modeled equatorial electron drift paths corresponding to the cross-tail electric potential U in kV, related to total particle energy by $W = qU + \mu B$. The plasma sheet inner edge is modeled as the Alfven layer, in which the drift paths transition from open (i.e. into the magnetopause) versus closed (orbiting the Earth). Graphic from Fig. 3 of (Zhang et al., 2015).

its inner edge to a completely current-sheet-like configuration. This owes to the fact that the plasma sheet contains a core region known as the neutral sheet: the interface where the magnetotail lobe fields change direction, resulting in very low magnetic field strength (often single nTs to 10s of nT), and potentially sharp radius of curvature (on the order of the current sheet thickness), as low as 0.1 R_E. Consequently, isotropy boundaries tend to form near the inner edge of the plasma sheet, with particles typically remaining isotropic at poleward latitudes.

The plasma sheet is also host to particle precipitation and fluid instabilities, including the generation of plasma waves (Kalmoni et al., 2018), which impact the ionosphere. The effect is often to produce visible aurora, as well as other phenomena. The region is particularly active during events known as magnetic substorms, which act to release magnetic energy stored the tail lobes through field dissipation (reconnection) and reduction of the cross-tail current (thus imparting free energy along the modified field-line). The intensity of this process is typically estimated by an observable quantity known as the Auroral Electrojet (AE) index, measuring the magnetic field disturbances associated with plasma sheet particle currents flowing along field-lines into the ionosphere. As shown in Ch. 4, this effect is evident in the precipitating fluxes associated with IBs. This index may also be combined with Dst (or similar indices) to form planetary indices, such as Kp, to encode both equatorial and high-latitude activity.[23] All three activity indices are used in this work.

Table 1.1 summarizes the salient properties of each magnetospheric region. Other regions in the vicinity which can play an indirect role in isotropy boundary evolution are also included.

[23] See https://www.ncei.noaa.gov/products/geomagnetic-indices

Region	L	$\log_{10} B$ [nT]	$\log_{10} n_0$ [1/cm^3]	R_C [R_E]	E_e [keV]	E_p [keV]
Inner Belt	1.1-3	3-4	X	0.3-1.0	10-500	10^2-10^5
Plasmasphere	1.1-4	2-4	2-4	0.3-1.3	10^{-3}-10^{-2}	10^{-3}-10^{-2}
Outer Belt	3-6	2-3	X	1.3-2	10^1-10^4	X
Ring Current	4-7	2-3	0-2	1-2	X	10^0-10^3
Plasma Sheet	7-12	0-2	(-1)-0	0.1-1	10^0-10^2	10^0-10^2
Polar Cap (lobes)	>12	1-2	(-2)-(-1)	10^2-10^5	10^{-3}-10^{-1}	10^{-3}-10^{-1}

Table 1.1: Summary of magnetospheric regions and their important parameter ranges in the context of isotropy boundary characterization. A value of "X" indicates a quantity that is dominated by a different region at the same L-shell.

1.2 Introduction to charged particle isotropy boundaries (IBs)

With the essential geophysical toolkit in-hand, I now formally introduce the isotropy boundary, its history, and the motivations underlying my dissertation.

1.2.1 Discovery, definition, and particle signatures

As early as the 1960s, through the advent of radiation-detecting satellites, it had been discovered that along field-lines which map into the high-latitude ionosphere (beyond ±55° magnetic latitude), pitch-angle isotropized distributions of electrons and protons at energies exceeding 10s of keV could routinely be detected in particle flux measurements (O'Brien, 1964). Adding to the intrigue, the fluxes were found to remain almost entirely isotropic for an extended poleward latitudinal range, with an onset in isotropy at a particular time-varying magnetic latitude called the "trapping boundary" (or "ψ boundary") (Fritz, 1968). This boundary was found to correlate with intervals of geomagnetic storms (Williams and Ness, 1966), suggesting a cause related to solar driving. It was later discovered that this boundary seemed to behave differently near midnight versus at other MLTs (Fritz, 1970), indicating that large-scale magnetic field conditions may play a role in controlling the trapped and un-trapped populations. The latitude of the trapping boundary also appeared to have an energy-dependence, although it was arguably not until a decade later the first modern observations of what we today call the "isotropy boundary" were made by (Imhof et al., 1977, 1979) that this connection was definitively established. In particular, using RadSat

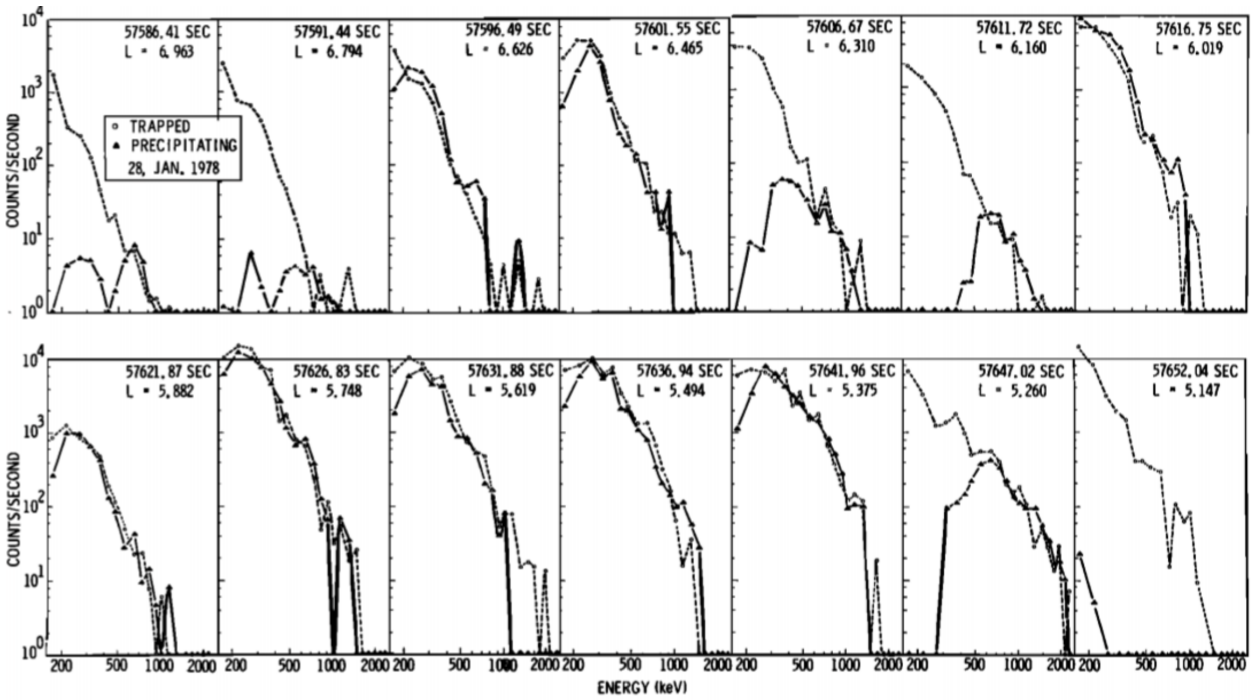

Fig. 5. Energy spectra of trapped (open circles connecteu by dotted lines) and precipitating (solid triangles connected by solid lines) electrons on successive satellite spins for one pass across the local midnight trapping boundary. For each of the trapped and precipitating electron spectra a subtraction has been made of the spectrum measured when the spectrometer was looking down the field line toward the atmosphere.

Figure 1.14: Fine-scale energy-latitude dispersion in the onset of isotropy as reported by (Imhof et al., 1977). As the satellite moves to progressively lower latitudes (L-shells), the ratio of precipitating to trapped fluxes reaches 1 for increasingly high energies, consistent with the more modern understanding of FLC scattering.

(1972-076B), these authors made the first fine-scale measurements of what is referred to as "energy-latitude dispersion" in the onset of isotropy, showing that over a wide range of energies near midnight (MLT∼0 hrs), 16 keV to 2.4 MeV electrons and 40-950 keV protons, a clearly negative dependence in L-shell versus energy was present. This strongly suggested that a fundamental connection to the magnetic field configuration in the magnetotail may be the explanation. For illustrative purposes, Fig. 1.14 shows the discovery of said energy-latitude dispersion (Fig. 5 in their publication).

The combination of an abrupt latitudinal onset in isotropy combined with an energy-latitude dispersion pattern later came to be formally known as the isotropy boundary (IB) for that particular particle species, energy, and magnetic local time (MLT) (Sergeev et al., 1983). From the vantage point of a satellite orbiting Earth, the IB was identified in particle

data by comparing locally parallel ($J_{\parallel}$) and perpendicular ($J_{\perp}$) pitch-angle spectra, denoting an IB crossing by the most equatorward latitude/shell satisfying $J_{\parallel} = J_{\perp}$. More recently, for satellites in polar Low Earth Orbit (LEO), this parallel-to-perp flux relationship has been well-approximated by $J_{prec}/J_{perp} \sim 1$, where J_{prec} is the population of particles in the local bounce loss-cone,[24] and J_{perp} is the population of bounce-mirroring particles. This approximation is used throughout the remainder of this work, to leverage aggregate pitch-angle spectra (or their fits) rather than infinitely resolved differential pitch angles (e.g. exactly 0° and 90°), which can be impractical to directly determine, due to instrumental limitations.

Both then and in the years leading up to this thesis, although it was known that magnetic fields were somehow involved, it had not been firmly established what mechanism(s) were responsible in forming the majority of IBs, or what the distribution and occurrence of such IBs were, outside of a limited range of energies, latitudes, MLT, or sample sizes. These questions are addressed in my research.

1.2.2 Review of past works, geophysical motivation, and open questions

As suggested above, the study of isotropy boundaries possesses a rich history of observations, theory, and modeling. In chronological order, I identify several seminal works which laid the foundation for my investigations here.

In the same year (1982), two independent but complementary studies established some of the first self-consistent theoretical explanations for how IBs could be generated. One study was by (Gray and Lee, 1982), in an unrelated line of investigations on non-adiabatic pitch-angle diffusion in the plasma sheet. These authors showed that in the presence of a Harris-like current sheet, varying the radius of curvature of the magnetic field in the current sheet center (approximated in more modern "neutral sheet" nomenclature by $R_C \sim B_z/\mu_0 j_y \sim B_z/(\partial B_x/\partial z)$) led to progressive breakdown in the first adiabatic invariant μ of particles mirroring along the field-lines. They showed that when the radius of curvature

[24] Unfortunately, for historical reasons, J_{perp} and $J_{\perp}$ do not represent the same quantity in this work, despite their similarity in name and context.

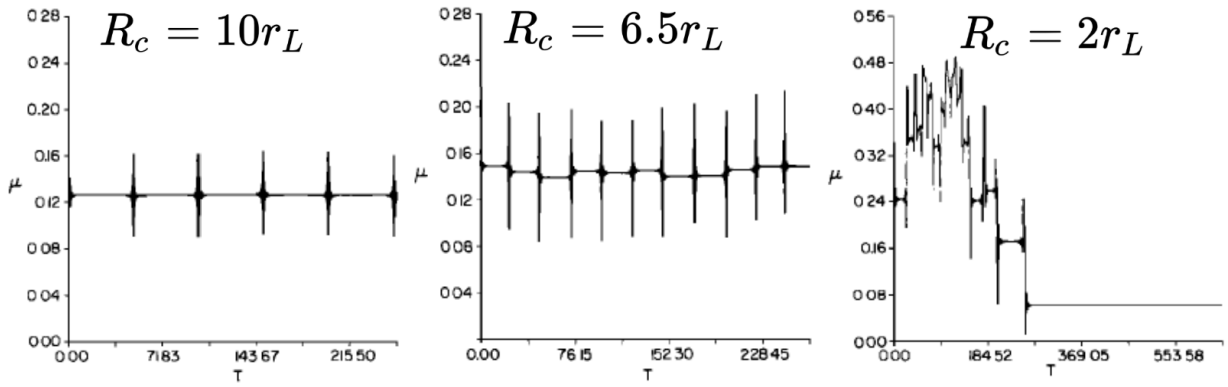

Figure 1.15: Variations in a particle's magnetic moment upon repeated current-sheet crossings under a given ratio of R_C to r_L, transitioning from adiabatic to non-adiabatic encounters. Adapted from Fig. 2 of (Gray and Lee, 1982).

was below an order of magnitude greater than the partical's equatorial gyro-radius r_L, the violations of μ became increasingly severe—reaching a point where an ensemble of particles would experience stochastic pitch-angle diffusion, resulting in isotropization upon at most a few bounce periods. This mechanism would later prove crucial in explaining one of the two competing theories for how IBs can form, as well as the theoretical model I present in Ch. 3. Fig. 1.15 shows this result from their work for normalized values of μ (modified slightly from their Fig. 2 to include the ratio of R_C to r_L).

Around the same time,[25] (Sergeev and Tsyganenko, 1982) demonstrated the conditions for the formation of the edge of the "trapping boundary" being due to pitch-angle scattering in the strong diffusion limit. This analysis was performed in a more realistic magnetosphere configuration, using an early version of the Tsyganenko (1981) field model, who found that a ratio of $R_C/r_L \sim 5 - 10$ would result in the breakdown of the trapping boundary. Later on, analyses of diffusion coefficients were developed into a more sophisticated framework by (Birmingham, 1984) for use in general "magnetodisks," such as at Jupiter, and by (Delcourt et al., 1996) and (Martin et al., 2000) to more explicitly characterize the types of motion involved in the $\kappa < 8$ regime, where κ is the ratio of minimum magnetic radius of curvature to maximum particle gyro-radius.

[25]Technically, this paper was published first.

The findings of these works imply that IB observations at different energies, times, and MLTs in polar LEO can be used to infer the magnetic field configuration far away from the planet, under many different geomagnetic conditions. It is thus valuable to characterize the distribution of these IBs versus all such parameters. Initial studies of this type were performed for limited energy ranges by (Sergeev et al., 1993) for protons using POES, and by (Imhof et al., 1997) for electrons using UARS (small sample size and limited orbit inclination). My research extends the notion of these prototypical works, which had not been performed statistically for electrons, nor for the more energetic $\geq$200 keV to $\sim$MeV proton IBs, which are thus key results presented in Chapter 3.

Another series of papers serve as the basis for Chapter 4, on the precipitation of energetic particles associated with loss-cone filling near isotropy boundaries. Two studies in particular were pivotal in inspiring the goal to study $\geq$50 keV electron and proton precipitation. These included (Sergeev et al., 1983), who used both modeling and ESRO 1A observations to establish that pitch-angle scattering from magnetic field-line curvature (now referred to as "FLC scattering," or "FLCS"), was the dominant source of energetic proton precipitation into the ionosphere from the plasma sheet. This work also established the critical ratio $\kappa_{cr} = R_{C,eq}/r_{L,eq}$ of equatorial radius of curvature to gyro-radius that would result in strong-diffusive scattering, with a nominal value of 8. This criterion is used in my thesis to derive the relativistic case (Ch. 3), and many others. Further, this work suggested that precipitation from these particles could be a useful tracer of activity in the magnetotail, which would later inspire many such papers mentioned in Chapters 3 and 4.

While these isotropic fluxes had been considered useful tracers of activity in the magnetosphere, it was not until later that a direct connection was suggested between the IB location and the occurrence of the peak in energetic particle precipitation impacting the ionosphere. Such a connection was first firmly established by (Newell et al., 1998), who showed using DMSP and POES, that the 30 keV proton IB was very strongly correlated with the peak in <30 keV proton precipitation. This came to be known as the "b2i" index, whose MLT-dependence and flux scaling was derived empirically. These authors did not

consider the case of more energetic particle precipitation or their IBs (likely due to instrumental and orbit limitations). However, as I demonstrate as a key finding in this work, for both electrons and protons, the associated >30 keV isotropic precipitation poleward of the IB can be highly significant, enhancing ionospheric conductivity by more than a factor of 2. Further, I show that the concept of the "b2i" can be extended to higher-energies, defining a curvature-dominated precipitation region between the plasma sheet and outer radiation belt (for electrons) and ring current (for protons). These findings are the focus of Ch. 4.

More recently, it has been questioned whether FLC is the dominant mechanism producing energetic electron and proton IBs. This is because wave-particle interactions, such as EMIC waves under certain conditions as discussed by (Liang et al., 2014; Sergeev et al., 2015b), can give rise to structures appearing to be isotropy boundaries. This question has historically been challenging to address directly by equatorial spacecraft, due to the vastness of the magnetotail and the need to serendipitously be in the correct place at the correct time. It has further been challenging to determine energy-latitude dispersion patterns over a wide range of finely-resolved energies, due to the lack of high-fidelity energy- and pitch-angle spectra in a polar orbit. In this work, I use data from the ELFIN mission to answer this question statistically, based on the distribution of energy-latitude dispersion patterns, and the significant improvement in instrumentation and data coverage compared to prior missions. These findings are also a key conclusion of Ch. 3.

Lastly, there has been considerable community interest in modeling the location of isotropy boundaries, without the need to rely on magnetic field models, which may impart significant uncertainties in field-line mapping and field strength. Such models have been developed for both storm-time and quiet time using POES data, combined with activity indices (e.g. Dst, sym-H, AE, Kp) and solar wind observables, such as (Dubyagin et al., 2018) and (Ma et al., 2022). These studies however were limited *only* to protons of 30-120 keV energies, and *no electrons*. They also relied on linear regression methods that, as I show, may be insufficient to quantify the correlation between IBs and their drivers. Ch. 5 derives an empirical model using techniques from information theory, such as Shannon Entropy, to

establish both linear and nonlinear correlations.

1.3 Thesis objectives and outline

Building on the preceding historical background and motivation, my thesis aims to answer the following questions:

1. **What is the spatiotemporal magnetic latitude distribution of 50 keV-3 MeV electron and 50 keV to ∼2 MeV proton isotropy boundaries? How do they vary with geomagnetic activity?**

2. **What is the dominant mechanism of IB formation as a function of particle species and energy? What is the occurrence frequency of non-FLC type energy-latitude dispersion?**

3. **What is the range of precipitating energy flux of ≥50 keV isotropic electrons and protons associated with FLCS poleward of IBs? What is the latitudinal extent of such fluxes, and how does it vary with activity?**

4. **Does energetic particle precipitation associated with the IB/FLCS mechanism have a non-negligible effect on the ionosphere? How does it fit in our current understanding of ionospheric processes?**

5. **Which geomagnetic activity indices and solar wind/magnetospheric observables correlate most strongly with the IB location as a function of energy and species?**

6. **How well can the predictive model of IB location based on information theory perform?**

With these questions in mind, the outline of this dissertation's chapters are as follows: Chapter 2 briefly summarizes the ELFIN mission and its data, which are used extensively

in this study to form the IB statistical characteristics. I also describe my work on the development of ELFIN's instruments, alongside their calibration and operation.

Chapter 3 explores the spatiotemporal aspects of IBs (Questions 1 and 2), including a theoretical model of the IB based on the FLCS and EMIC mechanisms, plus event selection criteria. The chapter presents distributions of each IB species versus MLT, energy, and activity. The energy-latitude dispersion patterns and their frequencies are compared with theoretical expectations of FLC scattering versus other mechanisms, such as waves and non-monotonic equatorial B_z gradients.

Chapter 4 investigates the $\geq$50 keV precipitating particle characteristics associated with the FLCS-dominated region poleward of IBs, including its impact on magnetosphere-ionosphere coupling (Questions 3 and 4). It is shown that such precipitation likely represents a significant and underappreciated source of ionization enhancements and global power input, at times rivaling the input from $\leq$30 keV auroral particles, thus warranting serious consideration in future models.

Chapter 5 examines the connection between drivers in the solar wind/magnetosphere and IBs, deriving a predictive model as a function of energy, alongside an error analysis (Questions 5 and 6). The model is chosen based on the simplest sets of basis terms which encode a wide range of time and spatial scales, and shown to perform as well (or better) than existing models at overlapping energies.

Chapter 6 summarizes the findings of this dissertation, and suggests possible future avenues for pursuit in this line of investigations.

CHAPTER 2

The Energetic Particle Detectors (EPD) onboard the ELFIN CubeSats

This chapter briefly introduces the ELFIN CubeSat mission and the development and testing of its instrumentation, including an Energetic Particle Detector for electrons (EPD-E) and ions (EPD-I), as well as a Fluxgate Magnetometer (FGM). In-situ particle flux and field measurements from these instruments are used as the primary dataset in my thesis, which provide a combination of energy and pitch-angle resolution that was well-suited for energetic ($\geq$50 keV) isotropy boundary investigations. I also describe the results achieved as the lead of the payload instruments team.

2.1 Mission overview

The Electron Losses and Fields Investigation (ELFIN) mission was a NASA/NSF-funded dual CubeSat mission developed primarily by students at UCLA (Angelopoulos et al., 2020), which launched in 2018 into 450 km circular polar orbit ($\sim$91° inclination), and re-entered the atmosphere in 2022. It was designed to study energetic electron and proton precipitation from the inner and outer radiation belts, ring current, plasma sheet, and polar cap. The two satellites were designated ELFIN-A and ELFIN-B, and consisted of an instruments stack (EPD and FGM), a deployable boom for magnetic isolation, an avionics stack with torquer coil-driven attitude control, batteries and solar panels, and a VHF/UHF radio with

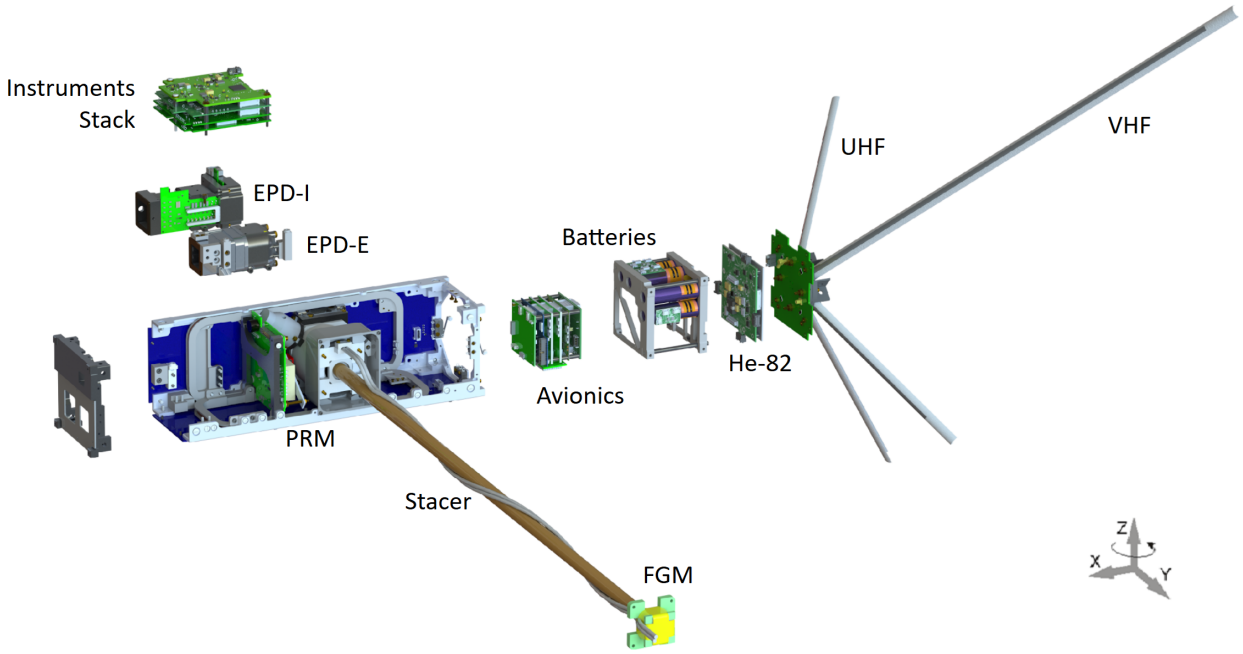

Figure 2.1: Exploded view of one ELFIN CubeSat containing the instruments stack, a deployable magnetic "boom" (stacer) to isolate the fluxgate magnetometer, an avionics stack with "torquer coils" for attitude control, batteries (plus solar panels), and He-82 VHF/UHF radio transceiver with deployable "tuna can" antenna.

deployable antenna. The total volume of each satellite was nominally 3U[1], plus a slight additional volume for the deployable antenna. Fig. 2.1[2] shows an exploded view of the satellite components. This chapter focuses specifically on the instruments stack, which I helped to develop, test, and operate. Additional technical details may be found in (Tsai et al., 2025).

[1]The unit "U" is standard form-factor multiple of CubeSat volume, representing a cube of 1 liter interior (10 cm edges).

[2]Images courtesy of ELFIN team. The EPDs and payload electronics boards conformed to a 1U volume and <5 W power draw. See https://elfin.igpp.ucla.edu/

2.2 The ELFIN EPDs

2.2.1 Instrument specifications

The ELFIN EPDs consisted of a set of two silicon detector stacks to separately measure energetic electron and proton impacts, shown in Fig. 2.2. The EPD-E consisted of 6 square detectors of active area 1 cm^2, including a 500 μm front detector (E1), followed by two 1000 μm detectors (E2, E3), followed by two 2000 μm "ganged" detectors[3] (E4, E5), and a final 500 μm detector (E6). The instrument was shielded by an enclosure of brass, aluminum, and tantalum to deflect and absorb particles outside of the intended fields of view.

The EPD-I had a stack consisting of only two 500 μm detectors (P1 and P2), where P1 was used to sense proton impacts up to ~6 MeV, and P2 was used to eliminate penetrating electron contamination by anti-coincidence logic. This sensor head required fewer detectors to measure the same energy range due to the fact that protons (and heavier ions) have a much larger Coulomb scattering cross-section than electrons, and therefore tend to be much more efficient in their energy deposition per unit length (dE/dx).

2.2.2 Pulse-height analysis and channel efficiencies

The EPDs nominally measure the differential-directional fluxes of 50 keV to 5 MeV electrons (22.5° full-width FoV, geometric factor 0.15 cm^2-str) and protons (~0.01 cm^2-str), and a boom-deployed 3-axis Fluxgate Magnetometer (FGM) sampling the background field at 80 samples/sec.

Particle counts and energies were determined using digitally sampled pulse-height analysis (PHA) on the output of a pulse-shaping pre-amplifier, configured to sense silicon detector impact events. The preamp pulse shaper rise time was 2.4 μs, which established the nominal dead time of the system. Particle counts were binned into 16 logarithmically-spaced energy channels, satisfying the constraint that the energy width dE of each bin was less than 0.4

[3]Detector "ganging" refers to placing two thinner detectors together in an electrically parallel configuration to form an effectively thicker detector at a lower bias voltage.

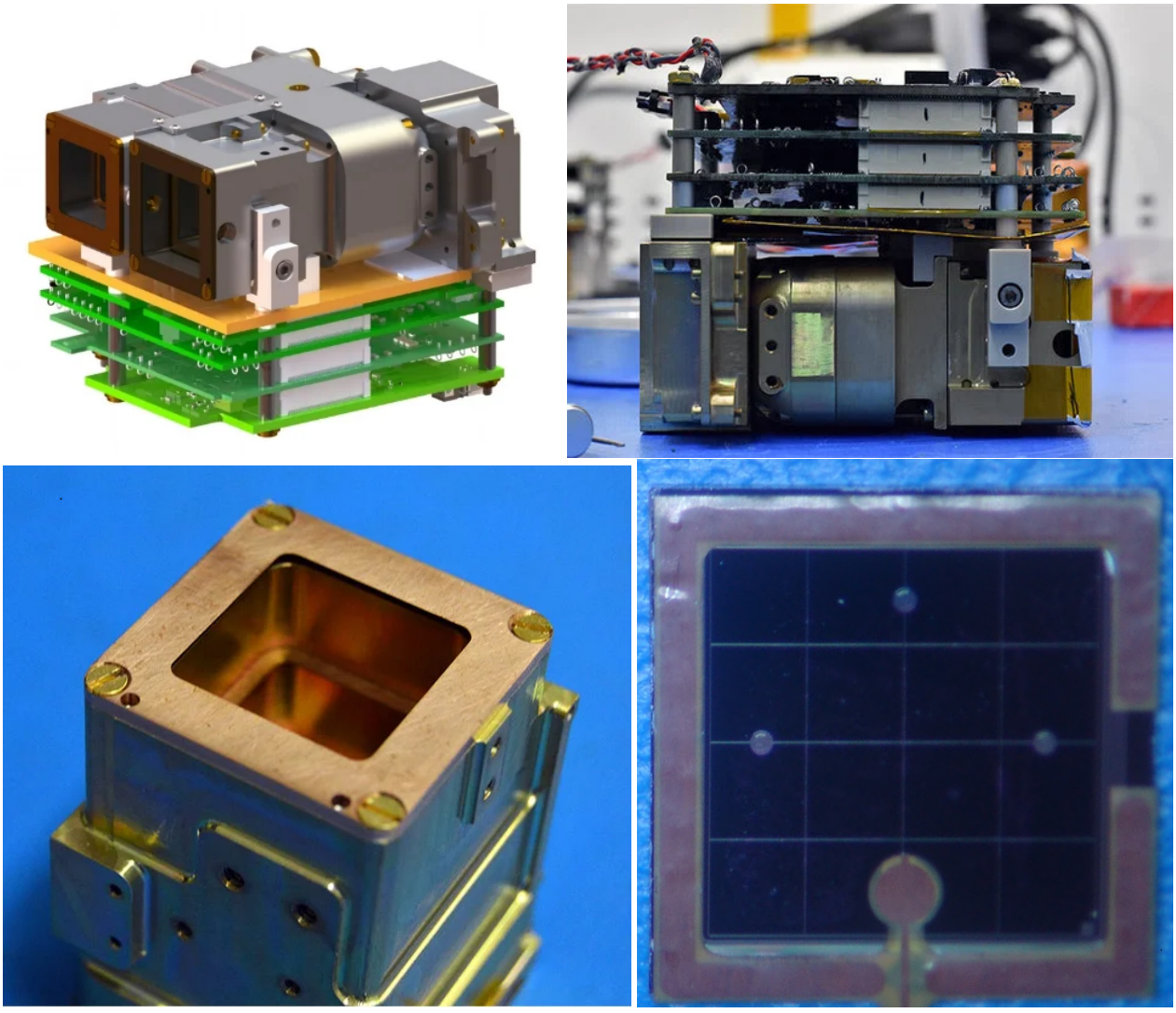

Figure 2.2: Top left: CAD illustration of the EPD-E/I electronics stack with sensor heads attached. Top right: Flight-model payload electronics stack and EPD-E/I sensor heads. Bottom left: Sensor head aperture field of view and knife edges. Bottom right: cross-section of silicon detector active area (1 cm^2).

times the central energy E of the bin; that is, $dE/E \leq 0.4$. The log-mean energies of each discrete channel, in keV, were: [63.2, 98., 138.6, 183.3, 238.1, 305.2, 385.2, 520.5, 753.0, 1081.7, 1529.7, 2121.3, 2894., 3728.6, 4906.1, 5800.].

Because energetic electrons tend to scatter easily within solid materials, it was necessary to introduce an inversion matrix to correct the inefficiencies caused by partial energy deposition within the silicon active area. We achieved "channel efficiency" corrections by simulating a large population of incident mono-energetic electrons, and repeating the process at regular energy steps to determine the most likely energy deposition combination on each detector. This was done using the GEANT4 code (Agostinelli et al., 2003), which provides a high-fidelity energetic particle and radiation tracing simulation framework in the presence of matter and fields (originally developed for particle accelerator and medical radiation treatment applications). From this, we devised a channel efficiency correction matrix $\mathbf{A}^{-1}$, shown in Fig. 2.3. The deposited energies mostly correspond to their true binned energy, up until approximately 3 MeV, at which point the instrument significantly loses sensitivity (resulting in "channel mixing"). This is a limitation of the silicon stack thickness, and explains why many ELFIN events do not usually show appreciable counts above 3 MeV (despite being theoretically capable of detection). In practice, only the diagonal terms of the inverse matrix were retained in the EPD calibration routines. Proton events, on the other hand, did not require a channel efficiency correction, because they typically deposit their full energy upon impact.

2.2.3 Contamination rejection and coincidence logic

Proton contamination up to ~700 keV on the EPD-E was mitigated using an aperture foil, composed of a three-layer composite of 0.5 μm of aluminum (ρ_m = 2.7 g/cm^3), 10 μm of lexan polycarbonate (ρ_m = 1.2 g/cm^3), and 0.5 μm aluminum, which had minimal effect on incident electrons above 50 keV. Protons with energies above 700 keV could technically begin to reach the front detector, although with significantly reduced energy as to appear at most as a small noise signal in the background low-energy electron fluxes. Electron

$$J_{e,obs}(E_i) = \sum_j A_{ij} J_{e,true}(E_j)$$

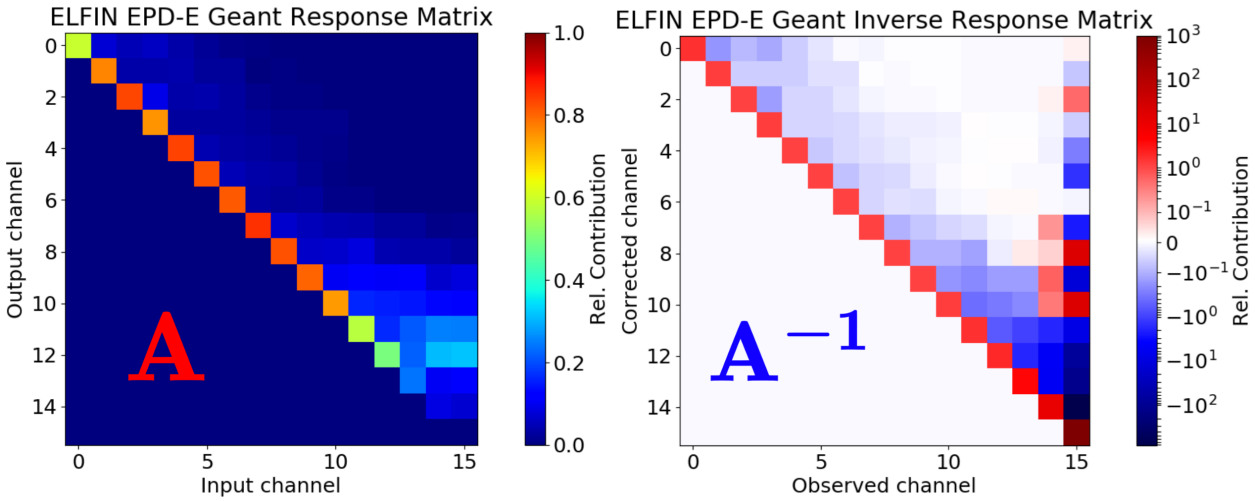

Channel log-mean energies (keV): [63.2, 98., 138.6, 183.3, 238.1, 305.2, 385.2, 520.5, 753.0, 1081.7, 1529.7, 2121.3, 2894., 3728.6, 4906.1, 5800.]

Figure 2.3: Left: EPD silicon detector channel response matrix $\mathbf{A}$, mapping the true input electron energies into the probability space of partially deposited energies. Right: Channel efficiency inversion matrix $\mathbf{A}^{-1}$ used to invert the channel efficiencies.

contamination on the EPD-I was mitigated using an octupolar magnetic broom filter and two-detector anti-coincidence logic, which leverages the fact that energetic protons below 10 MeV will tend to deposit all of their energy on the front detector, while electrons over several hundred keV will tend to pass through to the next detector in the stack, and can thus be discriminated. Contamination by side-penetrating particles was mitigated by a combination of dense shielding surrounding the look directions and knife-edge surfaces to limit the field of view via specular reflection of particles, as well as detector stack coincidence logic. In order for an electron count to be considered valid (i.e., coming from within the intended field of view), it must deposit energy on only consecutive front detectors, such as E1, or E1+E2, ..., E1+...+E6. In an opposite example, if the energy was deposited on a combination such as E3 only, the count would be rejected as side-penetrating. This required that the noise thresholds of the system were tuned to reject spurious noise counts, which we performed on-orbit during early commissioning of the instruments.

2.2.4 Dead time correction

Due to the way the coincidence logic was implemented in the EPD-E, an in-progress counting event was not considered complete until the signal on every detector in the stack dropped below its triggering threshold. This implies that if a high energy count occurs in the middle of a low energy counting window, the low energy count will tend to be overridden by the higher energy count. This means that the ELFIN EPDs follow a "paralyzable" type of detector model (Usman and Patil, 2018), in which the system can be locked out if counts repeatedly occur within the nominal rise time of the preamp pulse shaper. This results in a detected count rate affected not only by the counts of the particular energy channel, but also by the sum of those in energy channels above it.

In order to correct the data for this effect, we devised an energy-dependent counting correction factor to each differential channel. Under the assumption of Poisson counting statistics and the above count summing condition, the detected (overlapping) count rates are related to the true count rate by:

$$R_{E,det} = R_E \exp\left(-\frac{R_E}{R_\tau}\right) \tag{2.1}$$

where $R_{E,det}$ are the detected count rates in the channel of energy E *summed* with those above it, R_E is the true count rate of the channel containing the energy E, and R_τ is the reciprocal of the dead time $\tau = 2.4$ μs/count. The solution to R_E is given by the lower real branch (argument $> -1/e$) of the Lambert W function (Corless et al., 1996) for all energy channels, if the particular channel had non-zero counts. We note that upper real branch (argument $< -1/e$) solutions are also possible; however, these resulted in large discontinuous jumps in fluxes between lower energy channels and those at higher energies (presumed unsaturated). Thus, we nominally take the lower branch to be correct.

2.2.5 Magnetic spin sectoring

The satellites were spinning with a period of 2.8 s in a plane nominally containing the parallel and perpendicular directions to the background magnetic field, allowing for onboard spin phase/pitch-angle determination using instantaneous FGM readings. Each spin period was subdivided into 16 consecutive spin sectors, providing $\Delta T \sim 175$ ms time resolution per sector. This was achieved by developing an on-board algorithm to sense the instantaneous crossing of either the field-aligned or perpendicular directions of the local magnetic field. Fig. 2.4 show an example of how this is achieved on one of the FGM data axes, using a simulated spin curve in the presence of a noise signal. In practice, fhe time-derivative of the signal was used in order to eliminate any potential field offsets. The method was tested in-lab using a field coil driver in a "shield can" at the nominal spin rate.

2.2.6 Calibration

The EPD energy channels were calibrated using a tandem combination of GEANT4 simulations of known radioisotope spectra, and then subjecting the actual instrument to these isotopes in the lab. We tried a number of different sealed source alpha and beta emitters, deciding finally that Ru-106 proved to be an ideal EPD-E reference source. Fig. 2.5 shows the calibration result which determined the EPD-E energy channel gains and offsets used in flight. For the EPD-I, the Am-241 alpha+gamma emitter was used for calibration (not shown).

2.2.7 Data products

The raw data collected by the EPDs were count rates as a function of energy channel, spin sector, and time. On the ground, these data were converted to calibrated differential-directional number fluxes and pitch-angle spectra, in units of $1/\text{cm}^2$-s-str-MeV. Fig. 2.6 shows an example ELFIN-B collection on 2020-09-02, corresponding to the 6-7 minute interval following the orbit path shown in the top left. The collection began over the northern polar cap, and

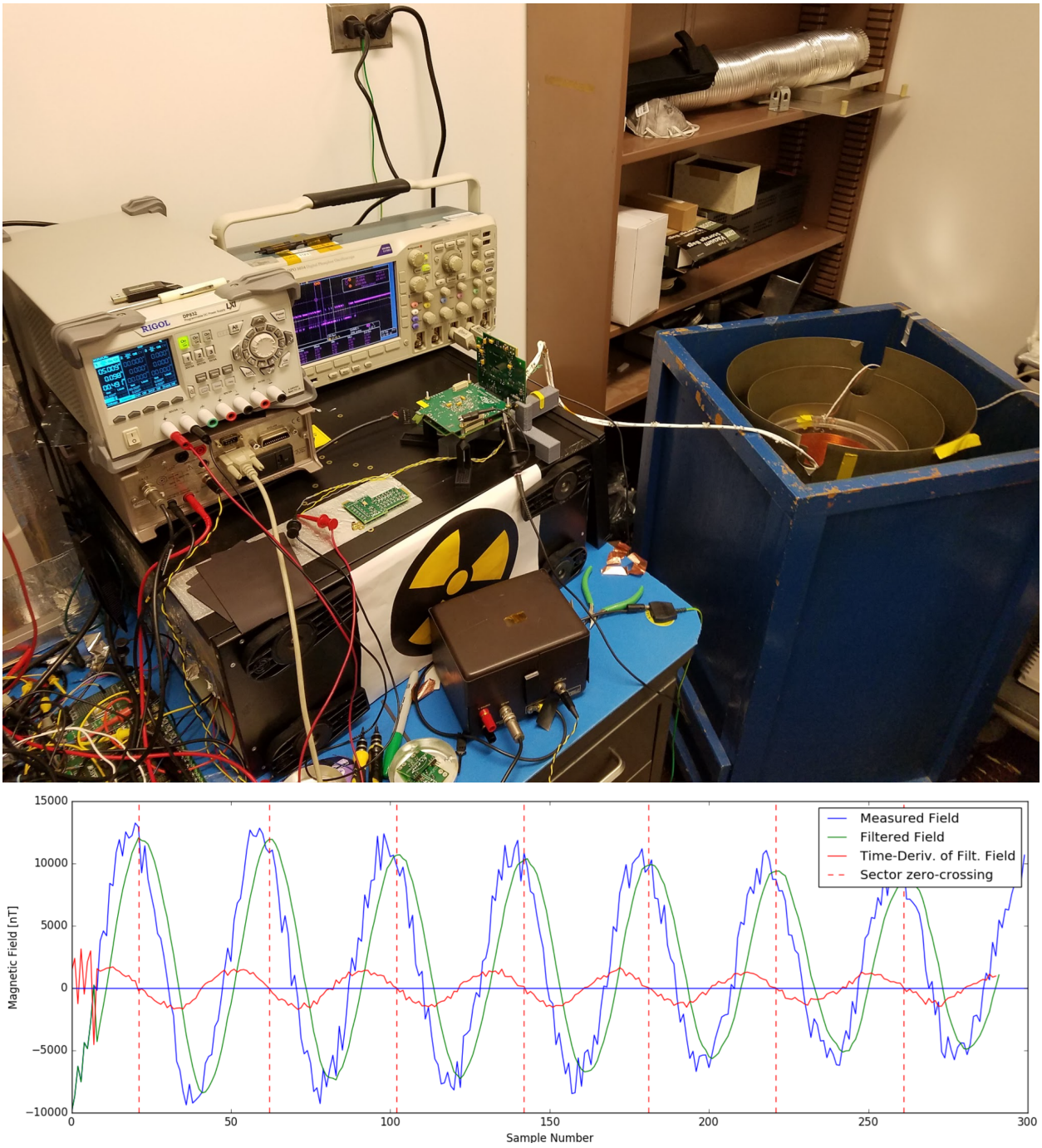

Figure 2.4: Top: "Shield can" setup of the magnetic spin sectoring algorithm, in which a sinusoidal magnetic field is applied along one of the FGM instrument axes at the nominal spacecraft spin rate. Bottom: Simulated model results of the on-orbit spin sector period and phase determination, used to determine the local particle pitch-angles.

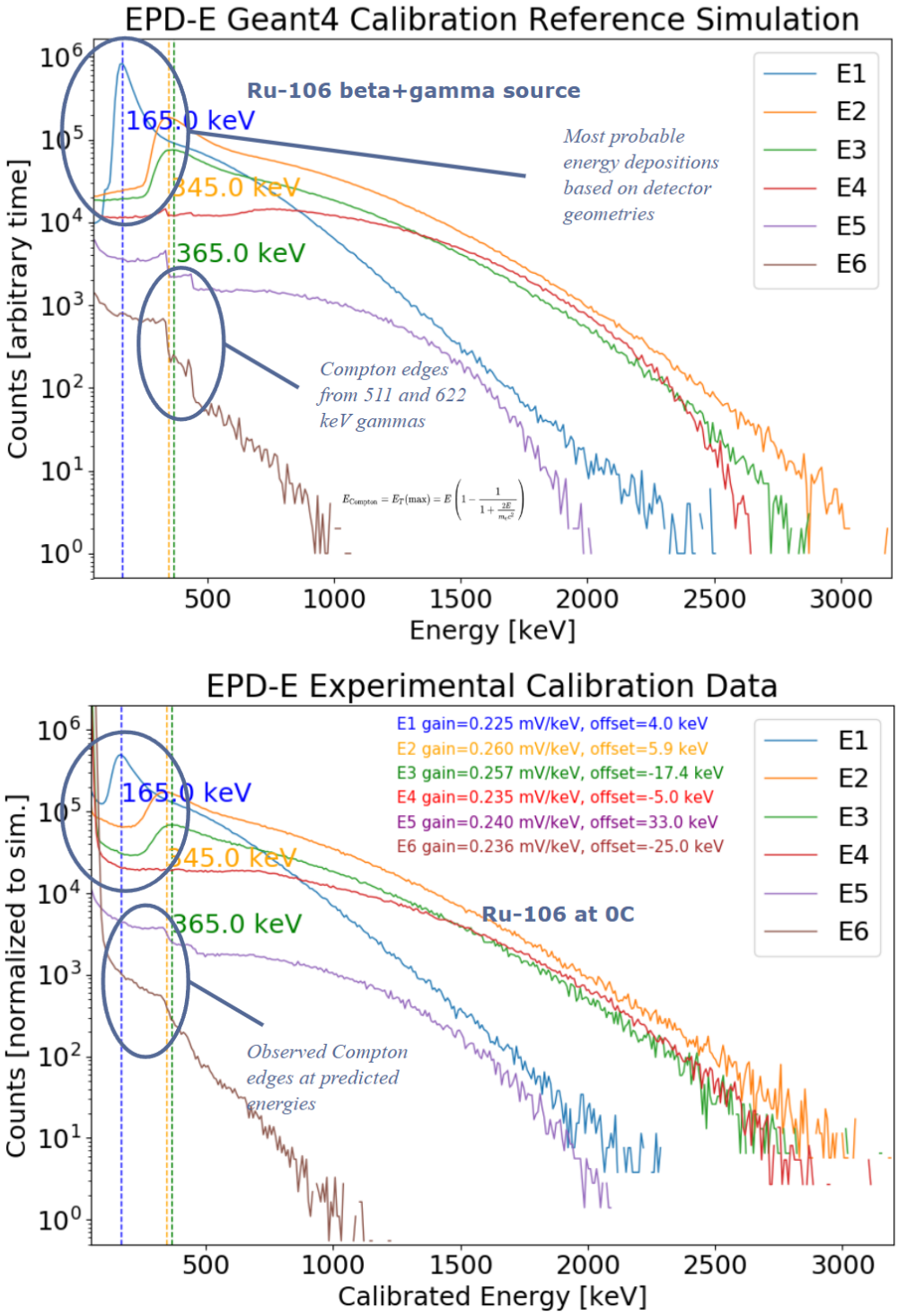

Figure 2.5: Top: GEANT4 simulation of the Ru-106 radioisotope beta and gamma ray source, as detected by the EPD-E. Bottom: Actual calibration curves from this isotope in the lab, used to determine the flight energy gain and offsets.

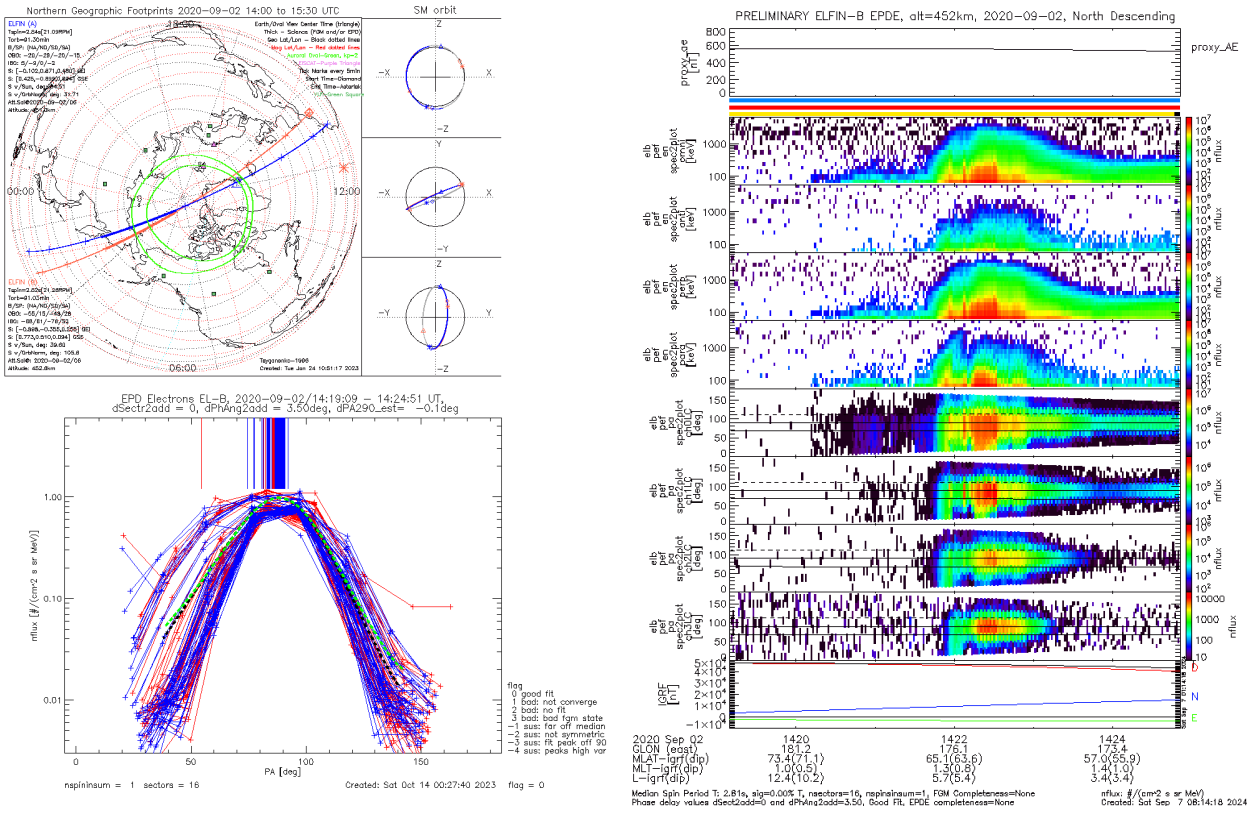

Figure 2.6: Top left: Example north descending orbits of ELFIN-A and ELFIN-B on 2020-09-02. Right: Example summary plot from the ELFIN data website showing a 6-7 minute ELFIN-B outer radiation belt collection. Bottom left: Pitch-angle spectra fits on the particle fluxes versus apparent spin phase, used to determine the pitch-angle distribution and its phase delay. Higher-resolution versions of these panels may be found at this link: https://plots.elfin.ucla.edu/summary.php

descended equatorward in latitude, crossing the plasma sheet into the outer radiation belt.[4] The panels on the right, in order, show the instantaneous AE index (geomagnetic activity), followed by number fluxes in omnidirectional, anti-parallel, perpendicular, and parallel pitch-angle bins. The next four panels show the pitch-angle spectra in selected energy ranges. The bottom left of Fig. 2.6 shows the pitch-angle fitting process of this 6-7 minute collection, relying on a polynomial fit to determine the minimum error phase offset in the spin period. The last panel shows the local IGRF magnetic field strength at the satellite location, while the annotations show the instantaneous spacecraft location in various coordinate systems.

[4]Incidentally, this was the canonical isotropy boundary event examined in (Wilkins et al., 2023).

It is these data that are used throughout the remainder of the Chapters herein. The ELFIN mission and its instruments also set a modern standard for scientific achievement by a relatively inexpensive development project run by a student team. I am personally grateful and proud to have had the opportunity to contribute.

CHAPTER 3

Spatiotemporal characteristics of energetic electron and proton isotropy boundaries

In this chapter, I use ELFIN data to address Questions 1 and 2 of my thesis objectives, to determine the spatiotemporal characteristics of 50 keV to 3 MeV electron and 50 keV to ∼2 MeV proton isotropy boundaries. Here, "spatiotemporal" refers to variations in IB latitude and its energy-latitude dispersion, as a function of magnetic local time (MLT) and evolving geomagnetic conditions. I relate these findings to implications about large-scale magnetic field configurations at quiet and active times, including implications of cross-tail current-sheet thinning. In tandem with energy-latitude dispersion patterns, I also describe the most probable IB generation mechanism between monotonic equatorial ∇B_z FLC-type scattering and plasma waves/reverse B_z gradients.

3.1 Introduction

A primary objective in studying Earth's magnetosphere-ionosphere system is to characterize the sources and mechanisms of energetic charged-particle precipitation into the atmosphere, and the large-scale magnetospheric processes which enable them. In this work, I focus on a particular population of energetic particles which experience loss-cone filling due to isotropization of their equatorial pitch-angle distributions. Mapped into the ionosphere, these isotropized distributions can be continually detected at energies exceeding 10s of keV in particle flux measurements. Such distributions often transition abruptly from anisotropy to isotropy at a specific magnetic latitude, known as the isotropy boundary (IB) for that

particular particle species, energy, and magnetic local time (MLT) (Sergeev et al., 1983). An IB crossing in particle data can be identified by the location where nearly equal precipitating (J_{prec}) and locally-mirroring (J_{perp}) fluxes are first detected, i.e., $J_{prec}/J_{perp} \sim 1$. The IB detected at any one energy is often part of a continuous energy spectrum of particles which become isotropized in close latitudinal proximity. These IBs collectively form an energy-latitude dispersion pattern, encoding information about the underlying isotropization mechanism. The energy-dependent generation mechanism and time-evolution of these patterns have remained long-standing questions, with equatorial magnetic field-line curvature (FLC) scattering and wave-particle interactions being proposed as the primary processes (Ganushkina et al., 2005; Sergeev et al., 2015b).

As I demonstrate, the mechanism in this study most commonly observed to be compatible with 50 keV to ∼MeV nightside proton IB formation is FLC scattering (or "FLCS," occasionally referred to as "current-sheet scattering"), which occurs when the gyro-radius of energetic particles approaches length scales comparable to gradients in the background magnetic field. Isotropy boundaries produced by FLC at ≥50 keV energies have the potential to be geophysically important for several reasons. For one, they are associated with a robust multi-species pitch-angle scattering mechanism, affecting electrons, protons, and heavier ions—potentially all simultaneously—throughout much of the magnetosphere in the strong-diffusion limit. This can occur under any geomagnetic conditions, dependent only on the large-scale background magnetic field configuration (Sergeev et al., 1993), leading to the direct precipitation/loss of energetic particles (keVs and up) in the ring current, radiation belts, and plasma sheet (Imhof et al., 1997, 1979; Selesnick and Looper, 2023; Sergeev et al., 1983; Wilkins et al., 2023; Yu et al., 2020; Yue et al., 2014). Further, owing to the rapid pitch-angle diffusion (on the order of single bounce periods), particles undergoing such scattering provide a near-instantaneous tracer at Low Earth Orbit (LEO) of the distant equatorial magnetic field strength and curvature connected to the field-lines. By rapidly sampling the IB of different energy and species particles along the satellite orbit track, it is possible to create latitudinal profiles of the minimum particle energy required for isotropiza-

tion by FLC. This can be paired with equatorial observations or field models to determine the instantaneous equatorial magnetic field strength and curvature radius versus the radial distance from Earth, and ultimately the large-scale current systems which produce them (Newell et al., 1998; Sergeev et al., 1993; Shevchenko et al., 2010; Shi et al., 2024).

Proton IBs have a long history of observations, focusing primarily on detections at ≤120 keV energies (e.g., (Dubyagin et al., 2018; Ganushkina et al., 2005; Ilie et al., 2015; Imhof et al., 1977; Lvova et al., 2005; Newell et al., 1998; Sergeev et al., 1993, 2015a,b, 1983; Shevchenko et al., 2010; Yue et al., 2014)). In combination with simulations, these studies aimed to characterize or infer the distribution in magnetic latitude (or L-shell) and local time; the magnetic field configuration at the equatorial scattering location (e.g., R_C, B_z, and the "κ" parameter described later), or wave-particle interactions there; interpretations as open/closed drift shells and field-line boundaries; and the precipitation of energetic particles into the atmosphere due to isotropic loss-cone filling. Many of the aforementioned works relied on observations by Polar Operational Environmental Satellites (POES) and Defense Meteorological Satellite Program (DMSP), with ground observations to correlate precipitation signatures (e.g., (Donovan, 2003)). Due to their design considerations, these instruments were not particularly well-suited to resolving the more energetic (e.g., >200 keV) portion of the IBs most of the time. In tandem with such observations, simulations have been carried out either by particle tracing through field models or global fluid codes, or by estimating the effect of equatorial crossings as a quasi-linear diffusion process (Birmingham, 1984; Delcourt et al., 1996; Gray and Lee, 1982; Liang et al., 2014; Martin et al., 2000; Sergeev and Tsyganenko, 1982; Shi et al., 2024; Young, 2002; Young et al., 2008).

Here, I aim to extend the knowledge of proton isotropy boundary characteristics to include 200 keV to MeV energies, based on particle data from the ELFIN mission (Angelopoulos et al., 2020). Such characteristics have direct implications for magnetospheric ion losses, with the potential to result in significant precipitation into the ionosphere at auroral and sub-auroral latitudes. For example, nightside conductivity can be enhanced via ≥50 keV proton impact ionization over a range of altitudes, since the ionospheric penetration depth

and secondary electron ionization increases significantly for protons above 10s of keV up to MeV energies (Fang et al., 2007). Recent combined observations of ≥50 keV electron and proton precipitation, such as (Tian et al., 2022), have also demonstrated the contribution of 50-300 keV particles to Pedersen and Hall conductivity in EMIC wave events, resulting in enhancement down to 70 km, with energetic protons providing a significant contribution at altitudes 200 km and below. Along these lines, I show in Ch. 4 that the total precipitating power from isotropic ≥50 keV protons in close poleward vicinity to the IB can at times even rival the input power produced by <50 keV particles traditionally associated with the aurora (e.g. (Newell et al., 2009a)), suggesting it should be included in descriptions of the global energy budget.

Beyond large-scale power input, the role of ≥50 keV particles in various magnetosphere-ionosphere coupling processes is also of considerable interest. For instance, a recent case study of a Subauroral Polarization Stream (SAPS) event using ELFIN, DMSP, and THEMIS was reported by (Artemyev et al., 2024), who showed that the 100 keV to 1 MeV proton IB was embedded directly within the polarization stream, with ≥100 keV electron and proton fluxes more effectively delineating the flow boundary than <30 keV particles, indicative of MI coupling. In addition to affecting the ionosphere, the role of curvature scattering in the evolution of the ring current is also actively being considered, serving as a mechanism to explain observed deviations in Dst decay rates versus modeled predictions. Several recent simulation works have directly or indirectly-inferred the need for an additional scattering mechanism such as FLC to account for observations, which are further supported by this work (Cao et al., 2023; Chen et al., 2021; Dubyagin et al., 2020; Ebihara, 2003, 2019; Eshetu et al., 2021; Yu et al., 2020).

Contrary to proton IBs, electron IBs have received less attention, and their occurrence and properties have been poorly investigated (Capannolo et al., 2022; Sergeev et al., 2018). This has largely been due to similar observational constraints of proton studies, which have contended with limited latitudinal coverage (e.g. RadSat, UARS, Van Allen Probes, GOES, Geotail, THEMIS, etc.), or issues with particle detection capability, such as insufficient

electron pitch-angle resolution and energy range, dynamic range or sensitivity, uncertainties in sensor cross-calibration between look directions, and cross-species contamination (e.g. POES, DMSP). Because energetic electron IBs are found as high as 74°, exhibit orders of magnitude variation in flux and precipitation energy, and often appear poleward of proton IBs, previous studies were ill-equipped to fully characterize their properties. To address these issues, I used recently acquired data from the Electron Losses and Fields Investigation (ELFIN) satellites (Angelopoulos et al., 2020), whose observations from circular polar Low Earth Orbit (LEO) provide latitudinal coverage spanning 55° to 80°, 24 hours in aggregate local time, and electron energies between 50 keV and ∼5 MeV, with a single, low-noise, high-sensitivity, proton-rejecting electron sensor used to measure fluxes over all pitch-angles during each spin (once per 2.8 seconds).

Similar to protons as above, the properties and role of isotropic ≥100 keV electrons associated with IBs in several important magnetospheric and ionospheric processes have remained similarly veiled. For example, because FLCS-isotropized electrons can include populations of tens of keV and up to the MeV range, they can penetrate to to much lower altitudes into the high-latitude atmosphere than similar energy protons, including below 80 km (Fang et al., 2010). Additionally, because the FLCS isotropization mechanism can act rapidly (on the order of a bounce period) in the equatorial region where inward radial diffusion transports particles into the outer radiation belt, it can potentially prevent such particles from ever becoming trapped. These flux losses would not be accounted for as part of outer radiation belt precipitation due to being outside the trapped flux region (and indeed, has very recently been shown using ELFIN data as a depletion mechanism of outer belt electrons by (Artemyev et al., 2025)).

Such modeling efforts are also confounded by the fact that the isotropy boundary is difficult to recognize on equatorial spacecraft traversing the tail-dipole transition region, because the spacecraft must serendipitously be in the exact location at the correct time to cross the equatorial isotropic transition, and because the loss cone at the equator is only ∼1°, which is challenging to resolve by typical particle instruments. Thus, these fluxes are not

accounted for in energetic precipitation modeling and prediction based on such data. Further, beyond assessing the direct geophysical role played by isotropic electrons, knowledge of the IB location as a function of time can be a useful tool for near-instantaneous remote-sensing of the equatorial magnetic field configuration, and of the particle populations residing there. This can help refine equatorial magnetic field and particle flux models, especially when paired with equatorial satellites (Ilie et al., 2015; Sergeev et al., 1993, 2015a; Shevchenko et al., 2010).

While the majority of past investigations have focused on the nightside, I note that dayside IBs are also a theoretical possibility. For protons, such IBs have previously been reported near noon from both near-magnetopause equatorial curvature scattering, as well as through the polar cusps (Sergeev et al., 1997). Characterization of dayside properties is again more difficult for electrons, in that they typically occur at higher-latitudes than proton IBs, mapping them closer to the magnetopause. These regions are host to several processes such as magnetic reconnection (Trattner et al., 2021) and the Kelvin-Helmholtz instability (Kim et al., 2022), which can give rise to similar dispersive isotropic particle scattering onto Earth-connected field lines. Observations of protons falling into these categories have long been made; the latter of which are often grouped into the umbrella of "magnetopause scattering" (e.g. (Lyons et al., 1987)). These cases are not the focus of this study; however, they present a challenge in distinguishing events which are genuinely due to an equatorial magnetospheric process versus other sources.

For polar spacecraft in LEO, at high latitudes where IBs are found, there can also be significant field-line mapping uncertainty in the vicinity the polar cusp and cap. In such instances, an event appearing to be at noon could actually map to the distant nightside through the polar cap. Similarly at dawn and dusk, equatorial field-line traces may also exhibit an abrupt variation in projected MLT as the spacecraft move toward the poles, obfuscating genuine fluxes from lower-latitude MLTs in the crossing. For all of these reasons, I pursued a conservative approach in IB event classification, separating events from the database which map too close to the magnetopause using a technique described in the Methods section.

3.2 Theoretical models of IB formation

To gain insight into the two primary mechanisms of IB formation, I here provide a theoretical model of the minimum particle kinetic energy required for their formation by (1) field-line curvature (FLC) scattering, and (2) wave-particle gyro-resonance. I have introduced a relativistic correction to the minimum scattering energy, which has not to my knowledge been reported previously. Such a correction is required due to the fact that the rest mass of an electron is 511 keV, which is within the range of kinetic energies addressed in this work (the Lorentz factor of these electrons thus may deviate significantly from unity).

3.2.1 Generation by field-line curvature scattering

Throughout much of the magnetosphere, charged particles travel along field lines, permitting guiding-center drift and bounce motions with associated adiabatic invariants. However, under the conditions described in Ch. 1, these invariants can be violated. One such breakdown results in the formation of isotropy boundaries: the abrupt variation of a particle's first adiabatic invariant (μ) upon encountering the region of sufficiently weak/sharply-curved magnetic field geometry. The condition for this breakdown is the particle's equatorial gyro-radius (r_L) beginning to approach the scale length of magnetic field variations, quantified by the curvature radius (R_C) of the local equatorial field configuration, where $R_C = \left|(\hat{\mathbf{b}} \cdot \nabla)\hat{\mathbf{b}}\right|^{-1}$, and $\hat{\mathbf{b}} = \mathbf{B}/B$ is the unit tangent vector to the magnetic field $\mathbf{B}$. As previously mentioned, such a scenario occurs for example at the center of current sheets, including Earth's cross-tail current, where only a small (1 nT to 10s of nT) neutral sheet B_z component exists.

In the preceding equatorial crossing scenario, the effect of the interaction between the particle and field depends highly on the ratio of the equatorial magnetic curvature radius to particle gyro-radius, defined in prevailing literature as $\kappa^2 = R_C/r_L$. When $\kappa^2 \gg 10$, typical adiabatic guiding-center motion results, with conservation of μ (Gray and Lee, 1982). The range of $\kappa^2 \lesssim 1$ results in Speiser-like motion (Martin et al., 2000; Speiser, 1965), while $3 \lesssim \kappa^2 \lesssim \kappa_{cr}^2$ results in pitch-angle scattering in the strong-diffusion limit (Delcourt

et al., 1996; Martin et al., 2000; Sergeev et al., 1993, 1983), producing isotropized particle fluxes, where κ_{cr}^2 is a critical parameter dependent on the geometry within and outside the equatorial region. The quantity κ_{cr}^2 is typically taken to have an *a priori* value of 8 (Sergeev et al., 1983), and can be understood intuitively as corresponding to a Harris-type current sheet with constant B_{normal} (Gray and Lee, 1982). In actual observations, the value of κ_{cr} has been inferred to span the range of 3 to 33 (Ilie et al., 2015; Sergeev et al., 2015a), although this likely includes both FLC and wave-particle processes at the values exceeding 8. Additionally, for particles heavier than electrons (e.g. protons), the effect of curvature off of the equator also affects the scattering (Young, 2002). These correction terms are proportional to d^2R_C/ds^2 and d^2B/ds^2, which affect the minimum gyro-radius for strong diffusive scattering, where s is the particle trajectory in the vicinity of the equator.

The relationship $\kappa^2 = \kappa_{cr}^2$ establishes a minimum gyro-radius required for strong diffusive pitch-angle scattering, which can be re-cast in the form of a minimum particle perpendicular kinetic energy E_{min}. As I derived for (Wilkins et al., 2023), a relativistic form of this equation (excluding the Young et al. off-equator corrections) is given by:

$$E_{min} = (\gamma_{min} - 1)mc^2 = \left[\left(1 + \left[\frac{qBR_C}{\kappa_{cr}^2 mc}\right]^2\right)^{1/2} - 1\right] mc^2 \tag{3.1}$$

where γ is the particle Lorentz factor, m and q are the mass and charge of the particle, respectively, B is the magnetic field strength, R_C is the curvature radius of the magnetic field, and c is the speed of light.

This relation encodes several important features between the minimum scattering energy and the equatorial magnetic conditions:

$$E_{min} \to \infty \text{ as } B \to \infty \tag{3.2}$$

$$E_{min} \to \infty \text{ as } R_C \to \infty \tag{3.3}$$

$$E_{min} \to \infty \text{ as } m \to 0 \tag{3.4}$$

$$E_{min} \approx q^2B^2R_C^2/2\kappa_{cr}^2 m \text{ for } v \ll c \tag{3.5}$$

These conditions explain why electron and proton IBs caused by FLC do not occur at the same location for the same energy: they differ significantly in their mass, and thus require different curvature and field strengths. To see this variation by location in the magnetosphere, Figure 3.1 shows an example of a spatial profile (GSM noon-midnight xz-cut) of the minimum particle energy E_{min} (Eqn. 3.1) for particle isotropization due to FLC for electrons (top) and protons (bottom) on 2022-08-04 at 06:08 UT. The (Tsyganenko, 1989) external field model and the International Geomagnetic Reference Field (IGRF) internal field model (Alken et al., 2021) were used to evaluate the magnetic field strength and curvature in space. For both electrons and protons, it can be seen that along any given field line, the curvature and field strength in the vicinity of the geomagnetic equator determine the minimum particle energy required for isotropization by FLC. The magnetic latitude of the field line connected to the equatorial scattering region establishes where the IB could be observable in the ionosphere.

I note that the energy-latitude dispersion signatures (change in IB energy versus change in latitude detected in the ionosphere) compatible with the monotonically-decreasing equatorial B_z profile illustrated in Fig. 3.1 are entirely negative (i.e., more energetic particles first isotropized closer to the equator). It is on this basis that IB observations can be classified as likely being of a traditional equatorial FLC-scattering origin. However, transient localized non-monotonic gradients in B_z in the neutral sheet are also possible, and can give rise to mesoscale ($< 1°$) positive dispersion for some energies, even though the scattering mechanism is still technically field-line curvature (Sergeev et al., 2018). Processes such as scattering by waves (e.g. EMIC), described next, can also produce localized isotropy boundaries for keV and greater energies. (Sergeev et al., 2015b). These interactions tend to produce positive energy-latitude dispersion, which can exist separately from the main FLC IB, or be mixed within it, as a mesoscale structure. To gain insight into the likelihood of the particular IB formation mechanism as a function of energy, I characterize the distribution of dispersion slope at each point in each detected dispersion pattern.

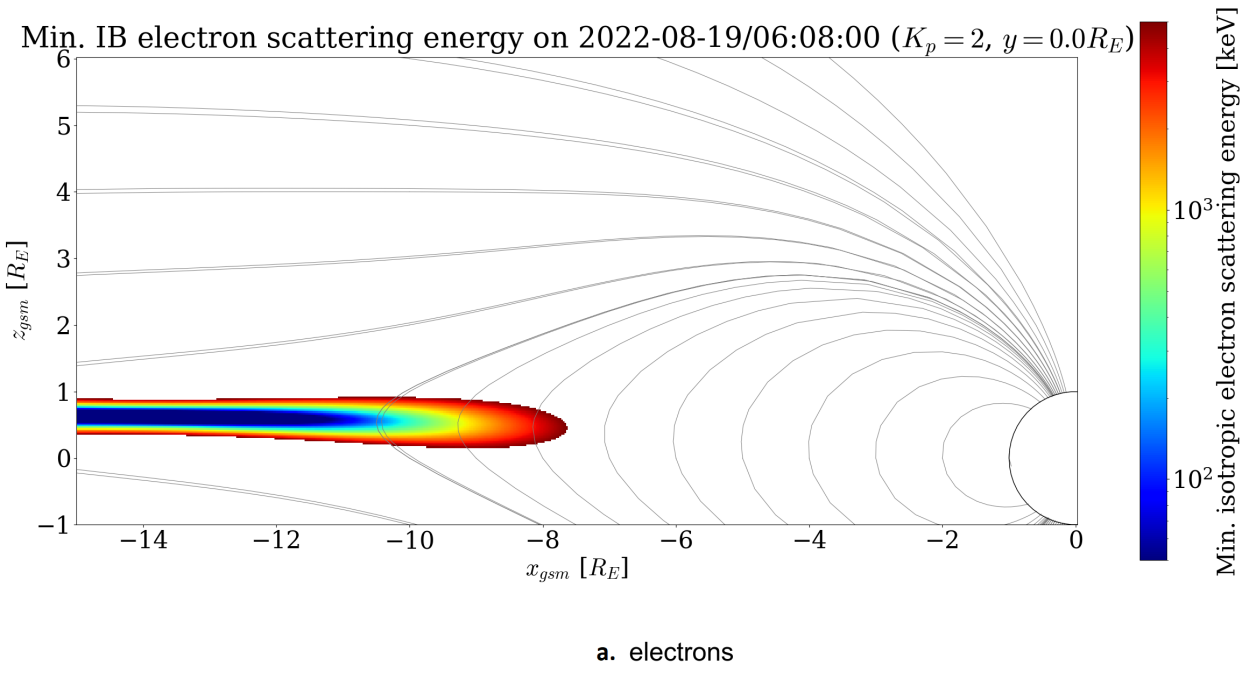

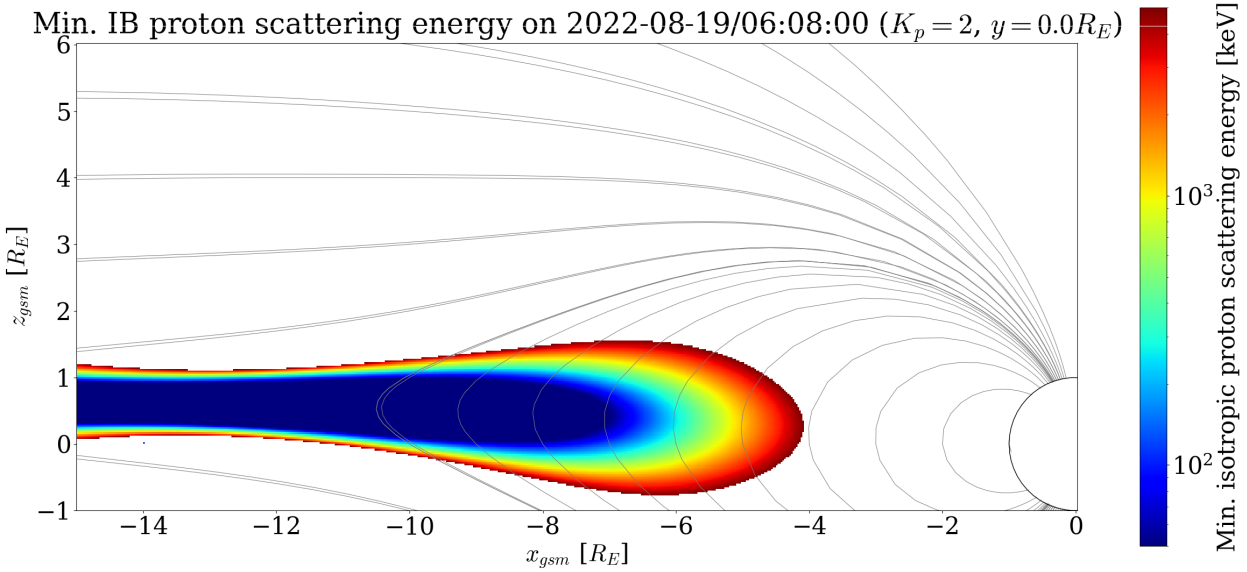

Figure 3.1: Modeled spatial profile (GSM noon-midnight cut) of the minimum kinetic energy required to experience strong-diffusion pitch-angle scattering by field-line curvature (T89 field model), resulting in isotropic distributions observed at LEO (defined in Eqn. 3.1). Top Panel shows the profile for electrons, while the bottom Panel is for protons. The IB is nominally determined by the absolute minimum energy along the field line at the magnetic equator. Electrons experience FLC scattering in a narrow region confined to the equator at L-shells in the typical vicinity of the outer radiation belts and plasma sheet. Protons of the same energy are initially isotropized at lower L-shells in the vicinity of the ring current.

3.2.2 Generation by wave-particle gyro-resonance

The second method of pitch-angle scattering which can result in an energy-latitude dispersion pattern is the resonance of particle gyro-motion with polarized electromagnetic plasma waves. Several types of waves in the magnetosphere have this capability. One such important example reported by (Liang et al., 2014) is the parallel-propagating left-hand polarized electromagnetic ion-cyclotron (EMIC) wave, which can be found in the equatorial region in the vicinity of both electron and proton IBs. To understand how this occurs, I consider the wave propagation characteristics leading to the particle interaction. Looking ahead to Ch. 4, both electron and proton IBs form at lower latitudes than the high-beta (thermal pressure-dominated) plasma sheet, which implies that the cold plasma dispersion relation may be presumed. For parallel EMIC waves, this is given by:

$$\frac{c^2 k_{\parallel}^2}{\omega^2} = 1 - \frac{\omega_{pe}^2}{\omega(\omega + \omega_{ce})} - \sum_i \frac{\omega_{pi}^2}{\omega(\omega - \omega_{ci})} \tag{3.6}$$

where ω is the wave frequency, $k_{\parallel}$ is the parallel wave-number, c is the speed of light, $\omega_p = \sqrt{nq^2/\varepsilon_0 m}$ is the species-dependent plasma frequency, $\omega_c = |q|B/\gamma m$ is the species-dependent cyclotron frequency, n is the particle species number density, q is the particle charge, B is the magnetic field strength, m is the particle mass, γ is the particle Lorentz factor, and the sum i is over each ion species (predominantly H^+, with small amounts of He^+ and O^+).

The condition for N^{th}-order particle gyro-resonance is met when the Doppler-shifted frequency seen in the co-moving parallel frame matches a harmonic of its cyclotron frequency; that is:

$$\omega - k_{\parallel} v_{\parallel} = N\omega_c/\gamma \tag{3.7}$$

The relative sign of the frequencies in this expression depend on the "handedness" of the wave polarization and particle gyro-motion. Both EMIC waves and protons are left-handed; thus, within a particular ion EMIC frequency band (below its gyro-frequency), the protons must have a negative $v_{\parallel}$ (opposite direction as the wave parallel phase velocity) in order to

"blue-shift" the frequency toward resonance. The resonance condition can be rearranged to determine the minimum parallel speed required for strong diffusive scattering, and thus the corresponding required minimum relativistic kinetic energy $E_{min} = (\gamma_{min} - 1)mc^2$. This energy depends on $v_\parallel^2$, and thus:

$$v_{min}^2 \equiv v_\parallel^2 = \left(\frac{\omega}{k_\parallel}\right)^2 \left[\frac{N}{\gamma}\frac{\omega_c}{\omega} - 1\right]^2 \tag{3.8}$$

This defines an energy minimum, rather than an exact resonant energy, for two reasons. First, for protons of energies much less than their rest mass (938 MeV), the perpendicular velocity ($v_\perp$) does not appear in Eqn. 3.7 ($\gamma \sim 1$), and therefore the total particle energy can take on a range of upper values, provided the gyro-radius remains less than the spatial scale of the wave-packet. Electrons also experience a minimum scattering energy, although its scaling with the phase velocity is more attenuated as compared with protons, due to the non-negligible Lorentz factor at 100s of keV and MeV electron energies. Second, even if the particle energy is not perfectly-matched to the Doppler-shifted gyro-frequency, there will exist a range of higher energies which continue to experience less efficient but non-negligible pitch-angle scattering upon several bounce periods, leading again to isotropization.

In the typical circumstance of hydrogen-band EMIC waves ($\omega_{c,He^+} < \omega < \omega_{c,H^+}$), at locations where proton IBs have traditionally been observed, (Liang et al., 2014) showed that this resonance mechanism can produce 10s of keV proton IBs, with $N = 1$ being the dominant harmonic. I point out that such waves can also resonate with electrons at much higher energies ($\omega_{ce} \gg \omega$), requiring the particle to instead move in the same direction as $\mathbf{k}_\parallel$, in order to Doppler-shift it into right-circular polarization (same angular velocity direction as the electron gyro-motion). Since particles are undergoing equatorial bounce motion, the necessary parallel velocity orientation is satisfied in at least one half-period for both electrons and protons.

The above authors concluded that the proton energy-latitude dispersion in their EMIC wave events were positive (opposite to the typical FLC scattering case). Their findings are

summarized in Fig. 3.2 below, including an example profile of equatorial minimum proton scattering energy by H^+ and He^+ band EMIC waves.

In the case described by (Liang et al., 2014) above, the minimum energy decreased with radial distance from the planet, although it can also increase, depending on the background conditions. To see how this can occur, I examine the radial variation in minimum scattering energy (again represented by v_{min}^2). Combining the Eqns. 3.6 with 3.8, I observe that for a particular band of EMIC wave, the sign of the dominant radial distance variation d/dr (a proxy of energy-latitude dispersion) depends on the ratio of variation in magnetic field strength to density:

$$\frac{d}{dr}v_{min}^2 \propto \frac{1}{B}\frac{dB}{dr}\left(\frac{1}{n}\frac{dn}{dr}\right)^{-1} \tag{3.9}$$

where n and B are the plasma density and magnetic field strength in the region of interest. The radial variation in minimum energy for strong-diffusive scattering by equatorial EMIC waves can be reduced to the question of whether the local magnetic field strength drops off more rapidly than the plasma density (primarily H^+). This is often the case at L-shells beyond the plasmasphere, but does not necessarily always hold. A similar circumstance exists for the case of electrons with other types of waves, including right-hand polarized waves such as the whistler mode, as for example described by (Artemyev et al., 2023).

However, unlike the case of FLCS, the energy-dependent scattering efficiency of particles by gyro-resonance requires active power input to increase the magnitude of the wave electric field, in order to achieve stronger acceleration per gyro-period. Consequently, the less energetic a gyro-resonant particle is, the more its perpendicular velocity will be modified by the same wave electric field over the same time window. As described in (Liang et al., 2014), it is this fact that can explain the positive energy-latitude seen in many EMIC wave events, even though the minimum scattering energy may decrease away from Earth akin to FLCS. This is because EMIC waves are typically generated with a maximum power at L-shells $L > 4$, and decrease toward Earth. Thus, IBs generated by this radial profile in wave power would exhibit positive energy-latitude dispersion, since the wave power is sufficient to isotropize, for example, 100 keV protons, but not 1 MeV protons, at the same location. The (potentially)

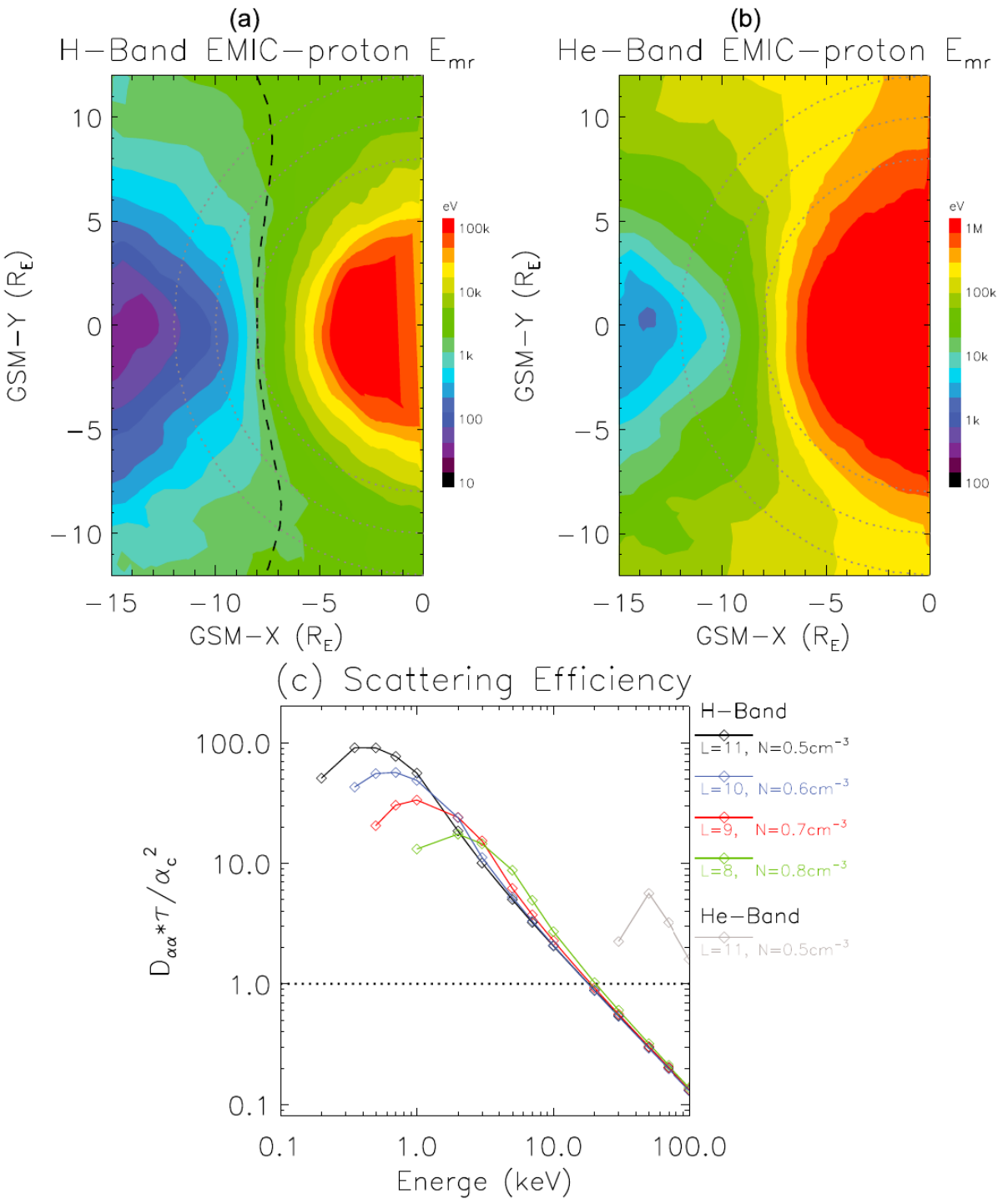

Figure 3.2: Modeled minimum equatorial proton kinetic energy for gyro-resonance with H-band EMIC waves (top left) and He-band waves (right), along with the effective strength of the quasi-linear diffusion coefficient of the process as a function of proton energy and L-shell (bottom). Despite the minimum scattering energy decreasing with radial distance, the efficiency of the gyro-resonant scattering results in positive energy-latitude dispersion, owing to the spatial distribution of EMIC wave power decreasing toward Earth. Taken from Fig. 3 of (Liang et al., 2014)

gyro-resonant waves involved are not measure directly in my work, but are inferred based on this type of energy-latitude dispersion pattern.

3.3 Methods

I now describe the observational methods used to form the electron and proton IB event databases, and how the data were used to characterize their spatiotemporal properties.

3.3.1 Particle data

The dataset used in this study is electron and proton particle flux measurements spanning 2019-2022 from the ELFIN mission (Angelopoulos et al., 2020), composed of two small satellites (3U+ CubeSats) in polar Low Earth Orbit (LEO). For most of the mission, the satellites were at ∼450 km altitude, drifting approximately 1 hour in local time per month, with a slight difference in altitude allowing the two satellites to nearly overlap in local time/latitude every six months, allowing for spatio-temporal observations. Over the final six months of the mission (March-September 2022), the altitudes decayed rapidly from 420 km to roughly 300 km due to atmospheric drag, followed by terminal reentry. Chapter 2 covered the technical specifications of the EPD-E and EPD-I instruments, whose data form the basis for my work. For purposes of IB identification, I did not attempt to evaluate the exact flux at pitch-angles of 0° and 90°, but rather approximated them by the ratio of fluxes in the local loss-cone to the mirroring population (e.g. J_{prec}/J_{perp}).

The particle loss cones were computed locally at every timeseries data step by tracing the instantaneous IGRF field at the spacecraft location poleward to a bounce altitude of 100 km, with any such particles with mirror points at or below this altitude considered lost. The instantaneous magnetic latitude at each data sample was computed by tracing the spacecraft location to the magnetic equator, treating the radial foot-point distance from the earth as its equivalent dipole L-shell (L), determining the magnetic latitude θ through the-well known dipole relationship $1/L = \cos^2(\theta)$. In cases where Eqn. 3.1 was evaluated, the T89 model

was used to perform tracing.

I note that in this work, all ion counts are presumed to be protons, although the EPD-I did not possess the capability to resolve ion composition. This presents the possibility of false counting; however, the data were collected during non-strong storm intervals (min Dst >-50 nT) in which proton fluxes are expected to dominate all other energetic (>50 keV) species, such as O^+ found in the intense storm-time ring current (Daglis et al., 1999; Yue et al., 2019).

3.3.2 Formative events in this study

Events in this study are composed of 6-7 minute ELFIN science zone collections, typically spanning ±55° to ±80° in IGRF magnetic latitude in a single hemisphere, traversing field lines which map into the outer radiation belt, ring current, plasma sheet, and polar cap. For a collection to qualify as a sample in the statistics, I required that the observations covered a range of pitch-angles sufficient to resolve precipitating to mirroring flux ratios, and that the latitudinal coverage of the collection spanned at least IGRF $3 < L < 8$, to ensure that higher-latitude IBs were not artificially under-represented.

Additionally, IBs whose lowest-latitude equatorial foot-points mapped within 3 Re of the magnetopause were excluded from the study, as their origin can be ambiguous (e.g. magnetopause shadowing or reconnection), per the method discussed in (Wilkins et al., 2023). The magnetopause criterion affected only 3 proton events, but did affect a fraction of electron cases particularly near dawn and on the dayside, as later shown. The data were also inspected for instrumental data issues, with such cases removed. I refer to ELFIN collections that meet these qualifying validation criteria (independent of whether they contain IBs) as Qualifying Science Zones (QSZs), resulting in 4123 electron QSZs and 288 proton QSZs. For electrons, given the multi-year collection of the data, all MLTs were sampled with a minimum of 50 events per hourly MLT bin. For protons, data was only available in the final months of the mission, on the nightside in a normal-like distribution between 1700 and 0400 hours (peaked between 22-23 MLT). This resulted in an order of magnitude more electron

than proton QSZs for the statistics.

A prototypical qualifying science zone collection on 2022-08-19 containing both electron and proton IBs observed by ELFIN-B is presented in Figure 3.3, as shown in (Wilkins et al., 2025). The satellite begins in the southern hemisphere around -55° in magnetic latitude around 23.5 hours MLT, collecting for ∼7 minutes, spanning latitudes mapping into the the outer radiation belt, ring current, and plasma sheet. Panels (a) and (b) show the energy flux spectrograms of locally mirroring (J_{perp}) and precipitating (J_{prec}) electrons respectively, with Panel (c) showing the precipitating-to-trapped flux ratio $R_I = J_{prec}/J_{perp}$ for electrons. Between 0605 and 0608 UT, the spacecraft sees well-populated locally-mirroring energetic electron fluxes with a low isotropy ratio, corresponding to dynamics controlled by a strong dipole field. However, around 0608 UT a rapid rise in isotropy from $R_I < 0.6$ to $R_I \sim 1$ is observed across all energy channels. This energy-latitude dispersion signature is consistent with isotropy boundary formation caused by FLC scattering in the presence of a monotonically-decreasing equatorial B_z profile (as in Fig. 3.1). Panel (d) shows the predicted IB locations using T89 and Eqn. 1 (blue curve) versus the observed IBs (red curve), where it is seen that T89 predicted a similar energy-latitude dispersion slope, but with a slight overestimation of the IB latitude mapped to the tail. (Deviations between field model predictions and IB observations present a potentially rich line of investigations, and are beyond the scope of this study.) Panel (e) shows the instantaneous integral (over energy and pitch-angle) precipitating energy-flux of isotropic ≥50 keV electrons at the spacecraft location, where it can be seen that the region within and immediately poleward of the IB crossing produces significant power on the order of 0.1 to 1.0 erg/cm^2-s, and is the dominant latitudinal range of ≥50 keV electron precipitation in this event, contributing 71% of the total high-latitude energetic precipitation at this MLT.

Panels (f) through (k) are corresponding stack plots for protons, equivalent to Panels (a) through (e) for electrons, over the same time interval and latitude range. In this case, there are nearly zero counts of either precipitating or mirroring protons at lower latitude, corresponding to a typical off-equator pitch-angle distribution in the ring current. However,

similar to electrons, near 06:06:30 UT, an abrupt rise in isotropic fluxes is observed across all proton energies, akin to the energy-latitude dispersion predicted for FLC-scattered protons in Fig. 3.1. In this case, the model prediction is very close to observation. As with the electron IB, precipitating energy fluxes from poleward isotropic protons rise significantly relative to other latitudes, contributing 90% of the total high-latitude $\geq$50 keV proton precipitation at this MLT, although distributed over a broader range of latitudes than for electrons. For reference, Panel (l) shows the local IGRF field at the spacecraft location.

3.3.3 Event classification and characteristics

ELFIN particle collections, such as shown in Fig. 3.3, form the basis for event characterization in this study. To classify the events, each qualifying science zone was inspected for the presence of an electron (IBe) and or proton (IBp) isotropy boundary. In this context, "IB" refers interchangeably to the aggregate of multiple individual isotropy boundaries of different energy channels, forming an energy-latitude dispersion pattern in any given satellite pass. IB presence was assessed by subjecting each species' isotropy ratio $R_I = J_{prec}/J_{perp}$ to the following criteria:

1. A poleward transition from anisotropic to isotropic fluxes (defined as passing from $R_I < 0.6$ to $R_I > 0.6$) in a specific energy channel, followed by $R_I \sim 1$ for at least 50% of the poleward spin periods;

2. At least three energy channels individually satisfying condition (1); and

3. All energy channels eventually satisfy condition (1) at some shared latitude (regardless of particular energy-latitude dispersion pattern) if they exceeded the minimum count rate uncertainty.

In the context of evaluating conditions (1) and (3), the quantity R_I was taken equal to zero in the circumstance of low count rates (e.g. for 0 counts, or for $dQ/Q \geq 1$, where dQ is the counting uncertainty in flux Q). QSZs that met all of conditions (1), (2), and (3) were marked as containing an IB.

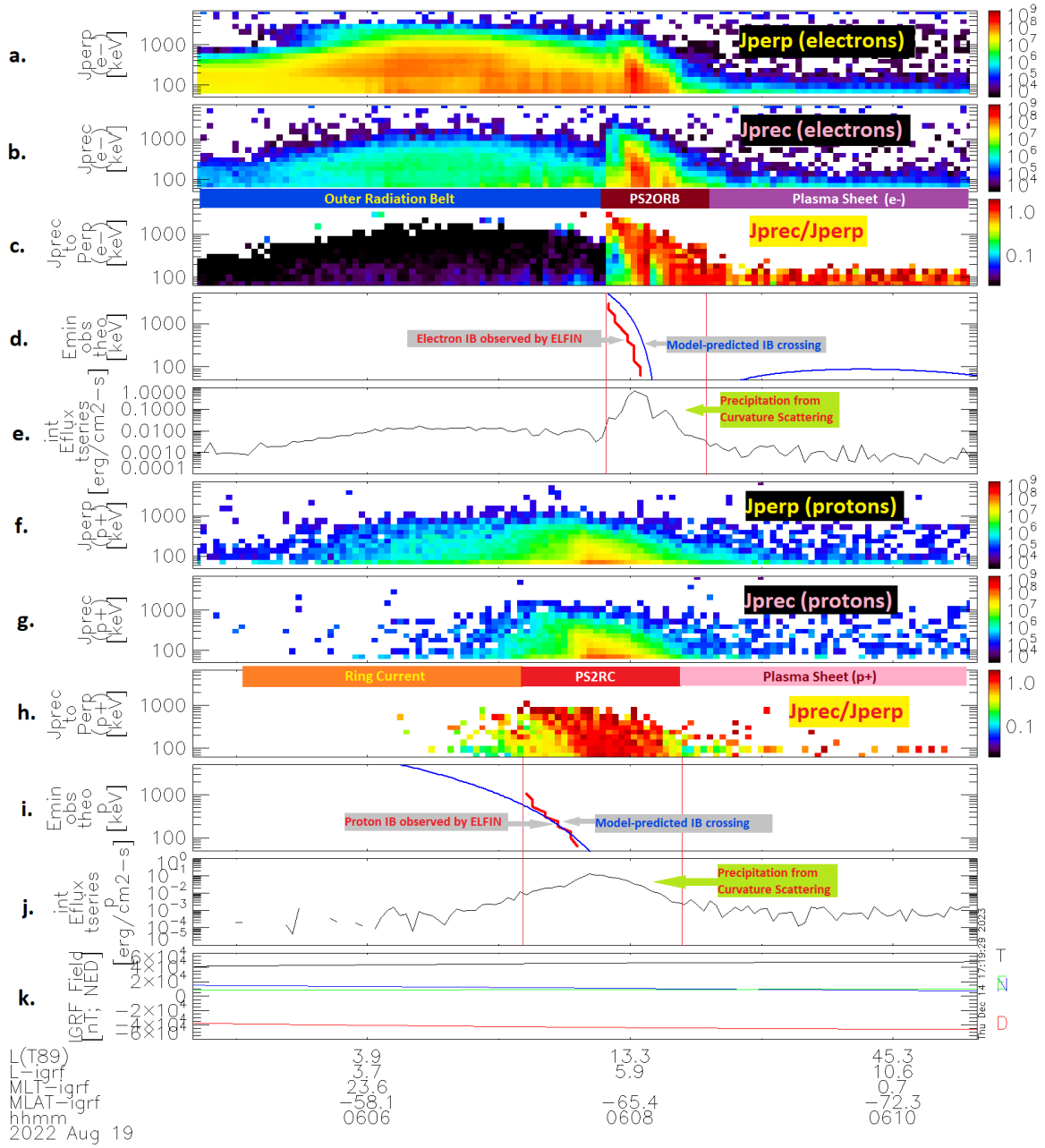

Figure 3.3: Prototypical ELFIN electron+proton IB event on 2022-08-19/06:05 UT. Panels (a) and (b) contain the precipitating (J_{prec}) and locally-mirroring (J_{perp}) energy-time spectrograms; panel (c) is the isotropy ratio $R_I = J_{prec}/J_{perp}$. The spacecraft starts in the southern outer radiation belt around $-55°$ MLAT, encountering a rapid rise from low isotropy to $R_I \sim 1$ across all energy channels from 06:07:50 UT to 06:08:10 UT, marking the crossing of 50 keV to 3 MeV electron isotropy boundaries. Panel (d) shows the theoretical IB prediction using Eqn. 3.1 and T89 (blue) compared with observations (red). Panel (e) shows the instantaneous integral precipitating energy flux. The red bars denote the region considered to be the region of precipitation associated with the IB for electrons (the "PS2ORB") and protons (the "PS2RC"). Panels (f)-(k) represent the equivalent quantities for protons as Panels (a)-(e), where the spacecraft begins in the ring current, with highly anisotropic fluxes. A 50 keV to 1 MeV proton IB is then encountered around 06:07:30 at the higher L-shell portion of the ring current ($L \sim 5.5$).

For the events determined to contain an IB, the magnetic latitude/L-shell at the crossing location of each energy channel were recorded, along with the crossing MLT. I also computed the energy-latitude dispersion of the IB crossing as a function of energy. For purposes of this study, I count any type of dispersion toward IB occurrence, interpreting non-positive dispersion to be associated with FLC, and making no attempt to determine the event-specific generation mechanism of positive dispersion (e.g. waves or reverse B_z gradient). The dispersion slope $dMLAT/dE$ was computed for each energy channel E_i in the IB using the following two-point differencing average:

$$\left(\frac{dMLAT}{dE}\right)_{E_i} = \frac{1}{2}\left(\frac{MLAT_{E_i} - MLAT_{E_{i-1}}}{E_i - E_{i-1}} + \frac{MLAT_{E_i-1} - MLAT_{E_{i-2}}}{E_{i-1} - E_{i-2}}\right) \tag{3.10}$$

where $MLAT_{E_i}$ is the magnetic latitude of the IB crossing in ELFIN's i^{th} energy channel (E_i). The two-point average was employed to minimize variance due to count rates in meeting condition (1) of the IB selection criteria (i.e., fluctuations near the 0.6 isotropy ratio threshold). The average was performed downward in energy rather than upward, owing to the fact that count rates generally increase with decreasing energy. The lowest two energy channels (63 keV and 98 keV) do not have their dispersion statistics reported, as each channel must have at least two below it to evaluate Eqn. 3.2.

3.4 Results

3.4.1 Spatiotemporal characteristics of electron IBs

To provide an initial picture of the spatial distribution of electron IBs in my dataset, the equatorial footpoints corresponding to the minimum and maximum L-shell of field-line traces bounding the IB dispersion region (based on T89) are shown in Figure 3.4 top as a scatter plot, projected in the equatorial GSM xy-plane. The points marked L_{min} represent the most Earthward portions of the IB crossings (typically corresponding to the highest-present electron energy IB; variable from event to event), and the point marked L_{max} similarly represents

the furthest portion of the IB dispersion in the crossings (almost always corresponding to the 50 keV electron IB). I note that while these field-lines have been associated with L-shells, the T89 field is increasingly non-dipolar with increasing distances in the tail, with the footpoint of the traces serving to approximate the distance from Earth where the particles originate in the magnetosphere. The static reference-magnetopause based on (Fairfield, 1971) is shown (solid) alongside the 3 earth radius cutoff (dashed) used to discern IB-like signatures of ambiguous origin, which are marked in silver and black, (counted as non-IB but otherwise valid events)and discounted from the main statistics. It is evident that projected isotropy boundary locations span a wide range of MLTs and mapped equatorial distances throughout much of the nightside magnetosphere, with typical estimated distances from Earth between 4 and 20 Earth radii.

As mentioned earlier, a fraction of the IB-like electron events traced too close to the magnetopause to make a definite assessment of their origin. Fig. 3.4 bottom panel shows the MLT distribution of these events, which are confined primarily to the dayside and pre-noon. These events may correspond to equatorial FLCS, compatible with the near-magnetopause equatorial FLCS and polar cusp sources described for protons by (Sergeev et al., 1997). However, it is not possible to know with certainty using the ELFIN dataset alone. Additionally, while still exhibiting isotropic energetic electrons, the cases are also distinguished by their low net precipitation (not shown) as compared to the nightside and lower dayside latitudes.

Figure 3.5 shows the electron IB spatial distribution. Top Panel depicts the histogram of isotropy boundary occurrence (absolute and normalized) versus MLT in my database, binned with a bin size $\Delta MLT = 1$ hour. Blue bars denote the number distribution of all QSZ events in my database, orange bars depict the number of events with an IB (both referring to the absolute numbers on the left vertical axis), and red line is the normalized occurrence rate of IB crossings versus MLT in the dataset (corresponding to the right vertical axis), computed as the ratio of the orange to blue values. A running average with $\pm$1-hour MLT window was applied to the data, to improve statistics and accommodate potential uncertainties in field-line mappings.

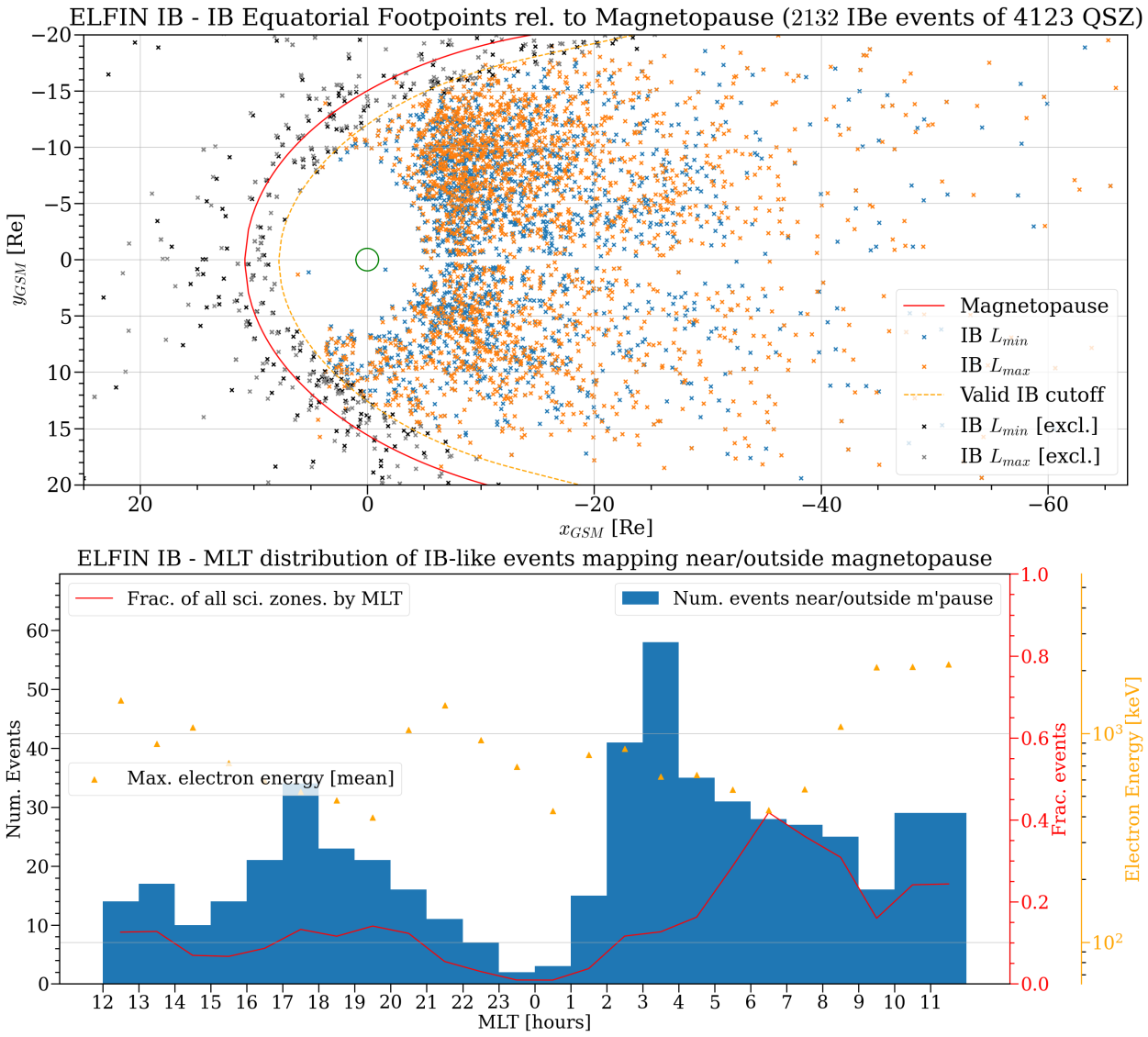

Figure 3.4: Top: Spatial distribution of electron isotropy boundary locations in my dataset, observed by ELFIN and magnetically mapped to the equator using T89. Points marked in blue represent the closest Earthward footpoint of each observed IB energy-latitude dispersion pattern. Orange points represent the furthest footpoint in the IB dispersion signature. Points marked in gray and black are equivalent properties for IB-like events which mapped too close to the magnetopause (solid red line). Those crossings (both gray and black) have been excluded from the main dataset as being of ambiguous source region origin, based on the criterion that the lowest latitude portion of the IB is within 3 Earth radii inside of the Fairfield magnetopause (dashed yellow line). Bottom: Distribution of IB-like events which were excluded due to proximity to the magnetopause.

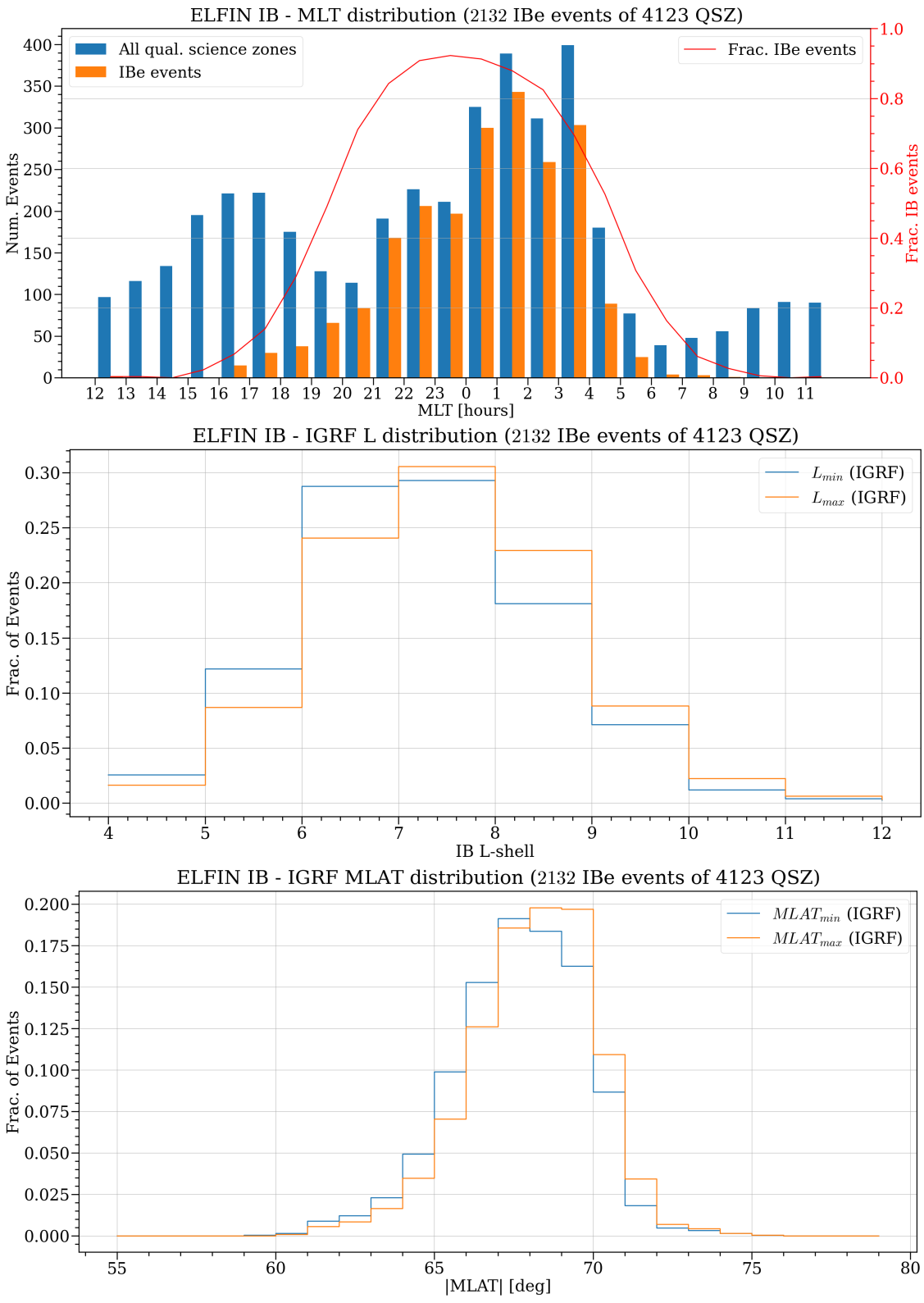

Figure 3.5: Top: Observational occurrence rates of electron IB crossings versus MLT. Middle: Versus L-shell. Bottom: Versus magnetic latitude. Min and max refer to the low and high latitude boundary of the energy-latitude dispersion pattern. Median values for L-shell and MLAT are shown in the panels.

I find that ≥50 keV electron IB energy-latitude dispersion patterns could be detected by ELFIN in 2132 of 4123 QSZs, in up to 90% of events near midnight, and exhibit a sustained detection rate of ≥80% between 21 to 01 MLT. Their occurrence gradually declines towards near-zero at pre-dawn pre-noon (7 MLT) and near dusk (16 MLT). The peak occurrence is not centered at midnight but at pre-midnight, but rather around 22 MLT. (The apparent peaks in event number around 01 and 15 MLT are due to biases in the ELFIN collection intervals used in the study.)

The associated spatial distribution of these IB events binned by L-shell ($\Delta L = 1$) and magnetic latitude (ΔMLAT = 1°) using the IGRF model are shown in Fig. 3.5 middle and top, respectively. IGRF alone, not T89, was used to compute the distribution in this case to provide a static reference independent of the behavior of the magnetic field far from earth, with the caveat that this will typically underestimate the true L-shell and latitude mappings at the nightside as distances from Earth increase. I observe that electron IBs span a wide range of IGRF L-shells (4 to beyond 12), and are most commonly found to span L-shells 6-8, typically corresponding to the tail-dipole transition region, or PS2ORB interface region. As anticipated from the L-shell to |MLAT| equivalence in mapping, a similar trend is observed in magnetic latitude: a broad range of occurrences between 60° to 74°, with peaks around 66°-70°. Additionally, I checked the occurrence of IB crossings versus the geomagnetic activity indices AE, Dst, and Kp (not shown), and found them to not vary appreciably from the overall MLT distribution described here (although the MLAT, range of isotropized electron energies, and total associated precipitation certainly *do* depend on activity, as shown later).

In these events, I also characterized the minimum and maximum electron energies of the observed dispersion in the IB crossings, alongside the latitudinal spread and dispersive slope ("sharpness"), versus MLT and activity. Given that the IB generation mechanism is based on the background magnetic field configuration and the local availability of energetic particles (e.g. injections), as well as waves, it is reasonable to expect that the level of geomagnetic activity and solar driving at the time of (and preceding) the crossing would affect the electron energies appearing in the IB, as well as the latitude and slope of isotropic dispersion. In order

to provide an assessment of this activity-dependent behavior, I separated the dataset into two categories: quiet-time intervals with 1 hour average AE less than 200 nT, and non-quiet intervals with 1 hour average AE above 200 nT. This choice of hourly-average AE split the dataset roughly in half, and emphasized the high-latitude precipitation component of IBs (described in Ch. 4).

Figure 3.6 displays the activity-dependent minimum and maximum observed IB electron energies versus MLT, where solid points represent the mean values and error bars represent the occurrence-weighted standard deviation about the mean. Fig. 3.6 top shows the minimum and maximum electron energies appearing in the dispersion of IB crossings within the ELFIN EPD instrument sensitivity and energy limits. For low activity (AE<200 nT) the electron energies span a typical maximum of 700-800 keV, peaking at MLTs near midnight, and trailing toward a lower average maximum in the 300-400 keV range near dawk and dusk. For higher activity (AE>200 nT), the maximum energies rise dramatically to a mean of 2 MeV, and are shifted in local time to pre-midnight (peaking around 22 MLT), with the maximum energies falling to 800-900 keV at MLTs approaching dawn and dusk. The apparent shift in peak energy to the pre-midnight during active times is consistent with the IB being supplied by frequent (possibly continual) local energetic flux injections in the tail at these MLTs (Gabrielse et al., 2014; Liu et al., 2016), which are isotropized. At both quiet and non-quiet times the low-energy minimum of the IB is almost always the lowest energy channel resolvable by the ELFIN EPD (∼62 keV mean). This suggests that the IB likely extends to lower energies than ELFIN can resolve, and that such fluxes are highly available in the tail at the rates reflected by IB occurrence in each MLT sector. Similarly, I note that the IBs may extend to higher energies as well, but with fluxes so low as to drop below the one-count level sensitivity of the ELFIN EPDs.

I also determined the MLT distribution of the bounds and slope of the energy-latitude dispersion in the IB crossings. Fig. 3.6 middle shows the range of latitudes (and overlaid L-shells) subtended by the energy-latitude dispersion patterns. The quantities denoted “min”

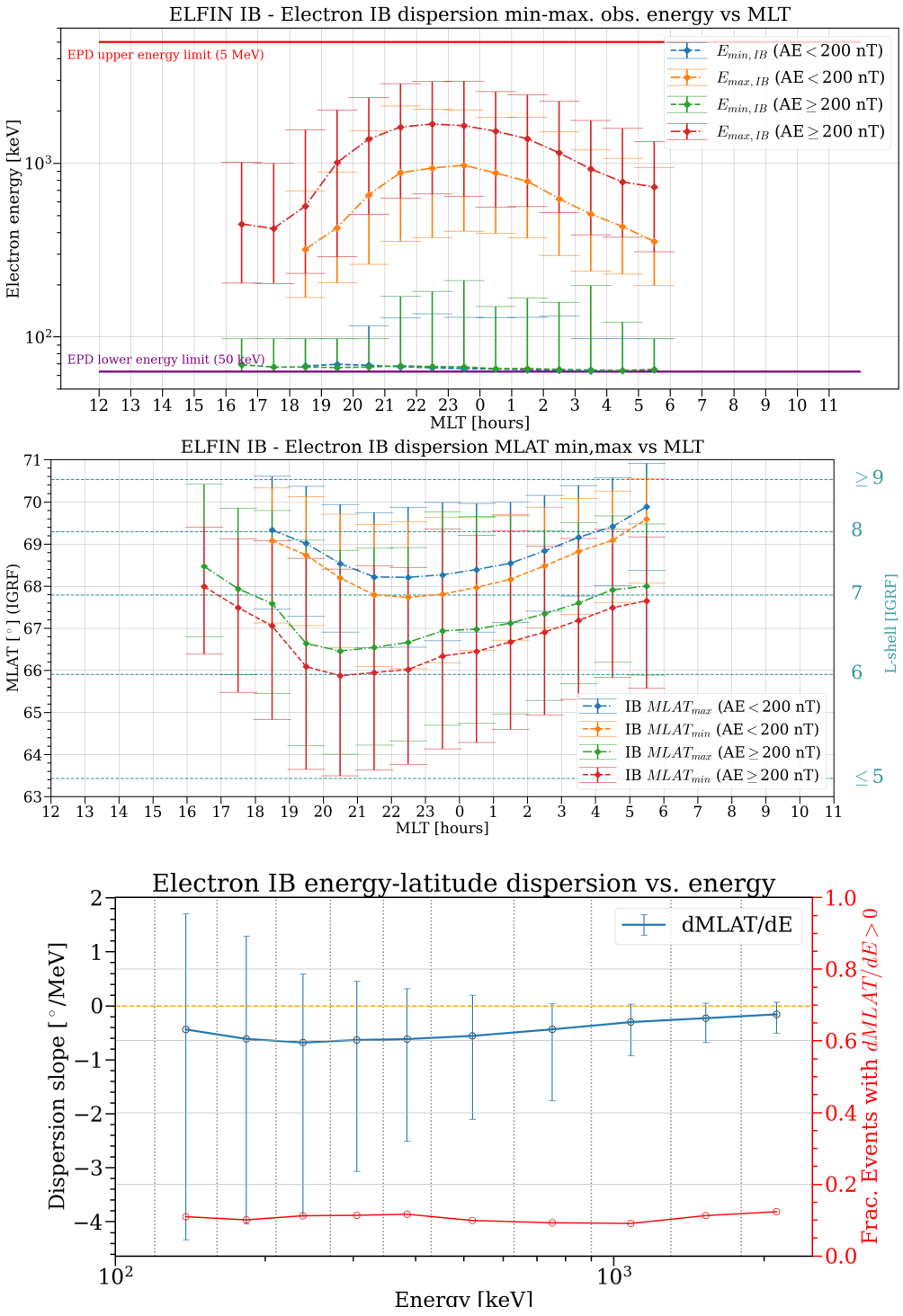

Figure 3.6: Top: Distribution of minimum and maximum energies detected in the electron IB dispersion patterns versus MLT, for quiet and active intervals. Middle: MLT distribution of the minimum and maximum MLAT of the dispersion. Bottom: Distribution of energy-latitude dispersion slope for all events and MLTs versus energy, and probability of a given event having positive dispersion.

reflect the most Earthward portion of the dispersion while the "max" values mark the more distant location at which the lowest energy channel is first observed to become isotropic. The results show that at low activity, there is a bowl-shape distribution with global minimum around 22 MLT with $L_{min} \sim 7.1$, $L_{max} \sim 7.3$ and $MLAT_{min} \sim 67.6°$, $MLAT_{max} \sim 67.9°$, rising to a maximum of $L_{min} \sim 8.6$, $L_{max} \sim 8.9$ and $MLAT_{min} \sim 69.8°$, $MLAT_{max} \sim 70.0°$ at 5-6 MLT. Interestingly at both activity levels the mean latitudinal width (max minus min) of the dispersion in the crossings is nearly constant across MLT, suggesting a highly persistent supply of injected particles of appropriate energies (top panel) and appropriate background field configuration across many local times on the nightside, such that particles are repeatably affected by the same mechanism. At higher activity, IB dispersion is found consistently at lower latitudes across all MLTs, with the emergence of a break from the symmetric bowl-shape distribution around 22 MLT. This feature is again consistent with the appearance of energetic electron injections at lower latitudes, e.g. during substorms. Rather than being localized to a single MLT, the active time latitudinal onset minima are instead spread between 20-23 MLT, taking on values of $L_{min} \sim 6.3$, $L_{max} \sim 6.5$ and $MLAT_{min} \sim 65.9°$, $MLAT_{max} \sim 66.5°$ and maxima around 4-5 MLT of $L_{min} \sim 7.6$, $L_{max} \sim 8.0$ and $MLAT_{min} \sim 68.4°$, $MLAT_{max} \sim 68.8°$. I note that MLT sectors with fewer than 5 IB events are not shown, which is the reason there are no data points for certain active time versus quiet time MLTs.

Based on the observed energy and latitudinal ranges of the IB crossings, I also computed the energy-latitude dispersion slopes $dMLAT/dE$ versus energy in Fig. 3.6. As mentioned in the introduction, the slope of energy-latitude dispersion (positive vs. negative) is a fundamental discriminating characteristic of the generation mechanism of isotropy boundaries. It is therefore also important to determine the fraction of events satisfying this criterion, overplotted in red.

The distribution exhibits several important and previously unreported characteristics in describing the magnetospheric origin of electron IBs. First, the average energy-latitude dispersion slope is negative for all energies, with only a 10% chance of being positive in any given

energy channel. **This strongly suggests that the origin of most ≥50 keV electron IBs is predominantly equatorial FLC, rather than wave-particle interactions.** This conclusion is further supported by the fact that above 200 keV, the slope of the dispersion decreases in magnitude. This is consistent with the electrons experiencing a stronger dipole field and larger radius of curvature closer to dipole-like portion of the tail-dipole transition region (rather than neutral sheet).

An additional observation concerns the spread and inflection of the <200 keV population of electron IBs. At these energies, the deviation from the mean values is much larger, and exhibits opposite characteristics in the decreasing magnitude trend at higher energies. **This suggests that wave-particle interactions are more typically mixed-in with the FLC mechanism at <200 keV energies in the formation of electron IBs.**

3.4.2 Spatiotemporal characteristics of proton IBs

I now perform a similar analysis for proton IBs as reported above for electrons. Figure 3.7 shows the scatter plot in the GSM xy-plane of the equatorial field-line projections of electron (top) and proton IB (bottom) locations, corresponding to the minimum (typically highest-energy) and maximum (typically lowest-energy) magnetic latitude of each IB dispersion pattern. Events where the lowest-latitude equatorial foot-point of the IB mapped within 3 Re of the magnetopause were excluded from the statistics (marked "excl."). It can be seen that detections of both electron and proton IBs are widely distributed across the nightside, with protons generally occurring at lower projected L-shells. I note that the true magnetospheric MLT range of proton IBs extends beyond what is shown in the scatter plot; the lack of reported occurrence is simply due to lack of satellite coverage there. The statistics of electron IBs have also been updated to include more than double the events considered in Wilkins et al. (2023), with selected average properties over-plotted with proton results for comparison.

Figure 3.8 (top) shows the distribution in MLT ($\Delta MLT = 1$ hr) of proton QSZs (blue bars) and IBp events (orange bars), with the occurrence rates per MLT bin (ratio of orange to blue bars) plotted in red. The plot shows that proton IBs are observed by ELFIN between

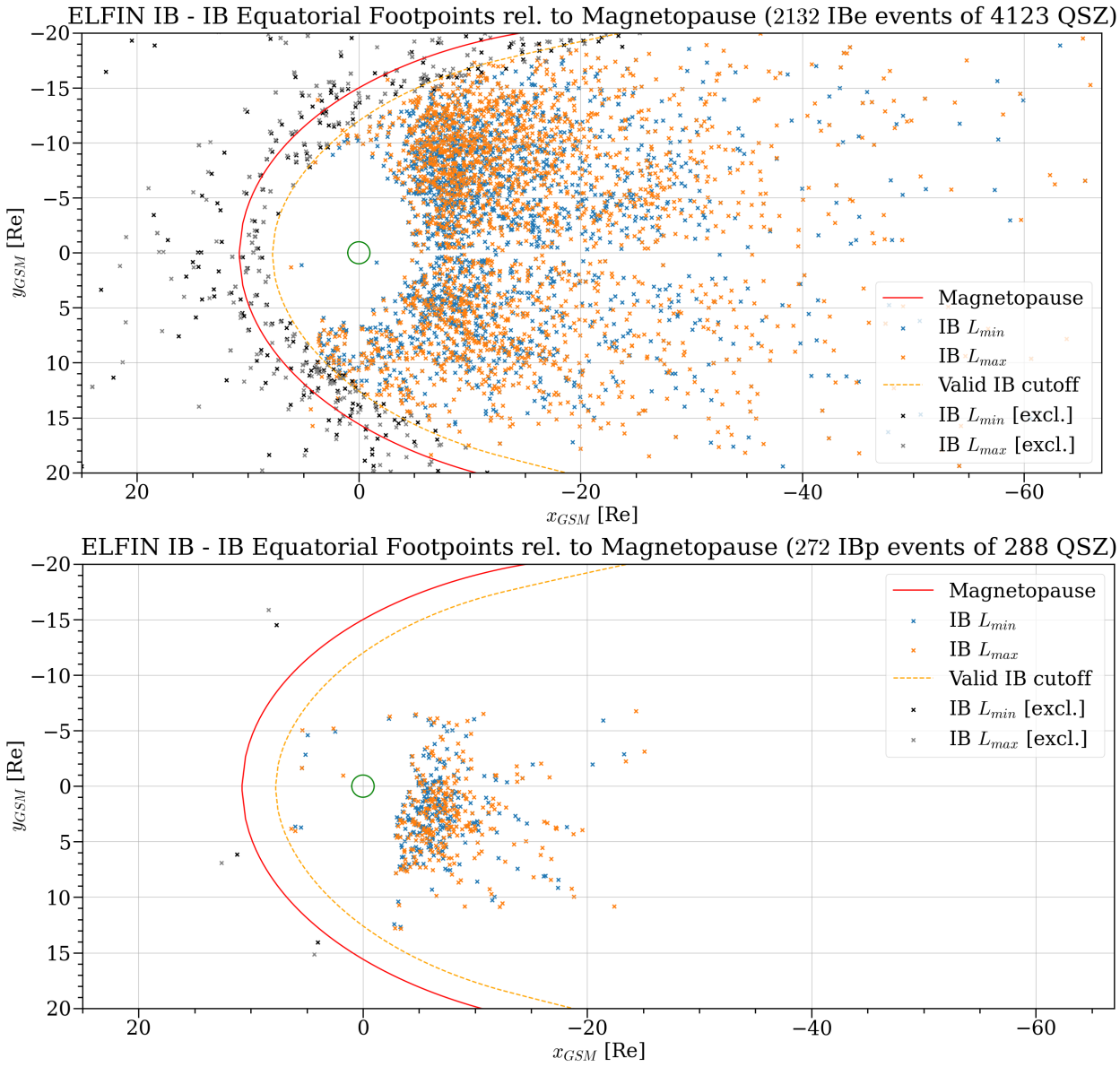

Figure 3.7: Spatial distribution of IB energy-latitude dispersion patterns projected into the magnetotail for electrons (top, as a comparison), and protons (bottom). The significant difference in the number of IBs between species is due to the ELFIN mission only collecting proton data for the final months of the mission.

90% to ∼100% of the time between 1900 and 0300 MLT, with occurrence rates unreported for MLT bins with fewer than 5 IBs. To reduce the potential for azimuthal mapping uncertainties due to the IGRF model lacking an external field, I applied a ±1 hour MLT averaging filter to the occurrence rate curve. Of the 288 proton QSZs, 272 contained proton IBs, resulting in an overall detection rate of 94.4%. The equivalent occurrence rate for electron IBs is shown in purple, with electron IBs found by ELFIN to be jointly detectable with protons up to 80% of the time.

Fig. 3.8 middle and bottom show the MLT-aggregated distribution in IGRF L-shell and magnetic latitude (MLAT), respectively, of the proton IB minimum and maximum projected boundaries of the dispersion pattern. The most common bounds are between IGRF L=5 to L=6, or 64° to 66° in MLAT, which covers a range typically associated with the higher-latitude portion of the ring current. This is in contrast to electron IBs, which were found in (Wilkins et al., 2023) to be between L=7 to L=8, or ΔL =1-2 higher in typical separation.

Figure 3.9 (a) and (b) show the activity dependence versus MLT of the detected proton IBs in MLAT and particle energy extrema, where "active" intervals are defined as 1 hour average AE above 200 nT preceding the ELFIN collection (median level in the database). Panel (a) shows the distribution of minimum and maximum proton energy associated with the IB dispersion pattern. Across all activity and represented MLTs, the minimum recorded isotropic energy is the lowest energy ELFIN can resolve (∼50 keV), suggesting the IBs likely always extend to lower energies. However the maximum detected isotropic energy exhibits a clear dependence with both MLT and activity. At non-active time, the typical peak proton energy is around 600 keV between 23 to 01 MLT, dropping to 300-400 keV near dusk/dawn. At active times, the mean peak energy reaches 900 keV to 1 MeV, shifting in MLT to 21-23 hours, dropping to 600-700 keV between 01-02 MLT. I note that while the EPD-I can detect protons differentially up to ∼5 MeV, the maximum detected energy is in practice limited by the instrument geometric factor. The reported maximum energies should therefore be interpreted as a lower bound to the upper-most energies in the true IB dispersion patterns (in the limit of perfect sensitivity).

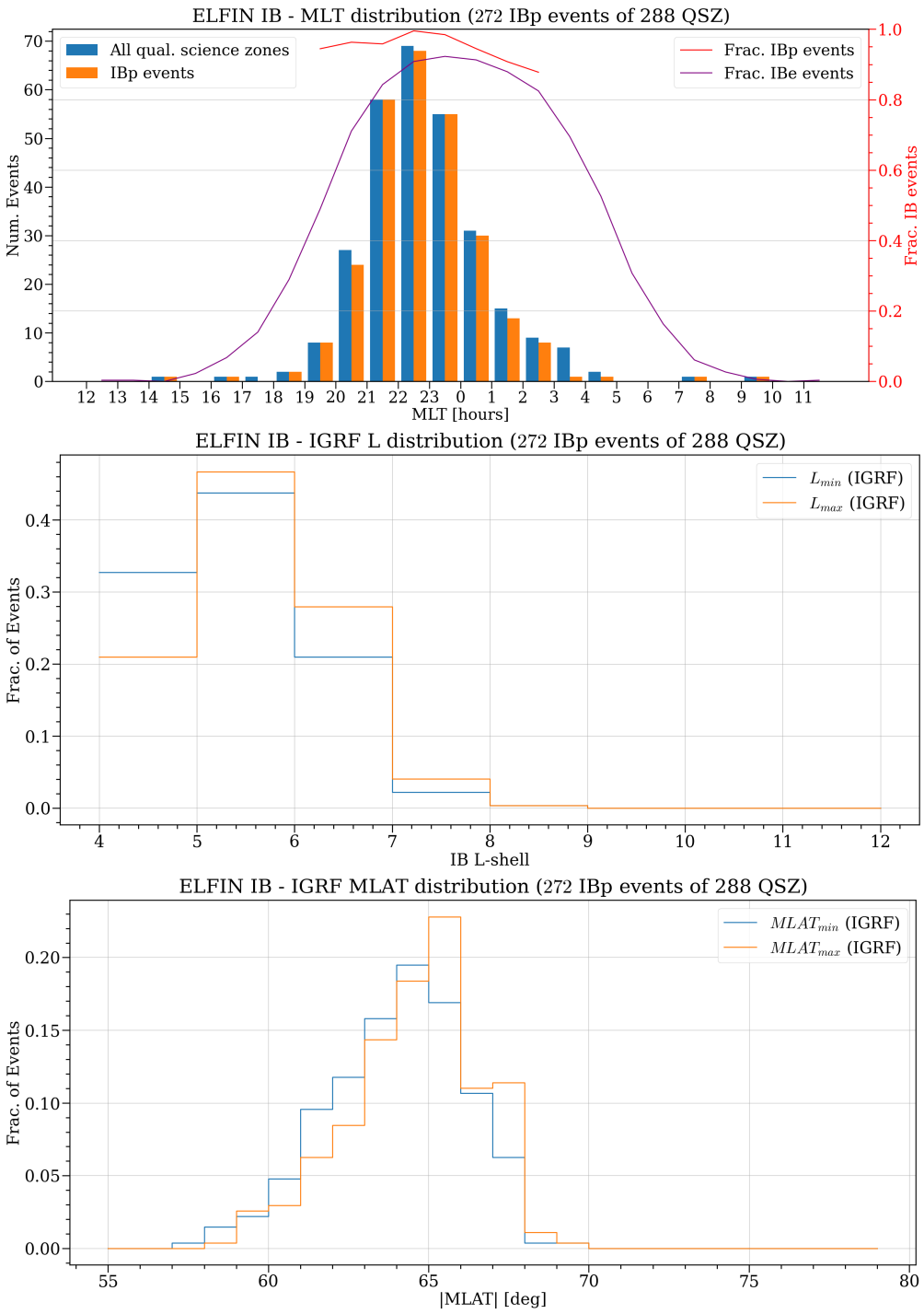

Figure 3.8: Detected occurrence rate and spatial distribution of proton IBs. Top Panel shows the distribution of proton IB events versus MLT, with the total number of ELFIN crossings in blue, and the overlapping orange bars indicating the total number of proton IB events. The red curve represents the detection occurrence rate for each hourly MLT bin, normalizing for satellite crossing residence. The occurrence rate of electron IBs is overplotted in purple for comparison. Middle and Bottom panels show the spatial distribution of proton IBs in L-shell (IGRF) and MLAT (IGRF) aggregated over all local times.

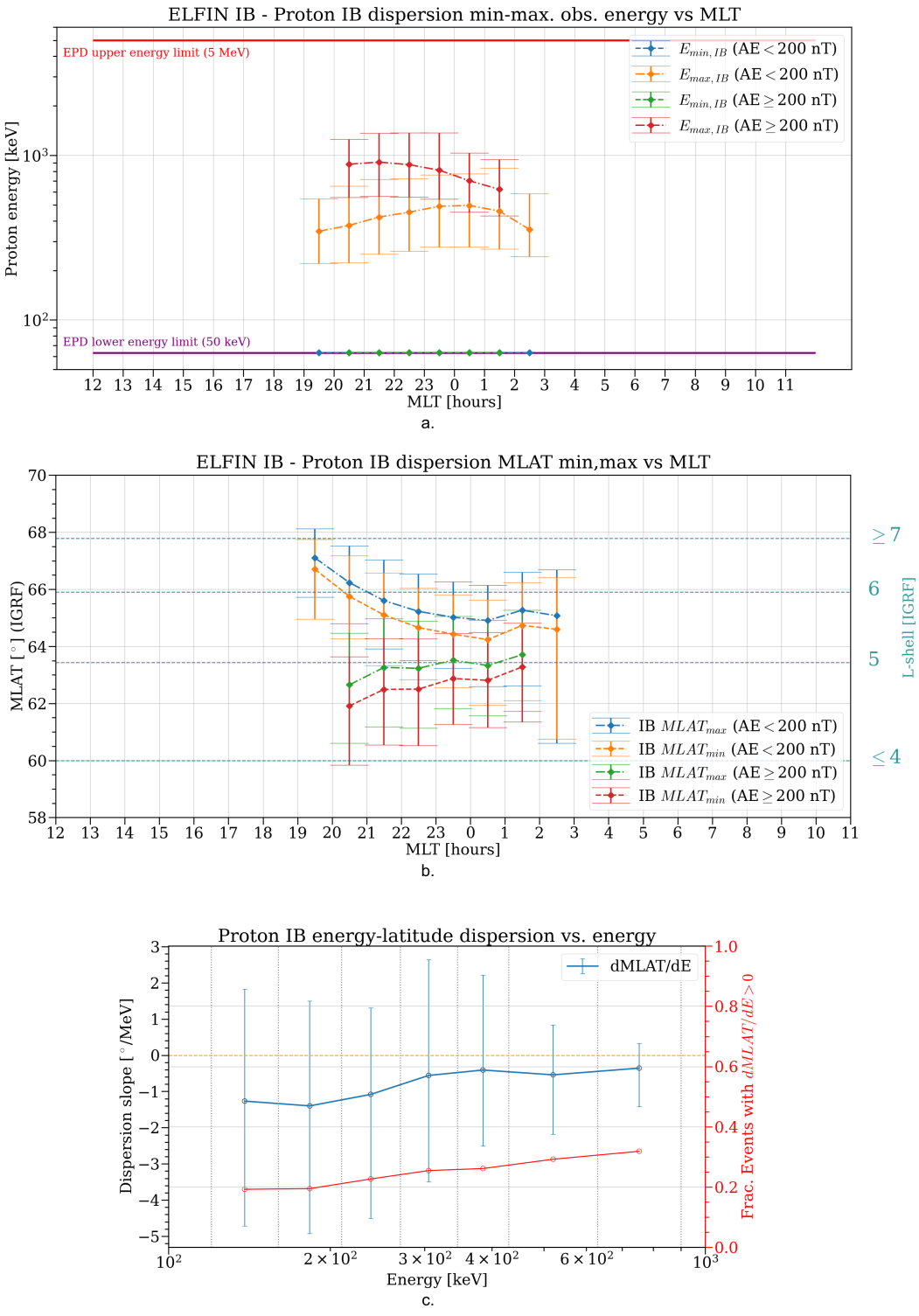

Figure 3.9: MLT distribution of proton IB characteristic means and standard deviations versus activity. Panel (a) shows the minimum and maximum energies (bounding a continuous energy spectrum) appearing in the IB crossings. The minimum energy is typically the lowest ELFIN can resolve. Panel (b) shows the MLAT and L-shell behavior versus activity. Panels (c) and (d) show the energy-latitude dispersion slopes for these cases. The absolute values are plotted, although the slope values are all implicitly negative.

Panel (b) shows the distribution of lower- and upper- ("min/max") latitude of the proton IB dispersion patterns, with L-shells over-plotted. At non-active time, a bowl-shape distribution similar to electron IBs is seen centered closest on 00-01 MLT (anti-symmetric to the 22-23 MLT from electrons). At active times the distribution shifts to pre-midnight and moves radially inward by 1-2 L-shells, peaking at 20-21 MLT. Electron IBs as in (Wilkins et al., 2023) exhibit a similar active-time distribution around 20-22 MLT, suggesting the same or similar processes control them, such as cross-tail current sheet thinning.

Panel (c) shows the mean MLT- and activity-aggregated slope of the energy-latitude dispersion patterns versus proton energy, along with their two-sided standard deviations. It can be seen that the typical slope for any detected IB energy is negative (compatible with monotonic B_z FLC scattering), with a 20%-30% of any particular energy channel exhibiting non-negative dispersion (suggesting a different source mechanism, such as wave-particle scattering or non-monotonic B_z profile). I note that this percentage is independent for each energy channel, often resulting in mesoscale positive dispersion structures embedded within the otherwise negative IB dispersion pattern at other energies. The lower energies ($\sim$100 keV) had a mean dispersion slope around -1°/MeV, while higher channels ($\sim$800 keV) were around -0.2°/MeV. This energy-dependent change in slope magnitude is consistent with an equatorial magnetic field which, when followed Earthward, increases in strength and curvature radius faster than in the distant neutral sheet (e.g., moving from tail-like current sheet to more dipole-like field), as in Fig. 3.1.

3.5 Summary and discussion

In this work, I analyzed ELFIN observations from polar LEO to determine the observational characteristics of 2132 electron isotropy events covering 50 keV to 3 MeV energies, and 272 proton isotropy boundary events covering 50 keV to $\sim$2 MeV energies. I found that IB dispersion patterns can be well-recognized across the nightside for both species, with >80% observational occurrence between 21 and 01 for electrons, and 19 and 03 MLT for protons, typically spanning 66°-70° (L of 6-8) for electrons, and 64°-66° (L of 5-6) for protons

between the highest- and lowest-energy portion of the IB, with variations depending on geomagnetic activity and MLT. For protons IBs, the latitudinal distribution is similar to the large-sample size results of (Dubyagin et al., 2018; Lvova et al., 2005; Ma et al., 2022) for the commonly shared MLTs and energy ranges of 50-120 keV, exhibiting a sinusoidal-type form with minimum (absolute) latitude centered between midnight and 01 MLT, with overlapping latitudinal range.

I also examined the slope of electron and proton IB energy-latitude dispersion patterns, finding that in 90% of cases for electrons, and 70%-80% of cases for protons, energy channels exhibited negative dispersion (higher energy IBs appearing equatorward of the adjacent lower energy channel). The magnitude of the dispersion slope tended toward zero with increasing energies (i.e., requiring more change in proton energy to achieve the same change in IB latitude). This can be interpreted to result from the more rapid increase in equatorial magnetic field strength and curvature at distances closer to the Earth, where the dipole field has increasing effect relative to magnetotail current systems. These combined properties reveal that the monotonic FLC mechanism is a consistent explanation for most electron and proton IBs from 10s of keV to MeVs. However, in 10%-30% of cases, each energy channel independently displayed positive dispersion structures embedded within the larger overall dispersion pattern. This suggests that mesoscale processes can be superposed on the equatorial background field, such as wave-particle interactions (e.g. with EMIC), or transient disturbances from current systems in vicinity to the IB. The 50-200 keV range of electrons and 300-500 keV range of protons in particular seem to exhibit the widest variance in slope, suggesting it may be preferentially affected by waves. These may be related to the phenomenon reported by (Artemyev et al., 2023), in which electron IBs occasionally exhibit dispersion that is atypical of FLC, resulting from energetic proton precipitation that modifies the equatorial plasma conditions for wave generation and interactions with particles. The emergence of these embedded structures presents an interesting avenue for further study.

In the context of the ring current and storms, the proton IB location and its absolute/relative precipitating power evidently all scale directly with Dst. This agrees with

(Dubyagin et al., 2018), who showed similar variation in 30 keV proton IBs with sym-H and dynamic pressure, which I extended to higher energies (up to MeVs). This also supports the notion that FLC scattering of ring current protons presents a potentially significant means of depleting such fluxes at higher L-shells, affecting their contribution to Dst during storm main phase and recovery as suggested by (Yu et al., 2020). Unfortunately ELFIN was only active during moderate strength events (Dst $\sim$ -50 nT), which necessitates further investigation using similar observations for more intense storms (min. Dst $<$ -100 nT) to determine whether this correlation continues, and how curvature scattering affects heavier energetic ions, such as O^+, in the ring current. Comparisons with ring current loss rates due to other processes in these scenarios, such as charge exchange and Coulomb scattering, are necessary to determine the relative impact of FLC.

I also compared proton IB properties with electron IBs observed with ELFIN, finding that at quiet time, both exhibit a largely symmetric distribution in MLT, with proton IBs centered 1-2 hours post-midnight, and electrons 1-2 hours pre-midnight. This separation presumably involves the charge- and or mass-dependent properties affecting their azimuthal drift paths. Electron IBs were typically found 1-2 IGRF L-shells higher for the same energy channel. However, at active times, IBs of both species tend to shift to lower latitudes in the pre-midnight sector, suggesting such cases share similar driving, such as the intersection of tail injections with pre-midnight current-sheet thinning. This study aimed to provide a picture of the wider-energy dependent features of proton IBs. However, it was limited in the number of events that were collected before the spacecraft de-orbited. For this reason, the occurrence rate statistics outside of 19-03 MLT could not be evaluated. The observations were also constrained by the geometric factor of the ion detector, which limited sensitivity above $\geq$2 MeV energies despite the silicon enabling detection of >5 MeV protons. For some events, this restricted my determination of the highest-energy portions of the proton IBs, which likely extend above 2 MeV at fluxes below ELFIN's 1-count level. Further observations with increased sensitivity payloads would be beneficial in continuing this line of investigations, including at the flanks and on the dayside, to more fully constrain proton IB characteristics

at $\geq$200 keV energies. Further ground observations to determine the effect of the harder-energy spectrum (MeV and up) precipitation would also be useful, as many such studies have focused on only the lower (10s of keV) portion of the precipitation from the plasma sheet.

Combined with the electron IB observations, I mention that the ELFIN dataset provides a suitable platform from which to derive a predictive model of IB properties of both species, given predictors such as magnetospheric state variables (e.g. Dst), instantaneous solar wind coupling (e.g., by IMF B_z and dynamic pressure), and geometric orientation effects such as MLT and dipole tilt. Such models have been derived for 30-115 keV protons, e.g. (Dubyagin et al., 2018; Lvova et al., 2005; Ma et al., 2022), but not for higher 100s of keV to MeV energy protons, nor for electrons. Improved IB prediction models incorporating electrons and >115 keV protons would thus be valuable to increase the ability to predict precipitation and space weather, as well as constrain magnetic field models by tuning their average properties to match observations. This idea is developed in Ch. 6.

CHAPTER 4

Curvature-dominated precipitation poleward of isotropy boundaries

In this chapter, I address Questions 3 and 4 to quantify the distribution and geophysical effects of energetic ($\geq$50 keV) isotropic electron and proton precipitation in the poleward vicinity of isotropy boundaries. I identify a previously unreported range of latitudes poleward of IBs that tend to generate intense number fluxes, at energies which exceed the typical plasma sheet population. I show that these latitudinal ranges may be considered novel FLC-dominated transition regions between the plasma sheet and outer radiation belt for electrons ("PS2ORB"), and between the plasma sheet and ring current for protons ("PS2RC"). I find that the latitudinal extent and total $\geq$50 keV precipitating power of these regions vary highly with MLT and geomagnetic activity, in accordance with large-scale magnetospheric evolution, such as preferential cross-tail current sheet thinning. At times, this source rivals even the conventional $<$50 keV atmospheric power input into the auroral oval, on the order of GWs. Lastly, combined with the spatiotemporal results from Ch. 3, I show that this precipitation can impact sub-auroral latitudes, imparting a significant ionospheric conductivity enhancement that would not typically be achieved by conventional auroral precipitation.

4.1 Introduction

Poleward of the IB, the modeled minimum FLC-scattering energies in Fig. 3.1 predict that such particles continue to be isotropized (i.e. filled loss-cones), leading to an extended high-latitude region of $\geq$50 keV precipitation. This includes the plasma sheet proper, whose

bulk proton population is isotropic at energies of ∼10s of keV to low 100s of keV. However, rather than being uniformly distributed in latitude (e.g. throughout the plasma sheet), this precipitation has been shown to exhibit preferential locations of peak intensity. A critical finding using ≤30 keV DMSP observations is pointed out by (Newell et al., 1998): in general, proton precipitation appeared to be most intense in close poleward vicinity to the proton IB, as well as preferentially in the pre-midnight sector. They attributed special significance to this latitude, referring to the location as the "b2i" index, demonstrating its correlation with magnetotail stretching (and thus curvature) using equatorial magnetic field inclination measurements taken in GEO by NOAA's Geostationary Operational Environmental Satellites (GOES). Optical signatures of the index have also been derived in proton aurora using ground imagers, such as the work of (Donovan, 2003), further confirming the properties and importance of the b2i index as inferred by DMSP.

To motivate this thinking, we may look at Fig. 4.1, taken from Fig. 1 in (Newell et al., 1998), showing an example in TIROS data (the precursor to NOAA POES/MetOp) from 1979 of the b2i index and its relationship to the detected proton IBs. The Top Panel shows the total energy flux of 0.3-20 keV protons as a function of magnetic latitude during a southern satellite pass near midnight MLT. It can be observed that at the most equatorward latitudes (furthest to the right), there is very little 20 keV precipitation, likely owing to being in the highly anisotropic main bulk of the ring current. However, upon moving southward (poleward) and crossing the 30 keV IB (marked "O" in the second panel), this precipitation abruptly rises to its maximum value, and remains high for an extended poleward range. These authors found that this relationship between peak flux intensity and IB location was generally the case, and suggested a deep connection to the configuration and dynamics of the magnetotail.

In the context of this Chapter, we may note by inspecting Panels 3 and 4, this detector evidently lacked sufficient sensitivity to resolve the precipitation at higher energies (i.e., fluxes at or below the one count level). The authors therefore did not consider the more energetic portion of these fluxes, and attributed only a single "b2i" reference energy (nominally the

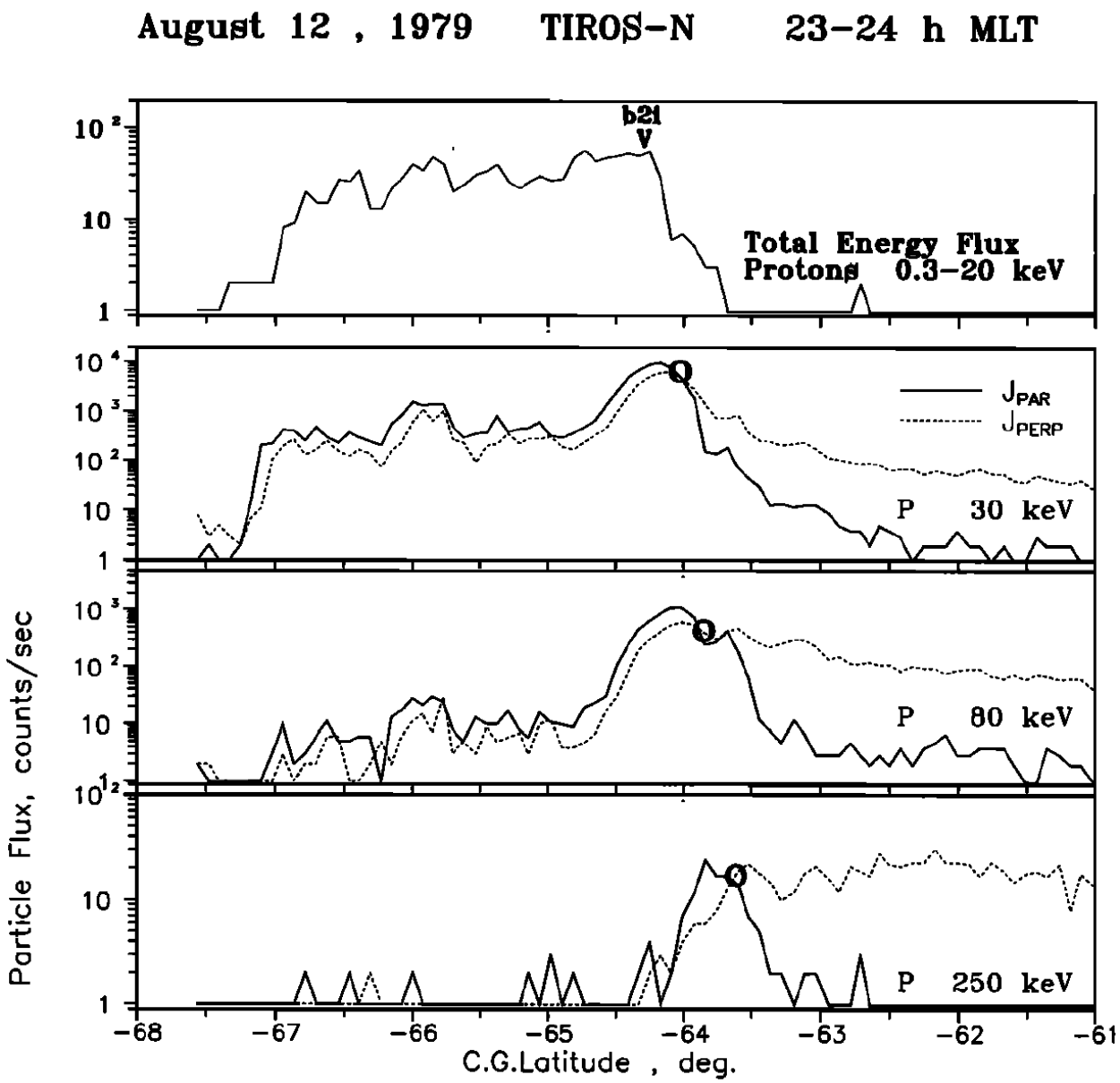

Figure 4.1: TIROS-1 crossing of the 30, 80, and 250 keV proton IBs in a southern satellite pass, showing that the peak in 0.3-20 keV proton precipitation occurs at the "b2i," immediately poleward of the 30 keV IB. Copied from Fig. 1 of (Newell et al., 1998).

30 keV IB). As I will soon show, the >20 keV portion portion of this precipitation is non-negligible, and spans a wider range of latitudes than just the location of a single reference energy IB.

The physical rationale for studying such precipitation is largely its connection to the ionosphere, and in the evolution of the ring current and outer radiation belts. Plasma sheet electrons and protons in the 10s of keV range in particular are those primarily responsible for generating visible auroral phenomena, and their precipitation has thus been extensively studied. However, critically, the contributions above 30 keV energies remain largely unexplored, despite the potential for significant ionospheric effect (Mukhopadhyay et al., 2022).

To understand why the ≥50 keV fluxes can have a significant ionospheric impact, we may refer to Fig. 4.2, adapted from Fig. 2 of (Fang et al., 2010) and Fig. 7 of (Fang et al., 2013), which shows the altitude profiles of ionospheric ionization enhancements for a given mono-energetic precipitating electron beam (left) and protons (right), under the assumption of an energy flux of ∼1 erg/cm^2-s. *As we can see, the lower the particle energy, the more shallow the penetration into the ionosphere.* **Crucially, this implies that ionization enhancements on the nightside ionosphere below ∼100 km altitude cannot be directly explained or caused by ≤30 keV precipitation from the plasma sheet.** This implies that enhancements of the ionosphere in the lower E and upper D regions likely require a much more energetic source of particles, in the 100s of keV to MeV range. This is the population of electrons and protons I investigate here.

In anticipation of this work's findings, I also introduce two other figures, which provide important context on the potential ionospheric significance of the ≥50 keV isotropic precipitation. First is Fig. 4.3, taken from Fig. 9 of (Newell and Gjerloev, 2011), which shows the typical variation in ionospheric power input from traditional auroral sources, including broadband aurora (wide-energy electron precipitation due to kinetic Alfven waves), mono-energetic electron ("inverted-V" field-aligned potential) aurora, and proton precipitation aurora, as defined in (Newell et al., 2009a), and are typically less than 30 keV in energy for all processes. Inspecting the Panels of Fig. 9, we can see that these processes each typically

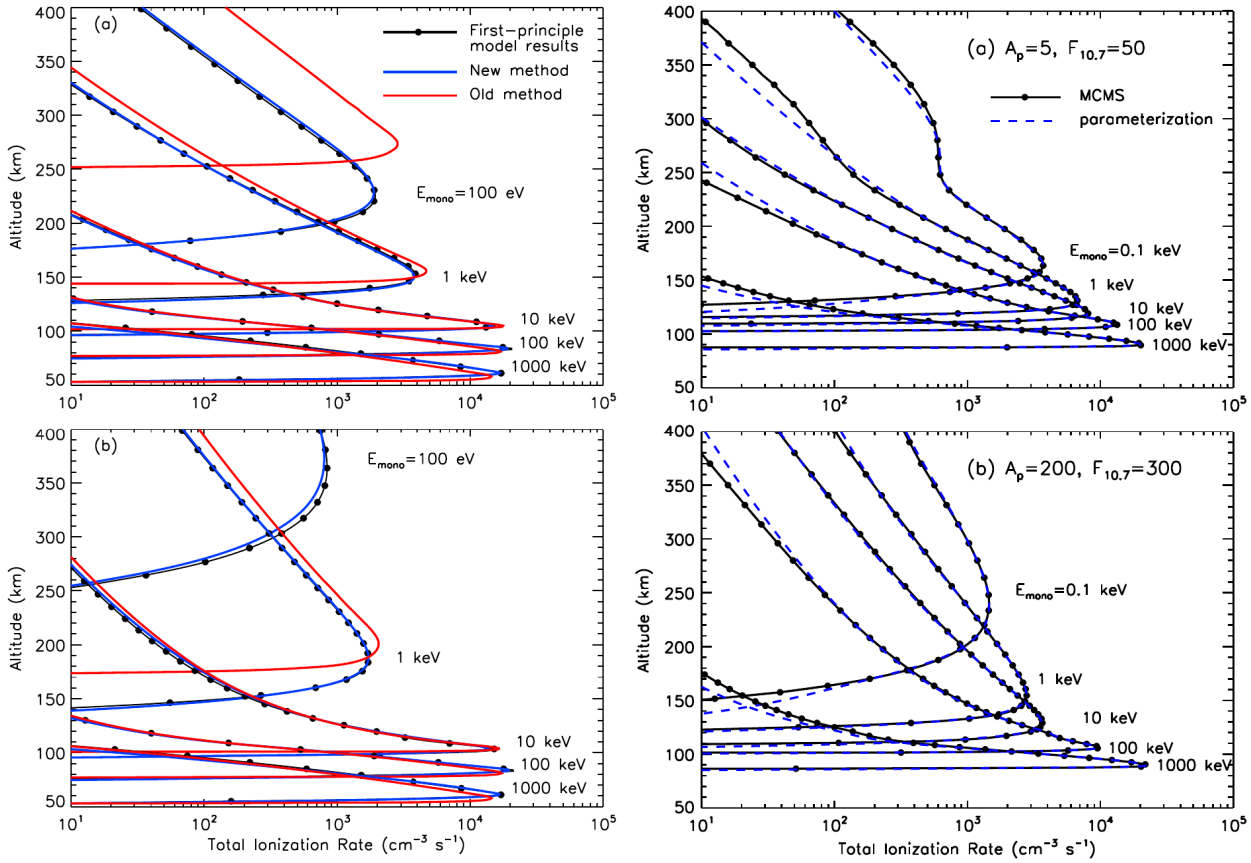

Figure 4.2: Altitude profiles of ionization rates generated by mono-energetic particle beam precipitation of electrons (left) and protons (right), at an input energy flux of 1 erg/cm^2-s. Adapted from Fig. 2 of (Fang et al., 2010) and Fig. 7 of (Fang et al., 2013).

provide 100s of MW to several GW of precipitating power into the ionosphere over common geomagnetic activity conditions (SME is akin to AE). As I show in the Results, ≥50 keV electron and proton precipitation within the PS2ORB/PS2RC can also provide these levels of integral precipitating energy flux, and over a range of altitudes that both intersects with the main auroral oval, as well as extends equatorward in latitude.

To see how these fluxes can be significant in affecting the nightside ionosphere, I refer to the recent work of (Tian et al., 2022), who showed using POES and an ionospheric conductivity model, that 50 keV to several hundred keV electron and proton precipitation associated with EMIC wave scattering, at comparable flux levels to those seen in the PS2ORB/PS2RC, could have a dramatic effect on the Pedersen and Hall conductivities near dusk. This result is captured in Fig. 4.4, taken from Fig. 4 of that work. It can be seen that in the case with EMIC-driven precipitation (right side), the conductivities were enhanced by up to a factor of 3 – a very significant increase. It is reasonable to conclude that similar enhancements could arise at other MLTs on the nightside, where isotropic particles associated with the IB precipitate. The total amount of precipitating energy flux in the PS2ORB/PS2RC, and their peak energy, latitudinal range, and MLT are thus important parameters to characterize, which I perform in the remainder of this work.

4.2 The PS2ORB and PS2RC interfaces: Novel regions of energetic particle precipitation

4.2.1 Definition, latitudinal bounds, and operational identification

In defining an equivalent to the b2i index for more energetic precipitation, I find that for 100s of keV to MeV protons, such intense precipitation can be distributed over a wider range of latitudes than can be reasonably described by a single-point index (see Results). I therefore establish an operational criterion to bound the latitudinal range involved, starting with the lowest-latitude portion of the IB dispersion pattern detected in each individual collection, and terminating poleward at the plasma sheet inner edge. I refer to the region bounded by

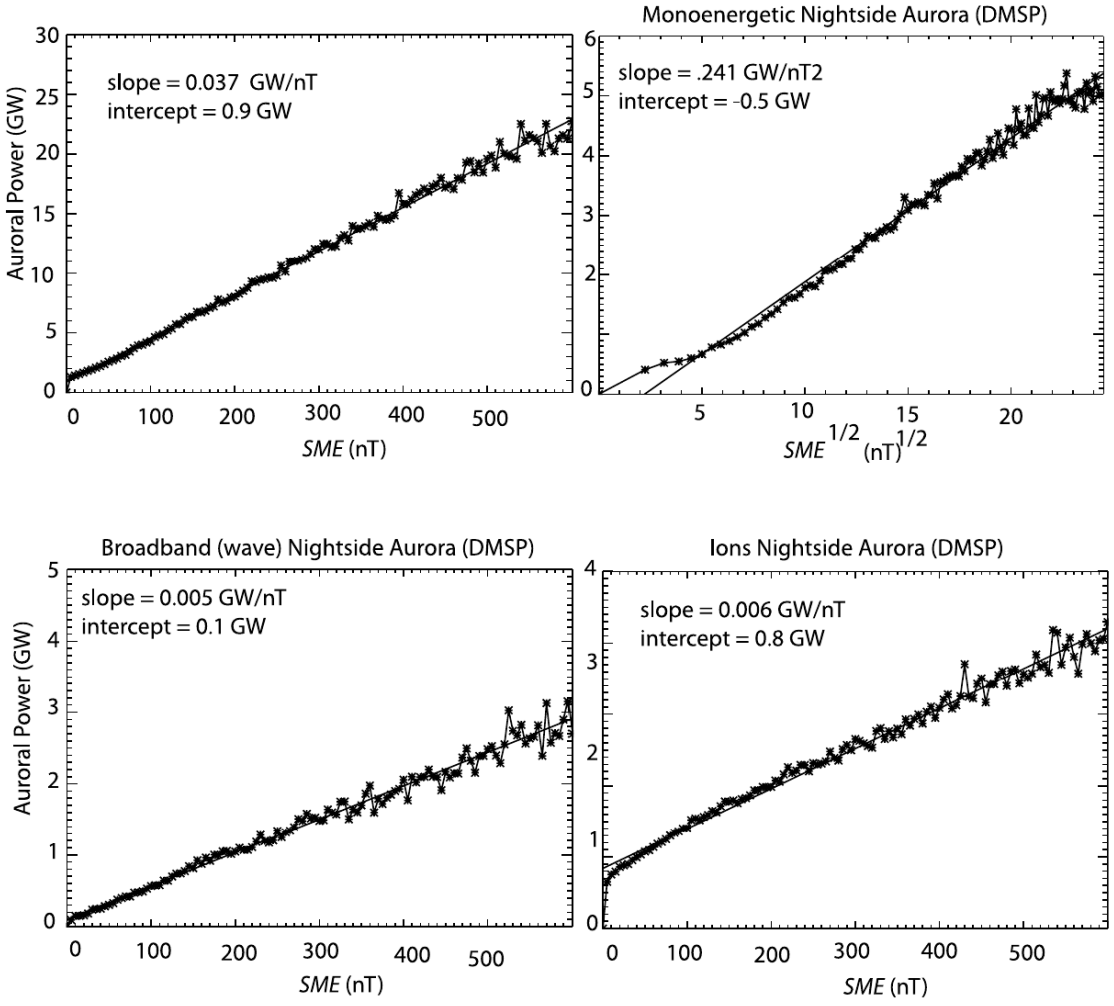

Figure 4.3: Distribution of auroral power input versus SME (akin to AE), for later comparison with the power from $\geq$50 keV particle precipitation in the PS2ORB/PS2RC. Taken from Fig. 9 of (Newell and Gjerloev, 2011).

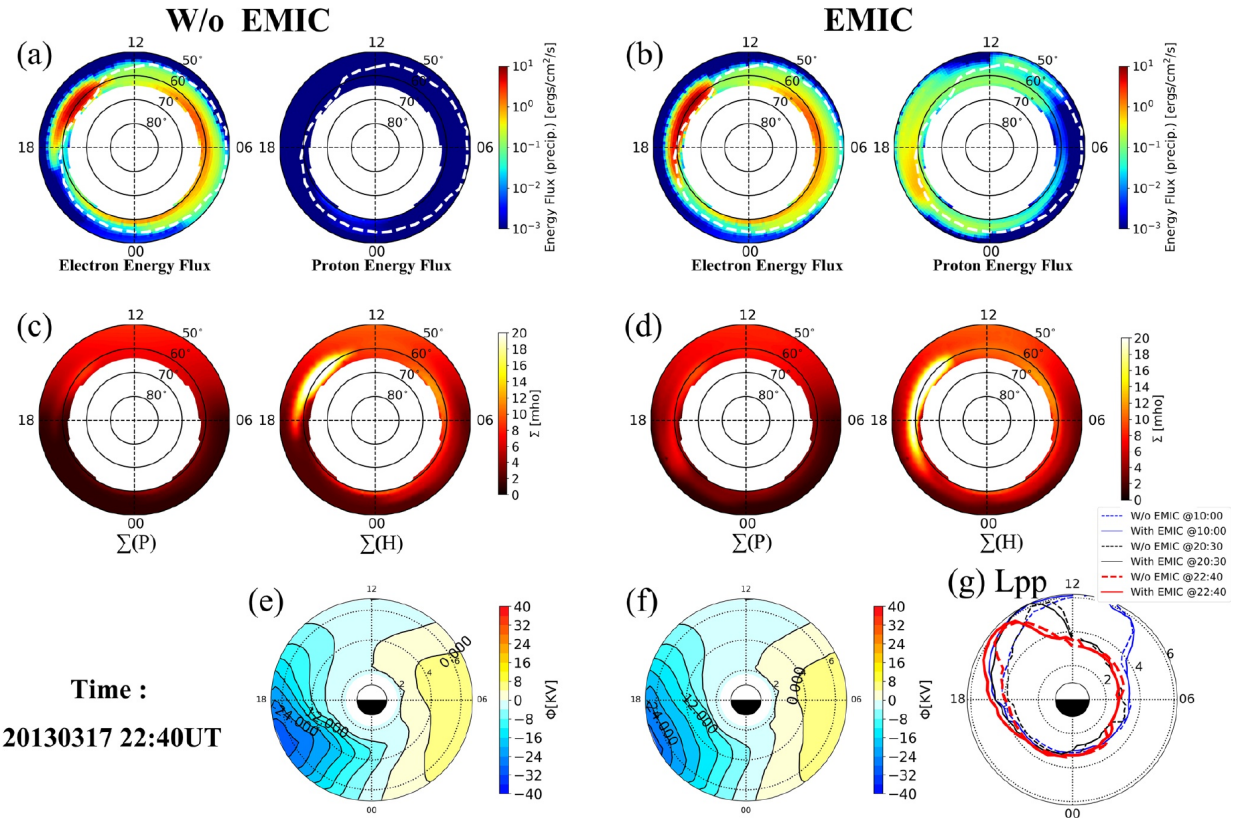

Figure 4.4: Demonstration of the role of EMIC-driven ≥50 keV electron and proton precipitation in enhancing the Pedersen and Hall conductivities near dusk, serving to motivate the possibility of similar effect at other MLTs due to FLC scattering poleward of the IB. Taken from Fig. 4 of (Tian et al., 2022).

these latitudes as the Plasma Sheet-to-Ring Current ("PS2RC") interface for proton IBs, and the Outer Radiation Belt-to-Plasma Sheet ("PS2ORB") interface for electron IBs, describing an FLC-dominated precipitation region equatorward of the plasma sheet inner edge. The IB thus can be thought of an energy-dependent outer boundary for stable trapping of electrons in the outer radiation belt, and protons in the ring current.

The rationale for using the plasma sheet inner edge as the latitudinal cutoff is both rooted in physical intuition, and in practicality. It is well-known that the plasma sheet has a relatively uniform distribution in particle energy and spectral hardness (Christon et al., 1989, 1991), which does not tend to vary in the extreme manner as found in the region equatorward of its inner edge (i.e., the outer ring current and radiation belts). **This equatorward region is therefore phenomenologically different in its characteristics than the plasma sheet, being a location where particles typically associated with the inner magnetosphere may directly interact with the magnetic energy conversion processes of the tail, thus leading to both highly energetic particle injections and number fluxes, which are immediately affected by FLC scattering and waves.** The plasma sheet inner edge is therefore an important and useful geophysical boundary in which to distinguish particles associated with the IB, versus the more distant magnetotail.

The second reason for taking the boundary at the plasma sheet inner edge is that it can be identified straightforwardly in ELFIN particle data. One way to operationally identify the instantaneous inner edge is to look for the satellite location at which fluxes associated with the plasma sheet drop below a particular detection threshold. This approach was employed for example by (Vasyliunas, 1968) with OGO data, who used 40 keV electron flux dropouts to infer the inner edge of the plasma sheet. However, those authors used substantially different instrumentation; thus, the particular cutoff criterion requires special consideration of the orbit and instrumentation.

In my study, I marked this edge by the instantaneous latitude poleward of the IB at which omnidirectional $\geq$300 keV electrons and protons dropped below detectable levels. This criterion is based on the results of (Christon et al., 1989, 1991), who used ISEE data to

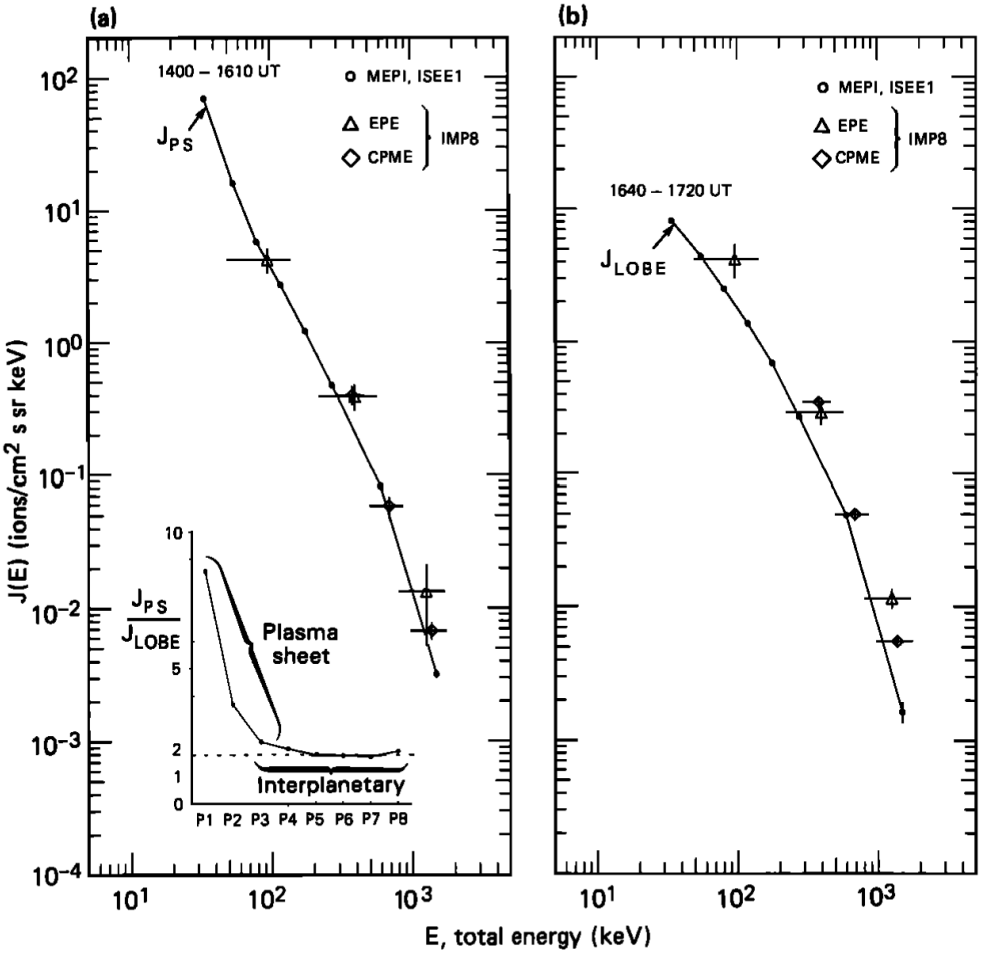

Figure 4.5: Typical number fluxes of protons in the central plasma sheet in two different time intervals on the same day. Taken from Fig. 2 of (Christon et al., 1989).

characterize the typical isotropic proton differential-directional number fluxes of the central plasma sheet at quiet and active times. This can be seen for example in Fig. 4.5 based on Fig. 2 of (Christon et al., 1989). These authors found that equatorial isotropic 300 keV electrons and protons typically appear with fluxes on the order of 10^{-1}/cm^2-s-str-keV, which, when scaled by the ELFIN EPD geometric factors, integration time, and energy bin widths, and pitch-angle, are below the one-count level for detection at the satellite location in polar LEO.

4.2.2 Precipitation and the poleward FLC-region associated with the IB

Using this definition of the proton PS2RC and the electron PS2ORB, I characterized the precipitation from isotropic ≥50 keV particles in the localized poleward vicinity of the IB. The instantaneous precipitating energy flux of each isotropic species was computed by integrating over all loss-cone pitch-angles and observed energies poleward of their respective IB, assuming 2π steradian incidence on the atmosphere. The instantaneous precipitating fluxes were averaged over the range of poleward latitudes in which they were collected, resulting in an average integral-energy flux in units of erg/cm^2-s for each individual science zone, herein referred to as "IEflux." (I note that because the satellites were in circular polar orbit with a short integration interval, elapsed collection time is interchangeable with subtended latitude from satellite motion.) The total power deposition of the collection (e.g., in Watts), can be estimated by scaling over the atmospheric area subtended by the orbit track in the PS2RC/PS2ORB, and the azimuthal width of the hourly MLT bin.

Figure 4.6 provides an example event containing a canonical PS2ORB region, captured by ELFIN-B on 2022-09-02. A 50 keV to 3 MeV electron IB energy-latitude dispersion pattern is evident in the crossing, where the PS2ORB region can be clearly seen as a separate intense region of energetic particle precipitation poleward of anisotropic outer radiation belt, and equatorward of the isotropic plasma sheet (marked in red bars), where the fluxes are relatively capped at 100-200 keV energies. The Bottom Panel shows the instantaneous precipitating energy flux of ≥50 keV isotropic loss-cone electrons. *A highly-energetic precipitation structure can clearly be observed separately from the regions of the outer radiation belt (lower latitudes) and plasma sheet (higher latitudes), approaching a precipitating power of 1 erg/cm^2-s.* This can be compared with the wave-particle interaction occurring within the lower-latitude radiation belt in this same event, which provides slightly more power, but at considerably lower energies (and thus would affect the ionosphere differently).

In order to assess the geophysical significance of FLC-caused ≥50 keV precipitation in the PS2RC/PS2ORB compared to other magnetospheric sources (regardless of underlying mechanism), I also separated the latitudinal range of the ELFIN collections into (1) the en-

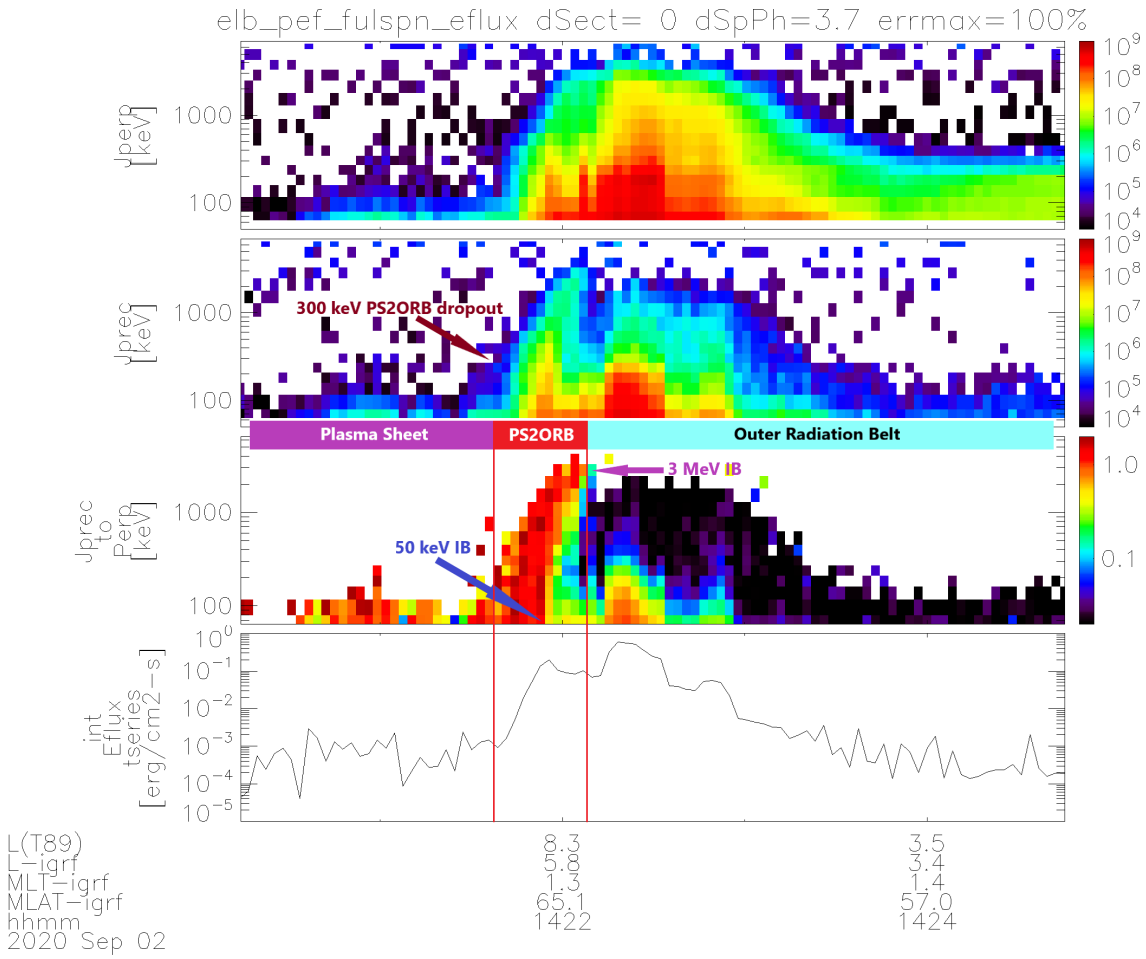

Figure 4.6: Example ELFIN electron IB event showing a canonical example of the "plasma sheet-to-outer radiation belt" transition region (red bars). Top Panel shows perp electron flux, second Panel shows precipitating electron flux, while the third is the their ratio, showing a 50 keV to 3 MeV IB crossing, which bounds the equatorward side of the PS2ORB. The poleward boundary is the 300 keV omnidirectional flux dropout location, marking the operational plasma sheet inner edge. Bottom Panel shows the instantaneous precipitating energy flux from isotropic $\geq$50 keV loss-cone electrons.

tire science zone (nominally 55-80° in |MLAT|, including outer radiation belt, ring current, and portions of the plasma sheet/polar cap); (2) all latitudes poleward of the IB, including plasma sheet and polar cap (up to 80°); and (3) latitudes solely within the PS2RC (protons)/PS2ORB (electrons), representing the amount of precipitation that is presumed to be associated with energetic FLC scattering localized to the IB. I also determined the MLT distribution of precipitation (IEflux) and its ratio to the high-latitude region total at that MLT. The precipitation ratio is computed by integrating proton IEflux over the latitudinal extent of the PS2RC or PS2ORB, then dividing by the equivalent IEflux integrated over that of regions (1) or (2).

4.3 Results

4.3.1 Latitudinal characteristics of the PS2ORB/PS2RC interface

I begin the results by discussing the latitudinal characteristics of the PS2ORB and PS2RC interfaces. The first question is the effect of the 300 keV flux dropout criterion, versus using some other reference energy. Fig. 4.7 Top and Middle provide an assessment of how separated the main plasma sheet is from the electron IB crossing as a function of the chosen reference drop-out energy. It can be seen that below 300 keV, there is a clear jump in the energy-latitude slope, suggesting using a lower reference energy would very likely also include the plasma sheet proper (and thus not accurately capture the dynamical region immediately poleward of the IB). The Bottom panel shows the distribution in latitudinal extent of the PS2ORB versus MLT, at quiet and active times. It can be seen that during quiet intervals, the PS2ORB tends to be relatively narrow in latitude ($\sim$1°) across all local times. However, at active times, the region expands dramatically between midnight and dawn, suggesting a much wider latitudinal extent of particle injections and particle isotropization (e.g., by more favorable FLC scattering conditions). The asymmetry is also consistent with the typical drift direction of near-equatorial electrons experiencing gradient, curvature, and diamagnetic (plasma pressure gradient) drifts. As we will see, the opposite asymmetry occurs for protons.

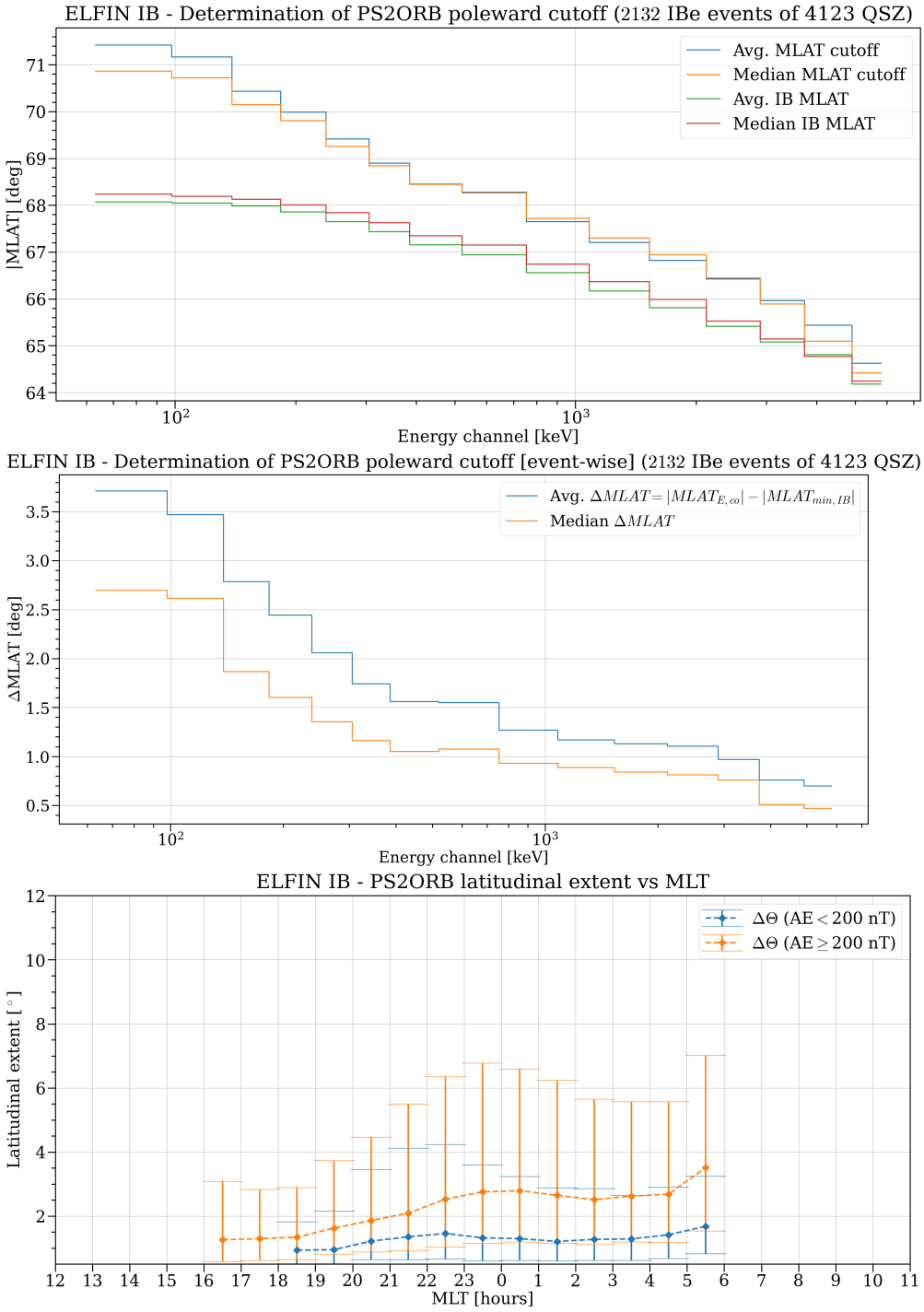

Figure 4.7: Assessment of 300 keV omnidirectional electron flux dropout criterion in defining the PS2ORB poleward boundary. Top Panel shows the absolute MLAT over all IB events by energy channel for which an IB was observed compared with the poleward latitude at which omnidirecitonal fluxes of that energy drop out. The middle Panel shows the event-wise difference across the database. The bottom Panel shows the PS2ORB latitudinal width $\Delta\Theta$ distribution versus MLT and activity, based on the 300 keV drop-out criterion.

I next performed the same analysis for protons. The top Panel of Fig. 4.8 shows the energy-dependent mean and median locations for proton IBs and the location of poleward omnidirectional flux dropouts. It can be seen that there is a near uniform 2-3° difference in latitude between these curves above 200-300 keV, while the difference rapidly rises at lower energies to over 6°. Such a large latitudinal range between the IB and dropout for energies 50-200 keV suggests that some or all of the plasma sheet would probably be included in the PS2RC if a criterion in this energy range were used to define the poleward boundary, while the much narrower width at higher energies suggests a separate transition region population. The middle Panel shows the mean and median event-wise difference between the IB and the omnidirectional flux dropout vs energy. This plot reveals a similar trend at energies below 200-300 keV, which, along with the top Panel and earlier count rate analysis, suggests 300 keV is a reasonable proxy through which to determine a conservative poleward cutoff of the more energetic non-plasma sheet population.

Based on the above dropout criterion, Fig. 4.8 bottom Panel shows the typical width in latitude ($\Delta\theta$) of the PS2RC region versus MLT and activity. At non-active times, the latitudinal extent is typically 2°-3° across all sampled local times. At active times, the PS2RC interface expands dramatically in the pre-midnight sector, growing from a mean value of 3.5° at 01-02 hours to 6° between 20-21 hours. The expansion evidently stems from the IB moving to lower latitudes, combined with more energetic protons appearing at higher latitudes at the same MLT, associated with the elevated magnetospheric activity/tail configuration. It is also in the opposite MLT sector as the enhancement as the PS2ORB latitudinal extent, suggesting again that charge-dependent azimuthal drifts are likely involved, such as perhaps related to partial ring current formation.

4.3.2 Particle precipitation associated with poleward FLC

With the latitudinal ranges defined as above, I present the results from analysis of $\geq$50 keV electron and proton precipitation.

Fig. 4.9 shows the distribution of averaged integral precipitating electron energy flux

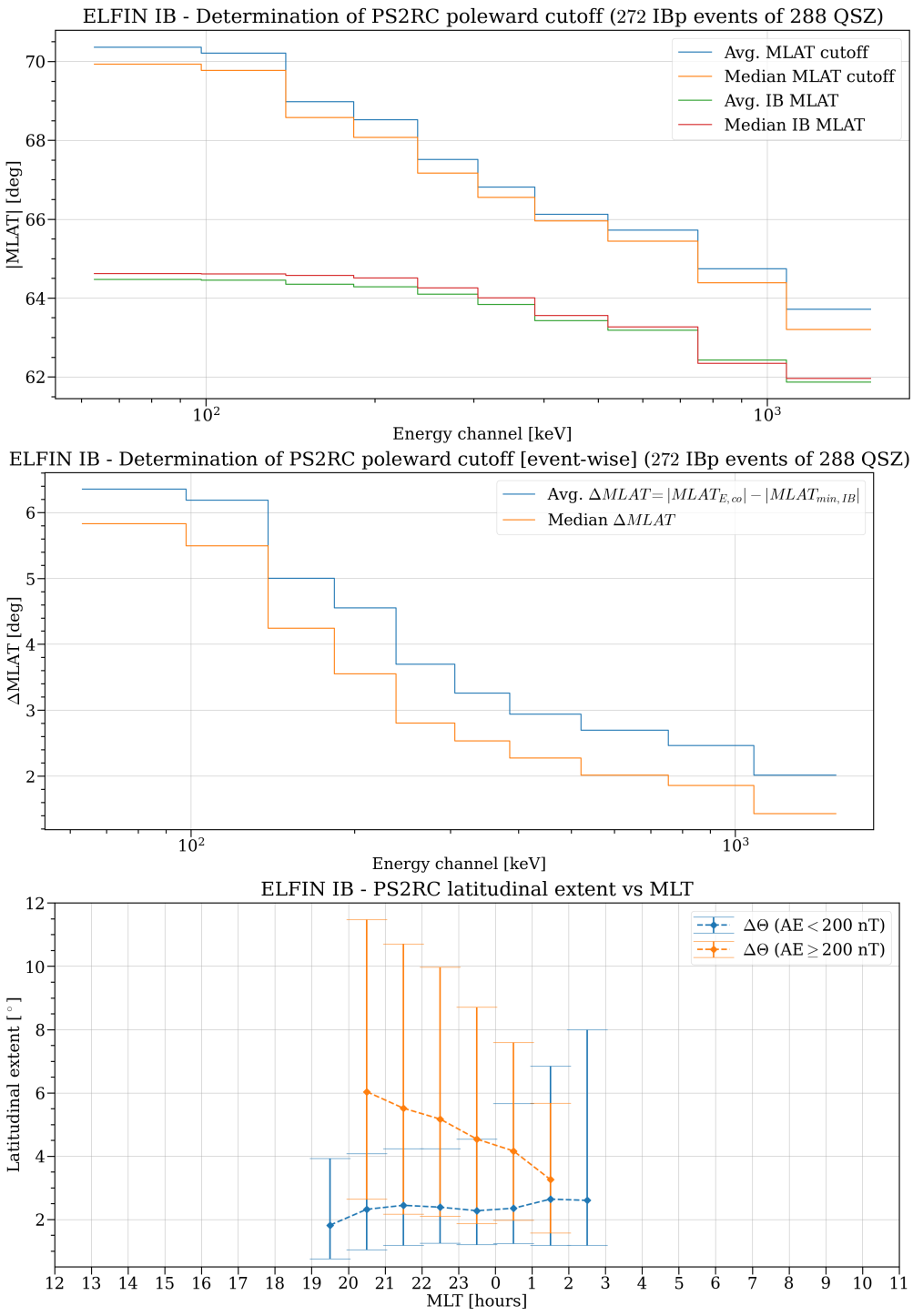

Figure 4.8: Assessment of 300 keV omnidirectional proton flux dropout criterion in defining the PS2RC poleward boundary. Top Panel shows the absolute MLAT over all IB events by energy channel for which an IB was observed compared with the poleward latitude at which omnidirecitonal fluxes of that energy drop out. The middle Panel shows the event-wise difference across the database. The bottom Panel shows the PS2RC latitudinal width $\Delta\Theta$ distribution versus MLT and activity, based on the 300 keV drop-out criterion.

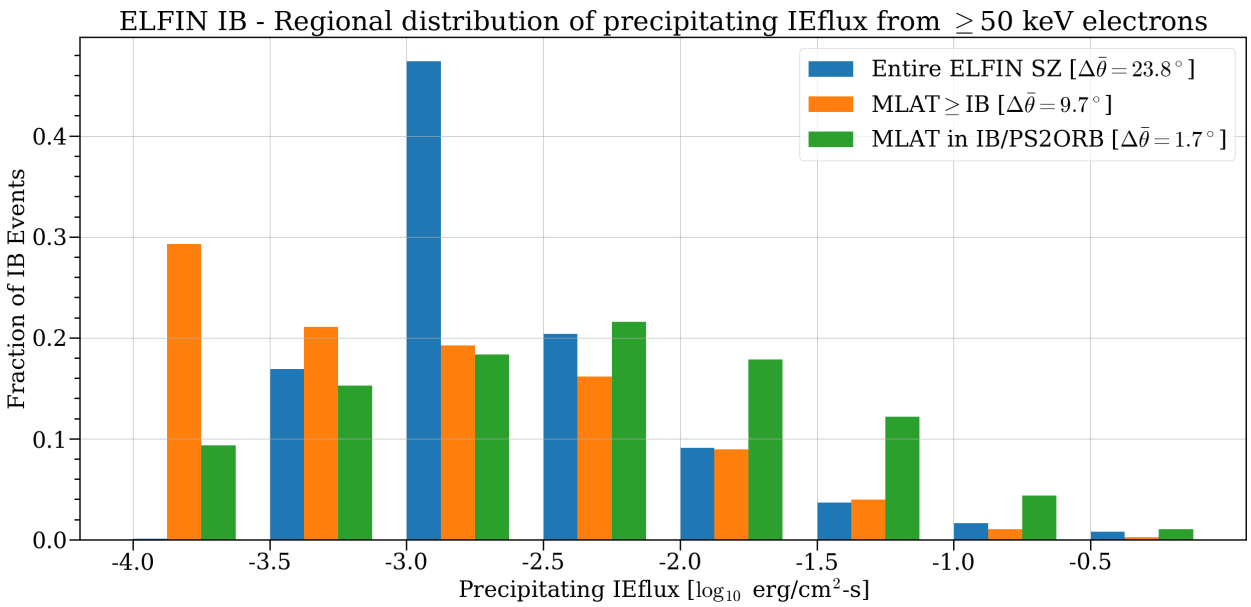

Figure 4.9: Distribution of latitude (crossing-time) averaged integral precipitating energy flux (IEflux) from >50 keV electrons in different latitudinal ranges of the ELFIN IB event dataset. Blue bars represent the entire ELFIN science zone (nominally 55° to 80° latitude), including ring current, outer radiation belt, plasma sheet, and partial polar cap. Orange bars represent all latitudes poleward of IBs, including the PS2ORB region, but not terminating at its poleward boundary. Green bars represent fluxes within the IB and PS2ORB interface.

in each of the above regions, as well as the latitudinal extent ($\Delta\bar{\theta}$) of the three regions described above. I find that of these regions, the PS2ORB tends to have the highest average integral precipitating ≥50 keV electron energy flux (often the order of $10^{-2.5}$ to 10^{-1} erg/cm^2-s), and is typically concentrated to 1.7° in latitude, suggesting it is a significant source of precipitation acting over latitudes in the vicinity of the IB.

Fig. 4.10 shows the distribution of averaged integral precipitating proton energy flux in each of the above regions, as well as the latitudinal extent ($\Delta\bar{\theta}$) of the three regions described above. I find that of these regions, the PS2RC tends to have the highest average integral precipitating ≥50 keV proton energy flux (on the order of 10^{-1} to 10^{-2} erg/cm^2-s), and is typically concentrated to 3.4° in latitude, suggesting it is a significant source of precipitation acting over auroral/sub-auroral latitudes, over a wider typical range than electrons.

Fig. 11 top Panel depicts the MLT distribution of electron (PS2ORB) precipitation ratio, and the bottom Panel depicts the precipitating IEflux versus local time over all events

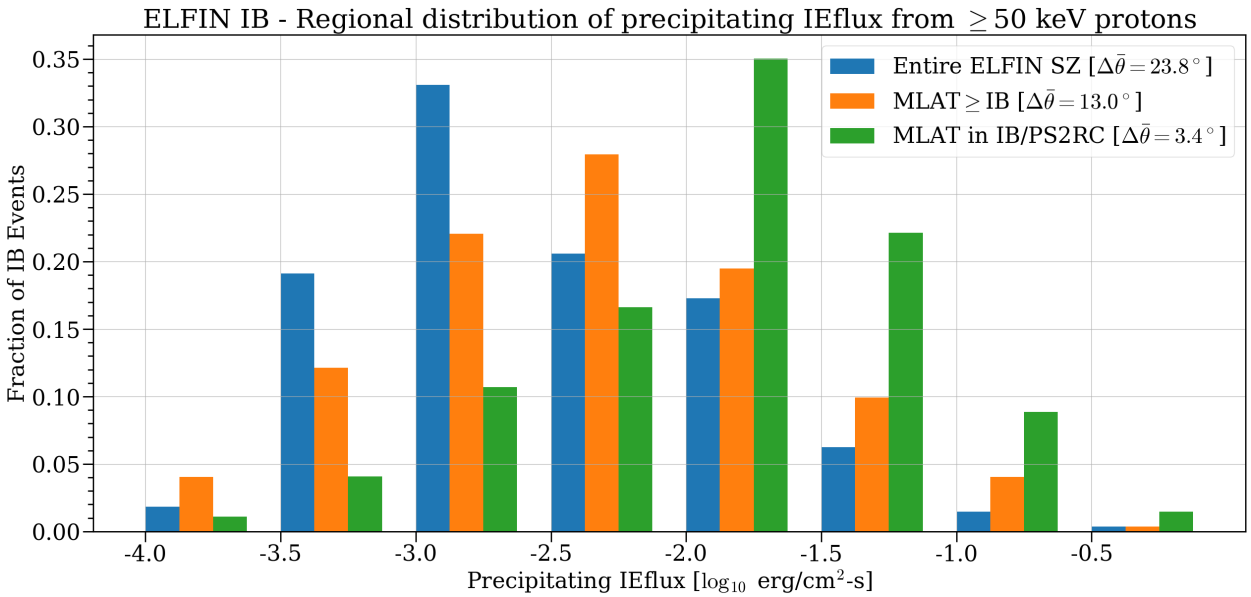

Figure 4.10: Distribution of latitude (crossing-time) averaged integral precipitating energy flux (IEflux) from >50 keV electrons in different latitudinal ranges of the ELFIN IB event dataset. Blue bars represent the entire ELFIN science zone (nominally 55° to 80° latitude), including ring current, outer radiation belt, plasma sheet, and partial polar cap. Orange bars represent all latitudes poleward of IBs, including the PS2ORB region, but not terminating at its poleward boundary. Green bars represent fluxes within the IB and PS2ORB interface.

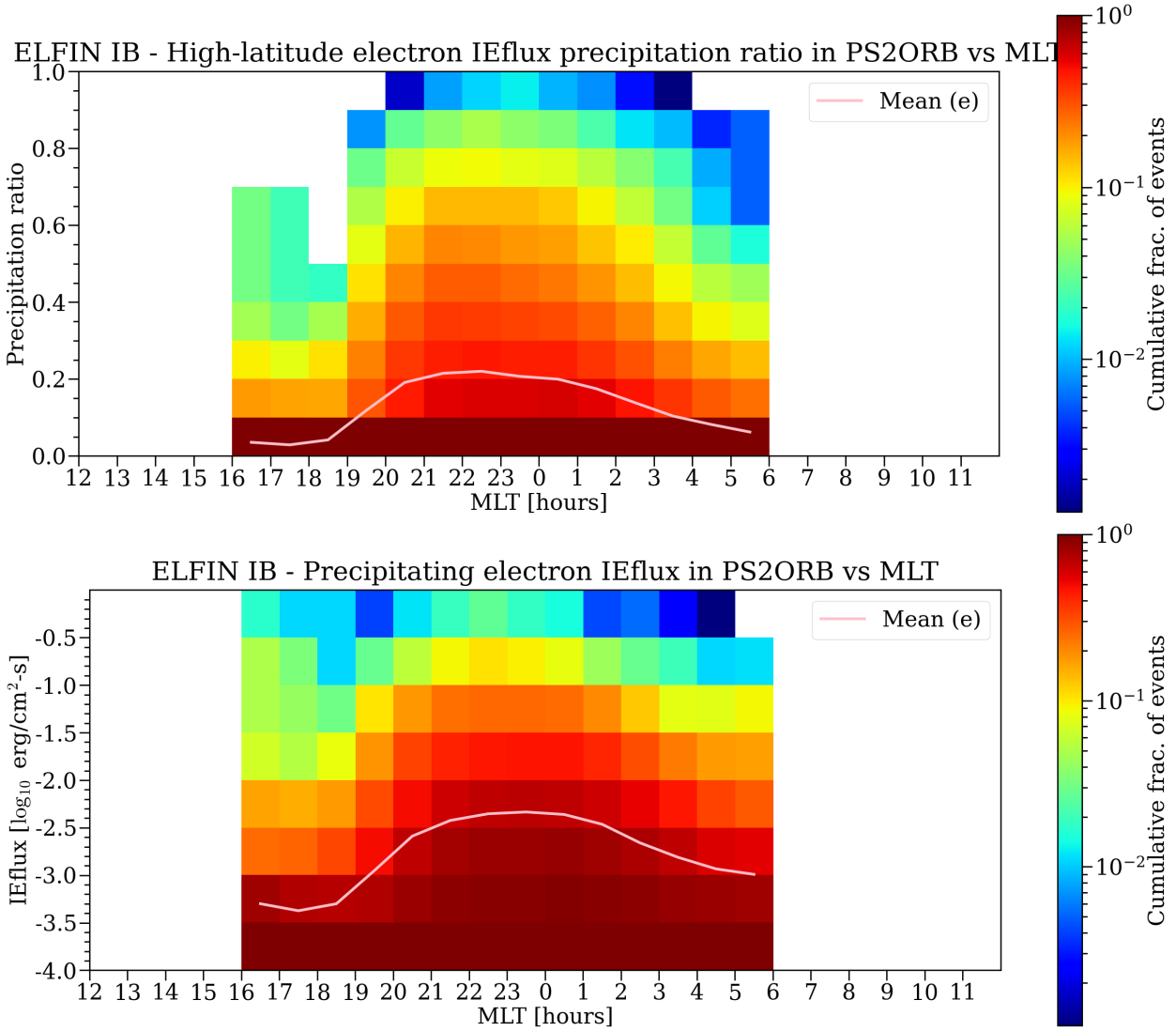

Figure 4.11: Cumulative distribution in MLT of >50 keV isotropic electron integral precipitating energy flux (IEflux) ratios (top) and the IEfluxes (bottom). The precipitation ratio is computed by integrating the proton precipitation in the PS2ORB, and dividing by the total for the science zone (55°-80°) in that MLT bin. The color scale is interpreted as the cumulative probability of exceeding all values below a particular value on the vertical axis. The bottom Panel reveals the trends in latitude-averaged precipitating electron energy-flux within the PS2ORB.

containing IBs. The color scale represents the cumulative probability of exceeding all values below the position on the vertical axis. The mean values of IEflux and the precipitation ratio in each MLT bin of the distribution. In the top Panel, electrons exhibit a slightly skewed distribution in the amount of high-latitude particle power FLC precipitates, often around 20% of the total high-latitude $\geq$50 keV electron power, and dropping to 10% approaching dusk/dawn, although the total power can sometimes approach 100% (precipitation ratio $\sim$ 1) at MLTs near 22. The trend is similar for electrons, except the proton precipitation ratio is typically around three times larger across the nightside. In the bottom Panel, we see a similar symmetric distribution of IEflux, with electrons typically precipitating with energy flux on the order of 10^{-2} erg/cm^2-s versus MLT, but at times exceeding 1 erg/cm^2-s between 21-01 MLT.

Using the precipitating IEflux from Figs. 4.11,12 bottom and the PS2ORB/PS2RC latitudinal extent from Figs. 4.7,8 bottom, I also computed an order-of-magnitude estimate of MLT-aggregated total precipitating power across the nightside, along with a lower bound for the maximum power isotropic proton precipitation in the PS PS2RC may instantaneously provide. Assuming 111 km/$^\circ$ of latitude, 1 hour MLT $\sim$ 15°, I find that the typical precipitating power of isotropic protons by FLC is on the order of 100 MW, but at the most active times may exceed 10 GW across the nightside. This typically exceeds the equivalent power provided by $\geq$50 keV electron IB precipitation, which is often around 10 MW across the nightside, but can exceed 1 GW at the most active times. I note also that the PS2ORB is, on average, 1/2 to 1/3 the extent of the PS2RC, and thus typically a more localized precipitation source.

Lastly, I characterized the MLT-aggregated precipitation versus geomagnetic activity (AE, Dst, Kp) of the PS2ORB and PS2RC. Figs. 4.13 and 4.14 show the resulting distribution of IEfluxes (left column) and precipitation ratio (right column), versus AE (100 nT bins; 3-hour average), Dst (10 nT bins), and Kp, using the same definitions for the precipitation ratio and net total average precipitating energy flux as in Figs. 4.11,12. The mean values of the distribution for protons and electrons are over-plotted in pink and purple, respectively.

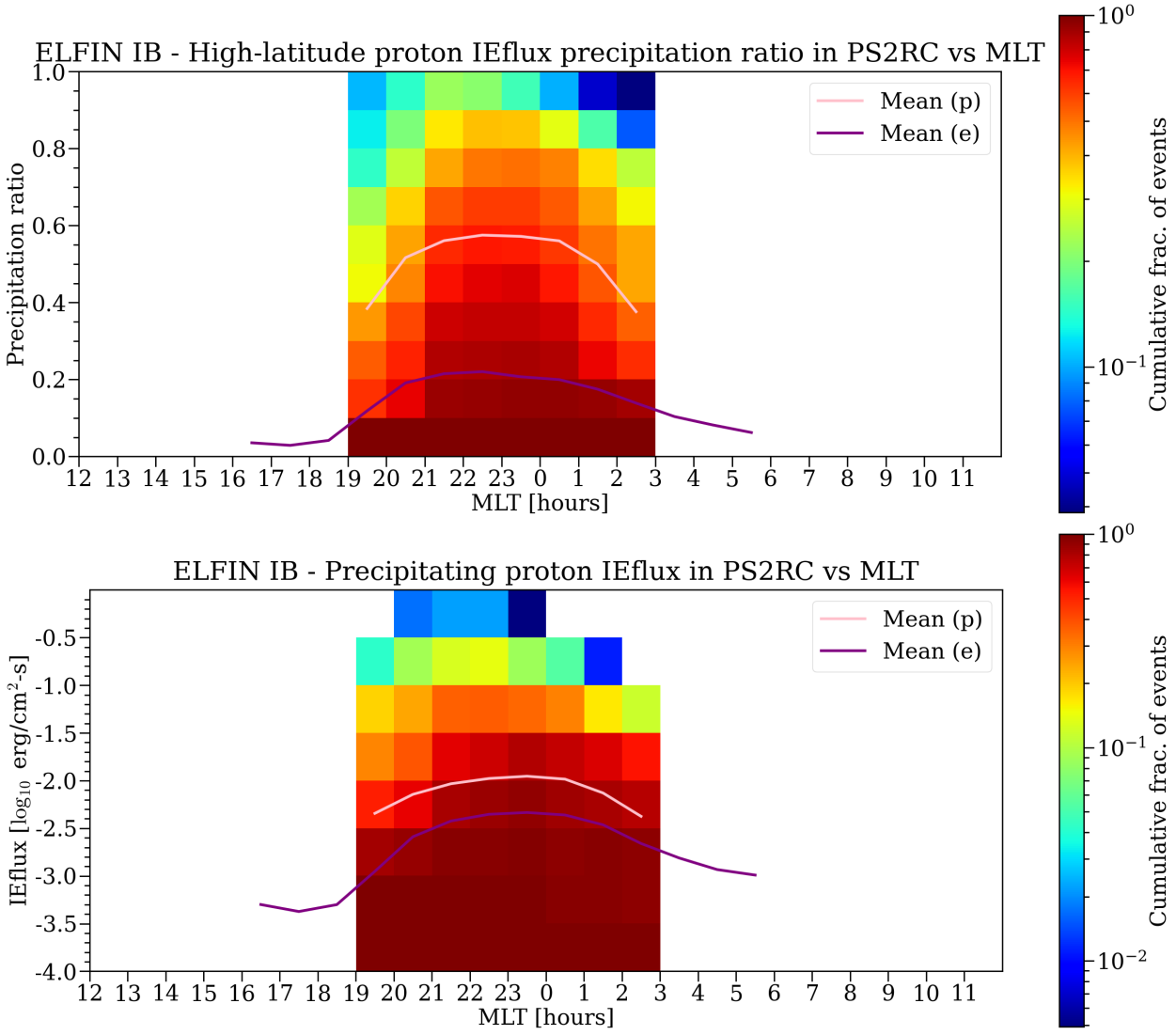

Figure 4.12: Cumulative distribution in MLT of >50 keV isotropic proton integral precipitating energy flux (IEflux) ratios (top) and the IEfluxes (bottom). The precipitation ratio is computed by integrating the proton precipitation in the PS2RC, and dividing by the total for the science zone (55°-80°) in that MLT bin. The color scale is interpreted as the cumulative probability of exceeding all values below a particular value on the vertical axis. Equivalent electron IB mean values (non-cumulative) are over-plotted in purple (normalized by their own >50 keV precipitation separately from protons). The bottom Panel reveals the trends in latitude-averaged precipitating energy-flux within the PS2RC (protons) and PS2ORB (electrons), respectively.

For AE (top Panel), an apparent increase in both the average precipitation ratio and integral energy flux are observed as AE increases from 0-200 nT (quiet time), with increases above 200 nT (active times), for which proton almost always exceeds 70% of the high-latitude total, providing between 10^{-2} and 10^{0} erg/cm^2-s. Electrons follow a similar trend, but are lower in average precipitation ratio and IEflux intensity. For Dst (middle), proton precipitation rises dramatically as Dst decreases from 0 nT, suggesting that FLC is likely the dominant pitch-angle scattering mechanism resulting in the precipitation of energetic ring current and plasma sheet protons at active times, including moderate strength storms. Below -30 nT, the precipitation tends to represent between 70% to 100% of the total $\geq$50 keV precipitation, with average fluxes between 0.1 and 1 erg/cm^2-s, dropping to 40% for Dst $\sim$ 0 nT with average flux between $10^{-2.5}$ to 10^{-2} erg/cm^2-s. As with AE, electrons show a similar trend versus Dst, although they exhibit a slight increase for positive Dst—possibly exhibiting species-dependent behavior during for example Storm Sudden Commencements (SSCs). For Kp (bottom Panel), the trend is similar to AE, with Kp=3 roughly corresponding to AE=200 nT. The trends were similar for 1 hour average AE (not shown).

4.4 Summary and discussion

My findings demonstrate that isotropic $\geq$50 keV electron and proton precipitation in the poleward proximity to isotropy boundaries can be geophysically significant in connecting the magnetosphere and ionosphere. As shown in Figs. 4.11,12 this source typically accounts for 50% to 100% of the total $\geq$50 keV nightside proton loss-cone precipitation and 10-20% of electron precipitation between $\pm$55° and $\pm$80° latitude, with proton IEflux between 10^{-2} to 10^{0} erg/cm^2-s, extending 2° to 6° in latitude, dependent on MLT and activity. This results in typical hemisphere-integrated PS2RC power on the order of 100s of MW across the nightside, but in some events, exceeded 10 GW. This can be compared to the power from <30 keV particles in broadband and diffuse aurora reported by (Newell et al., 2009a), which are also on the order of 10s of GW under active conditions, suggesting that energetic precipitation in the PS2RC may at times represent a large and unreported fraction of the overall power

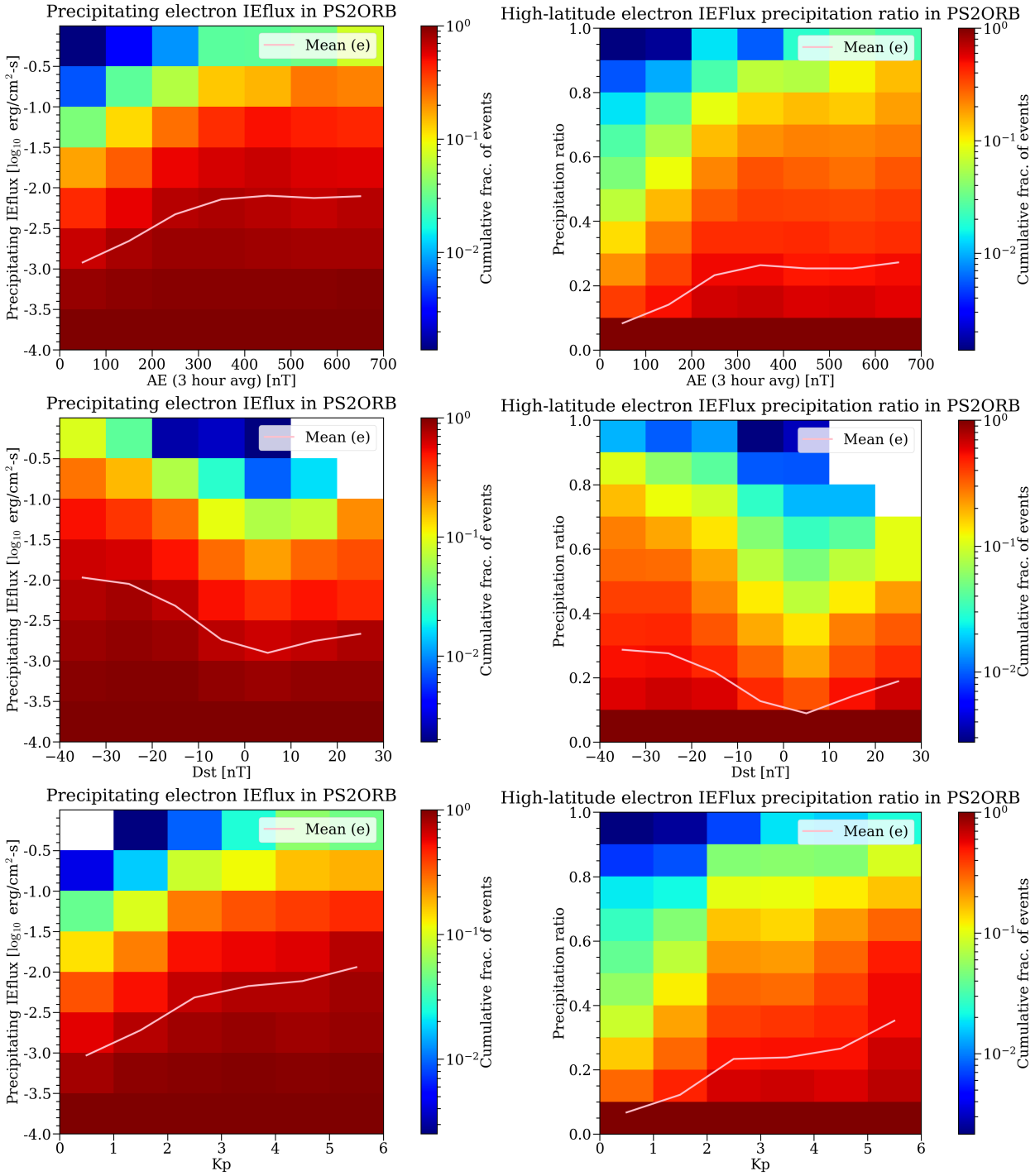

Figure 4.13: Electron/PS2ORB precipitation ratio (left-column) and latitude-averaged integral precipitating energy-fluxes (IEfluxes; right-column) versus the geomagnetic activity indices AE (3-hour average; top), Dst (middle), and Kp (bottom). Quantities are equivalent to those described in Fig. 4.11.

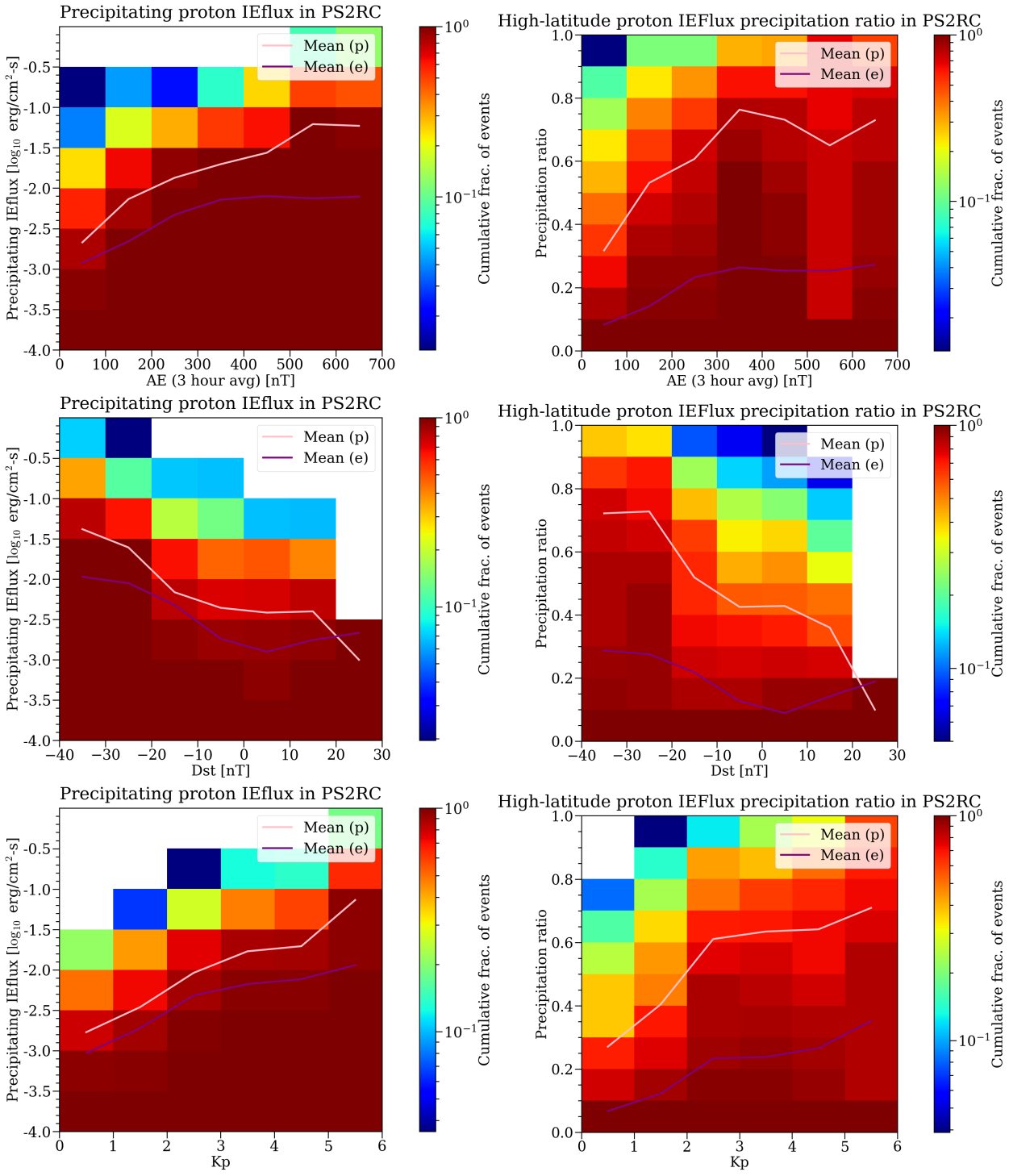

Figure 4.14: Proton/PS2RC precipitation ratio (left-column) and latitude-averaged integral precipitating energy-fluxes (IEfluxes; right-column) versus the geomagnetic activity indices AE (3-hour average; top), Dst (middle), and Kp (bottom). Quantities are equivalent to those described in Fig. 4.12.

input.

The PS2RC and PS2ORB IEflux may connect to a range of dynamic magnetosphere-ionosphere coupling processes as well. For example, in the SAPS ≥50 keV proton precipitation reported by (Artemyev et al., 2024), the PS2RC generated an IEflux of $10^{-1.3}$ erg/cm^2-s, which my statistics show occurs with up to 100% probability of exceedance as AE increases, suggesting such coupling may be commonplace. In addition, the latitudinal range of ≥50 keV PS2RC precipitation presumably encompasses the peak in <30 keV precipitation reported by (Newell et al., 1998) (referred to as the "b2i index"), suggesting that the PS2RC extends this notion to higher energies and total power, as well as for electrons and the equivalent "b2e" index. Application of the ionization rate model in (Fang et al., 2013) to the PS2RC IEflux distribution reveals that a 50 keV to ∼MeV proton spectrum will generally result in ionization enhancements from 80 to 200 km, with the peak occurring between 90 and 120 km, with a rate between 10^2 and 10^4/cm^3-s. This can be related to the conductivity effects of ≥50 keV proton precipitation from EMICs in (Tian et al., 2022), where those authors found that 120 km Pederson conductivity at dusk was increased by a factor of 2-3 for incident power on the order of 10^{-1} erg/cm^2-s—well within the range of PS2RC IEflux, implying this ionization may be significant across the nightside. Further, given that the PS2RC encompasses sub-auroral latitudes, it may fill a niche role in ionization enhancements, since equivalent lower-energy electron and proton precipitation is usually absent equatorward of the auroral zone. I suggest these effects should be included in conductivity models, such as in the recommendation of (Liemohn, 2020) to improve upon the Robinson formula (Robinson et al., 1987), which only incorporates ≤30 keV electrons, and neglects protons.

From the perspective of large-scale magnetospheric evolution, I identify the PS2ORB/PS2RC as an important phenomenological region within the dipole-to-tail transition, being collocated with significant heating, energy conversion, and current sheet thinning during active intervals, such as storms and substorms. I find that its dynamics can be well-captured from low-Earth orbit in J_{prec}/J_{perp} ratios. This is because the equatorial energy flux remains isotropic along the field line, implying fluxes detected from LEO originating in the

PS2ORB/PS2RC are a good proxy of equatorial flux, since they are well-isotropized by FLC scattering. Therefore my results are a good approximation of the evolution of this region in MLAT. The westward and equatorward progression with activity can be thought of as due to the plasma sheet ion heating, resulting in higher ion pressure moving closer to Earth, likely due to plasma sheet injections. This increases the thermal plasma pressure in the near-Earth regions, which acts to reduce the equatorial B_z and hence thin the current sheet (Lu et al., 2018). The equatorial B_z reduction and cross-tail current enhancement near pre-midnight likely cause the current sheet to move closer to Earth, as observed.

Proton IBs are found to have their poleward precipitation extend over a more extensive range of latitudes (3°-6°), while those of electrons tend to be more concentrated (1°-3°). Interestingly, the latitudinal width of the PS2RC region grows significantly in the pre-midnight sector during active times, which, in addition to large-scale current sheet thinning and displacement, could also be related to the evolution and decay of the partial ring current. IBs of both species have the potential to precipitate significant power from $\geq$50 keV particles; however, protons typically provide $\sim$three times as much on average, extending more broadly in latitude, while electrons tend to have substantial precipitation in the immediate poleward vicinity of the IB. I point out, however, that the latitudinal extent of the PS2RC and PS2ORB were computed using geographic extent of polar satellite motion, in part to avoid relying on field-line tracing which can be problematic in slant satellite crossings. Near the flanks, especially near dawn and dusk, such a mapping based on geographic latitude may deviate from the effective magnetic latitude subtended, and resulting in an overestimate of the extent.

CHAPTER 5

Empirical model of energetic electron and proton isotropy boundaries

5.1 Introduction

In this Chapter, I address Questions 5 and 6 in developing an empirical predictive model of 50 keV to ∼3 MeV electron and 50 keV to ∼1 MeV proton isotropy boundaries, based on observable quantities in the solar wind and magnetosphere. Viewed from the perspective of the ionosphere, the isotropy boundary (IB) of a given particle species, energy, and magnetic local time (MLT) is the magnetic latitude poleward of which persistently isotropic pitch-angle distributions ($J_{prec}/J_{perp} \sim 1$ are first observed (Sergeev and Tsyganenko, 1982; Sergeev et al., 1983). Prior works have demonstrated that this isotropization results from pitch-angle scattering in the strong diffusion limit at the distant magnetic equator, either by magnetic field-line curvature (FLC) (Delcourt et al., 1996; Martin et al., 2000; Sergeev et al., 1993, 1983; Wilkins et al., 2023, 2025), or by wave-particle interactions there, such as by electromagnetic ion-cyclotron (EMIC) waves (Ganushkina et al., 2005; Liang et al., 2014; Sergeev et al., 2015b), with FLC scattering tending to be the most common mechanism.

Knowledge of the IB location is important for several reasons. For one, it encodes near-instantaneous information (timescale of single bounce periods) about the conditions in the equatorial magnetosphere, such the state of magnetotail stretching (e.g. radius of curvature due to large-scale currents), as well as the magnetic field strength B_z in the neutral sheet. The energy-latitude dispersion pattern of the IB additionally encodes information about the equatorial field strength gradient ∇B_z, in turn providing a measure of the transition region

where the dipole-like field with mostly closed drift-shells becomes tail-like. In this way, the ≥50 keV proton IB acts as natural separator of the ring current from the proton plasma sheet, and the ≥50 keV electron IB acts a natural separator of the outer radiation belt from the electron plasma sheet. Correspondingly, the latitudes extended poleward of the IB are often associated with significant localized precipitation from isotropic ≥50 keV particles. These energies exceed typical 1-10 keVs from the plasma sheet, and consequently result in significant ionization enhancements across a deeper range of altitudes in the ionosphere than typical auroral phenomena (Newell et al., 1998; Wilkins et al., 2023, 2025). As I show in this work, the ≥50 keV IB location is strongly correlated with both the intensity and latitudinal extent of energetic particle precipitation in these interface regions. Thus, by knowing the IB location as a function of MLT, particle species, and energy as a function of time, models of both the large-scale magnetic field and particle fluxes can be observationally constrained.

Preceding works have aimed to model the IB (or its equivalent equatorial scattering conditions/location) using particle tracing and diffusion simulations in the presence of analytical background field models (e.g. (Tsyganenko, 1989)) or global fluid codes (Birmingham, 1984; Delcourt et al., 1996; Gray and Lee, 1982; Martin et al., 2000; Sergeev and Tsyganenko, 1982; Shi et al., 2024; Young, 2002; Young et al., 2008). These methods have succeeded in providing a baseline theoretical characterization of the expected IB location and energy-dispersion of particles. However, they are all intrinsically limited by the accuracy of the background field knowledge, such as its equatorial field-line mapping and its time variability over a range of spatial scales, as well as the assumptions made about the scattering conditions (e.g. the κ_{cr} parameter). Additionally, simulation-based models can be computationally prohibitive, requiring specialized runs that may require vast computing resource (e.g. (Shi et al., 2024)). Such limitations can be mitigated by instead using direct observations of the IB latitude in ionosphere, which can be used to construct a readily-evaluated empirical model. In turn, this model can be combined with such simulations to constrain the complete picture of large-scale magnetic field and particle flux evolution. Despite this fruitful utility, until recently, large sample size observational IB characteristics have have focused on protons with energies

less than ∼100 keV using the NOAA POES satellites, as well as electrons and protons with energies less than ∼30 keV using DMSP (Dubyagin et al., 2018; Ganushkina et al., 2005; Ilie et al., 2015; Lvova et al., 2005; Newell et al., 1998; Sergeev et al., 1993, 2015a,b, 1983; Shevchenko et al., 2010; Yue et al., 2014). However, as recently shown by (Wilkins et al., 2023, 2025), both electron and proton IBs can be routinely detected at 50 keV to several MeV energies, representing an overlooked and substantial portion of the energy-latitude dispersion and energetic particle precipitation generated within the magnetotail. Thus far, such IBs have only been investigated across the nightside using the simulation approach.

IBs are generated as a result of large-scale processes occurring at the geomagnetic equator. Because of this, it is reasonable to expect that driving from the solar wind, as well as expect magnetospheric state (geomagnetic activity) and dipole tilt to have a potential impact. For example, dayside reconnection resulting from southward IMF B_z results in loading of the magnetotail, which can compresses/enhance the cross-tail current sheet, affecting the radius of curvature and field strength, and triggering particle energization and transport via reconnection. This would result in a change in the IB location mapped to the ionosphere by virtue modifying the minimum particle scattering energy (e.g. as in (Wilkins et al., 2023, 2025)), as well as supplying the initial energization for particles which eventually encounter such field lines. Given the solar wind-magnetosphere connection, I consider a number of observables in the solar wind, such as velocity, density, pressure, and interplanetary magnetic field. It is also reasonable to expect that during periods of elevated magnetospheric activity, e.g. during storms and substorms, the equatorial current systems which control the equatorial field curvature and strength would also be affected, along with the background plasma conditions for wave growth. I therefore also consider several activity indices, including Dst, AE, and Kp.

To motivate my study, I note that of the past works focusing on observational IB characteristics, none have developed an empirical predictive model of the ≥50 keV electron IB. Similarly, empirical models for proton IBs have been limited to ≤120 keV energies—hundreds of keV lower than the upper range appearing in the ring current and plasma sheet. These

lower-energy results include (Newell et al., 1998) who connected the proton IB location with the "b2i" index (latitude of peak < 30keV proton precipitation observed by DMSP) and MLT, establishing that this location often in near vicinity of auroral activity, such as proton aurora. A similar study by (Dubyagin et al., 2018) focused on the 30 keV proton IB modeled using POES during storm and recovery intervals as a function of MLT, sym-H, and solar wind dynamic pressure. These authors showed that a simple functional expression could typically predict the IB to within 2° of latitude error. A more recent and sophisticated approach of modeling the 39 and 115 keV proton IB was performed by (Ma et al., 2022), who applied linear regression to POES data to derive an empirical relationship in terms of MLT, sym-H, AE, solar wind dynamic pressure, and IMF B_z, as well as showed that the energy-latitude was typically negative (compatible with monotonic equatorial B_z gradients). These authors found similar results to (Dubyagin et al., 2018), as well as provided a first-cut model of the energy-latitude dispersion of the 39-115 keV IB.

In this work, I perform a similar analysis to (Ma et al., 2022) in establishing an empirical expression for the ≥50 keV electron and proton IB location as a function energy, MLT, and other observable drivers. An example of their 30-80 keV model data and overplotted model predictions are shown in Fig. 5.1. I make similar use of data from the Electron Losses and Fields Investigation (ELFIN) CubeSat mission from 2019-2022, which collected electron and proton pitch-angle spectra from 50 keV to several MeV, in polar LEO orbit. This dataset provides superior energy and pitch-angle resolution to platforms like POES, allowing for further characterization of the IB.

To characterize the relative significance of each observable in predicting IB locations, I made use of the information-theoretic metric known as mutual information (MI) (Camporeale et al., 2018), based on the concept of Shannon Entropy (Saraiva, 2023; Shannon, 1948). The MI (measured in bits) between two stochastic observables $\hat{x}$ and $\hat{y}$ binned into discrete distributions $\mathcal{X}$ and $\mathcal{Y}$ is given by:

$$MI(\hat{x},\hat{y}) = \sum_{x_i\in\mathcal{X},y_i\in\mathcal{Y}} p(x_i,y_i)\log_2\frac{p(x_i,y_i)}{p(x_i)p(y_i)} = H(\hat{x}) + H(\hat{y}) - H(\hat{x},\hat{y}) \tag{5.1}$$

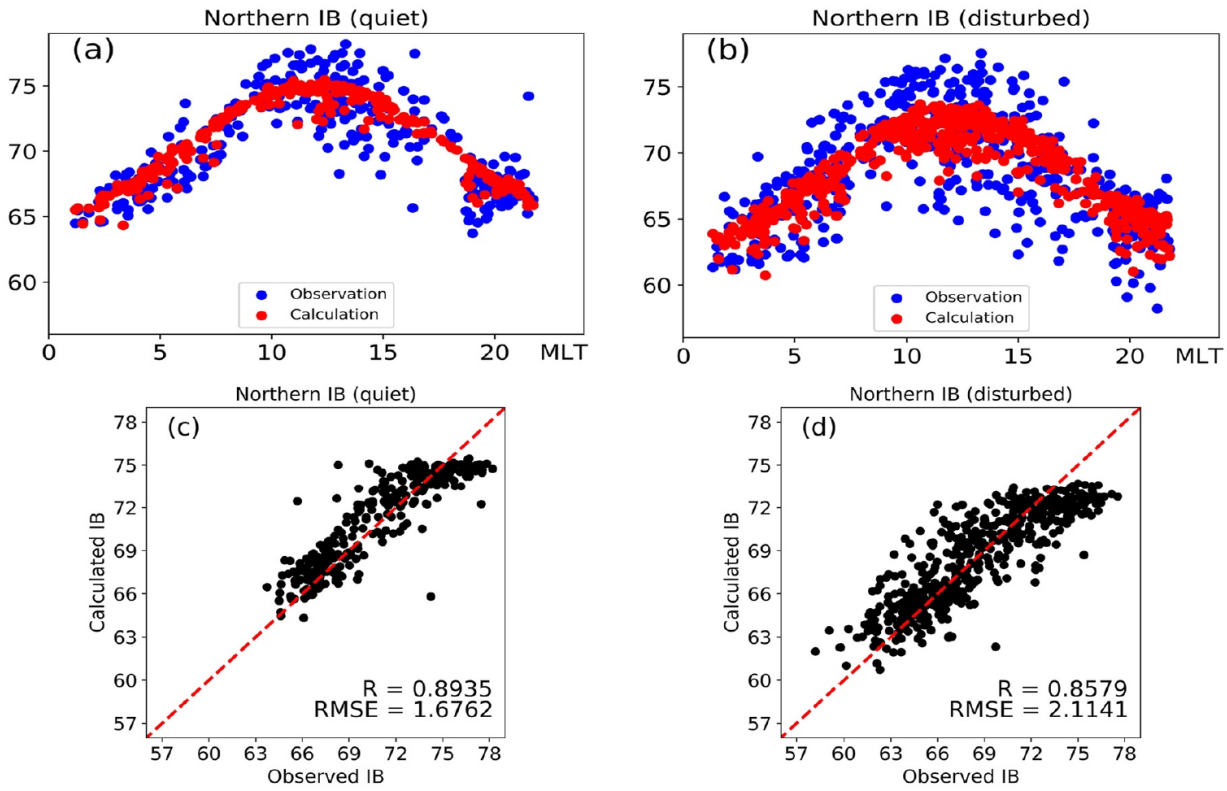

Figure 5.1: Example empirical predictive model for 30-80 keV protons constructed using POES observations. Taken from Fig. 4 of (Ma et al., 2022).

where $p(x_i, y_i)$ is the joint (covariant) probability of occurrence between two simultaneous observations $\hat{x}_i$ and $\hat{y}_i$, $p(x_i)$ and $p(y_i)$ are the independent observable probabilities, and H is the Shannon entropy. The strength of this method is that it does not require the presumption of a specific functional form of probability distribution (e.g. Gaussian), and can handle nonlinear forms that may confound a linear correlation analysis. This approach has recently begun to see use in the analysis of magnetospheric physics, for example in determining the coupling strength and timescales between radiation belt flux levels and solar wind drivers (Wing et al., 2022), and in connecting ionospheric currents to terrestrial radio emissions (Fogg et al., 2024).

5.2 Methods

5.2.1 Dataset

As mentioned above, the isotropy boundary events in this study were based on ≥50 keV differential-directional particle data from the ELFIN CubeSat mission (Angelopoulos et al., 2020) in polar LEO orbit (∼450 km) orbit, spanning 2019-2022. The data were binned into 16 energy channels and 16 spin sectors, spinning nominally with a period of 2.8s nominally containing parallel and perpendicular components to the magnetic field. Each data collection spanned 6-7 minutes, typically covering a single hemisphere from 55°-80° (absolute) IGRF latitude, including the ring current, outer radiation belt, plasma sheet, and a portion of the polar cap. The methodology for identifying IBs is taken from (Wilkins et al., 2025), which looked for energy-latitude dispersion patterns satisfying the following criteria: (1) an energy-dependent poleward transition from anisotropic to persistent isotropic pitch-angle distributions ($J_{prec}/J_{perp} \sim 1$); (2) at least three energy channels present in the dispersion pattern; and (3) all energy channels in the dispersion pattern eventually reaching simultaneous isotropy at some finite latitude. This resulted in 2132 electron IB dispersion patterns and 272 proton IB dispersion patterns, forming the magnetic latitude target features for model fitting. I note that proton data was only collected near the end of the mission, resulting in

many more electron events than protons.

The absolute magnetic latitude (MLAT) of each energy channel in the IB dispersion pattern is used as the model target. The IB MLATs are computed using the IGRF field model (Alken et al., 2021) under the assumption of a dipole-fit to the equatorial field-line trace through the instantaneous spacecraft location. Figure 5.2 shows the scatter of electron IBs (top) and proton IBs (bottom) as a function of energy and MLT, along with the mean value in each MLT bin. The marker size is scaled linearly with each energy channel in order to showcase the energy-latitude dispersion evident in the data. "Bullseye" events correspond to the case of very sharp energy-latitude dispersion (isotropization over the spatial scale of less than 1 spin period), while "teardrop" events correspond to negative energy-latitude dispersion patterns resulting from scattering by FLC in the presence of a monotonic radial B_z gradient. Events which break from these categories are indicative of mesoscale features, such as wave-particle interactions acting over a specific energy range, or localized B_z extrema affecting the FLC scattering profile (e.g. positive dispersion).

To construct the model, I made use of solar wind input observables contained in the OMNI database (Papitashvili et al., 2014). The dataset was provided at 5-minute and hourly average cadence, including solar wind velocity (V_{sw}), density (n_{sw}), dynamic pressure (P_{dyn}), as well as interplanetary electric field (E_{sw}) and magnetic field (IMF) magnitude and components (B; $B_{z,gsm}$; $B_{y,gsm}$), as well as the IMF clock angle (θ_{imf}). Magnetic local time (MLT) and dipole tilt (relative to the ecliptic) were evaluated based on the time and location of the ELFIN data. The hourly activity indices Dst (equatorial horizontal magnetic field deflection) and planetary Kp were also provided in the OMNI dataset, while the auroral electrojet (AE) index was provided by the ELFIN database. Additionally, the amount of precipitating energy flux ("IEflux") detected by ELFIN from isotropic $\geq$50 keV particles poleward of the IB were also recorded, using the same procedure in the aforementioned works, which quantified precipitating power in the plasma sheet-to-outer radiation belt (PS2ORB) region for electrons, and plasma sheet-to-ring current (PS2RC) region for protons, respectively.

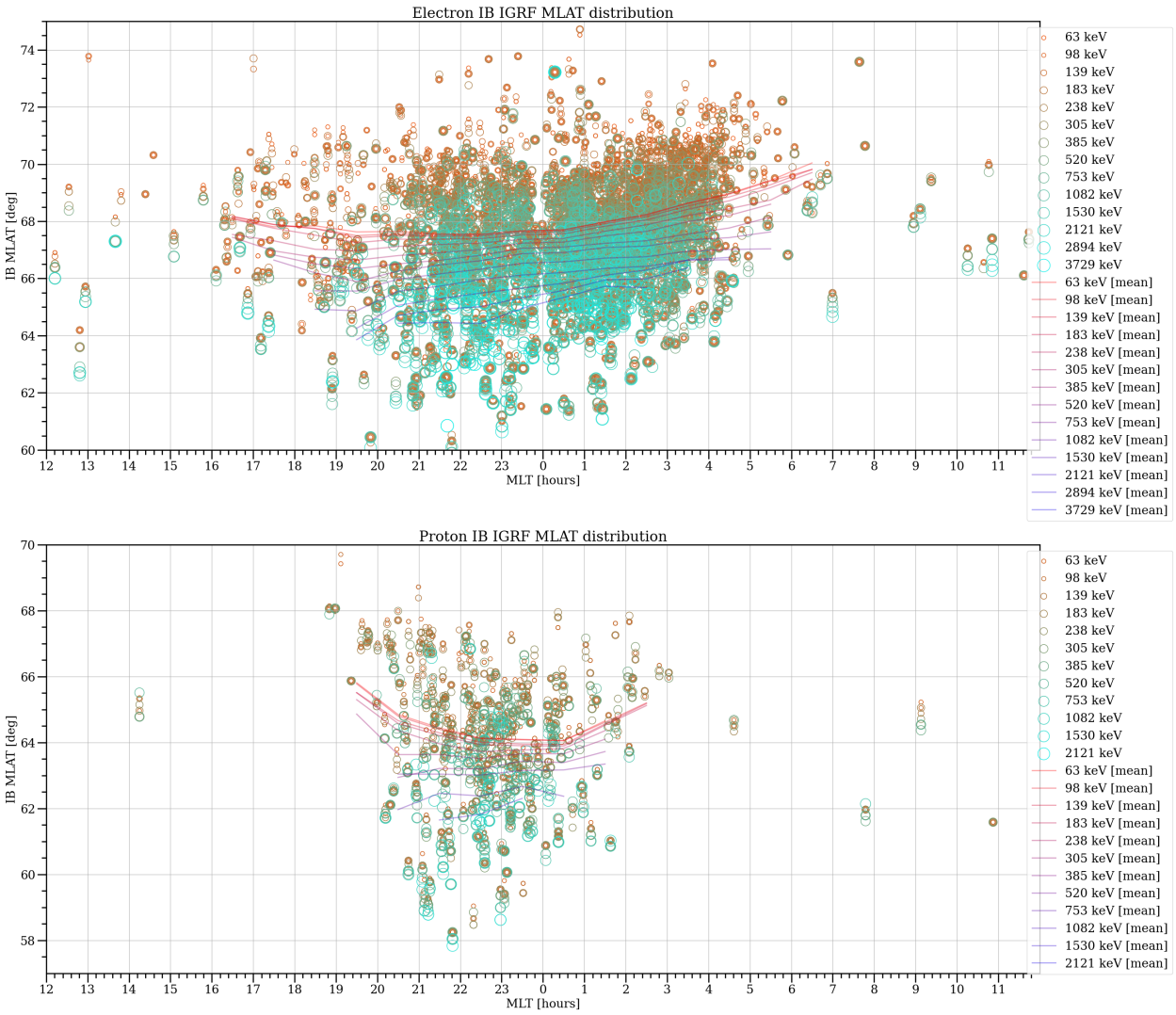

Figure 5.2: MLT scatter plot of ELFIN electron IB events (top) and proton IB events (bottom) in each energy channel. The radius of the circular markers is scaled linearly with the energy channel, allowing for identification of energy-latitude dispersion patterns within the same event. Note: the electron IB scale is at higher latitude than for protons.

5.2.2 Mutual information analysis

As mentioned in the introduction, I made use of Mutual Information (MI) in performing a ranking of the observables predicting the IB location. MI values inherently depend on the underlying binning scheme, and can vary appreciably for even the same inputs when the range and number of bins are changed. In order to normalize this effect, the data were binned self-consistently using a variant of the Sturges class interval criterion (Sturges, 1926), with the number of bins in each case taken to be $N_{bins} = 1 + \text{round}(\log_2 N_{IB,Echan,s})$, where $N_{IB,Echan}$ is the number of IB events in the particular energy channel and species of interest (e.g., 63 keV electrons). Bin sizes were chosen accordingly to span the minimum to maximum values in the sampling interval.

The theoretical MI between two uncorrelated random signals is zero by virtue of the property that $p(\hat{x}, \hat{y}) = p(\hat{x})p(\hat{y})$. However, in reality, finite sampling will lead to the appearance of non-zero MI values due to random correlation. To account for this effect, I introduce a random Gaussian signal into the MI analysis, using it as a baseline "signal-to-noise" level. This level can be interpreted as the MI below which an observable can no longer predict the IB to any degree better than guessing within the mean plus/minus the standard deviation. Above this level, the MI can be interpreted to reduce the variance in estimating the IB compared to a Gaussian predictor. In this case, the particular model variance depends on the choice of prediction function, which I quantify in the analysis.

5.2.3 Empirical model construction

I construct the empirical model as an explicit sum over a set of basis terms, derived from the observables forming a vector $\mathbf{v}$ at the time of and preceding the IB observation. That is,

$$IB_{E,s}(\mathbf{v}) = \sum_i f_i(v_i; a_i, b_i, ...)_{E,s} \tag{5.2}$$

where $IB_{E,s}$ is the IB for a particular energy (E) and species (s), f_i is a to-be-determined function of the i^{th} observable v_i, with tunable model coefficients $a_i, b_i, ...$ to be fit by the

observations. For the sake of practicality, I aimed to retain the fewest terms what would allow for IB variation in three (semi-independent) categories: (1) magnetospheric geometry factors (e.g. MLT, dipole tilt, and IMF clock angle); (2) magnetospheric state and activity (e.g. Dst, AE, Kp); and (3) direct solar wind driving (e.g. IMF B_z, P_{dyn}). I additionally note that the magnetosphere is known to exhibit hysteresis (e.g. the same Dst value may represent a different magnetospheric state depending on whether it is in storm main phase or recovery), requiring an additional term to encode this information. On this basis, my model requires at least four energy-dependent parameters to describe the IB location at any time.

To select which set of observable parameters v_i appear in the model, the MI values between the IB and each observable are compared, with the highest values in each of the three above categories nominally being retained, except in cases of comparable MI, where the basis was chosen to favor terms which have recognizable physical interpretations. To determine the functional form of each term in the model, I inspected the 2D probability distributions for the curve which approximates the most frequently occurring values, along with configurable coefficients to allow for minimization of the overall model error. The coefficients associated with each term were found using multi-variate non-linear least squares evaluated over the set of IB events. A Gaussian kernel density estimator (KDE) was used to account for non-uniform sampling in MLT in the fitting procedure. The model coefficients and standard error are reported in Results, along with the distribution of error for selected energy channels.

5.3 Results

5.3.1 Probability distributions and MI analysis

As part of the MI analysis, I computed the 2D probability distributions $p(\hat{x}, \hat{y})$, where $\hat{x}$ is the IB MLAT for a given species and energy, and $\hat{y}$ is the particular observable v_i in Eqn. 5.2. Examples of the subset of 63 keV probability distributions are shown in Fig. 5.3 for

electrons and Fig. 5.4 for protons, with

$$v_i \in \{AE_{1hr,avg}, |\mathbf{B}|_{imf}, B_{y,imf}, B_{z,imf}, Dst, Dst_{min,8hr}, IEflux_{IB}, \theta_{clk}, P_{dyn}, rand, \theta_{dip}, V_{sw}\}$$

where $Dst_{min,8hr}$ is the minimum Dst value encountered in the 8 hours preceding the IB observation (e.g. extrema during storm main phase), $IEflux_{IB}$ is latitude-averaged energy-integrated $\geq$50 keV isotropic precipitating energy flux in the region between the IB and inner edge of the plasma sheet, θ_{clk} is the IMF clock angle, $rand$ is a random Gaussian variable with the same mean and standard deviation as the IB, and θ_{dip} is the dipole tilt at the time of collection (angle between the GSM- and SM-z axes).

For 63 keV electrons, it can be seen that many types of distributions are possible, depending on the particular observable, with IMF By and the random Gaussian providing the least correlation, with many of the other parameters providing linear-like correlation. Interestingly Dst and its 8 hour minimum provide similar, yet independent trends. The best correlation is also interestingly with the amount of precipitation (IEflux) from isotropic particles, demonstrating that knowledge of the IB latitude is highly significant in predicting precipitation from $\geq$50 keV electrons on the high-latitude nightside. The distribution versus IMF clock angle is also interesting, showing clearly symmetric distributions about northward IMF, with the most extreme low-latitude IB events occurring near southward IMF Bz. Such features are similarly present in the higher-energy distributions (not shown).

For 63 keV protons, the trends are similar to electrons, with precipitation and Dst again being strongly correlated. In this case, IMF Bz, dynamic pressure, and AE also take on a comparatively more pronounced role. I note these observables, as they are later used in my prototype empirical modeling function.

From the distributions, I computed the MI values between the IB and each observable as a function of energy. Fig. 5.5 Top shows the results for electrons, and 5.5 Bottom for protons. As mentioned previously, each MI value was normalized relative to the result of computing the MI of the IB with a random Gaussian, with the total number of events in each

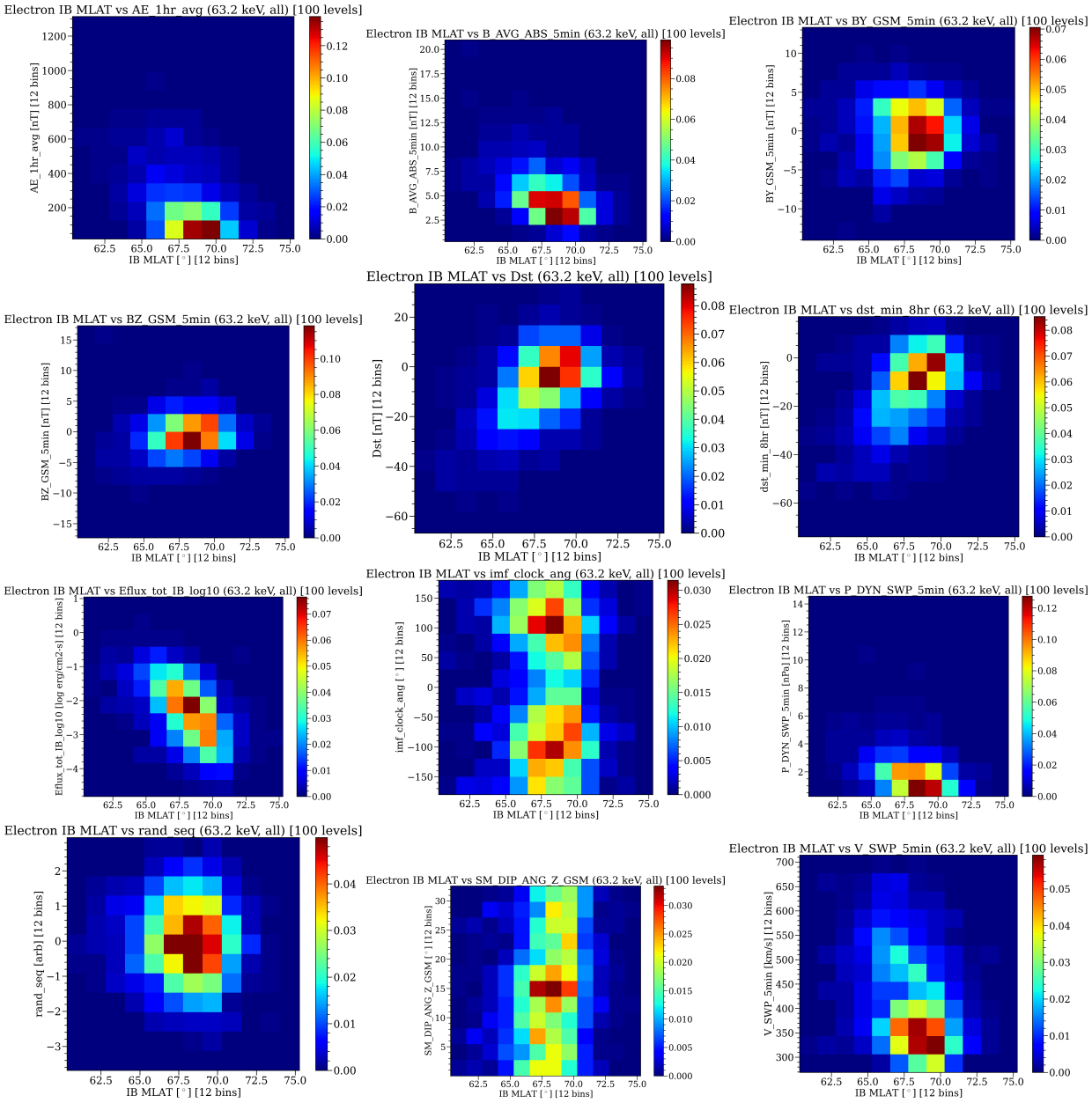

Figure 5.3: Electron IB probability distributions versus observables for the 63 keV energy channel. (See Methods for descriptions.)

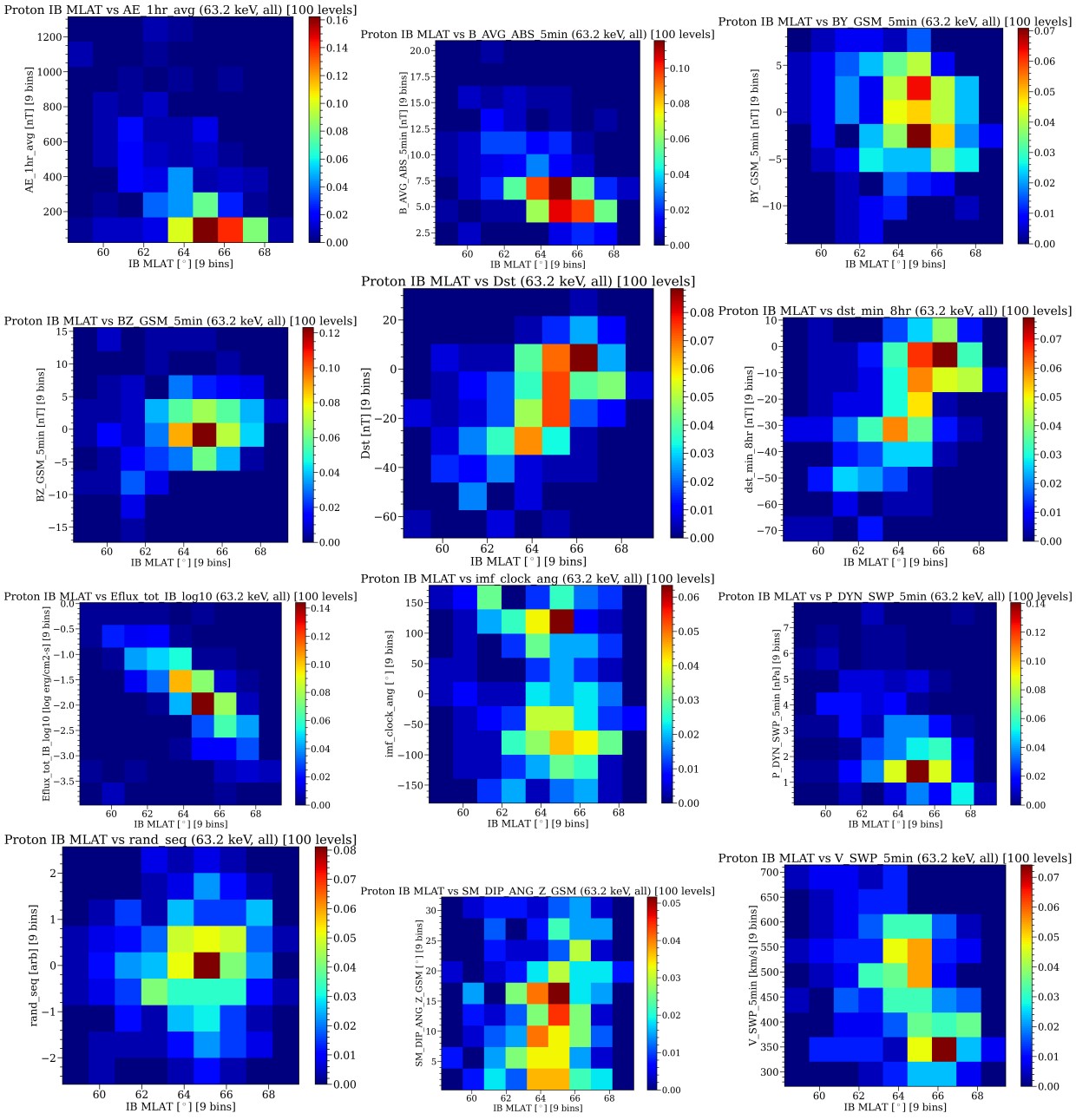

Figure 5.4: Proton IB probability distributions versus observables for the 63 keV energy channel. (See Methods for descriptions.)

energy channel plotted as red circles. As can be expected by virtue of increased sample sizes, the energy channels with more events tend to have more information encoded than lower sampling cases. In each case, the IB model fit result (described subsequently) is previewed as the dashed mustard line for comparison with the individual observables. Additionally, I plot the IB MI with IEflux (total isotropic precipitation of each respective particle species) as a red dashed line, although this is not a quantity that can be easily observed outside of real-time in-situ flux measurements in orbit, or by ground observations by scatter radar and auroral imaging. For the sake of practicality, I do not use this observable in the empirical model, but retain it in the MI analysis in order to demonstrate how strongly correlated the precipitation intensity is with IB location.

For electrons, Fig. 5.5 Top shows that of standard solar wind and activity indices, the best predictors (highest MI value averaged over all energies) tend to be Dst and its 8 hour minimum, as well as AE. None of the instantaneous solar wind drivers tend to encode significant more information than another, although information is certainly lost if at least one of them is not included in the model. Interestingly, solar wind density is by far the worst predictor, while dynamic pressure and velocity tend to nonetheless provide information content. Around 4 MeV, all of the MI values drop to the noise level, suggesting too few samples to fit a model.

For protons, Fig. 5.5 Bottom shows the equivalent MI values versus energy. The trends are similar to electrons, with dynamic pressure remaining a middle-of-the-pack solar wind observable for both electrons and protons. As with electrons, its precipitation is again observed to be the best correlated quantity. In this case, given the much lower total sample sizes, the noise level is reached around 1.5 MeV.

5.3.2 Empirical model: functional form and estimation uncertainties

Based on the preceding MI analysis, I elected a basis set of observables consisting of MLT, Dst, Dst (8hr min), and dynamic pressure for both electrons and protons. The functional form was found by inspecting the probability distributions visually and determining the

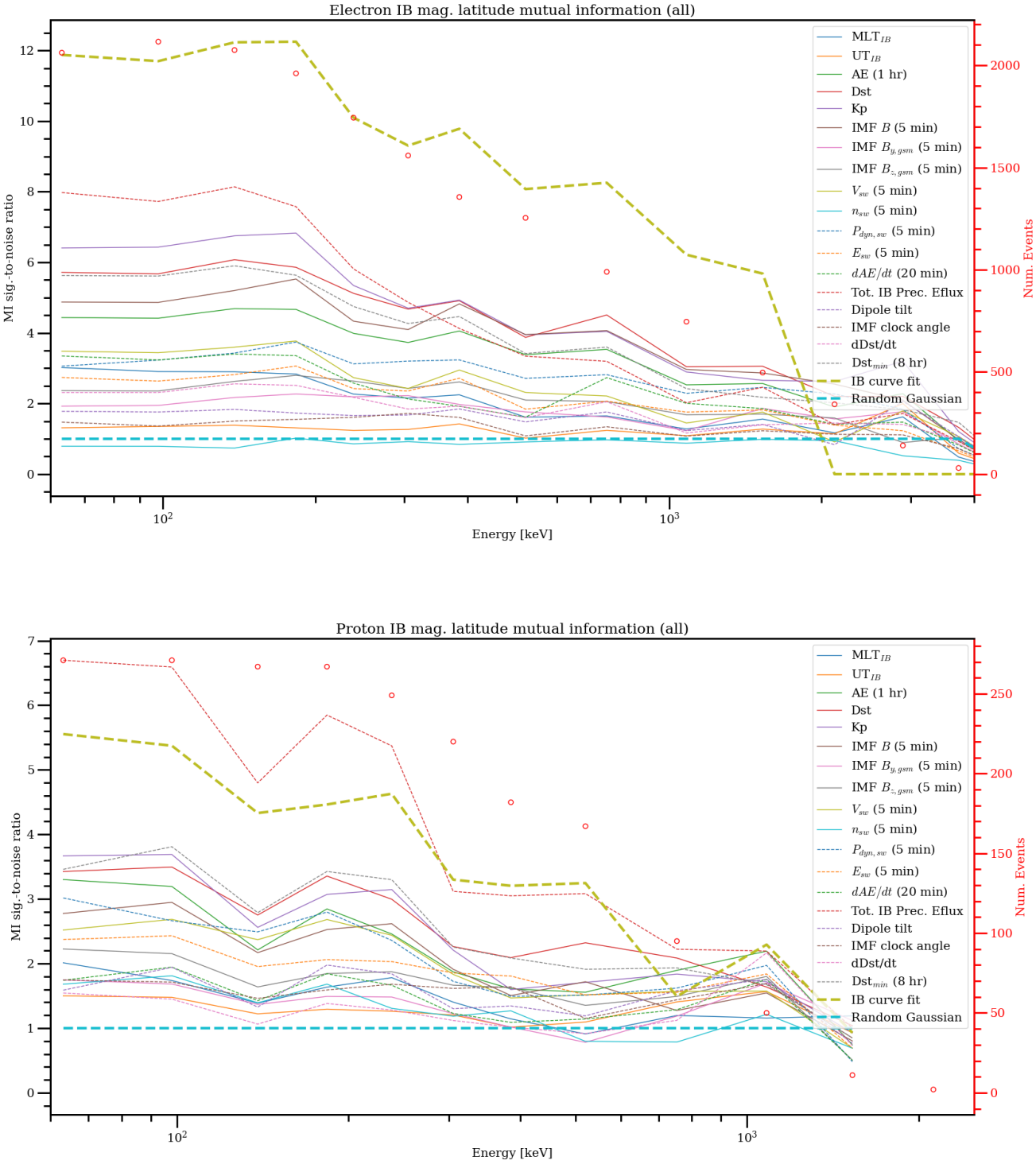

Figure 5.5: Mutual information (MI) analysis between electron IBs (top) and proton IBs (bottom) versus selected observables and energy channels. The MI values are normalized relative to a random Gaussian variable. Red dots indicate the number of events used to form the probability distributions used in the analysis.

curve that reproduces the most probable values at each latitude and energy. The prototype empirical model function (described in Eqn. 5.2) is given by:

$$IB_{E,s}(\mathbf{v}) = a + b \cdot \cos(\pi/12 \cdot MLT + c) + d \cdot AE_{1hr} + e \cdot Dst + f \cdot Dst_{min,8hr} + g \cdot P_{dyn,sw} \quad (5.3)$$

where the coefficients $a, b, ..., g$ were found by non-linear least squares in each energy channel.

Figure 5.6 shows an example scatter plot and mean of 63 keV electrons (top) and protons (middle), along with the histogram of model errors (bottom left and right). As can be seen, the mean curves are in excellent agreement, with many of the scatter points is close proximity to model points. In both cases, there is slight disagreement between the model and flank MLTs, likely owing to the omission of additional MLT-dependent model terms, such as preferential current-sheet thinning and other magnetic field variations. The most typical error is observed to be under 1° in latitude, with a standard deviation of ∼1.6°. The resulting MI from these model functions can be seen in Fig. 5.5 as the mustard dashed line, which significantly exceeds the individual MI values of the observables used to construct it. I note also that there are a number of high-latitude IBs that the model does a poor job of fitting. By manual inspection, I found many of these cases are in the vicinity of AE activations that may represent the onset of substorm phases, likely requiring a different set of observables or functional form to encode.

Lastly, Tables 5.1 and 5.2 summarize the fit coefficients and model errors (σ), revealing that 50 keV to ∼3 MeV electron IBs can be predicted with errors between 1.2°-1.6°, and 50 keV to ∼1.5 MeV protons with errors between 1.3°-1.6°. The fit coefficients additionally provide physical insight into the IBs, providing a relative magnitude and direction of much the IB location varies with each observable. As can be seen, the IBs tend to shift toward lower latitudes with AE, -Dst, and dynamic pressure—consistent with past model findings for protons at lower energies.

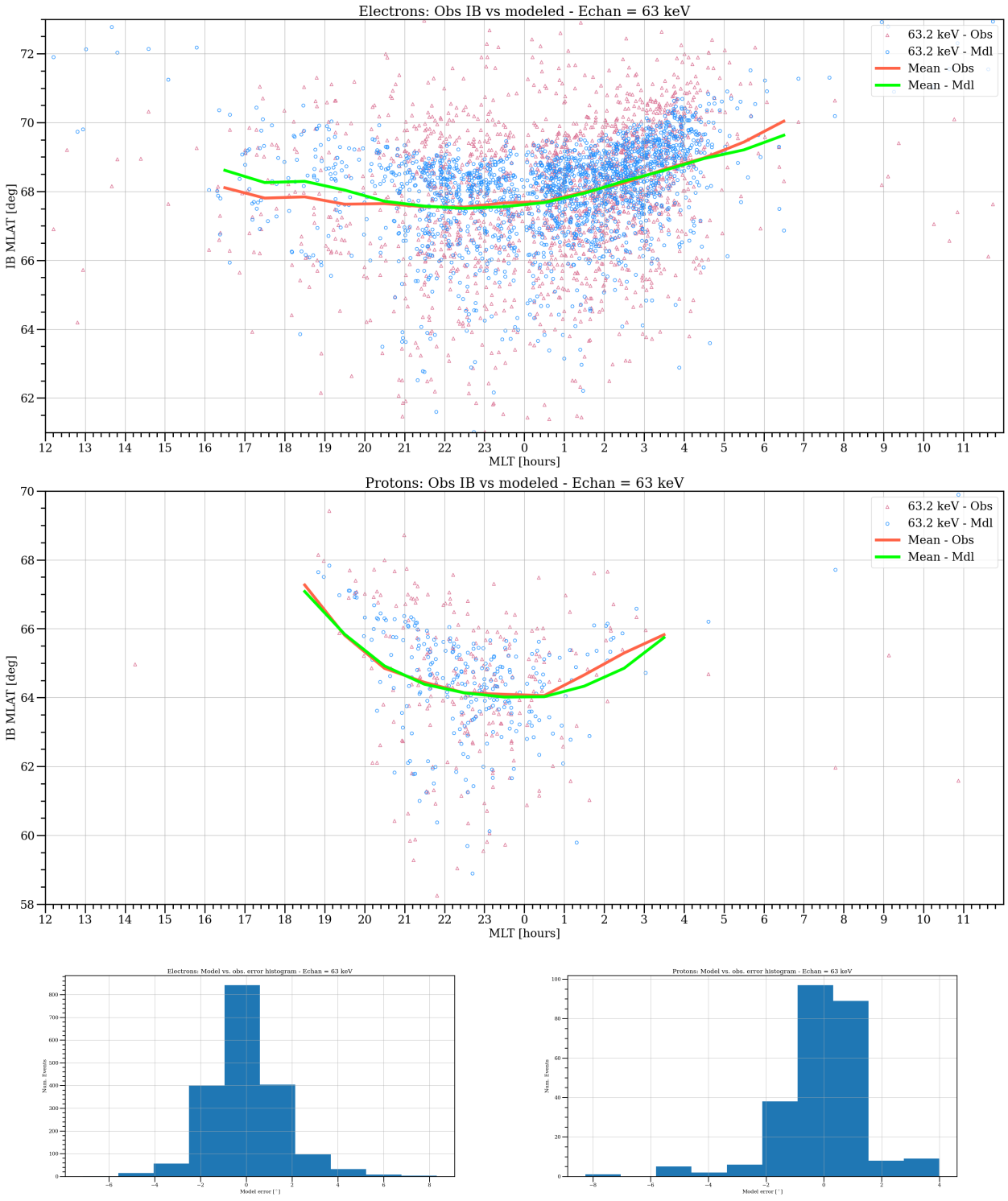

Figure 5.6: Comparison between observed and modeled 63 keV electron IBs (top) and proton IBs (middle), along with their respective error histograms (bottom left, right).

Energy [keV]	a [°]	b [°]	c [rad]	d [°/nT]	e [°/nT]	f [°/nT]	g [°/nPa]	σ [°]
63	7.16e+01	2.26e+00	3.25e+00	-9.06e-04	8.648e-02	-1.47e-02	-6.32e-01	1.57
98	7.14e+01	2.109e+00	3.29e+00	-9.00e-04	8.61e-02	-1.49e-02	-6.28e-01	1.57
139	7.13e+01	2.058e+00	3.28e+00	-8.11e-04	8.44e-02	-1.35e-02	-6.42e-01	1.57
183	7.12e+01	-2.02e+00	1.60e-01	-6.52e-04	8.70e-02	-1.76e-02	-6.38e-01	1.56
238	7.09e+01	-1.88e+00	1.75e-01	-7.75e-04	8.10e-02	-1.52e-02	-6.26e-01	1.50
305	7.06e+01	-1.73e+00	2.35e-01	-8.90e-04	8.18e-02	-1.83e-02	-6.26e-01	1.44
385	7.01e+01	-1.46e+00	2.40e-01	-9.46e-04	8.70e-02	-2.70e-02	-5.88e-01	1.39
521	6.96e+01	-1.12e+00	3.59e-01	-1.05e-03	8.56e-02	-2.73e-02	-5.87e-01	1.32
753	6.94e+01	-1.16e+00	3.58e-01	-1.32e-03	9.69e-02	-3.73e-02	-5.66e-01	1.22
1082	6.88e+01	-8.44e-01	5.35e-01	-9.81e-04	9.46e-02	-3.67e-02	-5.89e-01	1.19
1530	6.88e+01	-1.32e+00	5.10e-01	-7.10e-04	1.00e-01	-4.71e-02	-5.71e-01	1.26
2121	6.84e+01	-1.09e+00	7.57e-01	-5.58e-04	8.82e-02	-3.38e-02	-6.08e-01	1.25
2894	6.86e+01	-1.67e+00	7.33e-01	-1.83e-03	6.40e-02	-2.04e-02	-4.46e-01	1.32

Table 5.1: Electron IB empirical model coefficients and error versus energy channel for the functional form $IB_E(\mathbf{v}) = a + b \cdot \cos(\pi/12 \cdot MLT + c) + d \cdot AE_{1hr} + e \cdot Dst + f \cdot Dst_{min,8hr} + g \cdot P_{dyn,sw}$. The standard error between model and overall dataset is given by σ.

Energy [keV]	a [°]	b [°]	c [rad]	d [°/nT]	e [°/nT]	f [°/nT]	g [°/nPa]	σ [°]
63	6.97e+01	-3.62e+00	6.37e+00	-9.22e-04	4.65e-02	1.85e-03	-5.35e-01	1.55
98	6.97e+01	3.60e+00	3.25e+00	-9.90e-04	4.60e-02	1.04e-03	-5.41e-01	1.53
139	6.92e+01	3.28e+00	3.19e+00	-7.87e-04	4.63e-02	5.60e-03	-5.22e-01	1.52
183	6.978e+01	-3.94e+00	6.42e+00	-6.58e-04	4.67e-02	3.69e-03	-5.17e-01	1.60
238	7.020e+01	4.40e+00	3.34e+00	-7.34e-04	4.87e-02	2.88e-03	-5.02e-01	1.61
305	6.94e+01	3.56e+00	3.42e+00	-6.30e-04	3.98e-02	9.19e-03	-5.37e-01	1.56
385	6.72e+01	1.75e+00	3.31e+00	-3.27e-04	6.65e-02	-1.61e-02	-5.21e-01	1.27
521	6.78e+01	2.48+00	3.32e+00	-3.80e-04	5.81e-02	-7.77e-03	-5.17e-01	1.31
753	6.21e+01	3.44e+00	4.72e-01	-2.58e-04	4.20e-02	9.37e-03	-5.13e-01	1.56
1082	6.23e+01	2.95e+00	3.22e-01	5.75e-04	6.16e-02	-4.35e-03	-5.85e-01	1.28

Table 5.2: Proton IB empirical model coefficients and error versus energy channel for the functional form $IB_E(\mathbf{v}) = a + b \cdot \cos(\pi/12 \cdot MLT + c) + d \cdot AE_{1hr} + e \cdot Dst + f \cdot Dst_{min,8hr} + g \cdot P_{dyn,sw}$. The standard error between model and overall dataset is given by σ.

5.4 Summary and discussion

In this work I combined ELFIN IB observations with OMNI solar wind data to create an empirical model of 50 keV to ∼3 MeV electron IBs and 50 keV to ∼1.5 MeV proton IBs on the nightside magnetosphere. The results were in qualitative results of past proton IB modeling studies using POES at <120 keV energies, such as (Dubyagin et al., 2018) and (Ma et al., 2022), with comparable or better performance (reduced relative error) at most energies.

Beyond serving a useful tool for determining the IB location at any time, the coefficients in Tables 1 and 2 reveal insight into the underlying mechanism of IB formation and its evolution in time. In particular, the coefficients listed under a represent a baseline latitude of the IB across all conditions experienced in the dataset. This quantity is monotonically decreasing in energy for all channels, consistent with an FLC scattering explanation in the presence of a monotonically decreasing B_z or R_c. The trend is similar for protons, although not completely monotonic, suggesting that mesoscale features were more common in these IBs. Surprisingly, the coefficient f attached to 8 hour Dst minimum is negative for all species and energies, while e (attached to latest Dst) is positive. This suggests that recent buildup of the ring current (or related current systems) may have a suppressive hysteresis effect on later Dst values, e.g. during storm recovery.

In forming the probability distributions of IB latitude versus IEflux (≥50 keV particle precipitation poleward of the IB), I found that in addition to the IB being in close vicinity to the peak of localized precipitation (i.e. the b2i index of (Newell et al., 1998)), the total precipitation intensity also directly correlates with the IB latitude. This holds for electron precipitation, suggesting an equivalent "b2e" interpretation. Combined, these properties demonstrate that knowledge of the IB location is an important tool in constraining high-latitude ≥50 keV precipitation.

Concerning limitations and future work, I note that the particular functional form provided here is not unique, nor necessarily the best possible expression. Future models, such

as those based on neural networks and other machine learning technique may provide better prediction power (albeit at the cost of potential difficulties understanding the physical intuition behind the coefficients). The model additionally did not consider explicit time-lag or covariance reduction between the observables, which are known to exist in solar wind quantities. Future work may benefit from the application of more advanced causality analysis techniques.

Additionally, as magnetic field models are continually being improved, an independent validation or comparison of this work would likely prove fruitful. It would be interesting to compare the IB latitudes computed from this empirical model with predictions based on κ_{cr}^2 using more sophisticated data-assimilated field-models, such as those employing techniques described by (Brito and Morley, 2017), with applications to recent Tsyganenko-Sitnov codes (e.g., TS04, TS07; (Sitnov et al., 2008; Tsyganenko and Andreeva, 2015)). Such models may provide complementary information to those of direct IB observations, and could perhaps be combined to synthesize higher fidelity predictions under quiet and active conditions.

I lastly note the outlier population of events which the model was unable to fit, which occurred at any latitude, but mostly at very high or very low latitude. Such events demonstrate poor MI with all observables I tried (not shown), although manual inspection has suggested such cases may occur in the vicinity of substorm phase transitions. The models of (Ma et al., 2022) and (Dubyagin et al., 2018) also encountered similar outliers that had yet to be explained, suggesting a potential avenue for later investigation. Further analysis using an onset event database may be beneficial in addressing these cases.

CHAPTER 6

Summary and future work

6.1 Thesis summary

This dissertation expounded on the characteristics of energetic ($\geq$50 keV) electron and proton isotropy boundaries in Earth's magnetosphere, extending prior studies which considered lower-energy particle populations. The isotropy boundary marked the location in the ionosphere where particle pitch-angle spectra transitioned abruptly from anisotropic isotropic fluxes, corresponding to a transition from adiabatic to non-adiabatic motion in the distant field-line mapped equatorial magnetosphere. The IBs were identified using data from the ELFIN CubeSat mission in polar LEO orbit, inspecting each particle detector energy channel for the sudden appearance of a sustained pitch-angle isotropy ratio $R_I = J_{prev}/J_{perp} \sim 1$. Their behavior during "quiet" and "active" geomagnetic intervals was assessed by separating the dataset into $AE < 200$ nT and $AE > 200$ nT (approximately the median AE).

In Chapter 3, I determined the IB latitude distribution versus MLT, energy, and geomagnetic activity at all local times for electrons, and on the nightside for protons. The range of IB latitudes was used to determine which regions of the magnetosphere may be affected by IB formation. The MLT variations of the IB with geomagnetic activity were examined and compared with expectations from current-sheet thinning. The differential energy-latitude dispersion patterns were used to infer the most likely source of particle isotropization, along with the relative occurrence rates and mesoscale nature of each.

In Chapter 4, I investigated the distribution of latitude-averaged energy-integral precipitating energy flux (IEflux) from isotropic $\geq$50 keV electrons and protons poleward of their respective IB. The proximity of intense precipitation to the close poleward vicinity of IBs

was explored, extending the notion of the "b2i" index to a finite latitudinal extent between the plasma sheet and outer radiation belt for electrons (PSORB), and ring current for protons (PS2ORB). The geomagnetic activity-dependence of the precipitation was compared with that of lower-energy (<30 keV) auroral diffuse and broadband auroral power inputs. The ability of the IB/FLC to generate ionization enhancements from precipitation within the PS2ORB/PS2RC was considered, alongside a case study showing how significant such ionization enhancements can be in increasing ionospheric Pedersen and Hall conductivity. MLT asymmetries in the latitudinal extent of the PS2ORB are at active times were also explored.

In Chapter 5, I derived an empirical predictive model of electron and proton isotropy boundaries. Techniques from information theory such as Shannon entropy were used to determine which observables in the solar wind (e.g. IMF B_z) and magnetosphere (e.g. activity indices like Dst). A basis set of four categories of distinct observables were chosen as a sum over particular functional forms of the basis observable set. Latitudinal errors in the model were assessed, and a noise threshold level was identified. The mutual information theory analysis was also applied to the amount of precipitating fluxes, and found to be a critical joint predictor.

6.2 Key findings and next steps

My thesis aimed to address six fundamental questions, whose answers and potential future lines of investigation are summarized below.

6.2.1 Spatiotemporal distribution and occurrence of IBs

I found that at quiet times, protons were typically 1-2 IGRF L-shells lower than their same-energy electron counterparts. The latitudinal and maximum detected energy in the dispersion pattern were nearly symmetric in MLT; protons were symmetric around 1-2 MLT, while electrons were symmetric around 22-23 MLT. At active times, the distributions shifted dra-

matically toward pre-midnight (∼22 MLT) and up to several degrees lower in IGRF latitude, and the peak detected particle energies in the dispersion pattern increased by ∼500 keV on average. Particle number fluxes at all energies in the IB crossing all generally increased as well, suggesting that the processes which caused the IBs to shift to lower latitudes also generated injections. This strongly suggests that the IB is a proxy of the evolution of large-scale evolution of magnetotail current-sheet thinning, acting as an interface between the inner magnetosphere and the outer region encompassing significant magnetic energy conversion.

The low-latitude evolution of the IB at active times also has significant implications at quiet vs active times. Since the general trend is to move to lower L-shells and pre-midnight MLTs, both the outer radiation belt and ring current can be significantly affected—providing an important energy-dependent constraint on particle lifetimes in these regions. Such effects have very recently begun to see investigation, such as (Artemyev et al., 2025), who found that isotropization associated with the IB does indeed play a crucial role in evolving the outer belt, and by (Cao et al., 2023) for the ring current.

Proton IBs were found to be detectable in 90-100% of satellite passes, suggesting they are always present on the nightside, up to at least ∼500 keV energy. This is consistent with past works which considered lower energy ranges, suggesting that the magnetotail always provides sources of energetic protons to replenish the scattered population. This is consistent with Dungey-type flux transport and tail injections, and further cements the significance of characterizing the IB.

Electron IBs were found to jointly occur up to a maximum of 90% near midnight, dropping below 50% near the flanks, and close to 0% on the dayside. This suggests that the particle transport and energization required for electron IB population may be more transient than for protons. This may be in part to the electron IBs occurring further into the magnetotail where the field strength is weaker, and the field-line curvature varies more frequently in time.

Electron IBs also exhibited a strong preference to appear close to the magnetopause near dawn, resulting in a high ratio of ambiguous/excluded events. It is unclear whether these IBs are of magnetospheric origin, and whether they are correctly field-line mapped

(e.g., erroneous due to slant spacecraft crossings over the poles), or what their generation mechanism is. It would be interesting in the future to model these IBs, to understand the extreme dawn-dusk asymmetry, and whether it is a consequence of preferential eastward electron azimuthal drift motion toward the magnetopause.

For protons, the ELFIN data unfortunately did not cover the dayside or dawn, and therefore the equivalent near-magnetopause variations were not investigated. It would be interesting to extend such observations using future missions at >200 keV energies, as current observing platforms are not well-suited to collecting the necessary data.

6.2.2 IB generation mechanisms and relative occurrence

In assessing the generation mechanism of IBs, I found that both electron and proton IBs primarily exhibit negative energy-latitude dispersion. In particular, each differential energy channel in the dispersion pattern had a 70-80% chance of being negative, with a 20-30% chance of opposite (positive) dispersion being mixed within the typically overall negative dispersion structure. Further, the average slope of the dispersion approached zero as the energies increased. This is consistent with an equatorial FLC scattering mechanism, in which more energetic particles are isotropized closer to Earth, in an increasingly stronger and more dipolar magnetic field configuration. On this basis, I conclude that the overall energy-latitude dispersion structures observed in most IBs are due to equatorial FLC scattering in the presence of approximately monotonic B_z profile.

While the overall structure is typically FLC-based, it was rare to observe a purely negative energy-latitude dispersion pattern. This implies that energy-dependent wave-particle processes or localized reverse ∇B_z gradients tend to occur within the larger overall IB crossing. It would be interesting to know specifically which processes these represent, what the relative occurrence of each is, and whether they result in a feedback process to self-evolve the IB back toward negative (quiescent magnetotail) dispersion. This can potentially be investigated using modeling, although serendipitous equatorial conjunctions may be necessary to develop sufficient sampling statistics, akin to (Artemyev et al., 2023).

6.2.3 Distribution of ≥50 keV poleward particle precipitation

I found that both electron and proton IBs can be associated with significant energetic (≥50 keV) particle precipitation in their immediate poleward vicinity, at times exceeding 1 erg/cm^2-s in energy-integral energy flux. I further identified that the bulk of this precipitation occurs over the range of latitudes between the IB and inner edge of the plasma sheet. Given the very high observational occurrence of both electron and proton IBs, and that the particles are always isotropic there (i.e., filled loss-cones), I conclude that these latitudinal ranges represent a curvature-dominated transition region of electron precipitation between the outer radiation belt and plasma sheet inner edge (the PS2ORB interface), and proton precipitation between the outer portion of the ring current and plasma sheet inner edge (the PS2RC interface).

I discovered that the latitudinal extent of these regions depends dramatically on MLT, species, and activity. At quiet time, both the PS2ORB and PS2RC are roughly MLT-agnostic, with a latitudinal extent of ∼1.5° for electrons and ∼2° for protons. However, at active times, the distributions become highly asymmetric in MLT, with the PS2RC (protons) latitudinal range often exceeding 6° in the pre-midnight sector, and the PS2ORB (electrons) exceeding 4° in the post-midnight sector. This suggests a fundamental dawn-dusk asymmetry in the locations of isotropic energetic electrons and protons at active times, possibility consistent with two separate "partial ring currents." It would be very interesting to model this effect, such as during substorms, and to determine its connections to auroral processes.

6.2.4 Ionospheric effects of ≥50 keV IB poleward precipitation

By comparing the particle energy ranges and IEflux in the PS2ORB and PS2RC, I discovered that such precipitation can have a significant impact on ionospheric ionization rates, and thus its Pedersen and Hall conductivity. By comparing with the particle impact ionization characteristics of (Fang et al., 2010) and (Fang et al., 2013), these fluxes can penetrate from 250 km all the way down to the ionospheric D-region (<80 km altitude), and occur at both

auroral and sub-auroral latitudes. This is in stark contrast to the primary plasma sheet auroral particle population, which is around 10 keV in energy, and can neither penetrate as deeply nor to sub-auroral latitudes, where conductivity is known to exist, but its source is not as well understood. This conclusion is supported by the fact that electron and proton fluxes in EMIC wave events, in an overlapping energy and latitudinal range as the PS2ORB/PS2RC, were reported by (Tian et al., 2022), who showed that ionospheric conductivities could be enhanced by a factor of 2-3, and therefore provided a very significant nightside contribution.

The total $\geq$50 keV power deposited in the high-latitude nightside ionosphere was around 10 MW for electrons and 100 MW for protons, although at active times, these rose to over 1 GW for electrons and 10 GW for protons. These power inputs can be compared with traditional sources of lesser energetic (<30 keV) precipitation observed by missions such as DMSP, where for example (Newell and Gjerloev, 2011) found that diffuse and broadband aurora also typically contribute on the order of GWs during active intervals. IBs and their poleward precipitation likely thus represent a significant ionospheric power source, and should be considered in future accounting of the global-scale energy budget.

The effect of this precipitation at sub-auroral latitudes is particularly of interest in future work, since $\geq$50 keV IBs have been shown for example by (Artemyev et al., 2024) to be embedded directly within phenomena such as Sub-Auroral Polarization Streams (SAPS). These authors found that the SAPS structure directly embedded the proton IB, and that its flow boundaries could be well-tracked by the locations of locally-intense $\geq$50 keV electron and proton precipitation. Future work in this area would be very interesting, and would benefit from a future in-situ observation platform at these latitudes similar to ELFIN, in order to develop statistics.

6.2.5 Solar wind and magnetospheric drivers of IBs

I also determined which observables in the solar wind and magnetosphere correlated most strongly with IB latitudes as a function of energy, as quantified using the information-theoretic measure of mutual information (MI), based on Shannon Entropy. I found that of

the activity indices considered, Dst tended to perform best, while AE and Kp were close seconds. I found that instantaneous solar wind drivers on their own tended to impart similar information content, with IMF components most affecting the proton IB, and solar wind velocity/dynamic pressure affecting electrons most.

Interestingly, the highest information content by far was that of the total precipitation (IEflux) in the PS2ORB for electron MI, and PS2RC for proton MI. This strongly suggests that the internal state of the magnetosphere at the time of the observations matters a great deal in the fine structure of the IBs, which cannot be easily predicted by solar wind and magnetospheric activity indices alone. This effect was revealed for example in the recent work of (Shi et al., 2024) during substorm evolution, who showed that localized features in equatorial currents were important in tracking the IB evolution over time. Future work will involve extending my model to accommodate substorm phase, e.g. using a substorm onset database.

6.2.6 Predictive capability of empirical IB models

I found that using a simple predictive model based on a set of four fundamental basis vectors, the IB location could typically be predicted to within 1° of error. This performs as well as (and sometimes better than) the recent <200 keV proton IB empirical models of (Dubyagin et al., 2018) and (Ma et al., 2022) based on POES data. The fundamental set of basis vectors included one of each of: (1) recent magnetospheric state (e.g. Dst), (2) magnetic local time (and/or dipole tilt and UT), (3) recent solar wind driving (e.g. dynamic pressure or IMF components), and (4) longer time-scale hysteresis of the magnetospheric state (e.g. 8 hour Dst minimum, to encode storm phase).

The empirical model predicted most IBs effectively; however, a population of outliers exist, which exhibit errors >2°. This population often appears at very active or quiet intervals, with many cases occurring either shortly before or after a substorm onset. Further investigation is needed to identify the cause of such errors, as well as possibility to determine the cross-correlation between the basis vectors used to predict the location, which may be

significant during such intervals. Further observables in the model may also prove useful, such as the state of magnetotail stretching inferred by platforms like GOES, as well as optical and radar ground stations to infer the equivalent of the instantaneous PS2ORB and PS2RC boundaries.

Additionally, it would be fruitful to assess the predicted IB latitudes from the empirical model here compared with predictions based on κ_{cr}^2 and more sophisticated data-assimilated field-models, such as those employing techniques described by (Brito and Morley, 2017), as well as other models which may emerge over time. As mentioned earlier, such models may provide complementary information to those of direct IB observations, and could perhaps be combined to synthesize higher fidelity predictions under quiet and active conditions, as well as gain physical insight into the drivers and localized/mesoscale features.

6.3 Future work

This work establishes that the nightside IB and its poleward FLC-dominated precipitation correspond to a special region of the magnetosphere, in which energetic particle injections and magnetic energy conversion often intersect with the outer portions of stably trapped particles in the inner magnetosphere. My study shows that, like those before it, IB observations are one of the most powerful tools in studying both localized and large-scale magnetospheric processes—all updated on the timescale of minutes, as detected in the LEO ionosphere. These can include the signatures of substorms, storms, auroral phenomena, magnetotail curvature and strength, equatorial particle injections, adiabatic and non-adiabatic particle acceleration, and many others. These observations have no direct equatorial satellite analogue, given the sheer volume of magnetotail that would need to be covered. Further still, ground observations are limited to specific latitudes, and are obscured by the ionosphere itself in the case of certain particle processes. IB observations are thus an invaluable means of studying the magnetosphere, and deserve continued mission and research consideration leading into the future.

Of the above possibilities, I identify one question in particular that would be especially interesting to address: the characteristics of sudden, MLT-localized precipitation due to the rapid development of the substorm current wedge (Walker et al., 2024). The formation of the wedge occurs over similar timescales to the particle bounce period, which changes the length of the field line (tens of minutes), but does not necessarily change its ionospheric footpoint. The IB latitude will thus be comparably fast in its variation to reflect the change in modified equatorial currents. Further, the process which generates the wedge simultaneously results in injections of energized particles, in locations nearby to where it also reduces B_z and R_C, due to the presence of field-aligned currents. Thus, the conditions are ideal for sudden and intense precipitation by the FLC mechanism. This also implies that, in addition to injections, any previously trapped outer belt and ring current particles in the vicinity of the wedge may also be suddenly precipitated, due to the abrupt change in B_z and R_C there. This question is challenging to address using both existing ground- and in-situ datasets (including ELFIN, due to the need for continuous coverage of the same invariant latitude over the timescale of wedge formation). It would therefore be of great interest to devise a future platform to study substorm evolution in this way, as well as its implications for magnetosphere-ionosphere coupling.

APPENDIX A

Appendix

A.1 ELFIN EPD technical specifications

Figure A.1 below provides a summary of the ELFIN Energetic Particle Detector electrical and digital specifications.

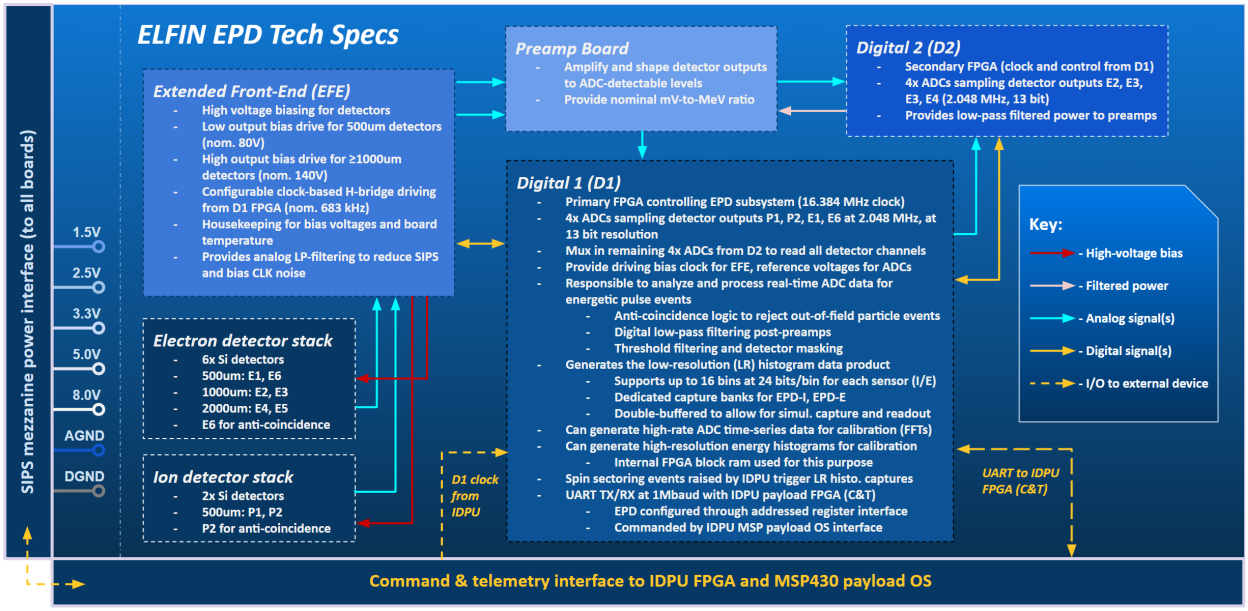

Figure A.1: Technical specification summary of the ELFIN EPD instrument.

Bibliography

Binod Adhikari, Subodh Dahal, Nirakar Sapkota, Prashrit Baruwal, Binod Bhattarai, Krishna Khanal, and Narayan P. Chapagain. Field-aligned current and polar cap potential and geomagnetic disturbances: A review of cross-correlation analysis. *Earth and Space Science*, 5(9):440–455, September 2018. ISSN 2333-5084. doi: 10.1029/2018ea000392. URL http://dx.doi.org/10.1029/2018EA000392.

S. Agostinelli, J. Allison, K. Amako, J. Apostolakis, H. Araujo, P. Arce, M. Asai, D. Axen, S. Banerjee, G. Barrand, F. Behner, L. Bellagamba, J. Boudreau, L. Broglia, A. Brunengo, H. Burkhardt, S. Chauvie, J. Chuma, R. Chytracek, G. Cooperman, G. Cosmo, P. Degtyarenko, A. Dell'Acqua, G. Depaola, D. Dietrich, R. Enami, A. Feliciello, C. Ferguson, H. Fesefeldt, G. Folger, F. Foppiano, A. Forti, S. Garelli, S. Giani, R. Giannitrapani, D. Gibin, J.J. Gómez Cadenas, I. González, G. Gracia Abril, G. Greeniaus, W. Greiner, V. Grichine, A. Grossheim, S. Guatelli, P. Gumplinger, R. Hamatsu, K. Hashimoto, H. Hasui, A. Heikkinen, A. Howard, V. Ivanchenko, A. Johnson, F.W. Jones, J. Kallenbach, N. Kanaya, M. Kawabata, Y. Kawabata, M. Kawaguti, S. Kelner, P. Kent, A. Kimura, T. Kodama, R. Kokoulin, M. Kossov, H. Kurashige, E. Lamanna, T. Lampén, V. Lara, V. Lefebure, F. Lei, M. Liendl, W. Lockman, F. Longo, S. Magni, M. Maire, E. Medernach, K. Minamimoto, P. Mora de Freitas, Y. Morita, K. Murakami, M. Nagamatu, R. Nartallo, P. Nieminen, T. Nishimura, K. Ohtsubo, M. Okamura, S. O'Neale, Y. Oohata, K. Paech, J. Perl, A. Pfeiffer, M.G. Pia, F. Ranjard, A. Rybin, S. Sadilov, E. Di Salvo, G. Santin, T. Sasaki, N. Savvas, Y. Sawada, S. Scherer, S. Sei, V. Sirotenko, D. Smith, N. Starkov, H. Stoecker, J. Sulkimo, M. Takahata, S. Tanaka, E. Tcherniaev, E. Safai Tehrani, M. Tropeano, P. Truscott, H. Uno, L. Urban, P. Urban, M. Verderi, A. Walkden, W. Wander, H. Weber, J.P. Wellisch, T. Wenaus, D.C. Williams, D. Wright, T. Yamada, H. Yoshida, and D. Zschiesche. Geant4—a simulation toolkit. *Nuclear Instruments and Methods in Physics Research Section A: Accelerators, Spectrometers, Detectors and Associated Equipment*, 506(3):250–303, July 2003. ISSN 0168-9002. doi: 10.1016/s0168-9002(03)01368-8.

URL http://dx.doi.org/10.1016/S0168-9002(03)01368-8.

Tommaso Alberti. The (un)predictable magnetosphere: the role of the internal dynamics. *Journal of Plasma Physics*, 88(1), February 2022. ISSN 1469-7807. doi: 10.1017/s0022377822000137. URL http://dx.doi.org/10.1017/S0022377822000137.

P. Alken, E. Thébault, C. D. Beggan, H. Amit, J. Aubert, J. Baerenzung, T. N. Bondar, W. J. Brown, S. Califf, A. Chambodut, A. Chulliat, G. A. Cox, C. C. Finlay, A. Fournier, N. Gillet, A. Grayver, M. D. Hammer, M. Holschneider, L. Huder, G. Hulot, T. Jager, C. Kloss, M. Korte, W. Kuang, A. Kuvshinov, B. Langlais, J.-M. Léger, V. Lesur, P. W. Livermore, F. J. Lowes, S. Macmillan, W. Magnes, M. Mandea, S. Marsal, J. Matzka, M. C. Metman, T. Minami, A. Morschhauser, J. E. Mound, M. Nair, S. Nakano, N. Olsen, F. J. Pavón-Carrasco, V. G. Petrov, G. Ropp, M. Rother, T. J. Sabaka, S. Sanchez, D. Saturnino, N. R. Schnepf, X. Shen, C. Stolle, A. Tangborn, L. Tøffner-Clausen, H. Toh, J. M. Torta, J. Varner, F. Vervelidou, P. Vigneron, I. Wardinski, J. Wicht, A. Woods, Y. Yang, Z. Zeren, and B. Zhou. International geomagnetic reference field: the thirteenth generation. *Earth, Planets and Space*, 73(1), February 2021. doi: 10.1186/s40623-020-01288-x. URL https://doi.org/10.1186/s40623-020-01288-x.

V. Angelopoulos, E. Tsai, L. Bingley, C. Shaffer, D. L. Turner, A. Runov, W. Li, J. Liu, A. V. Artemyev, X.-J. Zhang, R. J. Strangeway, R. E. Wirz, Y. Y. Shprits, V. A. Sergeev, R. P. Caron, M. Chung, P. Cruce, W. Greer, E. Grimes, K. Hector, M. J. Lawson, D. Leneman, E. V. Masongsong, C. L. Russell, C. Wilkins, D. Hinkley, J. B. Blake, N. Adair, M. Allen, M. Anderson, M. Arreola-Zamora, J. Artinger, J. Asher, D. Branchevsky, M. R. Capitelli, R. Castro, G. Chao, N. Chung, M. Cliffe, K. Colton, C. Costello, D. Depe, B. W. Domae, S. Eldin, L. Fitzgibbon, A. Flemming, I. Fox, D. M. Frederick, A. Gilbert, A. Gildemeister, A. Gonzalez, B. Hesford, S. Jha, N. Kang, J. King, R. Krieger, K. Lian, J. Mao, E. McKinney, J. P. Miller, A. Norris, M. Nuesca, A. Palla, E. S. Y. Park, C. E. Pedersen, Z. Qu, R. Rozario, E. Rye, R. Seaton, A. Subramanian, S. R. Sundin, A. Tan, W. Turner, A. J. Villegas, M. Wasden, G. Wing, C. Wong, E. Xie, S. Yamamoto, R. Yap, A. Zarifian,

and G. Y. Zhang. The ELFIN mission. *Space Science Reviews*, 216(5), July 2020. doi: 10.1007/s11214-020-00721-7. URL https://doi.org/10.1007/s11214-020-00721-7.

A. V. Artemyev, V. Angelopoulos, X.-J. Zhang, L. Chen, and A. Runov. Dispersed relativistic electron precipitation patterns between the ion and electron isotropy boundaries. *Journal of Geophysical Research: Space Physics*, 128(12), December 2023. ISSN 2169-9402. doi: 10.1029/2023ja032200. URL http://dx.doi.org/10.1029/2023JA032200.

A. V. Artemyev, V. Angelopoulos, X.-J. Zhang, J. Bortnik, Y. Miyoshi, C. Wilkins, S. Kasahara, T. Hori, A. Matsuoka, T. Mitani, T. Takashima, M. Teramoto, K. Yamamoto, and I. Shinohara. Coupling between earth's magnetotail and the outer radiation belt via field-line curvature scattering. *Journal of Geophysical Research: Space Physics*, 130(7), July 2025. ISSN 2169-9402. doi: 10.1029/2025ja034184. URL http://dx.doi.org/10.1029/2025JA034184.

Anton V. Artemyev, Ying Zou, Xiao-Jia Zhang, Xing Meng, and Vassilis Angelopoulos. Energetic particle precipitation in sub-auroral polarization streams. *Geophysical Research Letters*, 51(4), February 2024. ISSN 1944-8007. doi: 10.1029/2023gl107731. URL http://dx.doi.org/10.1029/2023GL107731.

W. I. Axford. Magnetospheric convection. *Reviews of Geophysics*, 7(1–2):421–459, February 1969. ISSN 1944-9208. doi: 10.1029/rg007i001p00421. URL http://dx.doi.org/10.1029/RG007i001p00421.

Dieter Bilitza, Michael Pezzopane, Vladimir Truhlik, David Altadill, Bodo W. Reinisch, and Alessio Pignalberi. The international reference ionosphere model: A review and description of an ionospheric benchmark. *Reviews of Geophysics*, 60(4), October 2022. ISSN 1944-9208. doi: 10.1029/2022rg000792. URL http://dx.doi.org/10.1029/2022RG000792.

Thomas J. Birmingham. Pitch angle diffusion in the jovian magnetodisc. *Journal of Geophysical Research*, 89(A5):2699, 1984. doi: 10.1029/ja089ia05p02699. URL https://doi.org/10.1029/ja089ia05p02699.

Joseph E. Borovsky and Juan Alejandro Valdivia. The earth's magnetosphere: A systems science overview and assessment. *Surveys in Geophysics*, 39(5):817–859, July 2018. ISSN 1573-0956. doi: 10.1007/s10712-018-9487-x. URL http://dx.doi.org/10.1007/s10712-018-9487-x.

Thiago V. Brito and Steven K. Morley. Improving empirical magnetic field models by fitting to in situ data using an optimized parameter approach. *Space Weather*, 15(12):1628–1648, December 2017. ISSN 1542-7390. doi: 10.1002/2017sw001702. URL http://dx.doi.org/10.1002/2017SW001702.

Enrico Camporeale, Simon Wing, and Jay R. Johnson. *Machine Learning Techniques for Space Weather*. Elsevier, 2018. ISBN 9780128117880. doi: 10.1016/c2016-0-01976-9. URL http://dx.doi.org/10.1016/C2016-0-01976-9.

Xing Cao, Binbin Ni, Yiqun Yu, Longxing Ma, Peng Lu, and Xiaoyu Wang. Comparison of ring current proton losses between contributions from scattering by field line curvature and emic waves. *Journal of Geophysical Research: Space Physics*, 128(12), December 2023. ISSN 2169-9402. doi: 10.1029/2023ja031904. URL http://dx.doi.org/10.1029/2023JA031904.

L. Capannolo, W. Li, R. Millan, D. Smith, N. Sivadas, J. Sample, and S. Shekhar. Relativistic electron precipitation near midnight: Drivers, distribution, and properties. *Journal of Geophysical Research: Space Physics*, 127(1), January 2022. doi: 10.1029/2021ja030111. URL https://doi.org/10.1029/2021ja030111.

Nathan Case. Solar wind-magnetosphere interactions: A statistical analysis of spacecraft measurements, 2014. URL https://www.researchgate.net/doi/10.13140/2.1.2588.8321.

Ao Chen, Chao Yue, Hongfei Chen, Qiugang Zong, Suiyan Fu, Yongfu Wang, and Jie Ren. Ring current decay during geomagnetic storm recovery phase: Comparison between rbsp observations and theoretical modeling. *Journal of Geophysical Research: Space Physics*,

126(1), January 2021. ISSN 2169-9402. doi: 10.1029/2020ja028500. URL http://dx.doi.org/10.1029/2020ja028500.

Francis F. Chen. *Introduction to Plasma Physics and Controlled Fusion*. Springer International Publishing, 2016. ISBN 9783319223094. doi: 10.1007/978-3-319-22309-4. URL http://dx.doi.org/10.1007/978-3-319-22309-4.

S. P. Christon, D. J. Williams, D. G. Mitchell, L. A. Frank, and C. Y. Huang. Spectral characteristics of plasma sheet ion and electron populations during undisturbed geomagnetic conditions. *Journal of Geophysical Research*, 94(A10):13409, 1989. doi: 10.1029/ja094ia10p13409. URL https://doi.org/10.1029/ja094ia10p13409.

S. P. Christon, D. J. Williams, D. G. Mitchell, C. Y. Huang, and L. A. Frank. Spectral characteristics of plasma sheet ion and electron populations during disturbed geomagnetic conditions. *Journal of Geophysical Research*, 96(A1):1, 1991. doi: 10.1029/90ja01633. URL https://doi.org/10.1029/90ja01633.

R. M. Corless, G. H. Gonnet, D. E. G. Hare, D. J. Jeffrey, and D. E. Knuth. On the lambertw function. *Advances in Computational Mathematics*, 5(1):329–359, December 1996. ISSN 1572-9044. doi: 10.1007/bf02124750. URL http://dx.doi.org/10.1007/BF02124750.

Ioannis A. Daglis, Richard M. Thorne, Wolfgang Baumjohann, and Stefano Orsini. The terrestrial ring current: Origin, formation, and decay. *Reviews of Geophysics*, 37(4):407–438, November 1999. ISSN 1944-9208. doi: 10.1029/1999rg900009. URL http://dx.doi.org/10.1029/1999RG900009.

D. C. Delcourt, J.-A. Sauvaud, R. F. Martin, and T. E. Moore. On the nonadiabatic precipitation of ions from the near-earth plasma sheet. *Journal of Geophysical Research: Space Physics*, 101(A8):17409–17418, August 1996. doi: 10.1029/96ja01006. URL https://doi.org/10.1029/96ja01006.

E. F. Donovan. Ground-based optical determination of the b2i boundary: A basis for

an optical MT-index. *Journal of Geophysical Research*, 108(A3), 2003. doi: 10.1029/2001ja009198. URL https://doi.org/10.1029/2001ja009198.

S. Dubyagin, N. Yu. Ganushkina, and V. Sergeev. Formation of 30 KeV proton isotropic boundaries during geomagnetic storms. *Journal of Geophysical Research: Space Physics*, 123(5):3436–3459, May 2018. doi: 10.1002/2017ja024587. URL https://doi.org/10.1002/2017ja024587.

S. Dubyagin, S. Apatenkov, E. Gordeev, N. Ganushkina, and Y. Zheng. Conditions of loss cone filling by scattering on the curved field lines for 30 kev protons during geomagnetic storm as inferred from numerical trajectory tracing. *Journal of Geophysical Research: Space Physics*, 126(1), December 2020. ISSN 2169-9402. doi: 10.1029/2020ja028490. URL http://dx.doi.org/10.1029/2020ja028490.

J. W. Dungey. Interplanetary magnetic field and the auroral zones. *Physical Review Letters*, 6(2):47–48, January 1961. ISSN 0031-9007. doi: 10.1103/physrevlett.6.47. URL http://dx.doi.org/10.1103/PhysRevLett.6.47.

Yusuke Ebihara. Numerical simulation of the ring current. *Space Science Reviews*, 105(1/2): 377–452, 2003. ISSN 0038-6308. doi: 10.1023/a:1023905607888. URL http://dx.doi.org/10.1023/a:1023905607888.

Yusuke Ebihara. Simulation study of near-earth space disturbances: 1. magnetic storms. *Progress in Earth and Planetary Science*, 6(1), February 2019. ISSN 2197-4284. doi: 10.1186/s40645-019-0264-3. URL http://dx.doi.org/10.1186/s40645-019-0264-3.

W. W. Eshetu, W. Tu, V. K. Jordanova, and M. Cowee. Quantifying the effect of magnetic field line curvature scattering on the loss of ring current ions. *Journal of Geophysical Research: Space Physics*, 126(1), January 2021. ISSN 2169-9402. doi: 10.1029/2020ja028497. URL http://dx.doi.org/10.1029/2020ja028497.

Matteo Faganello and Francesco Califano. Magnetized kelvin–helmholtz instability: theory and simulations in the earth's magnetosphere context. *Journal of Plasma Physics*, 83

(6), November 2017. ISSN 1469-7807. doi: 10.1017/s0022377817000770. URL http://dx.doi.org/10.1017/S0022377817000770.

Donald H. Fairfield. Average and unusual locations of the earth's magnetopause and bow shock. *Journal of Geophysical Research*, 76(28):6700–6716, October 1971. doi: 10.1029/ja076i028p06700. URL https://doi.org/10.1029/ja076i028p06700.

Xiaohua Fang, Michael W. Liemohn, Janet U. Kozyra, and David S. Evans. Global 30–240 kev proton precipitation in the 17–18 april 2002 geomagnetic storms: 2. conductances and beam spreading. *Journal of Geophysical Research: Space Physics*, 112(A5), May 2007. ISSN 0148-0227. doi: 10.1029/2006ja012113. URL http://dx.doi.org/10.1029/2006JA012113.

Xiaohua Fang, Cora E. Randall, Dirk Lummerzheim, Wenbin Wang, Gang Lu, Stanley C. Solomon, and Rudy A. Frahm. Parameterization of monoenergetic electron impact ionization. *Geophysical Research Letters*, 37(22):n/a–n/a, November 2010. doi: 10.1029/2010gl045406. URL https://doi.org/10.1029/2010gl045406.

Xiaohua Fang, Dirk Lummerzheim, and Charles H. Jackman. Proton impact ionization and a fast calculation method. *Journal of Geophysical Research: Space Physics*, 118 (8):5369–5378, August 2013. ISSN 2169-9402. doi: 10.1002/jgra.50484. URL http://dx.doi.org/10.1002/jgra.50484.

Alexandra Ruth Fogg, Caitríona M. Jackman, Sandra C. Chapman, James E. Waters, Aisling Bergin, Laurent Lamy, Karine Issautier, Baptiste Cecconi, and Xavier Bonnin. Quantification of magnetosphere–ionosphere coupling timescales using mutual information: response of terrestrial radio emissions and ionospheric–magnetospheric currents. *Nonlinear Processes in Geophysics*, 31(2):195–206, April 2024. ISSN 1607-7946. doi: 10.5194/npg-31-195-2024. URL http://dx.doi.org/10.5194/npg-31-195-2024.

V. Formisano. *The Earth's Bow Shock Fine Structure*, page 187–223. Springer Netherlands,

1974. ISBN 9789401021722. doi: 10.1007/978-94-010-2172-2_12. URL http://dx.doi.org/10.1007/978-94-010-2172-2_12.

Theodore A. Fritz. High-latitude outer-zone boundary region for ≥40-kev electrons during geomagnetically quiet period. *Journal of Geophysical Research*, 73(23):7245–7255, December 1968. ISSN 0148-0227. doi: 10.1029/ja073i023p07245. URL http://dx.doi.org/10.1029/JA073i023p07245.

Theodore A. Fritz. Study of the high-latitude, outer-zone boundary region for ≥40-kev electrons with satellite injun 3. *Journal of Geophysical Research*, 75(28):5387–5400, October 1970. ISSN 0148-0227. doi: 10.1029/ja075i028p05387. URL http://dx.doi.org/10.1029/JA075i028p05387.

C. Gabrielse, V. Angelopoulos, A. Runov, and D. L. Turner. Statistical characteristics of particle injections throughout the equatorial magnetotail. *Journal of Geophysical Research: Space Physics*, 119(4):2512–2535, April 2014. doi: 10.1002/2013ja019638. URL https://doi.org/10.1002/2013ja019638.

N. Yu. Ganushkina, T. I. Pulkkinen, M. V. Kubyshkina, V. A. Sergeev, E. A. Lvova, T. A. Yahnina, A. G. Yahnin, and T. Fritz. Proton isotropy boundaries as measured on mid- and low-altitude satellites. *Annales Geophysicae*, 23(5):1839–1847, July 2005. doi: 10.5194/angeo-23-1839-2005. URL https://doi.org/10.5194/angeo-23-1839-2005.

N. Yu. Ganushkina, M. W. Liemohn, and S. Dubyagin. Current systems in the earth's magnetosphere. *Reviews of Geophysics*, 56(2):309–332, April 2018. ISSN 1944-9208. doi: 10.1002/2017rg000590. URL http://dx.doi.org/10.1002/2017RG000590.

J. W. Gao, Z. J. Rong, Y. H. Cai, A. T. Y. Lui, A. A. Petrukovich, C. Shen, M. W. Dunlop, Y. Wei, and W. X. Wan. The distribution of two flapping types of magnetotail current sheet: Implication for the flapping mechanism. *Journal of Geophysical Research: Space Physics*, 123(9):7413–7423, September 2018. ISSN 2169-9402. doi: 10.1029/2018ja025695. URL http://dx.doi.org/10.1029/2018JA025695.

P. C. Gray and L. C. Lee. Particle pitch angle diffusion due to nonadiabatic effects in the plasma sheet. *Journal of Geophysical Research*, 87(A9):7445, 1982. doi: 10.1029/ja087ia09p07445. URL https://doi.org/10.1029/ja087ia09p07445.

S. Haaland, H. Hasegawa, G. Paschmann, B. Sonnerup, and M. Dunlop. 20 years of cluster observations: The magnetopause. *Journal of Geophysical Research: Space Physics*, 126 (8), August 2021. ISSN 2169-9402. doi: 10.1029/2021ja029362. URL http://dx.doi.org/10.1029/2021JA029362.

M. Hesse and P. A. Cassak. Magnetic reconnection in the space sciences: Past, present, and future. *Journal of Geophysical Research: Space Physics*, 125(2), January 2020. ISSN 2169-9402. doi: 10.1029/2018ja025935. URL http://dx.doi.org/10.1029/2018JA025935.

R. Ilie, N. Ganushkina, G. Toth, S. Dubyagin, and M. W. Liemohn. Testing the magnetotail configuration based on observations of low-altitude isotropic boundaries during quiet times. *Journal of Geophysical Research: Space Physics*, 120(12), December 2015. doi: 10.1002/2015ja021858. URL https://doi.org/10.1002/2015ja021858.

W. L. Imhof, J. B. Reagan, and E. E. Gaines. Fine-scale spatial structure in the pitch angle distributions of energetic particles near the midnight trapping boundary. *Journal of Geophysical Research*, 82(32):5215–5221, November 1977. doi: 10.1029/ja082i032p05215. URL https://doi.org/10.1029/ja082i032p05215.

W. L. Imhof, D. L. Chenette, E. E. Gaines, and J. D. Winningham. Characteristics of electrons at the trapping boundary of the radiation belt. *Journal of Geophysical Research: Space Physics*, 102(A1):95–104, January 1997. doi: 10.1029/96ja02797. URL https://doi.org/10.1029/96ja02797.

W.L. Imhof, J.B. Reagan, and E.E. Gaines. Studies of the sharply defined l-dependent energy threshold for isotropy at the midnight trapping boundary. *Journal of Geophysical Research*, 84(A11):6371, 1979. doi: 10.1029/ja084ia11p06371. URL https://doi.org/10.1029/ja084ia11p06371.

N. M. E. Kalmoni, I. J. Rae, C. E. J. Watt, K. R. Murphy, M. Samara, R. G. Michell, G. Grubbs, and C. Forsyth. A diagnosis of the plasma waves responsible for the explosive energy release of substorm onset. *Nature Communications*, 9(1), November 2018. ISSN 2041-1723. doi: 10.1038/s41467-018-07086-0. URL http://dx.doi.org/10.1038/s41467-018-07086-0.

E.-H. Kim, J. R. Johnson, and K. Nykyri. Coupling between alfvén wave and kelvin-helmholtz waves in the low latitude boundary layer. *Frontiers in Astronomy and Space Sciences*, 8, January 2022. doi: 10.3389/fspas.2021.785413. URL https://doi.org/10.3389/fspas.2021.785413.

Hannu E. J. Koskinen and Emilia K. J. Kilpua. *Plasma Waves in the Inner Magnetosphere*, page 85–119. Springer International Publishing, October 2021. ISBN 9783030821678. doi: 10.1007/978-3-030-82167-8_4. URL http://dx.doi.org/10.1007/978-3-030-82167-8_4.

K.R. Lang. *SOLAR SYSTEM — The Sun*, page 209–220. Elsevier, 2005. ISBN 9780123693969. doi: 10.1016/b0-12-369396-9/00078-2. URL http://dx.doi.org/10.1016/B0-12-369396-9/00078-2.

YuXuan Li, Chao Yue, Ying Liu, Qiu-Gang Zong, Hong Zou, and YuGuang Ye. Dynamics of the inner electron radiation belt: A review. *Earth and Planetary Physics*, 7(1):109–118, 2023. ISSN 2096-3955. doi: 10.26464/epp2023009. URL http://dx.doi.org/10.26464/epp2023009.

Jun Liang, E. Donovan, B. Ni, C. Yue, F. Jiang, and V. Angelopoulos. On an energy-latitude dispersion pattern of ion precipitation potentially associated with magnetospheric emic waves. *Journal of Geophysical Research: Space Physics*, 119(10):8137–8160, October 2014. ISSN 2169-9402. doi: 10.1002/2014ja020226. URL http://dx.doi.org/10.1002/2014JA020226.

Michael W. Liemohn. The case for improving the robinson formulas. *Journal of Geo-*

physical Research: Space Physics, 125(10), October 2020. ISSN 2169-9402. doi: 10.1029/2020ja028332. URL http://dx.doi.org/10.1029/2020JA028332.

Jiang Liu, V. Angelopoulos, Xiao-Jia Zhang, D. L. Turner, C. Gabrielse, A. Runov, Jinxing Li, H. O. Funsten, and H. E. Spence. Dipolarizing flux bundles in the cis-geosynchronous magnetosphere: Relationship between electric fields and energetic particle injections. *Journal of Geophysical Research: Space Physics*, 121(2):1362–1376, February 2016. doi: 10.1002/2015ja021691. URL https://doi.org/10.1002/2015ja021691.

San Lu, P. L. Pritchett, V. Angelopoulos, and A. V. Artemyev. Formation of dawn-dusk asymmetry in earth's magnetotail thin current sheet: A three-dimensional particle-in-cell simulation. *Journal of Geophysical Research: Space Physics*, 123(4):2801–2814, April 2018. doi: 10.1002/2017ja025095. URL https://doi.org/10.1002/2017ja025095.

E. A. Lucek, D. Constantinescu, M. L. Goldstein, J. Pickett, J. L. Pinçon, F. Sahraoui, R. A. Treumann, and S. N. Walker. The magnetosheath. *Space Science Reviews*, 118 (1–4):95–152, June 2005. ISSN 1572-9672. doi: 10.1007/s11214-005-3825-2. URL http://dx.doi.org/10.1007/s11214-005-3825-2.

R. Lundin, M. Yamauchi, J.-A. Sauvaud, and A. Balogh. Magnetospheric plasma boundaries: a test of the frozen-in magnetic field theorem. *Annales Geophysicae*, 23(7):2565–2578, October 2005. ISSN 1432-0576. doi: 10.5194/angeo-23-2565-2005. URL http://dx.doi.org/10.5194/angeo-23-2565-2005.

E. A. Lvova, V. A. Sergeev, and G. R. Bagautdinova. Statistical study of the proton isotropy boundary. *Annales Geophysicae*, 23(4):1311–1316, June 2005. ISSN 1432-0576. doi: 10.5194/angeo-23-1311-2005. URL http://dx.doi.org/10.5194/angeo-23-1311-2005.

L. R. Lyons, A. L. Vampola, and T. W. Speiser. Ion precipitation from the magnetopause current sheet. *Journal of Geophysical Research*, 92(A6):6147, 1987. doi: 10.1029/ja092ia06p06147. URL https://doi.org/10.1029/ja092ia06p06147.

Longxing Ma, Yiqun Yu, Xinbin Tian, and Jinbin Cao. An empirical model of the proton isotropic boundary (ib). *Journal of Geophysical Research: Space Physics*, 127(9), September 2022. ISSN 2169-9402. doi: 10.1029/2022ja030843. URL http://dx.doi.org/10.1029/2022JA030843.

R.F. Martin, D. Delcourt, D.L. Holland, and M.J. Asbury. Magnetotail particle distributions associated with pitch angle isotropization. *Journal of Atmospheric and Solar-Terrestrial Physics*, 62(6):513–519, April 2000. doi: 10.1016/s1364-6826(00)00020-1. URL https://doi.org/10.1016/s1364-6826(00)00020-1.

S. E. Milan, L. B. N. Clausen, J. C. Coxon, J. A. Carter, M.-T. Walach, K. Laundal, N. Østgaard, P. Tenfjord, J. Reistad, K. Snekvik, H. Korth, and B. J. Anderson. Overview of solar wind–magnetosphere–ionosphere–atmosphere coupling and the generation of magnetospheric currents. *Space Science Reviews*, 206(1–4):547–573, February 2017. ISSN 1572-9672. doi: 10.1007/s11214-017-0333-0. URL http://dx.doi.org/10.1007/s11214-017-0333-0.

Agnit Mukhopadhyay, Daniel Welling, Michael Liemohn, Aaron Ridley, Meghan Burleigh, Chen Wu, Shasha Zou, Hyunju Connor, Elizabeth Vandegriff, Pauline Dredger, and Gabor Tóth. Global driving of auroral precipitation: 1. balance of sources. *Journal of Geophysical Research: Space Physics*, 127(7), July 2022. ISSN 2169-9402. doi: 10.1029/2022ja030323. URL http://dx.doi.org/10.1029/2022JA030323.

P. T. Newell and J. W. Gjerloev. Evaluation of supermag auroral electrojet indices as indicators of substorms and auroral power. *Journal of Geophysical Research: Space Physics*, 116(A12), December 2011. ISSN 0148-0227. doi: 10.1029/2011ja016779. URL http://dx.doi.org/10.1029/2011JA016779.

P. T. Newell, T. Sotirelis, and S. Wing. Diffuse, monoenergetic, and broadband aurora: The global precipitation budget. *Journal of Geophysical Research: Space Physics*, 114 (A9):n/a–n/a, September 2009a. doi: 10.1029/2009ja014326. URL https://doi.org/10.1029/2009ja014326.

Patrick T. Newell, V. A. Sergeev, G. R. Bikkuzina, and S. Wing. Characterizing the state of the magnetosphere: Testing the ion precipitation maxima latitude (b2i) and the ion isotropy boundary. *Journal of Geophysical Research: Space Physics*, 103(A3):4739–4745, March 1998. doi: 10.1029/97ja03622. URL https://doi.org/10.1029/97ja03622.

Patrick T. Newell, Kan Liou, and Gordon R. Wilson. Polar cap particle precipitation and aurora: Review and commentary. *Journal of Atmospheric and Solar-Terrestrial Physics*, 71(2):199–215, February 2009b. ISSN 1364-6826. doi: 10.1016/j.jastp.2008.11.004. URL http://dx.doi.org/10.1016/j.jastp.2008.11.004.

A. Nishida. The earth's dynamic magnetotail. *Space Science Reviews*, 91(3–4):507–577, February 2000. ISSN 1572-9672. doi: 10.1023/a:1005223124330. URL http://dx.doi.org/10.1023/A:1005223124330.

Mitsuo Oka, Joachim Birn, Jan Egedal, Fan Guo, Robert E. Ergun, Drew L. Turner, Yuri Khotyaintsev, Kyoung-Joo Hwang, Ian J. Cohen, and James F. Drake. Particle acceleration by magnetic reconnection in geospace. *Space Science Reviews*, 219 (8), November 2023. ISSN 1572-9672. doi: 10.1007/s11214-023-01011-8. URL http://dx.doi.org/10.1007/s11214-023-01011-8.

B. J. O'Brien. High-latitude geophysical studies with satellite injun 3: 3. precipitation of electrons into the atmosphere. *Journal of Geophysical Research*, 69(1):13–43, January 1964. ISSN 0148-0227. doi: 10.1029/jz069i001p00013. URL http://dx.doi.org/10.1029/JZ069i001p00013.

Minna Palmroth, Urs Ganse, Yann Pfau-Kempf, Markus Battarbee, Lucile Turc, Thiago Brito, Maxime Grandin, Sanni Hoilijoki, Arto Sandroos, and Sebastian von Alfthan. Vlasov methods in space physics and astrophysics. *Living Reviews in Computational Astrophysics*, 4(1), August 2018. ISSN 2365-0524. doi: 10.1007/s41115-018-0003-2. URL http://dx.doi.org/10.1007/s41115-018-0003-2.

Natasha Papitashvili, Dieter Bilitza, and Joseph King. OMNI: A Description of Near-Earth

Solar Wind Environment. In *40th COSPAR Scientific Assembly*, volume 40, pages C0.1–12–14, January 2014.

Hannes Risken. *The Fokker-Planck Equation: Methods of Solution and Applications*. Springer Berlin Heidelberg, 1996. ISBN 9783642615443. doi: 10.1007/978-3-642-61544-3. URL http://dx.doi.org/10.1007/978-3-642-61544-3.

R. M. Robinson, R. R. Vondrak, K. Miller, T. Dabbs, and D. Hardy. On calculating ionospheric conductances from the flux and energy of precipitating electrons. *Journal of Geophysical Research: Space Physics*, 92(A3):2565–2569, March 1987. ISSN 0148-0227. doi: 10.1029/ja092ia03p02565. URL http://dx.doi.org/10.1029/JA092iA03p02565.

Alexis P. Rouillard, Nicholeen Viall, Viviane Pierrard, Christian Vocks, Lorenzo Matteini, Olga Alexandrova, Aleida K. Higginson, Benoit Lavraud, Michael Lavarra, Yihong Wu, Rui Pinto, Alessandro Bemporad, and Eduardo Sanchez-Diaz. The solar wind, April 2021. ISSN 2328-8779. URL http://dx.doi.org/10.1002/9781119815600.ch1.

C. T. Russell. Space physics: an introduction, by c. t. russell, j. g. luhmann and r. j. strangeway: Scope: textbook. level: postgraduates. *Contemporary Physics*, 58(2):199–199, February 2017. ISSN 1366-5812. doi: 10.1080/00107514.2017.1291726. URL http://dx.doi.org/10.1080/00107514.2017.1291726.

Michael J. Rycroft, R. Giles Harrison, Keri A. Nicoll, and Evgeny A. Mareev. An overview of earth's global electric circuit and atmospheric conductivity. *Space Science Reviews*, 137(1–4):83–105, May 2008. ISSN 1572-9672. doi: 10.1007/s11214-008-9368-6. URL http://dx.doi.org/10.1007/s11214-008-9368-6.

Paulo Saraiva. On shannon entropy and its applications. *Kuwait Journal of Science*, 50 (3):194–199, July 2023. ISSN 2307-4108. doi: 10.1016/j.kjs.2023.05.004. URL http://dx.doi.org/10.1016/j.kjs.2023.05.004.

Michael Schulz. *The Magnetosphere*, page 87–293. Elsevier, 1991. ISBN

9780123786746. doi: 10.1016/b978-0-12-378674-6.50008-x. URL http://dx.doi.org/10.1016/B978-0-12-378674-6.50008-X.

R. S. Selesnick and M. D. Looper. Field-line curvature scattering at the outer boundary of the proton radiation belt. *Journal of Geophysical Research: Space Physics*, 128(7), June 2023. ISSN 2169-9402. doi: 10.1029/2023ja031509. URL http://dx.doi.org/10.1029/2023ja031509.

V. A. Sergeev, M. Malkov, and K. Mursula. Testing the isotropic boundary algorithm method to evaluate the magnetic field configuration in the tail. *Journal of Geophysical Research: Space Physics*, 98(A5):7609–7620, May 1993. doi: 10.1029/92ja02587. URL https://doi.org/10.1029/92ja02587.

V. A. Sergeev, G. R. Bikkuzina, and P. T. Newell. Dayside isotropic precipitation of energetic protons. *Annales Geophysicae*, 15(10):1233–1245, October 1997. doi: 10.1007/s00585-997-1233-5. URL https://doi.org/10.1007/s00585-997-1233-5.

V. A. Sergeev, I. A. Chernyaev, V. Angelopoulos, and N. Y. Ganushkina. Magnetospheric conditions near the equatorial footpoints of proton isotropy boundaries. *Annales Geophysicae*, 33(12):1485–1493, December 2015a. doi: 10.5194/angeo-33-1485-2015. URL https://doi.org/10.5194/angeo-33-1485-2015.

V. A. Sergeev, S. A. Chernyaeva, S. V. Apatenkov, N. Y. Ganushkina, and S. V. Dubyagin. Energy–latitude dispersion patterns near the isotropy boundaries of energetic protons. *Annales Geophysicae*, 33(8):1059–1070, August 2015b. doi: 10.5194/angeo-33-1059-2015. URL https://doi.org/10.5194/angeo-33-1059-2015.

V. A. Sergeev, E. I. Gordeev, V. G. Merkin, and M. I. Sitnov. Does a local b-minimum appear in the tail current sheet during a substorm growth phase? *Geophysical Research Letters*, 45(6):2566–2573, March 2018. doi: 10.1002/2018gl077183. URL https://doi.org/10.1002/2018gl077183.

V.A. Sergeev and N.A. Tsyganenko. Energetic particle losses and trapping boundaries as deduced from calculations with a realistic magnetic field model. *Planetary and Space Science*, 30(10):999–1006, October 1982. doi: 10.1016/0032-0633(82)90149-0. URL https://doi.org/10.1016/0032-0633(82)90149-0.

V.A. Sergeev, E.M. Sazhina, N.A. Tsyganenko, J.Å. Lundblad, and F. Søraas. Pitch-angle scattering of energetic protons in the magnetotail current sheet as the dominant source of their isotropic precipitation into the nightside ionosphere. *Planetary and Space Science*, 31 (10):1147–1155, October 1983. doi: 10.1016/0032-0633(83)90103-4. URL https://doi.org/10.1016/0032-0633(83)90103-4.

C. E. Shannon. A mathematical theory of communication. *Bell System Technical Journal*, 27 (3):379–423, July 1948. ISSN 0005-8580. doi: 10.1002/j.1538-7305.1948.tb01338.x. URL http://dx.doi.org/10.1002/j.1538-7305.1948.tb01338.x.

I. G. Shevchenko, V. Sergeev, M. Kubyshkina, V. Angelopoulos, K. H. Glassmeier, and H. J. Singer. Estimation of magnetosphere-ionosphere mapping accuracy using isotropy boundary and THEMIS observations. *Journal of Geophysical Research: Space Physics*, 115(A11):n/a–n/a, November 2010. doi: 10.1029/2010ja015354. URL https://doi.org/10.1029/2010ja015354.

Xiaofei Shi, Grant K. Stephens, Anton V. Artemyev, Mikhail I. Sitnov, and Vassilis Angelopoulos. Picturing global substorm dynamics in the magnetotail using low-altitude elfin measurements and data mining-based magnetic field reconstructions. *Space Weather*, 22(10), October 2024. ISSN 1542-7390. doi: 10.1029/2024sw004062. URL http://dx.doi.org/10.1029/2024SW004062.

A.K. Singh, R.P. Singh, and Devendraa Siingh. State studies of earth's plasmasphere: A review. *Planetary and Space Science*, 59(9):810–834, July 2011. ISSN 0032-0633. doi: 10.1016/j.pss.2011.03.013. URL http://dx.doi.org/10.1016/j.pss.2011.03.013.

M. I. Sitnov, N. A. Tsyganenko, A. Y. Ukhorskiy, and P. C. Brandt. Dynamical data-

based modeling of the storm-time geomagnetic field with enhanced spatial resolution. *Journal of Geophysical Research: Space Physics*, 113(A7), July 2008. ISSN 0148-0227. doi: 10.1029/2007ja013003. URL http://dx.doi.org/10.1029/2007JA013003.

T. W. Speiser. Particle trajectories in model current sheets: 1. analytical solutions. *Journal of Geophysical Research*, 70(17):4219–4226, September 1965. doi: 10.1029/jz070i017p04219. URL https://doi.org/10.1029/jz070i017p04219.

R. J. Strangeway, R. E. Ergun, Y.-J. Su, C. W. Carlson, and R. C. Elphic. Factors controlling ionospheric outflows as observed at intermediate altitudes. *Journal of Geophysical Research: Space Physics*, 110(A3), March 2005. ISSN 0148-0227. doi: 10.1029/2004ja010829. URL http://dx.doi.org/10.1029/2004JA010829.

Herbert A. Sturges. The choice of a class interval. *Journal of the American Statistical Association*, 21(153):65–66, March 1926. ISSN 1537-274X. doi: 10.1080/01621459.1926.10502161. URL http://dx.doi.org/10.1080/01621459.1926.10502161.

SuperDARN. Ionospheric tutorial. https://superdarn.ca/tutorials-7, 2025. Accessed: 2025-10.

Xingbin Tian, Yiqun Yu, Minghui Zhu, Longxing Ma, Jinbin Cao, Shreedevi PR, Vania K. Jordanova, and Stanley C. Solomon. Effects of emic wave-driven proton precipitation on the ionosphere. *Journal of Geophysical Research: Space Physics*, 127(2), January 2022. ISSN 2169-9402. doi: 10.1029/2021ja030101. URL http://dx.doi.org/10.1029/2021JA030101.

K. J. Trattner, S. M. Petrinec, and S. A. Fuselier. The location of magnetic reconnection at earth's magnetopause. *Space Science Reviews*, 217(3), March 2021. doi: 10.1007/s11214-021-00817-8. URL https://doi.org/10.1007/s11214-021-00817-8.

Ethan Tsai, Akhil Palla, Austin Norris, James King, Cindy Russell, Sophie Ye, Jiashu Wu, Jason Mao, Sharvani Jha, Chanel Young, Graham Wing, Kevin Lian, Aiden Szeto, James Shiffer, Rishi Sankar, Kaivalya Tota, Annie Liu, Derek Lee, Uma Patil, Isabella

He, Jonathan Tam, Alex McDermott, Katrina Le, Suyash Kumar, Kelly Nguyen, Michelle Nguyen, Chen Yap, Erica Xie, James Tseng, Laura Iglesias, Alexandra Roosnovo, Wynne Turner, Reed Curtis, Colin Wilkins, Emmanuel Masongsong, Ryan Caron, Xiao-Jia Zhang, Anton Artemyev, and Vassilis Angelopoulos. Remote sensing of electron precipitation mechanisms enabled by elfin mission operations and adcs. *Advances in Space Research*, 75(9):6706–6733, May 2025. ISSN 0273-1177. doi: 10.1016/j.asr.2024.07.008. URL http://dx.doi.org/10.1016/j.asr.2024.07.008.

Bruce T. Tsurutani, Gary P. Zank, Veerle J. Sterken, Kazunari Shibata, Tsugunobu Nagai, Anthony J. Mannucci, David M. Malaspina, Gurbax S. Lakhina, Shrikanth G. Kanekal, Keisuke Hosokawa, Richard B. Horne, Rajkumar Hajra, Karl-Heinz Glassmeier, C. Trevor Gaunt, Peng-Fei Chen, and Syun-Ichi Akasofu. Space plasma physics: A review. *IEEE Transactions on Plasma Science*, 51(7):1595–1655, July 2023. ISSN 1939-9375. doi: 10.1109/tps.2022.3208906. URL http://dx.doi.org/10.1109/TPS.2022.3208906.

N. A. Tsyganenko and V. A. Andreeva. A forecasting model of the magnetosphere driven by an optimal solar wind coupling function. *Journal of Geophysical Research: Space Physics*, 120(10):8401–8425, October 2015. doi: 10.1002/2015ja021641. URL https://doi.org/10.1002/2015ja021641.

N.A. Tsyganenko. A magnetospheric magnetic field model with a warped tail current sheet. *Planetary and Space Science*, 37(1):5–20, January 1989. doi: 10.1016/0032-0633(89)90066-4. URL https://doi.org/10.1016/0032-0633(89)90066-4.

A. Y. Ukhorskiy and M. I. Sitnov. Dynamics of radiation belt particles. *Space Science Reviews*, 179(1–4):545–578, November 2012. ISSN 1572-9672. doi: 10.1007/s11214-012-9938-5. URL http://dx.doi.org/10.1007/s11214-012-9938-5.

Shoaib Usman and Amol Patil. Radiation detector deadtime and pile up: A review of the status of science. *Nuclear Engineering and Technology*, 50(7):1006–1016, October 2018. ISSN 1738-5733. doi: 10.1016/j.net.2018.06.014. URL http://dx.doi.org/10.1016/j.net.2018.06.014.

Vytenis M. Vasyliunas. *Low-Energy Electrons in the Magnetosphere as Observed by OGO-1 and OGO-3*, page 622–640. Springer Netherlands, 1968. ISBN 9789401034678. doi: 10.1007/978-94-010-3467-8_22. URL http://dx.doi.org/10.1007/978-94-010-3467-8_22.

Vytenis M. Vasyliunas. *Magnetospheric Plasma*, page 592–611. Springer Netherlands, 1972. ISBN 9789400936935. doi: 10.1007/978-94-009-3693-5_27. URL http://dx.doi.org/10.1007/978-94-009-3693-5_27.

Simon James Walker, Karl Magnus Laundal, Jone Peter Reistad, Spencer Mark Hatch, Anders Ohma, and Jesper Gjerloev. The ionospheric leg of the substorm current wedge: Combining iridium and ground magnetometers. *Journal of Geophysical Research: Space Physics*, 129(7), July 2024. ISSN 2169-9402. doi: 10.1029/2024ja032414. URL http://dx.doi.org/10.1029/2024JA032414.

C. Wilkins, V. Angelopoulos, A. Runov, A. Artemyev, X.-J. Zhang, J. Liu, and E. Tsai. Statistical characteristics of the electron isotropy boundary. *Journal of Geophysical Research: Space Physics*, 128(10), October 2023. ISSN 2169-9402. doi: 10.1029/2023ja031774. URL http://dx.doi.org/10.1029/2023JA031774.

C. Wilkins, V. Angelopoulos, A. Runov, A. Artemyev, X.-J. Zhang, J. Liu, and E. Tsai. Statistical characteristics of the proton isotropy boundary. *Journal of Geophysical Research: Space Physics*, (Accepted pending minor revision), September 2025. doi: 2024JA033412.

Donald J. Williams and Norman F. Ness. Simultaneous trapped electron and magnetic tail field observations. *Journal of Geophysical Research*, 71(21):5117–5128, November 1966. ISSN 0148-0227. doi: 10.1029/jz071i021p05117. URL http://dx.doi.org/10.1029/JZ071i021p05117.

Simon Wing, Jay R. Johnson, Drew L. Turner, Aleksandr Y. Ukhorskiy, and Alexander J. Boyd. Untangling the solar wind and magnetospheric drivers of the radiation belt electrons.

Journal of Geophysical Research: Space Physics, 127(4), April 2022. ISSN 2169-9402. doi: 10.1029/2021ja030246. URL http://dx.doi.org/10.1029/2021JA030246.

S. L. Young. Empirical model for μ-scattering caused by field line curvature in a realistic magnetosphere. *Journal of Geophysical Research*, 107(A6), 2002. doi: 10.1029/2000ja000294. URL https://doi.org/10.1029/2000ja000294.

S. L. Young, R. E. Denton, B. J. Anderson, and M. K. Hudson. Magnetic field line curvature induced pitch angle diffusion in the inner magnetosphere. *Journal of Geophysical Research: Space Physics*, 113(A3), March 2008. ISSN 0148-0227. doi: 10.1029/2006ja012133. URL http://dx.doi.org/10.1029/2006ja012133.

Yiqun Yu, Xingbin Tian, and Vania K. Jordanova. The effects of field line curvature (flc) scattering on ring current dynamics and isotropic boundary. *Journal of Geophysical Research: Space Physics*, 125(8), August 2020. ISSN 2169-9402. doi: 10.1029/2020ja027830. URL http://dx.doi.org/10.1029/2020ja027830.

Chao Yue, Chih-Ping Wang, Larry Lyons, Jun Liang, Eric F. Donovan, Sorin G. Zaharia, and Michael Henderson. Current sheet scattering and ion isotropic boundary under 3-d empirical force-balanced magnetic field. *Journal of Geophysical Research: Space Physics*, 119(10):8202–8211, October 2014. doi: 10.1002/2014ja020172. URL https://doi.org/10.1002/2014ja020172.

Chao Yue, Jacob Bortnik, Wen Li, Qianli Ma, Chih-Ping Wang, Richard M. Thorne, Larry Lyons, Geoffrey D. Reeves, Harlan E. Spence, Andrew J. Gerrard, Matina Gkioulidou, and Donald G. Mitchell. Oxygen ion dynamics in the earth's ring current: Van allen probes observations. *Journal of Geophysical Research: Space Physics*, 124(10):7786–7798, October 2019. ISSN 2169-9402. doi: 10.1029/2019ja026801. URL http://dx.doi.org/10.1029/2019JA026801.

D. Zhang, J. B. Cao, X. H. Wei, and L. Y. Li. New technique to calculate electron alfvén layer and its application in interpreting geosynchronous access of ps energetic electrons. *Journal*

of Geophysical Research: Space Physics, 120(3):1675–1683, March 2015. ISSN 2169-9402. doi: 10.1002/2014ja020670. URL http://dx.doi.org/10.1002/2014JA020670.

Chen Zhou, Guobin Yang, Binbin Ni, Zhengyu Zhao, Ze-jun Hu, and Run Shi. Strong diffusion limit in the realistic magnetosphere: Dependence on geomagnetic condition and spatial location. *Journal of Geophysical Research: Space Physics*, 118(1):118–131, January 2013. ISSN 2169-9402. doi: 10.1029/2012ja018207. URL http://dx.doi.org/10.1029/2012JA018207.